TESI DOCTORAL UPF / 2015

Exploring Functional Connectivity Dynamics in Brain Disorders

A Whole-Brain Computational Framework for Resting State fMRI Signals

Murat Demirtaş

Thesis Supervisor

Prof. Gustavo Deco

Department of Information and Communication Technologies

Universitat Pompeu Fabra

Barcelona, October 2015

To Funda

Acknowledgments

I must thank Gustavo Deco, before anyone else, for welcoming me into the astonishing world of neuroscience. Six years later, at the edge of a new stage in my life, I appreciate this as a brave decision. Having resigned from my suffocating job as an occupational health and safety engineer, and drifting around to find something to pursue, I found myself fascinated by the interconnections between the mind and mathematics during his lecture. I never thought whether this fascination was enough to take such as challenge, and luckily neither did Gustavo. It took time for me to realize that this was one of the biggest moments in my life: an opportunity to work with a great scientist and wonderful boss.

As the process evolved I experienced excitement, frustration, desperation and hope. Whatever I felt, my wife Funda was always there to share all these moments. Then, Deniz stepped into our lives from out of nowhere. Through sleepless nights, I tasted the most delightful exhaustions in my life. I am grateful to my wife and my son, perhaps not for making this piece of work easier but for making it meaningful and worth.

Thanks also go to Emma Muñoz, Charles Soriano, Narcis Cardoner, Pablo Villoslada, Jose Luis Molinuevo and Charles Falcon for their invaluable collaboration and contributions.

I am grateful to the TV3 Marato Foundation and the UPF Department of Information and Communication Technologies, which provided the funding for this thesis. I also acknowledge Xavier Binefa and Karim Lekadir. I was a pleasure to assist you in the courses on probability and statistics. I thank the UPF administrative staff members Lydia, Xavi, Florencia and Santa for their outstanding support and problem-solving abilities. Thanks to all my colleagues in CNS group; especially Adría for helping me to translate the abstract of my thesis to Catalan, Ruggero, Cristian, Mario, Andrea, Bea, Etienne, Matthieu, Mohit, Rikkert, Selen, Gerald, Adrian, and former members Miguel, Tristan, Joanna, Larissa, Marina, Andres, Pedro and Johann for their companionship

and the wonderful times at their legendary Christmas lunches and barbeques. It is also amazing to see how many generations I witnessed in the group. I also thank my friend Onuralp for dragging me to Barcelona, and for the fruitful discussions ranging from science to our own existence. Also, I thank Dr. Francisco Collazos Sanchez.

During the limited time out of my studies, for fostering me with their masterful skills, I thank Javier Ros (Pimoli) for teaching me flamenco guitar. I also thank Luis Traver for introducing me to the world of Aikido.

I also thank my alma mater, Middle East Technical University, for giving me the vision to “be” in the world learning, thinking, struggling, changing with prudence but also with a revolutionary spirit.

I thank Barcelona for being a great home.

And finally, I am grateful to my parents for everything they have done for me.

Abstract

Brain activity, on every scale, spontaneously fluctuates, thereby exhibiting complex, dynamic interactions that manifest rich synchronization patterns. The past ten years have been dominated by studies intended to further our understanding of the mechanisms behind the dynamic interactions within the brain through the basis of its structural and functional connectivity structures. Moreover, there is a tremendous effort to unveil the role that these interactions play in psychiatric disorders. This thesis addresses these questions from novel perspectives. The first pillar of this thesis is the time-varying nature of the dynamic interactions between brain regions. The second pillar is the role that FC dynamics play in clinical populations. The third pillar uncovers the connectivity structure that links the observed anatomical and functional connectivity patterns through computational modeling. The final pillar of the thesis proposes a mechanistic explanation for brain disorders.

Resum

L'activitat del cervell fluctua espontàniament a diferents escales i per tant exhibeix interaccions dinàmiques i complexes que manifesten patrons de sincronització rics. Durant els darrers deu anys han abundat els estudis orientats a comprendre els mecanismes que hi ha darrere les interaccions cerebrals basant-se en les seves estructures funcionals i estructurals. A més, existeix un esforç ingent per desvetllar el paper que aquestes interaccions juguen en els trastorns psiquiàtrics. Aquesta tesi aborda les qüestions esmentades des de noves perspectives. El primer pilar d'aquesta tesi és la naturalesa variable en el temps de la interacció dinàmica entre diferents regions del cervell. El segon pilar és el paper que aquesta dinàmica de connectivitat funcional juga en diferents poblacions clíniques. El tercer pilar es centra en l'ús de models computacionals per determinar l'estructura de connectivitat que relaciona els patrons de connectivitat funcional i anatòmics observats. El quart pilar de la tesi proposa una explicació del mecanisme dels trastorns cerebrals.

Preface

Technological advances in neuroimaging studies have begun to provide new tools with which to study the brain. Despite being in their infancy, these tools are flooding the field with information about brain function at a rate that has not heretofore been seen in the history of neuroscience. The scientific community is digesting this information with the aspiration to understand the complex mechanisms behind brain function. One of the most influential findings concerns the widespread complex interactions between brain regions in a spontaneous fashion (i.e., resting-state fluctuations). The question that must now be answered is how the complex interactions in the brain are related to the psychiatric disorders.

Specifically, neuroimaging techniques such as fMRI have provided robust evidence regarding large-scale coordinated fluctuations in the brain at rest (i.e., the subject is idled by her own pace, with no explicit physical or mental task being given). Within a short time, scientists around the world have reported complex spatiotemporal connectivity structures (i.e., resting-state networks; RSNs) appearing in resting-state neuroimaging recordings. In parallel, many studies have shown the clinical significance of RSNs in psychiatric disorders. The research has tackled the problem at the anatomical and functional connectivity levels. However, there is a huge overlap in the altered connectivity profiles between distinct clinical populations, and there are many controversies in regard to how these alterations relate to brain disorders. One major problem is that the connectivity patterns observed through the neuroimaging modalities are highly complex and interdependent. This makes the interpretation of the results non-trivial; hence the current approaches fail to provide a mechanistic understanding of brain function in the clinical context.

This work investigates the interplay between the static and dynamic properties of brain connectivity. We believe that the time-dependent changes in functional connectivity patterns contain information critical to our understanding of the disease dependent alterations in brain function. Furthermore, we assert that the complex neuroimaging data

cannot be grasped by relying solely on the current analysis techniques. Instead, we believe that the fundamental problem in contemporary neuroscience is the inadequacy of coherent, unifying theoretical models. For this reason we have endeavored to improve and implement available computational models as the means to unveil the underlying mechanisms behind the observed functional connectivity. Thus, in our research we relied on the definition of effective connectivity. We would consider it an honor and a privilege to add another drop to the ocean of knowledge.

The first chapter begins with an overview of the concepts that make up the framework of this thesis. We start with a brief introductory text regarding the clinical neuroscience, and then we review the recent advances in neuroimaging with a focus on resting-state fMRI. We introduce the up-to-date discussions and recent paradigm shifts in the field, such as dynamic functional connectivity. Then, in later sections, we provide an overview of the tools that aid in the investigation of connectivity in clinical populations, such as anatomical connectivity and statistical comparisons. Finally, we review the computational models that were used to link the structure and function.

Chapter II provides preliminary works that serve as a framework for the analyses in the prospective chapters. In this chapter we discuss how can we interpret the functional connectivity data and how can we deal with still-open questions such as global average signal.

Chapters III and IV introduce the analysis of FC dynamics in affective disorders. Chapter III comprises our effort to link the conventional FC changes in major depressive disorder to the dynamic FC. In this chapter we introduce the use of variability of FC. The following chapter (chapter IV) takes this approach a bit further, providing a mechanistic approach by which to understand the static and dynamic alterations in bipolar disorder. Specifically, this chapter introduces the use of computational, model-based estimation of whole-brain EC.

Chapters V and VI involve two studies regarding clinical conditions in the opposite side of the age spectrum: Intrauterine growth restriction (IUGR) and Alzheimer's disease

(AD). In these chapters we extend the approaches presented in chapter IV by using more advanced computational models. In chapter V, as an alternative to correlation-based FC measures, we study phase-lock values of newborns and infants with IUGR. The Kuramoto model allows us to simulate directly in the phase domain and thereby provide a trivial link between model and empirical connectivity measures. Chapter VI proposes a mechanistic model for the progression of Alzheimer's disease based on the alterations in functional connectivity.

The studies presented in Chapter III and Chapter IV are submitted to peer-reviewed journals with following titles:

Dynamic Functional Connectivity Reveals Altered Variability in Functional Connectivity Among Patients with Major Depressive Disorder.
Murat Demirtaş, Cristian Tornador, Carles Falcon, Marina López-Solà, Rosa Hernández-Ribas, Jesús Pujol, José M. Menchón, Narcis Cardoner, Carles Soriano Mas, Gustavo Deco

The Whole-Brain Based Mechanistic Model of the Resting-State Functional Connectivity Dynamics: A Pilot Study on Bipolar Disorder.
Murat Demirtaş, Dina Popovic, Eduart Vieta, Luis Pintor, Vesna Prckovska, Pablo Villoslada, Gustavo Deco

The manuscripts of the studies presented in Chapter V and Chapter VI are ready submit to peer-reviewed journals:

Altered Functional Connectivity Dynamics in Neonates and Infants with Intrauterine Growth Restriction: A Whole-Brain Model of Resting-State Functional Connectivity.
Murat Demirtaş, Emma Muñoz Moreno, Elisenda Eixarch, Gustavo Deco

The Alterations in Whole-Brain Connectivity Dynamics in Alzheimer's Disease Revealed by Variability of Functional Connectivity and Effective Connectivity.
Murat Demirtaş, Carles Falcon, Juan Domingo Gispert, Alan Tucholka, José Luis Molinuevo, Gustavo Deco

Table of Contents

I. Introduction

Men ought to know that from nothing else but the brain come joys, delights, laughter and sports, and sorrows, griefs, despondency, and lamentations

Hippocrates

We, as human beings, long ago realized the role that the jelly-like organ up in our heads plays in generating our experience. It was Hippocrates who, in around 400 B.C., took the brain as a medical subject from which all our mental disorders, as well as our experience, originate (Bear et al., 2007). Then Galen, in around 150 A.D., reported the relationship between nerves and muscles that give rise to our actions. However, we had to wait more than 2,000 years to catch a glimpse of how the brain might actually operate. In one line of research, scientists such as Golgi and Ramon y Cajal revealed the structure of the brain cells, finding different types of neurons with complex structures called dendrites and axons (Bear et al., 2007). At the other side of the story, there was growing evidence linking brain dysfunction and mental disorders. During the mid-twentieth century, Hodgkin and Huxley's seminal studies on the electrical properties of nerve cells led to the age of discovery of the dynamical functioning of the brain (Hodgkin and Huxley, 1952). Since then, the essence of this chain of events has been constant: The efforts to understand the structural architecture and functional dynamics of the brain brought forth the genesis of new knowledge in each field of research. However, clinical evidence was the major element that allowed us to make sense of such new knowledge. Moreover, embracing all the science-- bringing the observed evidence and hypothetical ideas to life--has always been limited to how well we could describe them mathematically.

I.I. From Mental Disorders to Brain Disorders

Phineas Gage, in 1868, survived an occupational accident in which an iron bar passed through the left side of his skull. As a result, the dramatic changes in his personality were attributed to the damage to his brain's left frontal lobe (Harlow, 1868). Seven years earlier, Paul Broca published the autopsy findings of Louis Victor Leborgne, who had experienced a sudden loss of his speech ability, and showed a lesion in the left inferior frontal gyrus (Broca, 1861). In the twentieth century, as a result of the removal of bilateral medial temporal lodes in epilepsy surgery, Henry Gustave Molaison (known as H.M.) lost his ability to transfer his short-term memory to long-term memory (Scoville and Milner, 1957). Finally, the behavioral changes due to the removal of interhemispheric connections were reported (Gazzaniga et al., 1963; Myers and Sperry, 1953). These four groundbreaking cases led to the idea of "dysconnexion syndromes," thus emphasizing the role of disconnection between cortical regions in the genesis of clinical disorders (Geschwind, 1965a, 1965b). During the past two decades, advances in neuroimaging have made it possible to test the disease related alterations using noninvasive techniques. Recently, the researchers were able to reconstruct the lesions in these seminal cases using diffusion weighted imaging (Schotten et al., 2015) (Figure I.1).

We shall not provide an overview of the literature of neuroimaging studies before we highlight the distinction between the aforementioned cases (i.e., Gage, Leborgne, and Molaison) and widespread psychiatric diseases. As an analogy, we can borrow the definition of "rare diseases," which has important implications in genetic research. Technological progress has allowed researchers to identify genetic markers of most rare diseases, mainly due to their extremely low prevalence and dramatic consequences (Aymé and Schmidtke, 2007). However, despite tremendous efforts the genetic origins of highly prevalent, complex diseases (such as psychiatric and developmental disorders) remain obscure (Motulsky, 2006). Similarly, the clinical populations of focus in this thesis, as in most of the recent literature, comprise highly prevalent, complex disorders (Major Depression Disorder, Bipolar Disorder, Intrauterine Growth Restriction and Alzheimer's Disease). Noting this, we argue that it is very unlikely that simple loci will be found for any of these disorders. Instead, we believe that the overlap, as well as poten-

tially contradictory findings, between different disorders is a natural consequence of the mechanisms behind the working principles of the brain. Therefore, we have focused, in a broader context, on the relationship between the large-scale spontaneous coordination in the brain and psychiatric disorders.

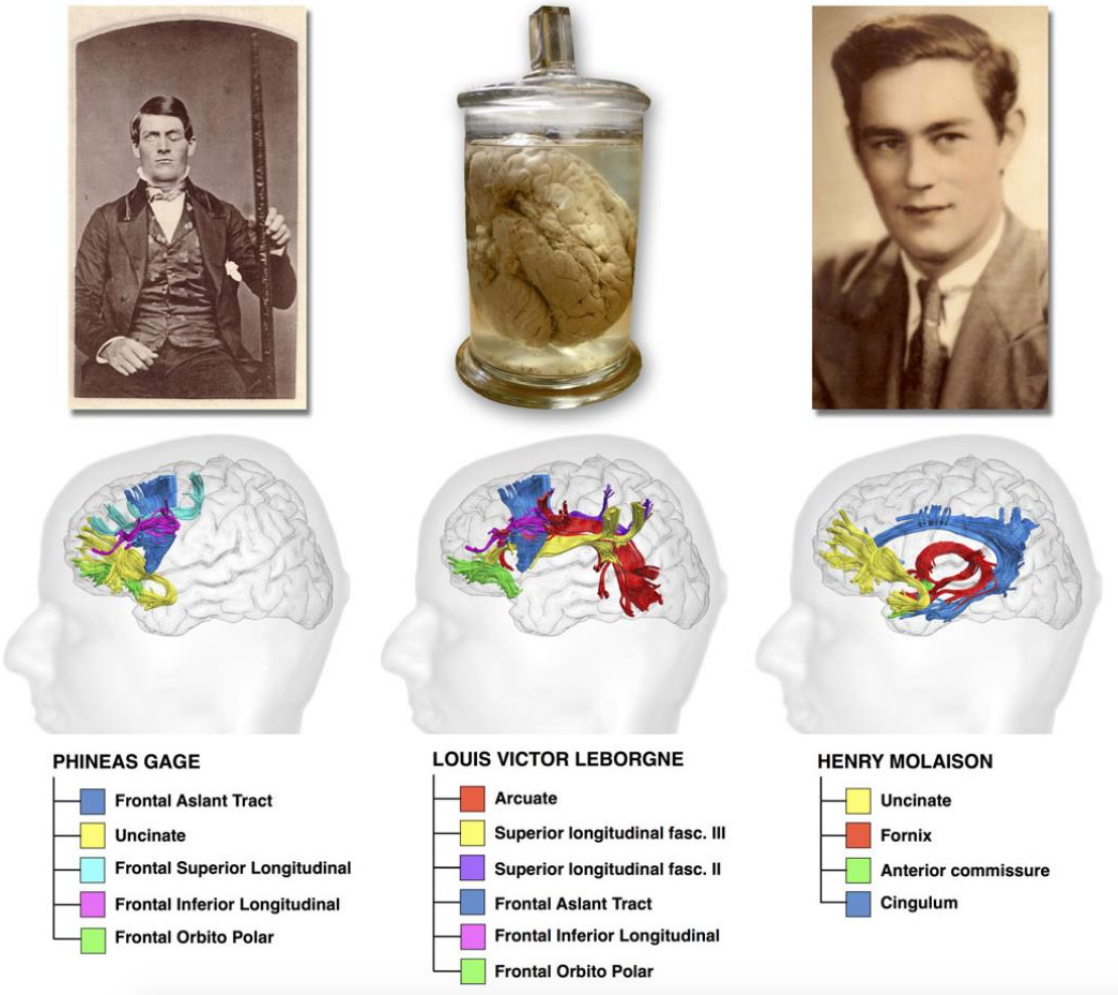

Figure I.1. Reconstructions of the lesions in the brains of Phineas Gage, Louis Victor Leborgne and Henry Molaison (adapted from Thiebaut de Schotten et al., 2015).

I.II. Neuroimaging of the Brain

Magnetic resonance imaging (MRI) and computed tomography (CT) were introduced (Herman, 2009) during the last quarter of the twentieth century. Both technologies allowed structural imaging of body tissues and became major tools in medical diagnostics. However, the use of MRI became relatively more popular because its working principles do not rely on ionized radiation. Shortly after, single-photon emission computed tomography (SPECT) and positron emission tomography (PET) techniques were implemented in brain research (Bailey et al., 2005; Herman, 2009). However, unlike, MRI and CT, these techniques also facilitated indirect measurement of brain activity based on fluctuations in metabolic demand due to underlying neuronal activity. Then a similar principle was implemented in MRI, whereby brain activity could be inferred by using blood-oxygen-level-dependent (BOLD) changes at each voxel (Ogawa et al., 1990). The widespread use of so-called functional MRI (fMRI) changed the extent of neuroscience research dramatically. Considering the low temporal resolution of fMRI, the use of magnetoencephalography (MEG) (Cohen, 1968) also increased in the past decade.

I.II.i . Evoked and Spontaneous Brain Activity

The high-temporal-resolution recordings of brain activity made it possible to compare the changes in brain signals provoked by a given task. Where possible, the task-evoked changes were measured by single-cell recordings or by regional recordings like local field potentials (LFP, i.e., the electrophysiological signal recorded via extracellular electrodes). These studies reported remarkable evidence showing how the information regarding the environment was encoded at the neuronal level. However, these invasive techniques were rarely used in human subjects, and it was not possible to account for changes in whole-brain activity with these techniques. An old and widely used technique--electroencephalography (EEG)--provided a measure for the changes in the brain's electrophysiological activity recorded noninvasively through the scalp (Swartz, 1998). By averaging the EEG signal while introducing a stimulus across trials, the

event-related potentials (ERPs) were estimated, reflecting the change in electrophysiological activity locked to the given stimulus. Several experimental paradigms, including oddball stimulus, revealed specific patterns of activity changes (such as Mismatch Negativity, or MMN) reflecting the complex organization of the neuronal assembles (Näätänen and Alho, 1995). The ERPs were shown to have clinical significance. For example, alterations in the ERPs of Alzheimer's patients (Boutros et al., 1995), or in the MMN-related ERPs of schizophrenia patients (Umbricht et al., 2003; Umbricht and Krljes, 2005).

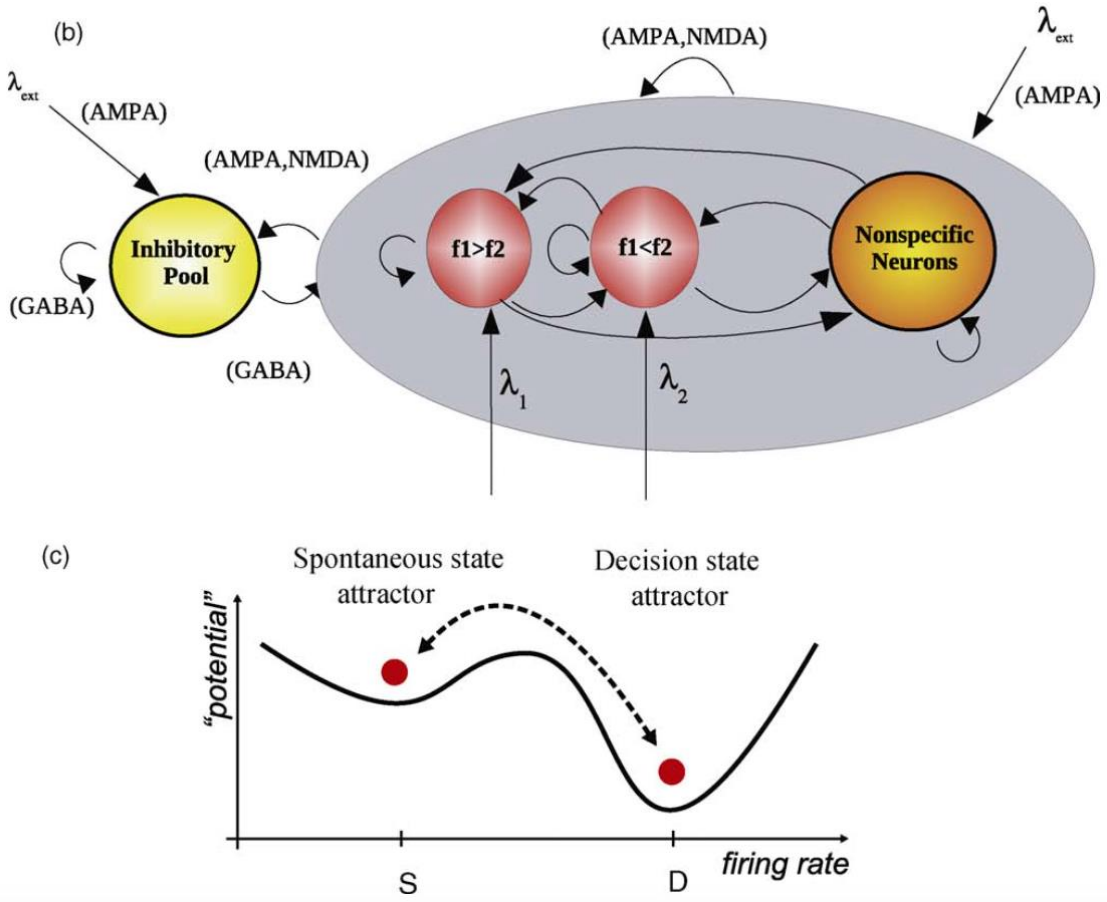

Figure I.2. Noise induced transitions in attractor models. Top: overview of the attractor neural network model. Bottom: Transition to decision attractor state from spontaneous state. (adapted from. Deco et al., 2009)

The high spatial resolution of fMRI motivated researchers to investigate task-evoked neuronal activations in the brain (Ogawa et al., 1990). A typical experimental procedure comprised the repetitive imaging of the brain during task and a period of resting state in

between tasks. A critical procedure in task fMRI studies was one in which the evoked activity was computed relative to the baseline activity recorded during the resting state. This baseline activity was deemed to be noise that was independent from the evoked responses. However, optical imaging of cat visual cortex showed that the ongoing (or spontaneous) activity in the cortex caused variability in the evoked responses (Arieli et al., 1996). At the same time (Biswal et al., 1995) found spontaneous coactivation in motor cortex during the resting state. Furthermore, other studies showed deactivations of certain regions during task performance (Mazoyer et al., 2001; Shulman et al., 1997).

It has long been known that spontaneous activity in the brain is an underlying working mechanism as opposed to being an observation error (Deco et al., 2009b; Deco and Thiele, 2009; Rolls and Deco, 2011)(Figure I.2). Spontaneous activity begins at the level of individual neurons. Many studies have shown how the noise in spiking neurons could shape complex phenomena such as complex oscillatory activity patterns, decision-making and MMN. As a result, current knowledge in neuroscience suggests that noise (spontaneous/ongoing activity) is one of the major blocks that define the complex organization of the brain.

I.II.ii . Foundations of Resting-State fMRI

The study that is considered the foundation of resting-state fMRI is Bharat Biswal's findings on low-frequency temporal correlations in the motor cortex during rest, implying that there is indeed functional connectivity between brain networks in the absence of any explicit task (Biswal et al., 1995). However, there was limited interest in rs-fMRI until the study by Gusnard and Raichle that pointed out the baseline activity in the brain and coined the term “default mode” in 2001 (Gusnard and Raichle, 2001). In the review, Gusnard and Raichle questioned the metabolic cost of baseline activity and pointed out the activations as well as deactivations in the brain during rest. Gusnard also discussed the relationship between resting-state FC and consciousness (Gusnard, 2005). Further evidence also supported the role of the medial prefrontal cortex and parietal cortex in mental self-representation (Lou et al., 2004). Furthermore, Raichle et al. (2001) emphasized that a functionally connected network of regions (comprising posterior cin-

gulate, precuneus, medial prefrontal cortex and hippocampus) is consistently observed during the baseline state, and defined this particular network as a default mode network (DMN) (Raichle et al., 2001). Gusnard emphasized the role of the medial prefrontal cortex during rest and self-referential mental activity (Gusnard et al., 2001). Later studies showed that most of the observed temporal correlations between regions were originated from low-frequency (0 – 0.01 Hz) fluctuations (Cordes et al., 2002, 2001). Another crucial finding was that the two core regions of DMN, i.e., the posterior cingulate and ventral anterior cingulate, are activated during rest and attenuated during cognitive processing (Greicius et al., 2003). These findings are also supported by Laufs' work on simultaneous EEG-fMRI recording, which suggests that DMN activity is related to alpha oscillations (Laufs et al., 2003).

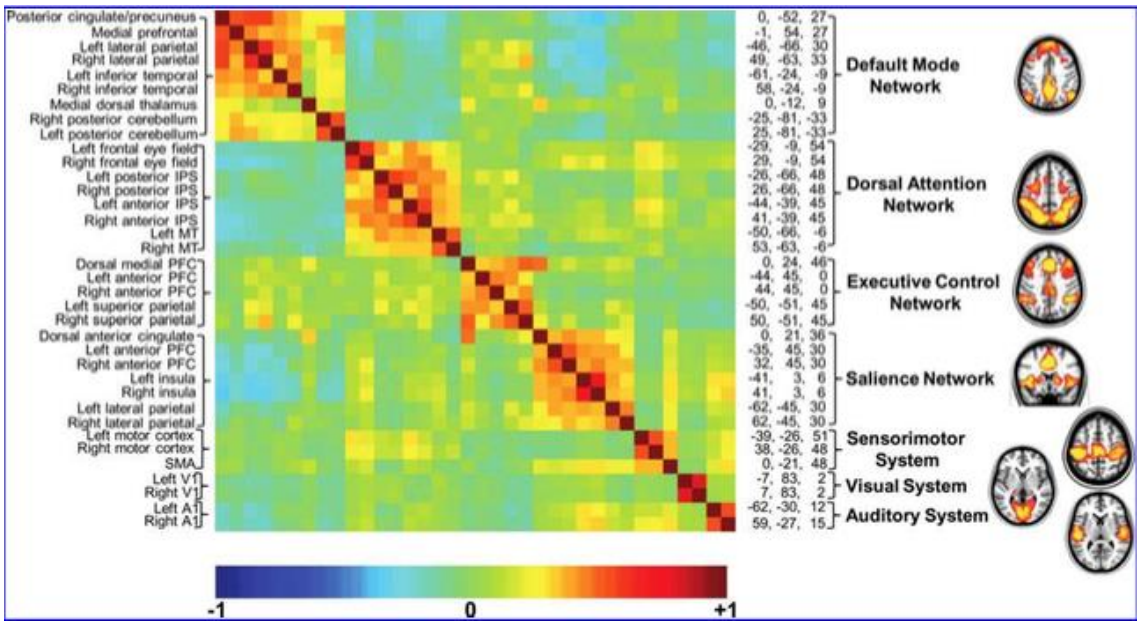

Figure I.3. The resting-state networks (RSNs) revealed by Independent Component Analysis (ICA) (adapted from Raichle, 2011).

The extent of resting-state fluctuations was increased as new evidence showed low-frequency fluctuation and temporal synchrony of BOLD signals not only persist, but also increased under sedation (J. Kiviniemi et al., 2005). In the same vein, the comparison of resting-state and early sleep stages showed that the low-frequency fluctuations increase during sleep (Fukunaga et al., 2006). Furthermore, another study investigated the DMN in anesthetized monkeys, showing that this network was still active during

anesthesia (Vincent et al., 2007). Other studies confirm the persistence of DMN during sleep and while under sedation (Greicius et al., 2008; Horovitz et al., 2009, 2008). The intra- and inter-variability of FC was also questioned, and some of the networks were found to be stable (Waites et al., 2005). Other studies also showed that RSNs are consistent among individuals (Damoiseaux et al., 2006).

Subsequent to the discovery of DMN, other resting-state networks were identified (Fransson, 2005) through a similar approach. Moreover, after Beckmann and Smith (2004) introduced the use of independent component analysis (ICA), many other RSNs were discovered (Beckmann et al., 2005)(Figure I.3). Another important finding was the inverse relationship between two major RSNs, namely task-positive (TPN) and task-negative (TNN) networks (Fox et al., 2005; Fox and Raichle, 2007)(Figure I.4). Methodological concerns were raised against the estimation of these anti-correlated networks (Murphy et al., 2009). However, the existence of anti-correlated networks was confirmed using alternative methodologies (Fox et al., 2009; Uddin et al., 2009).

The resting-state fMRI approach was subjected to many other criticisms in regard to its methodology. The most important concern was the difficulty in removing artifacts from resting-state BOLD signals. The possible confounds varied from movement artifacts and physiological artifact such as heart-rate variability and respiration to hardware- and software-related issues. The naming of RSNs was also controversial. Some studies suggested the term “temporally coherent networks” (Calhoun et al., 2008), while others argued that the current terminology does not reflect the phenomenon and instead preferred the term “intrinsic connectivity networks” (Habas et al., 2009).

Despite the criticisms, the evidence was in favor of the functional relevance of RSNs (De Luca et al., 2006). Several studies showed that learning could modify RSNs (Albert et al., 2009; Lewis et al., 2009). Graph theoretical analysis of resting-state FC found a relationship between IQ and efficiency (van den Heuvel et al., 2009b). After the developments in anatomical fiber tracking, Greicius et al. (2009) showed that the resting-state correlations were closely related to the underlying structural connectivity (Greicius et al., 2009). Later this finding was extended to include the structural origins of RSNs

(Damoiseaux and Greicius, 2009; van den Heuvel et al., 2009a). Structural analysis emphasized the role of high-influence regions (or hubs) in the emergence of FC (Achard et al., 2006). Computational models of resting-state activity further refined this relationship (Honey et al., 2009) and showed the effect of noise and delays in resting-state FC (Ghosh et al., 2008). Furthermore, computational models confirmed the existence of anti-correlated networks (Deco et al., 2009a).

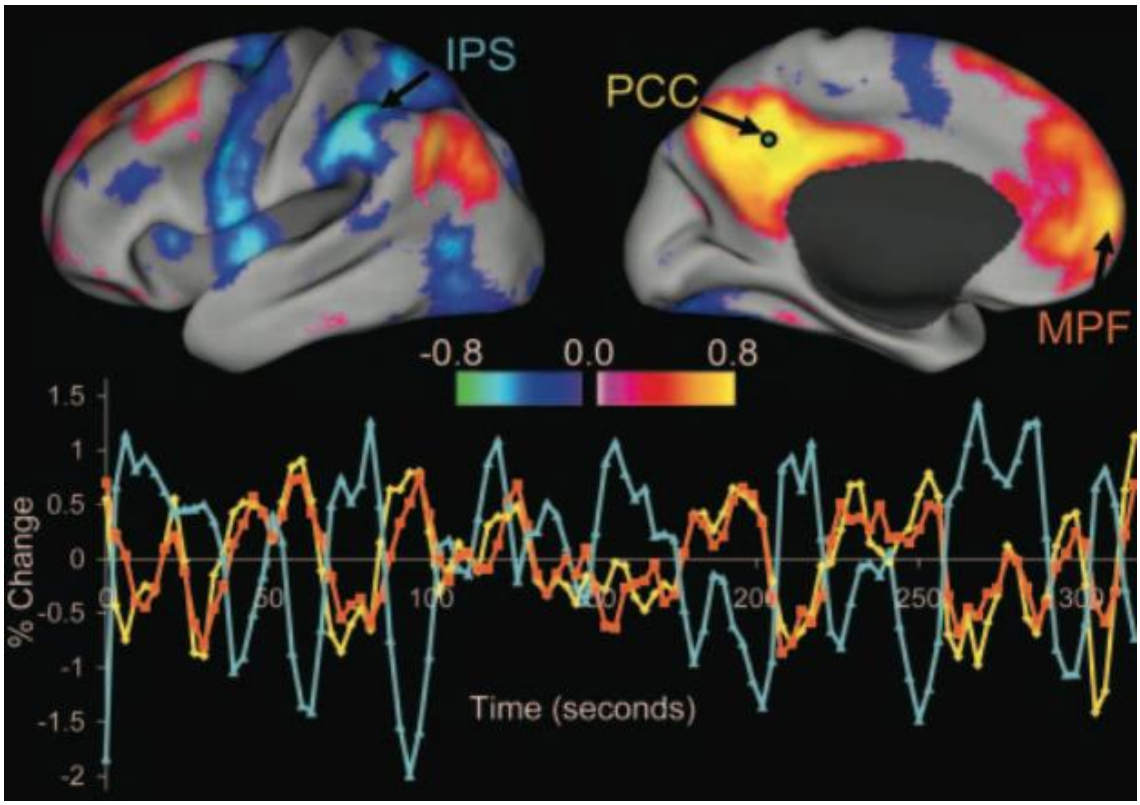

Figure I.4. Seed-based correlations of PCC illustrating anti-correlations. Top: Positive and negative correlated regions with PCC. Bottom: Time courses of PCC and IPS seeds (adapted from Fox et al., 2005).

The RSNs revealed by fMRI BOLD signals were also observed in other imaging modalities such as EEG (Mantini et al., 2007) and MEG (Brookes et al., 2011). Logothetis (2001) showed the neuronal origins of resting-state BOLD time signals by simultaneously recording local field potentials along with fMRI (Logothetis et al., 2001). Other multimodal imaging studies showed that the decrease of alpha and beta power was associated with the resting-state BOLD signals (Tagliazucchi et al., 2012b). Detailed in-

vestigations of regions related to DMN such as ACC (Margulies et al., 2007), and Precuneus (Cavanna and Trimble, 2006) were also conducted.

Finally, resting-state activity was investigated from a developmental perspective. The development of DMN and other RSNs showed particular patterns in children (Fair et al., 2009, 2008). Through the aging process, the DMN was attenuated by normal aging (Damoiseaux et al., 2008). Furthermore, the analysis of the changes in long-range connectivity by age revealed decreased co-activation between PCC and mPFC with respect to age (Andrews-Hanna et al., 2007).

I.II.iii . Functional Connectivity

The fundamental concept that uncovered the importance of resting-state fluctuations was the functional connectivity (FC) between brain regions (Friston, 2011). Paradoxically, FC has always been the most controversial concept in resting-state research. Various connectivity measures (such as correlation coefficient, phase coherence, mutual information, etc.) were explored in order to quantify FC. Among them, Pearson's correlation coefficient has been the most widely used measure for FC (Bandettini et al., 1993; Biswal et al., 1995).

The vulnerability of FC measures to the confounding factors such as physiological noise and the validity of the available statistical approaches were frequently addressed in methodological studies (Birn, 2012). Furthermore, relating the structural correlates of the connectivity to FC has been considered a highly complex, "multifaceted" problem (Horwitz, 2003; Rogers et al., 2007).

The beginning of the observations regarding the functionally correlated low-frequency spontaneous activity in the brain was based on seed-based analysis of FC (Biswal et al., 1995). Studies that led to the discovery of other resting-state networks followed seed-based analysis (Fransson, 2005; Greicius et al., 2003). In brief, seed-based analysis is a hypothesis-driven approach in which the FC of a predefined seed is estimated, thus ignoring the FC in the rest of the brain. The seeds are selected based on previous literature

that emphasizes the role of a specific region. For example, the studies that investigate the FC of task-negative or DMN often choose posterior cingulate as a seed of interest. The anti-correlations between resting-state networks were first observed in seed-based analyses (Fox et al., 2005)(Figure I.4).

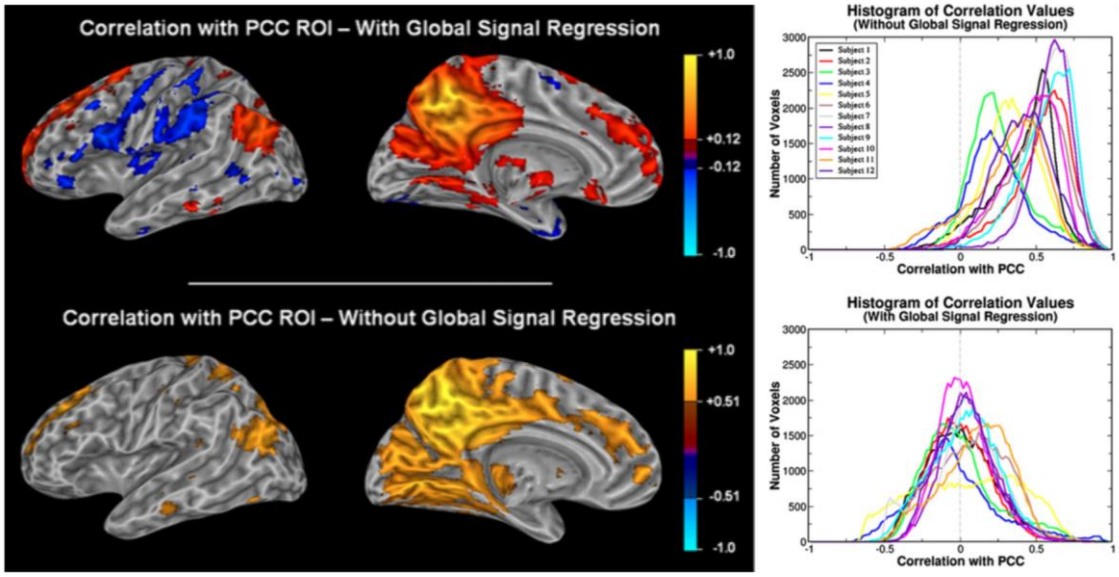

Figure I.5. Demonstration of artificially introduced anti-correlations. Left: correlations with PCC seed with and without global signal regression. Right histogram of correlation coefficients before and after global signal regression (adapted from Murphy et al., 2009).

The most frequently discussed concern occurred due to the impact of a standard preprocessing procedure that removes the global BOLD fluctuations from the signal (i.e., global signal regression). Global signal regression (GSR) was intended to remove the fluctuations in the BOLD signal that reflected correlated physiological artifacts rather than being of neuronal origin. A mathematical analysis of the procedure revealed that GSR artificially induces anti-correlations to the time series by shifting the distribution of correlation coefficients toward zero (Murphy et al., 2009)(Figure I.5). However, Fox et al., (2009) showed that the anti-correlations were also observed without GSR (Fox et al., 2009). Additionally, other studies found that the negative correlations might predict behavioral performance (Kelly et al., 2008).

Apart from the preprocessing concerns, seed-based correlations were problematic because they only reflected the hypothesis-driven information but ignored the remaining

interactions and introduced bias to the analysis. Furthermore, an increase in the number of seeds would cause additional problems due to difficulties in controlling type-I (and type-II) errors in statistical analyses (multiple comparisons). Independent component analysis (ICA) was proposed as a means to provide a solid statistical framework with which to analyze resting-state networks (Beckmann and Smith, 2004).

ICA decomposes the signal, which is assumed to be a mixture of independent, non-Gaussian sources, into additive components. After centering the signal on zero (subtracting the mean from the signal), whitening (decorrelating) and dimensionality reduction are performed (based on PCA or SVD), whereupon the components are extracted by minimizing the mutual information (independence) and maximizing the non-Gaussianity. Because fMRI signals comprise less temporal data than spatial data, ICAs are extracted spatially (Beckmann and Smith, 2004; Damoiseaux et al., 2006; De Luca et al., 2006). The drawback of the ICA approach is that the relevant ICs are manually identified and separated from physiological artifacts (De Luca et al., 2006).

I.II.iv . Dynamic Functional Connectivity

Another important debate regarding FC was the assumption that the correlation structure between regions is stationary over time. One of the first studies that investigated the temporal dynamics of resting state introduced a spatiotemporal model of RSNs based on the point process (Vedel Jensen and Thorarinsdottir, 2007). Later, the time-frequency analysis of RSNs based on wavelet analysis and sliding-window analysis revealed that the relationship between two major RSNs (TNN and TPN) changes over time (Chang and Glover, 2010). In brief, they illustrated that the temporal correlations between these network waxes and wanes in time. Non-stationary dynamics in the resting-state fluctuations were also observed in animal studies (Majeed et al., 2011, 2009; Thompson et al., 2013). These non-stationary dynamics were further confirmed by comparing the observed time-dependent changes in resting-state FC with a stationary null model (Zalesky et al., 2014)(Figure I.7). Many other studies argued for the non-stationarity of resting-state FC (reviewed by (Hutchison et al., 2013)) and that the fluctuations in dFC are periodic in nature (Handwerker et al., 2012). Moreover, the dynamic

changes in FC patterns are not limited to the time domain. Evidence suggests that variations in FC patterns are frequency-dependent (Salvador et al., 2007). The most conventional approach to the estimation of dFC is the sliding-window analysis approach, which involves the computation of FC for smaller chunks of windows over time (Allen et al., 2014)(Figure I.6).

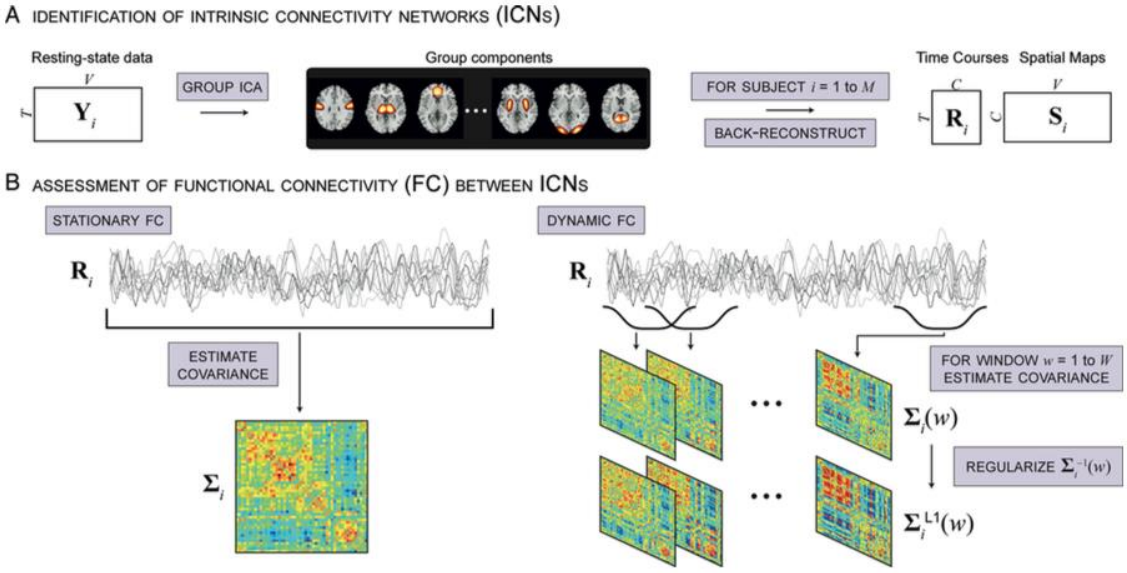

Figure I.6. The procedure for estimation of dynamic FC using sliding-window analysis and ICA (adapted from Allen et al., 2014).

Different approaches have also been proposed as the means to estimate dFC (Glerean et al., 2012; Kang et al., 2011; Smith et al., 2012; Tagliazucchi et al., 2012a). Tagliazhucchi et al. (2012) proposed the construction of co-activation patterns based on a point-process characterization of BOLD time series. Moreover, their work also illustrated criticality in the dynamics of FC. Smith et al., (2012) modified the widely used spatial ICA approach, and defined "temporal functional modes" in resting-state fMRI using the temporal counterpart of ICA. They also found that DMN is subdivided into distinct but spatially overlapping networks having their own temporal dynamics. This approach was further extended to create complex spatiotemporal maps among subjects (Harrison et al., 2015).

As an immediate implication of dynamic FC, several studies found differences in dynamical interplay between networks during task performance (Betti et al., 2013; Leonardi et al., 2014; Leonardi and Van De Ville, 2015). In another study, Kucyi and Davis (2014), found associations between the temporal variability in DMN (particularly in the medial temporal lobe) and the degree of ongoing mind wandering (Kucyi and Davis, 2014). A recent study showed that although the static organization of RSNs is stable across different age groups, the dynamical expression of these networks changes over time (Hutchison and Morton, 2015). Another study found increased repertoire of connectivity states in dFC after introducing a psychedelic chemical called psilocybin (Tagliazucchi et al., 2014). A recent study provided supporting evidence for the role of dynamic FC in the content of the experience using the dynamics in rs-fMRI of awake and anesthetized monkeys (Barttfeld et al., 2015). They found restricted functional repertoire in anesthetized monkeys and showed that the content of the dynamic configurations might be a signature of consciousness. The systematic comparison of task and resting-state activation showed that the precuneus--one of the core regions of DMN--is co-activated with fronto-parietal networks and serves as a dynamic hub (Utevsky et al., 2014).

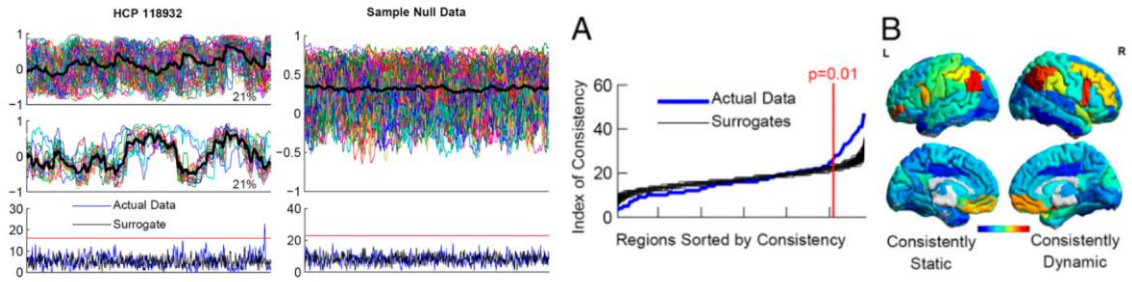

Figure I.7. Time-resolved FC. Top: Temporal evolution of functional connectivity for a single subject and surrogate data. Bottom: Regions showing static and dynamic FC (adapted from Zalesky et al., 2014).

Glerean et al., (2012) provided a different approach by which to tackle dFC. They proposed the use of instantaneous phases of the rs-fMRI BOLD time series, which were extracted using Hilbert transform (Glerean et al., 2012). Their approach allowed the representation of dFC in the same temporal resolution with the time series. However, they limited their analysis to the 0.04 - 0.07 Hz frequency band, as Hilbert transform requires

a narrowband signal to represent the phases reliably. The choice of this particular band was not arbitrary but was due to the fact that 0.04 - 0.07 Hz narrowband was the least noise-prone according to the rs-fMRI literature (Figure I.8).

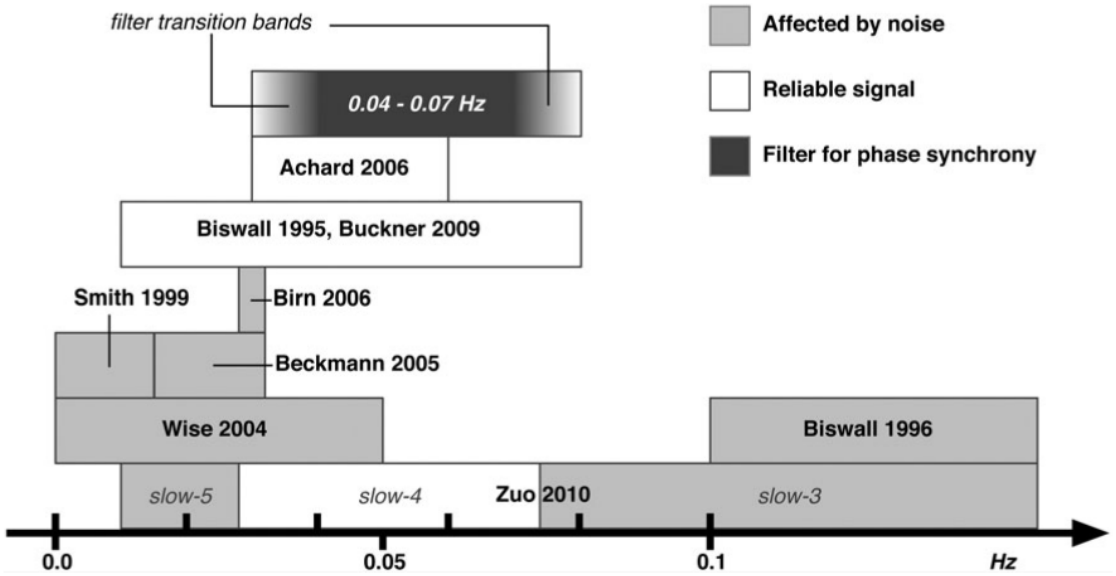

Figure I.8. Comparison of frequency bands used in rs-fMRI research. Shaded regions indicate the frequency bands that are affected by noise. 0.04 – 0.07 Hz frequency band was the most convenient (adapted from Glerean et al., 2012).

Sakoğlu et al., (2010) showed differences in static and dynamic functional network connectivity between schizophrenia patients and healthy controls (Sakoğlu et al., 2010). Subsequent studies also showed alterations in the dynamic FC of schizophrenia patients, such as dwell time of the states and disruptions in thalamo-cortical connectivity (Damaraju et al., 2014). Different methods, such as independent vector analysis, also showed altered variability between fronto-parietal, cerebellar and temporal regions in schizophrenia patients (Ma et al., 2014). Furthermore, the temporal changes in graph metrics found differences in schizophrenia patients (Yu et al., 2015). Another recent study compared dynamic FC networks in schizophrenia and bipolar Disorder (Rashid et al., 2014), finding differences in dynamic states in both disorders. Alterations in the dwell time of DMN were also observed between Alzheimer's Disease and mild cognitive impairment (Jones et al., 2012).

Concurrently, the possible mechanisms behind the dynamic FC were studied through means of large-scale computational modeling. Multivariate modeling of rs-fMRI BOLD signals showed two major states of activation representing high- and low-activity in DMN (Ferguson and Anderson, 2012). In another study, researchers used structural connectivity (obtained by DTI) to determine which regions played a role in orchestrating the dynamic FC (Lv et al., 2013). They found that the so-called hub routers were located in DMN, and they provided a clinical application of altered routers in post-traumatic stress disorder (PTSD) patients. Schmit et al., (2014), as one of the first mechanistic model approaches in clinical populations, used the Kuramoto model to study the abnormal synchronization patterns in various frequency bands in epilepsy patients using EEG (Schmidt et al., 2014). They found potential regions that might drive the seizures in those patients, and they showed the high predictive power of their analysis.

Deco et al., (submitted) showed that at-rest regions of the brain operate at the edge of a critical bifurcation point between the noisy and oscillatory regimes. They simulated rs-fMRI BOLD signals using the Hopf normal model and found that this critical point was also necessary for the generation of FC dynamics. Another recent study used the Fitz-Hugh-Nagumo model to investigate dynamics of resting-state signals (Vuksanović and Hövel, 2015). They showed that the observed resting-state signals emerged from the maximization of synchrony and variability in synchrony. Furthermore, the relationship between the criticality of brain states (specifically, FC dynamics) and consciousness was recently discussed (Carhart-Harris et al., 2014).

I.II.v . Measuring Structural Connectivity

The usual way to track the neural fibers in the brain, prior to the emergence of advanced neuroimaging techniques, involved invasive methods. Principally, these techniques were only suitable for use in animal studies, and they required the sacrifice of the animal being investigated. Chemical stains, which were injected to the fiber tracks, were then traced by slicing the brain into thin segments (Schmahmann et al., 2007; van der Want et al., 1997). Various studies contributed to the creation of large-scale connectivi-

ty profiles of macaque brain (Kötter, 2004; Stephan et al., 2001), and led to detailed topological analysis of brain connectivity. Although recent techniques such as CLARITY (Chung and Deisseroth, 2013) or saturated reconstruction (Kasthuri et al., 2015) provided very-high-resolution representation of fiber tracks, it was not possible measure anatomical connectivity of a living subject with available functional connectivity data.

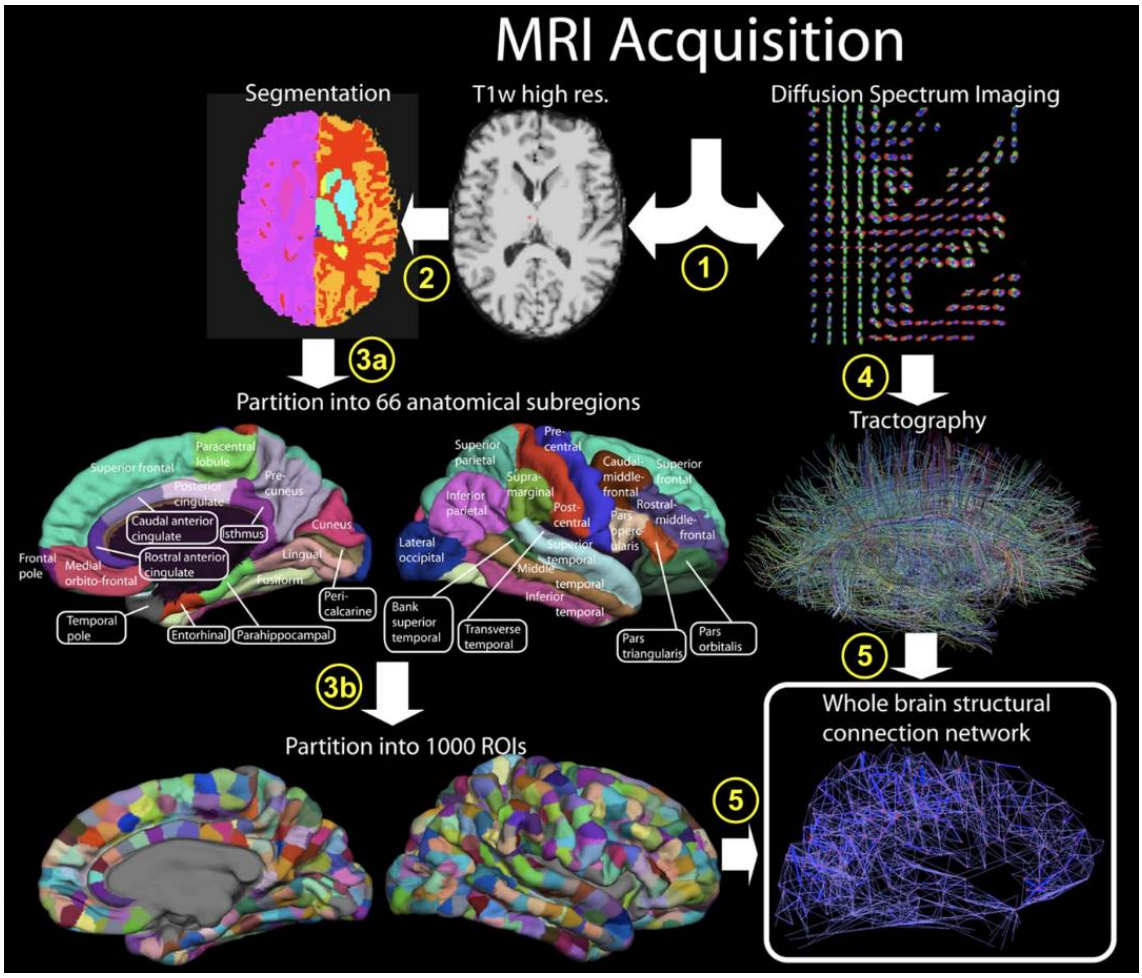

Figure I.9. Acquisition procedure of DTI. MRI images are segmented into parcels comprising 66 and 1000 ROIs. Neuronal fibers are extracted using tractography (adapted from Hagmann et al., 2008).

The idea of fiber tracking based on the bounded diffusion of water molecules in the fibers made it possible to create connectivity maps noninvasively (Conturo et al., 1999; Le Bihan et al., 1986). In the beginning, as an efficient method, diffusion tensor imaging (DTI) was proposed as a means to track the neural fibers (Basser et al., 1994; Le

Bihan and Iima, 2015). Later, the poor performance of DTI in distinguishing complex wiring structures, such as crossing fibers, led to more advanced methods such diffusion spectrum and diffusion weighted imaging (DSI and DWI) that would not compromise the computational efficiency (Fillard et al., 2011; Huisman, 2003; Wedeen et al., 2005). Studies that compared the performance of the noninvasive diffusion-based imaging and invasive techniques showed the validity of these methods (Gigandet et al., 2008; Schmahmann et al., 2007). These developments allowed the emergence of a new field regarding human connectome (Sporns et al., 2005)(Figure I.9).

Limitations were present in the anatomical tracking of the neural fibers, however. First, despite the improved new techniques that could be used to resolve crossing fibers, diffusion-based imaging still performed poorly in detecting interhemispheric connections. Another problem with anatomical connectivity is the complexity of subcortical structures. For example, the thalamus and cerebellum consist of numerous sub-regions with complex excitatory and inhibitory connections.

Additionally, the available connectivity maps of human brain coincided with another recently popularized field--graph theory--and provided an enormous literature on the topological features of brain connectivity.

I.II.vi . Topological Analysis of the Networks

Prior to the growing interest in large-scale neuronal interactions, the empirical and theoretical research in neuroscience dealt with the analysis of neuronal coding and alterations in brain activity in various brain areas. Recent advances provided large amounts of information regarding connectivity. Principally, these connectivity graphs relied on very simple structures (such as nodes and the edges of a graph), but their complexity grew exponentially with the increasing amount of information. Therefore, it became necessary to analyze and represent such graphs in a comprehensive way. Graph theory fulfilled this need by transforming connectivity information into mathematical objects. Although graph theory was widely used in social sciences during the latter half of the

twentieth century, its adaptation to brain networks is relatively recent (Felleman and Van Essen, 1991).

In graph theory, some spatially distributed objects were defined as nodes and the links that connects these objects were defined as edges. In regard to brain connectivity, where predefined brain regions were denoted as nodes, the neuronal fibers were considered as edges. The graphs are called binary if the edges take only the values 0 and 1 (connections either exist or do not exist), while the graphs with positive real-value edges are called weighted graphs.

The basic measures of graph connectivity (i.e., the basic graph metrics) describe how the edges are distributed in each graph (Figure I.10). Density, the most basic metric, quantifies whether the graph is densely or sparsely connected. The path length (L) measures the average number of edges in the shortest path between nodes. At the nodal level, the degree of a node is defined as the sum of the edges that are linked to that specific node. The weighted counterpart of nodal degree is called strength.

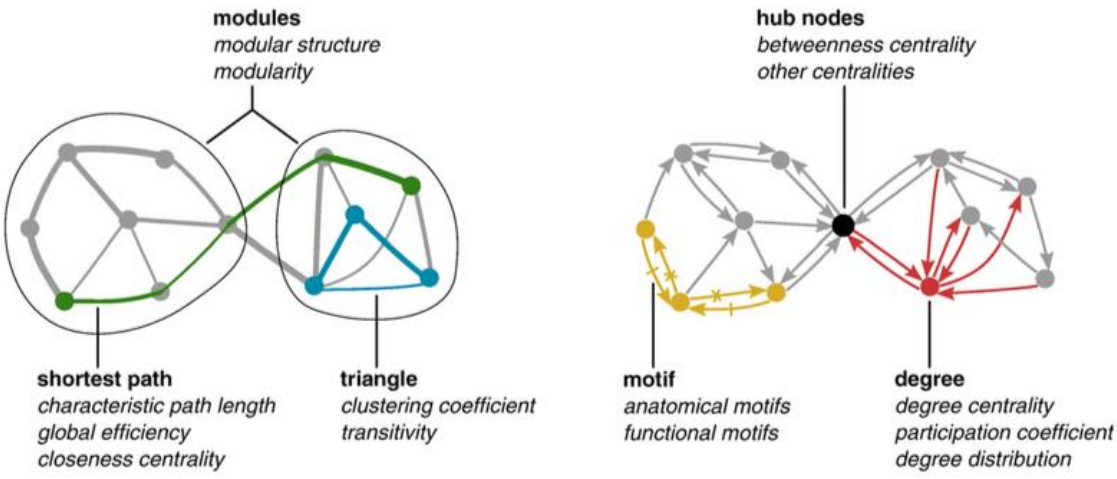

Figure I.10. Overview of widely used graph metrics. Left: two clusters of node forming modules. The blue lines indicate triangles and red lines indicate the shortest path. Right: demonstration of motifs and nodal metrics. The central node in which shortest paths are converging is the hub (adapted from Rubinov and Sporns, 2010).

These basic metrics are used to generate advanced graph metrics that can capture the more abstract properties of a graph. For example, the clustering coefficient C measures the ratio between the number of triangles that a node forms with its neighbors and the number of all possible triangles. As its name suggests, the average clustering coefficient quantifies how densely the nodes of a graph are connected with their neighbors:

$$C = \frac{1}{n}\sum_{i \in N} C_i = \frac{1}{n}\sum_{i \in N} \frac{2t_i}{k_i(k_i - 1)}$$

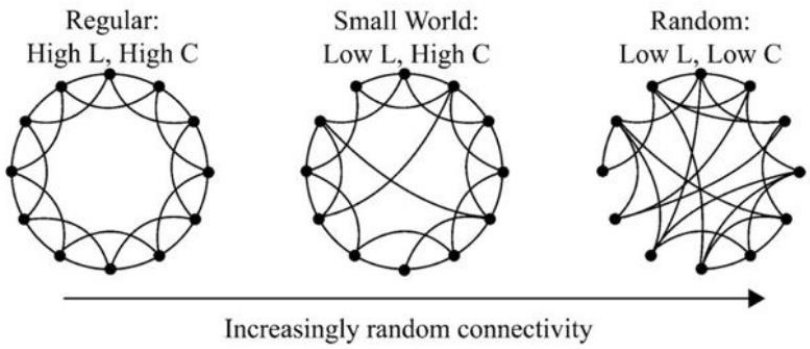

Figure I.11. Small-world structure (adapted from Watts and Strogatz, 1998).

It has been long known that many self-organizing, complex networks in nature show a particular property, namely a small world that makes the necessary steps to link any two nodes in the graph very efficient (Milgram, 1967; Travers and Milgram, 1969). Watts and Strogatz (1998) proposed a simple graph metric with which to quantify this property (Watts and Strogatz, 1998)(Figure I.11). By drawing the contrast between cyclic networks (i.e., high clustering coefficient, long path length) and random networks (i.e., low clustering coefficient, short path length), they showed that small-world networks unite short path lengths and high clustering coefficients. The proposed metric, small-wordness, quantified this relationship by comparing the ratio between clustering coefficient and path length with the surrogate networks equivalent in connection density:

$$S = \frac{C/C_{rand}}{L/L_{rand}}$$

Centrality, at the nodal level, measures the importance of a particular node in the graph. The betweenness centrality is measured as the number of shortest paths that pass through a particular node. Specifically, betweenness centrality reflects whether a node is a hub or an isolated node having little influence (Figure I.12). Many other graph metrics have been proposed and used in the context of brain connectivity (Rubinov and Sporns, 2010).

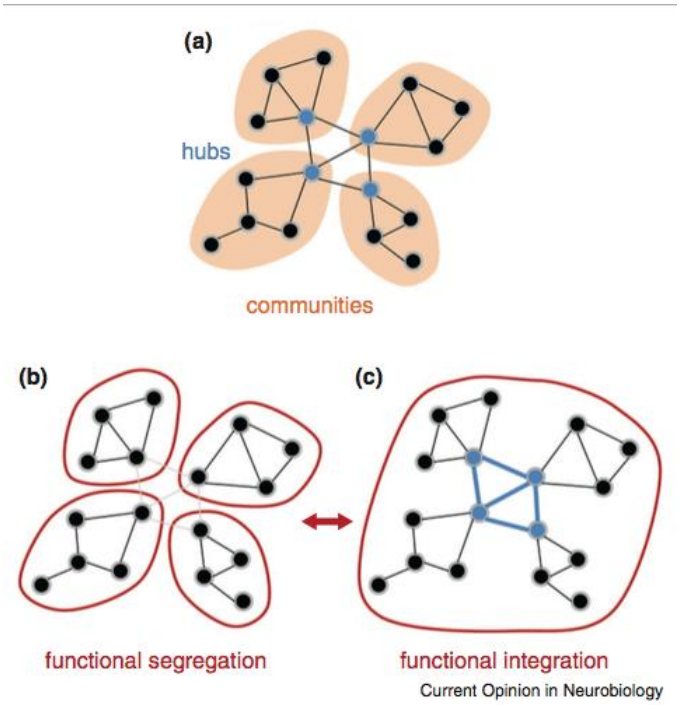

Figure I.12. a) Demonstration of communities (modules) and hubs; b-c) functional segregation and integration (adapted from Sporns et al., 2013).

Following the introduction of diffusion-based tractography, the topological characterization of brain connectivity took place immediately (Iturria-Medina et al., 2007). Shortly afterward, the small-world structure in human brain connectivity was revealed (Hagmann et al., 2007). Furthermore, the structural correlates of resting-state networks were identified using the topological properties of the brain (Hagmann et al., 2008a). This study showed that the regions forming the major resting-state networks (such as precuneus, posterior cingulate, paracentral lobule, superior and inferior parietal cortex) were the so-called structural core of the brain with higher degree, strength, efficiency and

centrality. Many other studies confirmed that these regions are hubs (i.e., high-degree, high-betweenness centrality nodes) that connect the entire network (Hagmann et al., 2008a; Nijhuis et al., 2013; Sporns, 2014; van den Heuvel and Sporns, 2013).

The topological properties of brain connectivity were immediately echoed in clinical neuroimaging studies. Researchers reported alterations in graph metrics in various clinical disorders (Alaerts et al., 2015).

I.II.vii . Comparing Connectivity Among Groups

In resting-state research, particularly in clinical applications, valid statistical approaches with which to make inferences on the differences between groups are essential. However, as the number of measures that can characterize brain connectivity increases, statistical comparison among groups becomes problematic. The relatively trivial problem is that not all of the measures fulfill the assumptions (such as Gaussianity) underlying the parametric statistical methods. The use of non-parametric methods, preferably permutation tests, can overcome this problem. Permutation tests adjust the selected test statistic based on randomly generated surrogate data.

A more serious problem arises with the increasing number of multiple comparisons. Statistical tests rely on a predefined p-value that controls the false positive rate (type-I error). For example, if the desired false positive rate is 0.05, it implies that the null hypothesis might be falsely rejected with a probability of 0.05. However, as the number of independent statistical tests increases, this probability accumulates. Briefly, if we perform N independent statistical tests with a desired p-value p, we expect to reject the null hypothesis incorrectly with a probability of $1 - (1 - p)^N$ as the so-called family-wise error rate (FWER). An aggressive approach by which to adjust the FWER is to use Bonferroni correction, which divides the desired p-value by the number of statistical tests (Dunn, 1959):

$$p_{FWER} \leq \frac{p}{N}$$

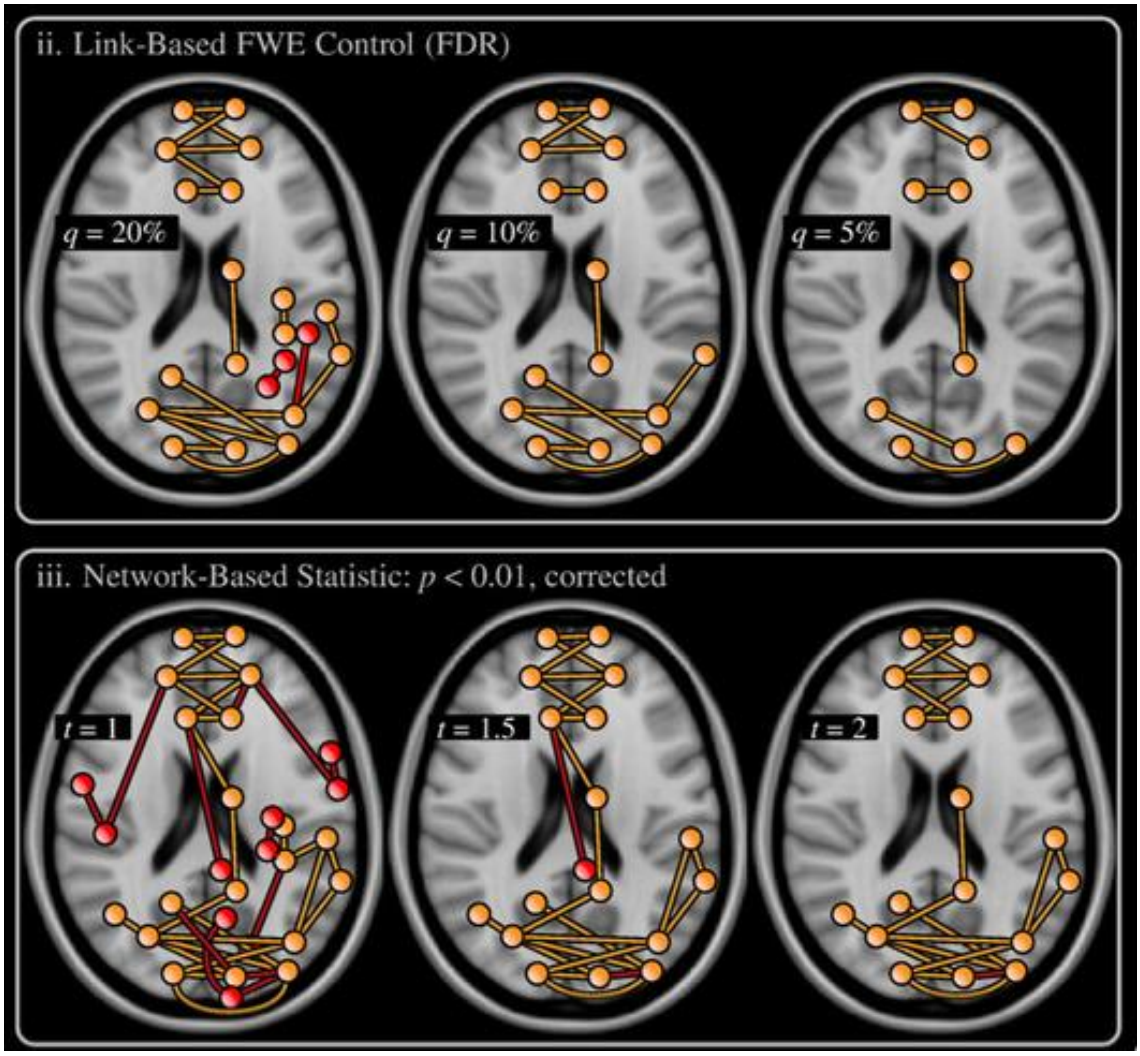

Figure I.13. Comparison of network based statistics (NBS) and link-based FDR correction (adapted from Zalesky et al., 2010).

However, this procedure increase false negative rates (type-II error) and, for a large number of N, makes it very unlikely to find significant differences. A reasonable alternative to Bonferroni correction is False Discovery Rate approach (Benjamini and Yekutieli, 2001). This approach controls type-I and type-II errors based on the expected value of the false discovery rate, where FP and TP are false positive and true positive rates, respectively:

$$FDR = E\left[\frac{FP}{FP + TP}\right]$$

The ordered p-values are tested for the criterion whereby j denotes the order and α is the desired false positive rate, the p-value is considered significant if:

$$p_j \leq \frac{j\alpha}{N}$$

Zalesky et al. proposed a different approach to compare connectivity between groups. They pointed to the fact that, in a network, the differences of interest will propagate through the existing connections (Zalesky et al., 2010)(Figure I.13). Therefore, the statistical significance of a connection (or a set of connections) cannot be considered as independent of others. Instead, the statistical test should rely on the significance of the differences in the networks as opposed to the connections. Accordingly, they introduced the Network Based Statistics (NBS) approach for the comparison of whole-brain connectivity among different groups.

I.II.viii . Resting State fMRI of the Clinical Populations

Apart from the rich properties of resting-state networks, they provide a very basic experimental procedure that involves no task. Therefore, its applications in clinical populations rely on underlying brain structure and dynamics, which makes the interpretation of the observed alterations in the populations relatively straightforward. The potential use of this new tool was emphasized shortly after its introduction (Greicius, 2008). During the past decade the clinical applications of rs-fMRI have grown exponentially: In summer 2015, a PubMed database search with the keywords "clinical resting-state fMRI" showed 1,234 published articles, half of which had been published within the past 18 months.

A small subset of clinical rs-fMRI studies involves schizophrenia (Bassett et al., 2012), major depression disorder (see chapter III.I.), bipolar Disorder (see chapter IV.I.), autism (Cerliani et al., 2015; Cherkassky et al., 2006; Lai et al., 2010; Maximo et al., 2013; Nomi and Uddin, 2015; Spisák et al., 2014; Weng et al., 2010), post-traumatic stress disorder (Kennis et al., 2015; Sadeh et al., 2015; Sripada et al., 2012; Yan et al., 2013); multiple sclerosis (Leonardi et al., 2013), Alzheimer's Disease and other demen-

tias (see chapter VI.I.). Bullmore, focusing on complexity, used the Hurst exponent to identify Alzheimer's patients using rs-fMRI (Maxim et al., 2005). Widespread reduction of FC was observed in schizophrenia patients (Liang et al., 2006; Liu et al., 2008; Salomon et al., 2011). Furthermore, the randomization of functional networks, decreased small-world properties, lower clustering coefficient and fewer high-degree hubs (Bassett et al., 2012; Liu et al., 2008; Lynall et al., 2010). Various studies tried to use resting-state FC to classify healthy and patient populations (Chen et al., 2015; Craddock et al., 2009). The connectomics-based whole-brain computational modeling studies also provide promising ideas for understanding disease mechanisms and designing novel therapeutic interventions (Deco and Kringelbach, 2014).

Despite the tremendous amount of research in clinical neuroimaging, there is an overlap between the observed significant differences among different clinical populations and inaccurate replications, consequently impeding the differentiation of the diseases (Kapur et al., 2012). Particularly, the default mode network was found to be crucial in various mental disorders (Broyd et al., 2009). Similarly, the core region of DMN--the posterior cingulate cortex--was altered in clinical populations (Leech and Sharp, 2014). Furthermore, some studies argued that there is need for change of approach in a broader context. Craddock and Owen (2010) suggested that mood and psychotic disorders might be treated separately. As another approach, phenotype-based diagnosis was proposed (Cuthbert and Insel, 2013).

I.III. Linking Structure and Function

As described previously, advances in DWI technology have made it possible to study anatomical connectivity in a noninvasive way. Moreover, the emergent field of graph theory made it possible to investigate and compare the topological features of structural and functional networks (Bullmore and Bassett, 2011; Hagmann et al., 2008b)(Figure I.14). Nevertheless, structure alone cannot account for the emergence of rich dynamical patterns in the functional organization of the brain. Computational modeling, on the other hand, allows researchers to link the structural architecture of the connectivity to

large-scale, spontaneous spatiotemporal fluctuations in the brain (Deco and Corbetta, 2011).

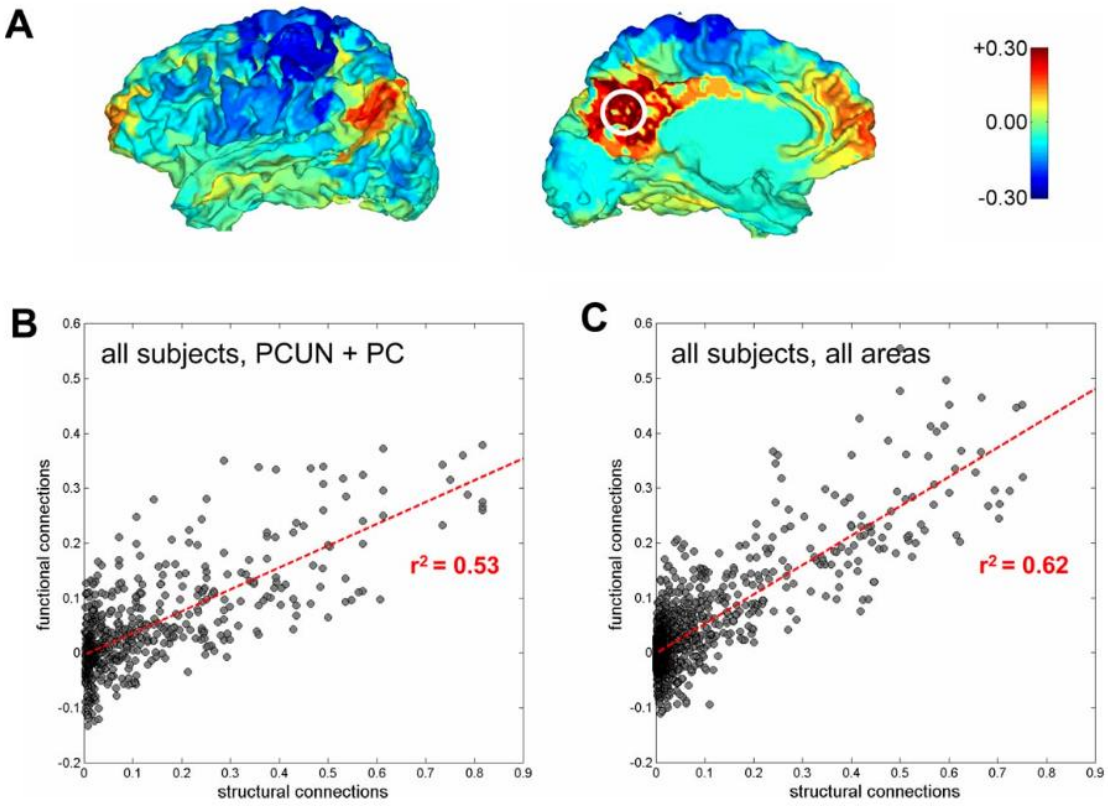

Figure I.14. The relationship between SC and FC (adapted from Hagmann et al., 2008).

Likewise, large-scale simulations that rely on microscopic description of the neurons have been shown to be feasible (Izhikevich and Edelman, 2008). First, however, the complexity of these models makes the interpretation of underlying mechanisms difficult. Secondly, current imaging techniques lack sufficient power to provide empirical evidence that covers micro- and macro-spatiotemporal dynamics. An alternative approach is to focus on the mesoscopic models that reduce the complexity of parametric space as well as the spatial resolution, and to explore the link between these models and empirical observations in the current neuroimaging modalities (Deco et al., 2009a). Mesoscopic neural-mass models, reinforced by the advancements in the anatomical tracking of connectivity, successfully replicated the resting-state fluctuations observed in fMRI (Cabral et al., 2011; Deco et al., 2009a; Deco and Jirsa, 2012; Ghosh et al., 2008; Honey et al., 2009), MEG (J. Cabral et al., 2014; Nakagawa et al., 2014), and EEG (Hindriks et al., 2014).

Briefly, these models define each brain region as a node and the anatomical link between two brain regions extracted using DWI techniques as an edge in the model. Both quantities are matched to the template that parcels the brain areas according to a standardized set of regions for the corresponding neuroimaging modality (see chapter I.II.v . and Figure I.9). Then, the simulated rs-fMRI BOLD time series were generated according to a proposed computational model.

The very first models studied the spontaneous neuronal fluctuations using conductance-based biophysical models (Breakspear et al., 2003; Honey et al., 2007) and the Fitz-Hugh-Nagumo model (Ghosh et al., 2008) based on the anatomical connectivity of the cortex in macaques (Kötter, 2004). Later, a similar approach was adapted to the neuronal population firing rate model introduced by (Wilson and Cowan, 1972), and showed how functional resting-state networks are dynamically organized near the bifurcation point (Deco et al., 2009a). In this model, in the absence of any external input, the internal noise of the system sustained the fluctuations, where the system showed empirically observed properties at the edge of the transition between stable and unstable states.

Following the developments in DWI techniques, conductance-based biophysical models were applied to simulate spontaneous fluctuations in the resting-state fMRI BOLD signals of healthy human subjects (Honey et al., 2009). Later, using an attractor network of spiking neurons, Deco and Jirsa (2012), showed that the simulated neuronal dynamics converged with the empirical observations in rs-FC at the edge of the instability in human subjects (Deco and Jirsa, 2012). The dynamic mean-field approximation of the same attractor model showed the organization of the spontaneous fluctuations constrained due to anatomical connectivity structure (Deco et al., 2013). Subsequently, by adding GABAergic inhibitory feedback loops into the mean-field approximation, Ponce-Alvarez et al., (2014) showed how large-scale synchronous networks emerged from local asynchronous spontaneous fluctuations (Deco et al., 2014b). In another recent study it was shown that a linear simple autoregressive model (SAR) might have better performance in predicting FC using SC but not in showing the non-stationary properties (Messé et al., 2015, 2014).

Another direction in the modeling approach emerged from the idea of non-linear interactions between coupled phase-oscillators (Cabral et al., 2011). Using the Kuramoto network model, this approach showed that the time delays of the couplings between nodes shaped the spontaneous synchronization patterns between regions along with the coupling strength between nodes and the level of noise (Cabral et al., 2011). Furthermore, the model illustrated the clinical implications of the large-scale simulations of resting-state activity by showing the relationship between alterations in topological properties in schizophrenia and the anatomical decoupling between brain regions (Cabral et al., 2012a, 2012b).

As reviewed above, two principle mechanisms were proposed as the means to explain the dynamics underlying resting-state FC: noise-driven spontaneous dynamics constrained by anatomical connectivity; and complex interactions between phase-oscillators shaped coupling, delays and noise. However, the relationship between these two mechanisms is non-trivial and possibly contradictory. To reconcile the discrepancy between these approaches, Deco et al. (submitted) proposed a model based on the normal form of supercritical Hopf bifurcation. This model showed that the brain regions at rest operate close to a critical point near the local supercritical Hopf bifurcation, in which each region manifests noise- and coupling-induced transitions between a stable fixed point (noisy fluctuations), and a limit-cycle attractor (noisy oscillations). This approach not only illustrated the emergence of synchronized networks but also the temporal variations of these synchronized networks.

The following section provides an overview of the details of the common large-scale computational models of the resting-state fMRI time series.

I.III.i . Converting Neuronal Activity to BOLD-fMRI Signal

The activity computed via the generative model can be transformed into a BOLD-fMRI signal using the Balloon-Windkessel hemodynamic model (Buxton et al., 1998; Friston et al., 2003). According to this model, the vasodilatory signal s_i, in node i increases due to the neuronal activity z_i. Thus the blood volume v_i, deoxyhemoglobin content q_i and

inflow f_i change in response to the vasodilatory signal. The set of coupled differential equations is shown below:

$$\frac{ds_i(t)}{dt} = z_i - k_i s_i - \gamma_i(f_i - 1)$$

$$\frac{df_i(t)}{dt} = s_i$$

$$\tau_i \frac{dv_i(t)}{dt} = f_i - v_i^{1/\alpha}$$

$$\tau_i \frac{dq_i(t)}{dt} = \frac{f_i(1-(1-\rho_i)^{1/f_i})}{\rho_i} - \frac{q_i v_i^{1/\alpha}}{v_i}$$

Finally, the BOLD signal y_i is computed as a static nonlinear function of blood volume and deoxyhemoglobin content:

$$y_i = V_0\left(7\rho_i(1-q_i) + 2\left(1-\frac{q_i}{v_i}\right) + (2q_i - 0.2)(1-v_i)\right)$$

where ρ is the resting oxygen extraction fraction and $V_o = 0.02$ is the resting blood volume fraction.

I.III.ii . Conductance-Based Biophysical Model

One of the first large-scale descriptions of the interregional anatomical connectivity of primate brain was done for the macaque cortex (Kötter, 2004). The macaque's anatomical connectivity was then used a structural basis for the study of large-scale dynamical coupling between brain regions (Honey et al., 2007). This model used a biophysical neural-mass model proposed by (Breakspear et al., 2003). The model was then adapted to simulate rs-FC in healthy human subjects (Honey et al., 2009) and the impact of lesions in human brain (Alstott et al., 2009).

The model adapted the conductance-based model that was proposed by Morris and Lecar (1981), which models the voltage-dependent sodium (Na) and calcium (Ca) channels as well as the relaxation in potassium (K) channels in the neurons, coupled by ligand-based excitatory synaptic currents.

The time evolution of membrane potential of an excitatory pyramidal cell, V, was defined as:

$$C\frac{dV}{dt} = -g_{Ca}m_{Ca}(V - V_{Ca}) - g_{Na}m_{Na}(V - V_{Na}) - g_K W(V - V_K) - g_L(V - V_L)$$

where C is the neural capacitance, g_{ion}, g_{Na}, g_K are the conductances; V_{Ca}, V_{Na}, V_K are the Nernst potentials; and m_{Ca}, m_{Na}, and W are the fraction of open ion channels of the Ca, Na, and K ions, respectively. The passive conductance and voltage of leaky ions are denoted as g_L and V_L.

For each ion, voltage-gates channels open when they exceed the threshold T_{ion}. The fraction of open ion channels m_{ion} for a large number of channels can be approximated as a sigmoid function based on the thresholds following Gaussian distribution with the variance δ_{ion}:

$$m_{ion} = 0.5\left(1 + tanh\left(\frac{V - T_{ion}}{\delta_{ion}}\right)\right)$$

The fraction of open potassium channels, W, was approximated with an exponential decay function. Where ϕ is the temperature-scaling factor, and τ is the relaxation time constant:

$$\frac{dW}{dt} = \frac{\phi(m_k - W)}{\tau}$$

Similarly, the average firing rates of excitatory (Q_V) and inhibitory (Q_Z) neurons were approximated over neural populations, assuming a Gaussian distribution with the variance δ, where Q_{max} is the maximum firing rate:

$$Q_V = 0.5Q_{V_{max}}\left(1 + tanh\left(\frac{V - V_T}{\delta_V}\right)\right)$$

$$Q_Z = 0.5Q_{Z_{max}}\left(1 + tanh\left(\frac{Z - V_T}{\delta_Z}\right)\right)$$

The synaptic interactions between excitatory and inhibitory populations were modeled as the mean firing rates propagated through synaptic factors for a_{ee} (excitatory-excitatory), a_{ei} (excitatory-inhibitory) and a_{ie} (inhibitory-excitatory) synapses. The excitatory-excitatory synapses were further modeled through the modulation of Na channels by AMPA receptors and of Ca channels by NMDA receptors. Where I_δ is the non-specific noisy subcortical excitation with the variance (δ) and r_{NMDA} is the ratio between NMDA and AMPA receptors, the membrane potential of excitatory (V) and inhibitory (Z) populations are computed as:

$$\frac{dV}{dt} = -(g_{Ca} + r_{NMDA}a_{ee}Q_V)m_{Ca}(V - V_{Ca}) - (g_{Na}m_{Na} + a_{ee}Q_V)(V - V_{Na}) - g_K W(V - V_K) - g_L(V - V_L) + a_{ie}ZQ_Z + a_{ne}I_\delta$$

$$\frac{dZ}{dt} = b(a_{ii}I_\delta + a_{ni}VQ_V)$$

Finally, for N coupled neural-masses, <.> denotes the average over neural-masses, the membrane potential V for the excitatory populations x_n:

$$\frac{dV(x_n)}{dt} = -(g_{Ca} + (1-c)r_{NMDA}a_{ee}Q_V(x_n) + c\, r_{NMDA}a_{ee}\langle Q_V(x_n)\rangle)m_{Ca}(V(x_n) - V_{Ca}) - (g_{Na}m_{Na} + (1-c)a_{ee}Q_V(x_n) + c\, a_{ee}\langle Q_V(x_n)\rangle)(V - V_{Na}) - g_K W(V(x_n) - V_K) - g_L(V(x_n) - V_L) + a_{ie}ZQ_Z(x_n) + a_{ne}I_\delta$$

The model did not include delays and noise, and the system was prone to instability due to chaotic non-linear dynamics.

I.III.iii . The FitzHugh-Nagumo Model

Following a similar approach, (Ghosh et al., 2008) modeled the spontaneous activity in neural-masses in macaque brain using FitzHugh-Nagumo model (Fitzhugh, 1961; Nagumo et al., 1962). In contrast to the conductance-based biophysical model, they investigated the role of time-delayed interactions between brain regions.

For each node n the dynamics were governed by the membrane potential (un), and the recovery potential (vn). The connectivity matrix (C) was scaled by a global coupling parameter (k), and time delays depending on the transmission velocities of the synapses. Given the functions g and h, defined in Fitzhugh, 1961 and Nagumo, 1962:

$$g(u_n, v_n) = \tau\left[v_n + \gamma u_n - \frac{u_n^3}{3}\right]$$

$$h(u_n, v_n) = -\frac{1}{\tau}[u_n + \beta v_n - \alpha]$$

and where η is the additive noise, the temporal evolution of the dynamics was computed according to:

$$\frac{du_n(t)}{dt} = g(u_n, v_n) - k\sum_{n=1}^{N} C_{np}u_p\left(t - \Delta t_{np}\right) + \eta_u(t)$$

$$\frac{dv_n(t)}{dt} = h\left(u_p, v_n\right) - \eta_v(t)$$

The system showed damped oscillations in the absence of connectivity, and showed dynamic fluctuations when the nodes were coupled. The system lost stability for a critical global coupling value, and illustrated the emergence of DMN for transmission velocities ranging from 5 to 10 m/s. The model also showed that the noise-driven oscillatory dynamics (10 Hz) at the edge of instability.

I.III.iv . The Wilson-Cowan Model

The Wilson-Cowan model also utilized to simulate the spontaneous activity in macaque cortex (Deco et al., 2009a). This model used the mean-field approximation of firing rates of excitatory and inhibitory neural masses (Wilson and Cowan, 1972). The model comprised modules of excitatory and inhibitory pools, where the dynamics of the excitatory (E(t)) and inhibitory pools were evolved according to following system of equations:

$$\tau_E \frac{dE(t)}{dt} = -E(t) + \phi\big(I_b + w_+ x(t) - I(t)\big) + \delta_E(t)$$

$$\tau_I \frac{dI(t)}{dt} = -I(t) + \phi\big(w_I E(t)\big) + \delta_I(t)$$

Where τ_m is the time constant and δ_m is the additive noise (m = {E,I}), w_+ is the efficiency of the excitatory recurrence, w_I is the excitatory-inhibitory efficiency, I_b is the non-specific background activity, and Φ is a non-linear sigmoid function that transforms the currents into firing rates, thus computed as:

$$\phi(x) = \frac{c}{1 - \exp\big(-a(x-b)\big)}$$

For the large-scale network, with N nodes, the Wilson-Cowan modules were coupled according the connectivity matrix (C), with delays D. The overall dynamics were then simulated as:

$$\tau_E \frac{dE_i(t)}{dt} = -E_i(t) + \phi\left(I_b + \alpha \sum_{j=1}^{N} C_{ji} E_j(t - D_{ji}) - I_i(t)\right) + \delta_i(t)$$

$$\tau_I \frac{dI_i(t)}{dt} = -I_i(t) + \phi\big(w_I E_i(t)\big) + \delta_i(t)$$

The global coupling strength was denoted as α, and the recurrent connectivity strengths were set to w_+/α. The rest of the parameters were defined as $\tau_E = 1$, $\tau_I = 0.2$, $w_+ = 1.5$, $a = 0.1$, $b = 40$, and $c = 100$.

Deco et al., (2009) set the spontaneous background activity (I_b) and the efficiency of recurrent connections (w_+) at the edge of a Hopf bifurcation and then investigated the role of global coupling, time delays and noise level. They showed spontaneous gamma (40 Hz) oscillations in the modules that were organized into two competing functional networks. They also showed anti-correlated networks fluctuating in a low-frequency band (0.1 Hz) consistent with the empirical findings (Fox et al., 2005).

I.III.v . The Kuramoto Model

A simplified model for the spontaneous interactions between brain regions was also proposed (Cabral et al., 2011). In this model the activity of each region was simulated using the Kuramoto model, which simulates the non-linear interactions between coupled oscillators (Kuramoto, 1986). Given N regions, where the phase of the oscillator i ($i = 1,\ldots,N$) at time t is denoted by φ_i, the time evolution of the phases is defined by:

$$\frac{d\varphi_i(t)}{dt} = \omega_i + \xi_i(t) + K\sum_{j=1}^{N} C_{ij}\sin\left(\varphi_j\left(t-\tau_{ij}\right)-\varphi_i(t)\right)$$

Here, ω_i is the natural frequency of each oscillator, K is the global coupling parameter, C_{ij} is the effective connectivity between nodes i and j, and ζ_i is uncorrelated Gaussian white noise with zero mean and standard deviation σ. The delay between nodes i and j, τ_{ij}, was incorporated using conduction velocity (V) and distance between two nodes (L_{ij}). The natural frequencies of each region were set to oscillate in the gamma frequency range (30-80 Hz), being drawn from a Gaussian distribution with 60 Hz mean and σ_f standard deviation. The simulated neuronal activity was then transformed into a BOLD signal using the Balloon-Windkesel model. Finally, they explored the parameter space for global coupling factor K and average delay $<\tau>$.

They showed that the optimal similarity between simulated and empirical FC (K = 18, $<\tau>$ = 11 ms) was observed at a point between fully synchronized and asynchronous regimes (Figure I.15). Furthermore, their model showed that the non-linear interactions between noisy oscillators led to the emergence of non-stationary connectivity patterns. Later, the model illustrated the alterations in global graph metrics in schizophrenia patients due to the impaired anatomical connectivity structure (Cabral et al., 2012a).

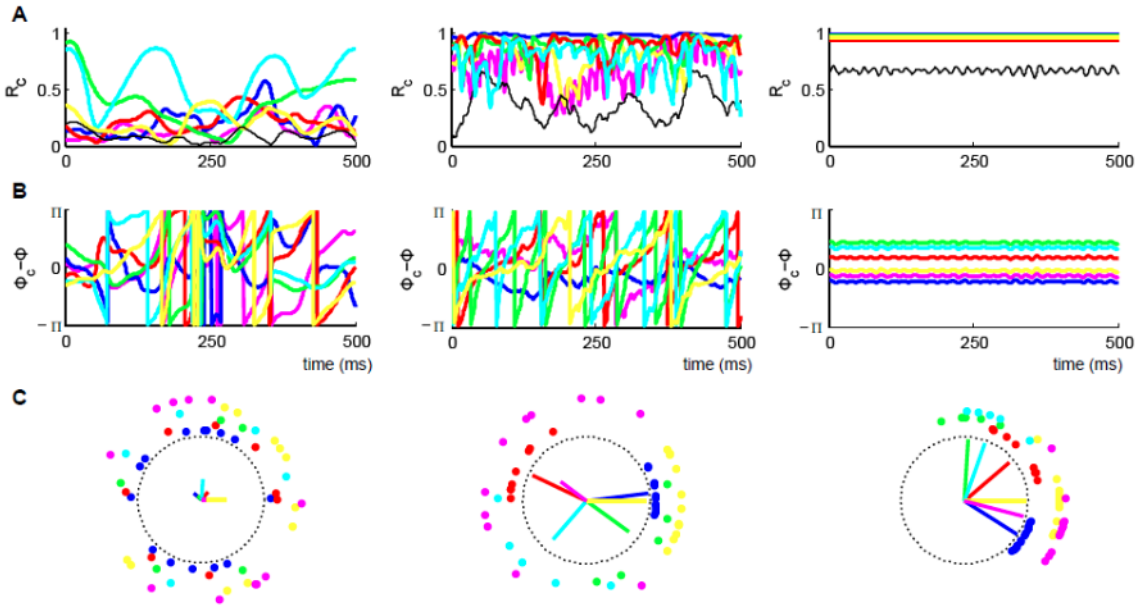

Figure I.15. Spatiotemporal dynamics of the Kuramoto model for different global coupling strengths. The left panel shows low coupling (uncoupled oscillators), the right panel shows high coupling (highly synchronized oscillators), and the middle panel shows optimal coupling strength giving rise to complex spatiotemporal patterns (adapted from Cabral et al., 2012).

A similar approach was used to directly simulate the slow fluctuation in BOLD signals (Ponce-Alvarez et al., 2015). In this model, the instantaneous phases of band-pass filtered (0.04-0.07 Hz) resting-state fMRI BOLD signals were acquired using Hilbert transform (see chapter I.II.iv .). The phase-locking value (PLV) between regions was estimated as:

$$PLV_{ij} = \left| \frac{1}{T} \sum_{t=1}^{T} e^{j[\varphi_i(t) - \varphi_j(t)]} \right|$$

Where $\varphi(t)$ is the instantaneous phase at time t and T is the total time. Subsequently, the PLV matrices were binarized using the threshold of $\pi/6$ (i.e., $Q_{ij} = 1$, if $PLV_{ij} > \pi/6$, and $Q_{ij} = 0$, otherwise). Thus the spatial connectivity patterns were estimated at each time point, thereby forming a synchronization tensor **T** with *n*x*n*x*T* dimension. The temporal community structure was then computed using non-negative tensor factorization (NNTF).

They showed a high overlap between the communities acquired by NNTF and independent components. The Kuramoto model was then adapted to simulate the BOLD time series. However, in this model they let each region oscillate at 0.05 Hz but omitted transmission delays. The model illustrated how time-varying connectivity structures are related to the non-linear interactions in complex networks. Crucially, the simulated network showed the characteristics of the empirical data, in which the metastability of the system was maximized.

The metastability was based on the overall phase synchrony at each time point computed through use of the Kuramoto order parameter R(t). Where *n* is the number of regions:

$$R(t) = \left| \frac{1}{n} \sum_{i=1}^{n} e^{j\varphi_i(t)} \right|$$

I.III.vi . The Spiking Neural Network Model

Another approach to simulation of spontaneous activity was proposed by (Deco and Jirsa, 2012) using an attractor model of spiking neurons. Following Brunel and Wang (2001), they used a leaky integrate and fire (LIF) dynamics.

Where C_m is membrane potential, g_m is membrane leak conductance, I_{syn} is total synaptic current and $V(t)$ and V_L are membrane potential and resting potential, respectively:

$$C_m \frac{dV(t)}{dt} + g_m(V(t) - V_L) = I_{syn}(t)$$

When the membrane potential reaches a certain threshold, it sends out a spike to all connected neurons and resets its membrane potential to the reset potential. Synaptic currents are mediated by excitatory (AMPA and NMDA) and inhibitory (GABA) receptors. Total synaptic current is given by:

$$I_{syn(t)} = I_{AMPA,ext}(t) + I_{AMPA,rec}(t) + I_{NMDA}(t) + I_{GABA}(t)$$

Where each individual current is defined as:

$$I_{AMPA,ext}(t) = g_{AMPA,ext}(V(t) - V_E) \sum_{j=1}^{N_{ext}} s_j^{AMPA,ext}(t)$$

$$I_{AMPA,rec}(t) = g_{AMPA,rex}(V(t) - V_E) \sum_{j=1}^{N_E} w_j s_j^{AMPA,rex}(t)$$

$$I_{NMDA}(t) = \frac{g_{NMDA}(V(t) - V_E)}{1 + [Mg^{2+}\exp(-0.062V(t))/3.57} \sum_{j=1}^{N_E} w_j s_j^{NMDA}(t)$$

$$I_{GABA}(t) = g_{GABA}(V(t) - V_I) \sum_{j=1}^{N_I} w_j s_j^{GABA}(t)$$

g indicates the receptor specific synaptic conductance, s_j is the fraction of open channels and w_j is the synaptic weight. V_E and V_I are the reversal potentials of the excitatory and inhibitory neurons, respectively. N_{ext} is the number of neurons encoding the spontaneous activity in the cortex, and N_E and N_I are the numbers of excitatory and inhibitory neurons in the network. The NMDA synaptic current is dependent on the membrane potential and controlled by the extracellular concentration of [Mg^{2+}].

Fractions of the open channels are calculated from:

$$\frac{ds_j^{AMPA,ext}(t)}{dt} = \frac{s_j^{AMPA,ext}(t)}{\tau_{AMPA}} + \sum_k \delta(t - t_j^k)$$

$$\frac{ds_j^{AMPA,rec}(t)}{dt} = \frac{s_j^{AMPA,rec}(t)}{\tau_{AMPA}} + \sum_k \delta\left(t - t_j^k\right)$$

$$\frac{ds_j^{NMDA}(t)}{dt} = \frac{s_j^{NMDA}(t)}{\tau_{NMDA,decay}} + \alpha x_j(t)\left(1 - s_j^{NMDA}(t)\right)$$

$$\frac{dx_j(t)}{dt} = \frac{x_j(t)}{\tau_{NMDA,rise}} + \sum_k \delta\left(t - t_j^k\right)$$

$$\frac{ds_j^{GABA}(t)}{dt} = \frac{s_j^{GABA}(t)}{\tau_{GABA}} + \sum_k \delta(t - t_j^k)$$

Where τ_{AMPA}, $\tau_{NMDA,decay}$ and τ_{GABA} are the decay times and $\tau_{NMDA,rise}$ is the rise time for the corresponding synapses. The sums over k represent the sums over spikes where δ(t) (δ-peaks) emitted by presynaptic neuron k at time t_j^k. All input is generated through a Poisson process.

Table I.1. Model parameters

Excitatory neurons		**Inhibitory neurons**		**Synapses**	
N_E	100 neurons	N_I	100 neurons	V_E	0 mV
C_m	0.5 nF	C_m	0.2 nF	V_I	-70 mV
g_m	25 nS	g_m	20 nS	τ_{AMPA}	2 ms
V_L	-70 mV	V_L	-70 mV	$\tau_{NMDA,rise}$	2 ms
V_{thr}	-50 mV	V_{thr}	-50 mV	$\tau_{NMDA,decay}$	100 ms
V_{reset}	-55 mV	V_{reset}	-55 mV	τ_{GABA}	10 ms
τ_{ref}	2 ms	τ_{ref}	1 ms	α	0.5 kHz
$g_{AMPA,ext}$	2.496 nS	$g_{AMPA,ext}$	1.944 nS	β	0.062
$g_{AMPA,rec}$	0.104 nS	$g_{AMPA,rec}$	0.081 nS	γ	0.28
$g_{NMDA,rec}$	0.327 nS	$g_{NMDA,rec}$	0.258 nS		
g_{GABA}	4.375 nS	g_{GABA}	3.4055 nS		

The equations are integrated using a fourth-order Runge-Kutta method with a time step of 0.02ms (see Table I.1. for model parameters). All neurons received external background input from 800 neurons producing uncorrelated Poisson spike trains:

$$\tau_n \frac{d\nu_{ext}^p(t)}{dt} = -\left(\nu_{ext}^p(t) - \nu_0\right) + \sigma_\nu \sqrt{2\tau_n} n^p(t)$$

The mean-field approximation of the population activity is also available for the model (Brunel and Wang, 2001). Briefly, mean-field approximation reduces the variables by describing the dynamics for each neural population. Thus the exploration of parameter space becomes computationally efficient. Where *V(t)* is the membrane potential, the mean-field approximation of the population activity is calculated in accordance with the following formula:

$$\tau_x \frac{dV(t)}{dt} = -V(t) + \mu_x + \sigma_x \sqrt{\tau_x} n(t)$$

Here *x* denotes each neural population while τ is the effective membrane time constant, μ is the mean membrane potential in the absence of spiking and fluctuations, σ is the magnitude of the fluctuations, and η is a Gaussian process with absolute exponentially decaying correlation function. Given an external incoming spike rate, υ_{ext}, inhibitory spiking rate, υ_I, the time constant $\tau_m = C_m/g_m$ ($m = \{E,I\}$), the quantities μ and σ are computed as:

$$\mu_x = \frac{(T_{ext}\nu_{ext} + T_{AMPA}n_x^{AMPA} + \rho_1 n_x^{NMDA})V_E + \rho_2 n_x^{NMDA}\langle V\rangle + T_1 n_x^{GABA}V_1 + V_L}{S_x}$$

$$\sigma_x^2 = \frac{g_{AMPA,ext}^2(\langle V\rangle - V_E)^2 N_{ext}\nu_{ext}\tau_{AMPA}^2\tau_x}{g_m^2\tau_m^2}$$

The remaining quantities are calculated as follows:

$$S_x = 1 + T_{ext}\nu_{ext} + T_{AMPA}n_x^{AMPA} + (\rho_1 + \rho_2)n_x^{NMDA} + T_1 n_x^{GABA}$$

$$\tau_x = \frac{C_m}{g_m S_x}$$

$$n_x^{AMPA} = \sum_{j=1}^{p} f_j w_{jx}^{AMPA}\nu_j$$

$$n_x^{NMDA} = \sum_{j=1}^{p} f_j w_{jx}^{NMDA} \psi(\nu_j)$$

$$n_x^{GABA} = \sum_{j=1}^{p} f_j w_{jx}^{GABA} \nu_j$$

$$\psi(\nu) = \frac{\nu\tau_{NMDA}}{1+\nu\tau_{NMDA}}\left(1 + \frac{1}{1+\nu\tau_{NMDA}} \sum_{n=1}^{\infty} \frac{\left(-\alpha\tau_{NMDA,rise}\right)^n T_n(\nu)}{(n+1)!}\right)$$

$$T_n(\nu) = \sum_{k=0}^{n} (-1)^k \binom{n}{k} \frac{\tau_{NMDA,rise}(1+\nu\tau_{NMDA})}{\tau_{NMDA,rise}(1+\tau_{NMDA}) + k\tau_{NMDA,decay}}$$

$$\tau_{NMDA} = \alpha\tau_{NMDA,rise}\tau_{NMDA,decay}$$

$$T_{ext} = \frac{g_{AMPA,ext}\tau_{AMPA}}{g_m}$$

$$T_{AMPA} = \frac{g_{AMPA,rec}N_E\tau_{AMPA}}{g_m}$$

$$\rho_1 = \frac{g_{NMDA}N_E}{g_m J}$$

$$\rho_2 = \beta\frac{g_{NMDA}N_E(\langle V_x\rangle - V_E)(J-1)}{g_m J^2}$$

$$J = 1 + \gamma\exp(-\beta\langle V_x\rangle)$$

$$T_1 = \frac{g_{GABA}N_I\tau_{GABA}}{g_m}$$

$$\langle V_x\rangle = \mu_x - (V_{thr} - V_{reset})\nu_x\tau_x$$

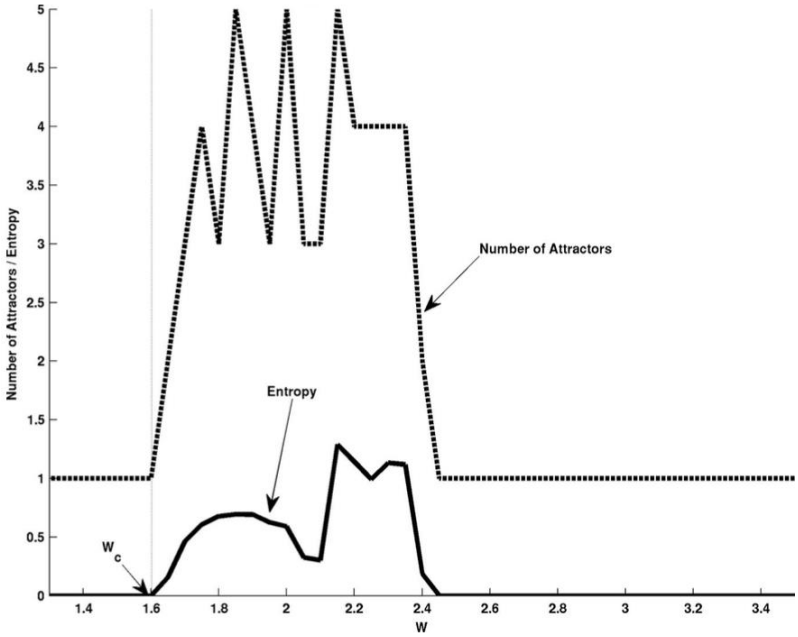

Figure I.16. Attractor landscape of the model. At critical coupling strength the system becomes multistable (adapted from Deco and Jirsa, 2012).

Here, p is the number of excitatory populations, f_x is the fraction of excitatory neurons, ω_{jx} is the weight of the connections from x to j, and v_x is the spiking rate of the excitatory population given by:

$$v_x = \phi(\mu_x, \sigma_x), x = 1, \dots, n$$

The function Φ denotes the transduction function of each population (x), which gives the output rate of the population in terms of the inputs:

$$\phi(\mu_x, \sigma_x) = \left(\tau_{rp} + \tau_x \int_{\beta(\mu_x,\sigma_x)}^{\alpha(\mu_x,\sigma_x)} du\sqrt{\pi}\exp(u^2)\,[1 + \mathrm{erf}(u)]\right)^{-1}$$

where *erf(u)* is the error function and τ_{rp} is the refractory period, the parameters α and β are computed as:

$$\alpha(\mu_x, \sigma_x) = \frac{(V_{thr} - \mu_x)}{\sigma_x}\left(1 + 0.5\frac{\tau_{AMPA}}{\tau_x}\right) + 1.03\sqrt{\frac{\tau_{AMPA}}{\tau_x}} - 0.5\frac{\tau_{AMPA}}{\tau_x}$$

$$\beta(\mu_x, \sigma_x) = \frac{(V_{reset} - \mu_x)}{\sigma_x}$$

Finally, the following differential equation yields to the population activity:

$$\tau_x \frac{d\nu_x}{dt} = -\nu_x + \phi(\mu_x, \sigma_x)$$

The mean-field approximation is evaluated for different initial conditions in order to confirm whether the populations are in the inactive (firing at 3 Hz) or the active (firing at 10 Hz) state. The procedure is repeated for different global coupling strengths. Subsequently, the number of attractors is counted if the firing rate of any population differs for a different initial condition. Then, where *p(i)* is the probability of being in attractor *i*, the entropy is calculated as:

$$H = -\sum_i p(i) log p(i)$$

The mean-field approximation allowed them to extract the attractor landscape of the cortical spiking activity (Figure I.16). The landscape of the attractors suggested that there was a critical global coupling factor in which the system became unstable. Furthermore, their model revealed that the greatest similarity between empirical and simulated FC was observed just before this critical point.

I.III.vii . Dynamic Mean Field Model

The mean-field approximation of spiking neural networks showed that the brain operates at the edge of instability, thus maximizing the dynamic repertoire of the possible states (Deco and Jirsa, 2012). However, the implementation of biophysical spiking neural network models is computationally expensive, which limits their scope. To overcome this problem, Deco et al. (2014a) adapted the dynamic mean-field approximation proposed by Wong and Wang (2006). The model was based on the spiking neural net-

work model presented in the previous section. Later, the dynamic mean-field approach was further extended to show the role of local feedback inhibition in whole-brain spontaneous fluctuations (Deco et al., 2014b). This model filled the gap between the observations of uncorrelated low firing-rate activity and intra-area correlations that were induced by long-range connections.

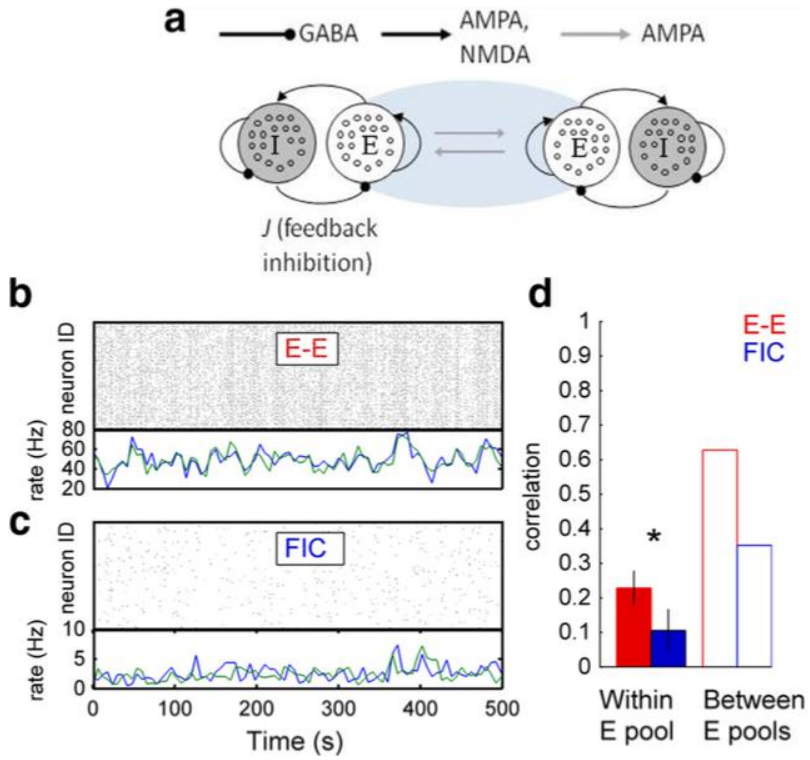

Figure I.17. a) balanced DMF model; b-c) spontaneous fluctuations with and without inhibition; d) correlations within and between pools (adapted from Deco and Ponce-Alvarez, 2014).

In the model the system of equations for the brain dynamics was described as follows:

Where $\mathbf{S}^{(m)} = \{S_i^{(m)} \dots S_N^{(m)}\}$, $\mathbf{I}_\eta^{(m)} = \{I_{\eta_i}^{(m)} \dots I_{\eta_N}^{(m)}\}$, N is the number of brain regions, and $m = \{E, I\}$ indicating excitatory and inhibitory populations.

$$\mathbf{I}^{(E)} = W_E I_0 + \mathbf{K}^{(E)}\mathbf{S}^{(E)} - \mathbf{J}_I\mathbf{S}^{(I)}$$

$$\mathbf{I}^{(I)} = W_I I_0 + \mathbf{K}^{(I)}\mathbf{S}^{(E)} - \mathbf{S}^{(I)}$$

$$\frac{\mathrm{d}\mathbf{S}^{(E)}}{dt} = -\frac{\mathbf{S}^{(E)}}{\tau_E} + \left(1 - \mathbf{S}^{(E)}\right)\gamma H^{(E)}\left(\mathbf{I}^{(E)}\right) + \sigma\boldsymbol{\upsilon}(t)$$

$$\frac{d\mathbf{S}^{(I)}}{dt} = -\frac{\mathbf{S}^{(I)}}{\tau_E} + H^{(I)}\left(\mathbf{I}^{(I)}\right) + \sigma\boldsymbol{\upsilon}(t)$$

$$H^{(m)}\left(\mathbf{I}^{(m)}\right) = \frac{a_m\mathbf{I}^{(m)} - b_m}{1 - e^{-d_m(a_m\mathbf{I}^{(m)} - b_m)}}$$

$$\mathbf{K}^{(E)} = J_{NMDA}\left(G\mathbf{C}^{(E)} + w_+\mathbf{I}\right)$$

$$\mathbf{K}^{(I)} = J_{NMDA}G(\boldsymbol{\lambda} \circ \mathbf{C}^{(E)})$$

I is the identity matrix, $\boldsymbol{\lambda}$ is binary matrix corresponding to the existence of feed-forward inhibitory links, *G* is the global coupling and **C** is the connectivity matrix.

Their results showed that highly synchronous excitatory activity was decorrelated in the presence of inhibitory local feedback preserving the correlated activity between excitatory populations (Figure I.17).

I.III.vii.a) Analytical Approximation for the Covariance of Activity

Another novel approach that was proposed by (Deco et al., 2014b) was the analytical approximation of covariance between neural populations using the moments method. Where synaptic activity in excitatory and inhibitory pools is denoted by $\mathbf{Y} = \{\mathbf{S}^{(m)}\}$, the covariance matrix **P** of the variable **Y** can be written as:

$$\mathbf{P} = \langle(\mathbf{Y} - \overline{\mathbf{Y}})(\mathbf{Y} - \overline{\mathbf{Y}})^T\rangle$$

Given the dynamical system (denoted by F(**Y**)) defined through the equations described in the previous subsection, and the covariance matrix of the input noise $\mathbf{Q}_n$, the temporal evolution of the covariance matrix is estimated as:

$$\frac{d\mathbf{P}}{dt} = (F(\mathbf{Y}) - \overline{\mathbf{Y}})(\mathbf{Y} - \overline{\mathbf{Y}})^T + (\mathbf{Y} - \overline{\mathbf{Y}})(F(\mathbf{Y}) - \overline{\mathbf{Y}})^T + \mathbf{Q}_\eta$$

Where **A** is the Jacobian of F(**Y**), the first-order Taylor expansion of F(**Y**) gives:

$$F(\mathbf{Y}) = F(\overline{\mathbf{Y}}) + \mathbf{A}(\mathbf{Y} - \overline{\mathbf{Y}})$$

Therefore, the expression in equation 8 is reduced to:

$$\frac{d\mathbf{P}}{dt} = \mathbf{AP} + \mathbf{PA}^T + \mathbf{Q}_n$$

Solving the equation for $\mathbf{AP} + \mathbf{PA}^T + \mathbf{Q}_n = 0$, using Eigen-decomposition of the Jacobian $\mathbf{A} = \mathbf{LDL}^{\dagger}$, where $\mathbf{D}$ is the diagonal matrix comprising the eigenvalues λ_i, and $\mathbf{L}$ is the eigenvectors. $\mathbf{P}$ is computed as $\mathbf{P} = \mathbf{LML}^{\dagger}$, where $\mathbf{M}_{ij} = -\widetilde{\mathbf{Q}}_{ij}/(\lambda_i + \lambda_j)$, and $\widetilde{\mathbf{Q}}_{ij} = \mathbf{L}^{-1}\mathbf{Q}_n\mathbf{L}^{-\dagger}$. Finally, the correlation coefficients between the variables are estimated using $r_{ij} = P_{ij}/\sqrt{P_{ii} \times P_{jj}}$.

The Jacobian of the system $\mathbf{A}$ is computed as follows: Where $\mathbf{I}$ is the identity matrix, $\mathbf{u}^{(m)}$ is the average currents, $\boldsymbol{\mu}^{(m)}$ as the average synaptic gating variables, the Jacobian Matrix $\mathbf{A} = \frac{\partial \boldsymbol{F}^{(m)}(\overline{\mathbf{Y}})}{\partial \mathbf{S}^{(m)}}$, where

$$\frac{\partial F^{(E)}(\overline{\mathbf{Y}})}{\partial \mathbf{S}^{(m)}} = \mathbf{K_1} \circ \left((1 - \boldsymbol{\mu})\frac{\partial H^{(E)}(\mathbf{u}^{(E)})}{\partial \mathbf{u}^{(E)}}\right) + \mathbf{I_1} \circ \left(-\frac{1}{\tau_E} - H^{(E)}(\mathbf{u}^{(E)})\right)$$

$$\frac{\partial F^{(I)}(\overline{\mathbf{Y}})}{\partial \mathbf{S}^{(m)}} = \mathbf{K_2} \circ \left(\frac{\partial H^{(I)}(\mathbf{u}^{(I)})}{\partial \mathbf{u}^{(I)}}\right) + \mathbf{I_2} \circ \left(-\frac{1}{\tau_I} - \frac{\partial H^{(I)}(\mathbf{u}^{(I)})}{\partial \mathbf{u}^{(I)}}\right)$$

$$K_1 = \begin{bmatrix} \mathbf{K}^{(E)} & 0 \\ 0 & \mathbf{J}^{\mathrm{I}}\mathbf{I} \end{bmatrix} \qquad K_2 = \begin{bmatrix} \mathbf{K}^{(I)} & 0 \\ 0 & \mathbf{I} \end{bmatrix} \qquad I_1 = \begin{bmatrix} \mathbf{I} & 0 \\ 0 & 0 \end{bmatrix} \qquad I_2 = \begin{bmatrix} 0 & 0 \\ 0 & \mathbf{I} \end{bmatrix}$$

Briefly, the moments method permits the approximation of simulated FC without the need to simulate large-scale simulations. The model also showed that, as in Deco and Jirsa (2012), the optimal similarity between simulated and empirical FC occurred at the edge of criticality. Furthermore, the existence of local feedback inhibition not only diminished the critical point but also enhanced the similarity between empirical and simulated FC (Figure I.18).

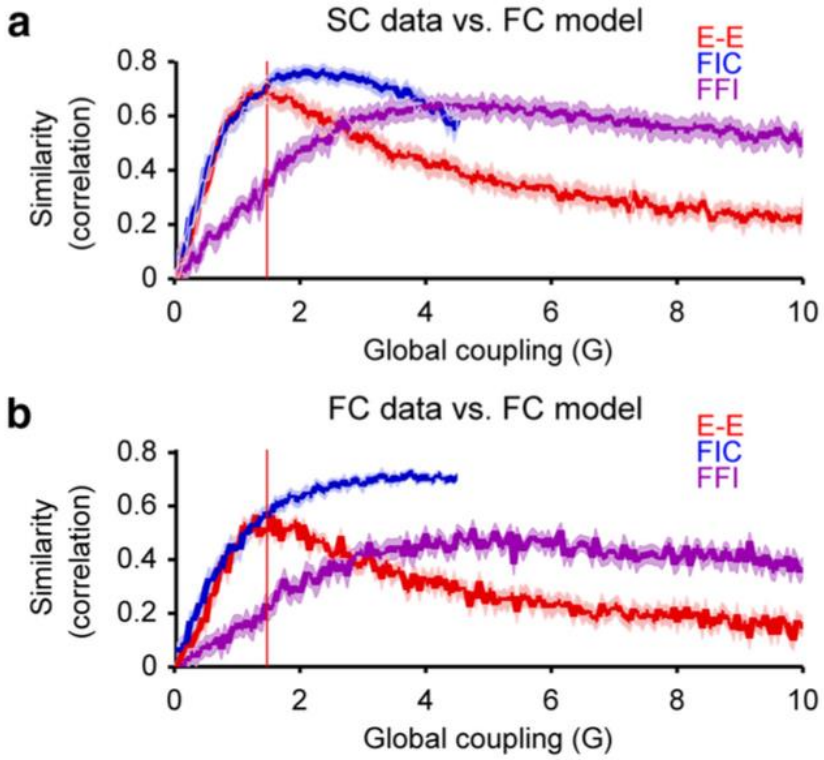

Figure I.18. Similarity between simulated and empirical FC with or without inhibition. a) SC-FC fit. b. eFC-sFC fit (adapted from Deco and Ponce-Alvarez, 2014).

I.III.viii . The Simple Autoregressive Model

Messé et al., (2014) proposed a simple model that can account for the temporal correlations in resting-state fMRI BOLD signals based on the spatial autoregressive model. Furthermore, by providing a comprehensive comparison of existing models (Wilson-Cowan, Kuramoto, FitzHugh-Nagumo, Neural Mass and Spike Attractor models, as presented in previous chapters) they argued that the spatial autoregressive model outperforms all other models regarding the similarity between empirical and simulated FC (Messé et al., 2015). They simulated the BOLD signal y_i using the spatial autoregressive model as follows:

$$y_i(t) = k \sum_{j \neq i} C_{ij} y_i + \sigma \eta_i(t)$$

Where y_i is the BOLD signal of node i, C_{ij} is the anatomical connectivity with zero-diagonal (C_{ii} = 0), $\eta(t)$ is standard Gaussian random variable ($\mu = 0, \sigma = 1$), and σ is the noise level set to 1. Thus the covariance matrix of **y** can be computed using:

$$\sigma^2(\mathbf{I} - k\mathbf{C})^{-1}(\mathbf{I} - k\mathbf{C})^{-t}$$

Despite its simplicity, they showed that the SAR model performed better than other models. Furthermore, SAR outperformed other models in regard to graph theoretical measures. However, they argued that SAR might be insufficient in showing the non-stationaries in the data (Messé et al., 2014). They also illustrated that the scale of the network (size of nodes) had a significant impact on the model's performance, and that the correlation between empirical and simulated FC measures was modest (Figure I.19).

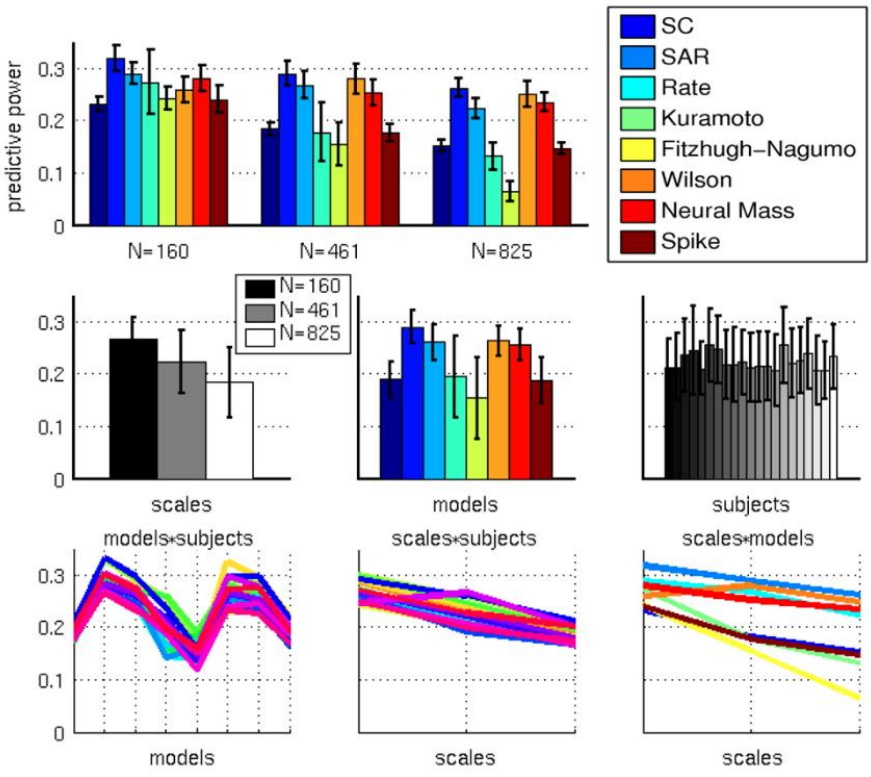

Figure I.19. Comparison of performances of the computational models of resting state (adapted from Messe et al., 2014).

I.III.ix . The Hopf Normal Model

The computational models introduced in previous subchapters are subject to two important problems. First, the fundamental mechanisms behind nonlinear dynamical models based on noise diffusion (e.g., the attractor network model) and coupled chaotic oscillator models (e.g., the Kuramoto model) are inconsistent, although the models are in agreement that the brain operates at a critical point that maximizes metastability. The noise-based models suggest that the temporal correlations in spontaneous activity emerge from the propagation of uncorrelated noise through the long-range anatomical connections. However, oscillation-based models explain the resting-state FC by means of complex interactions between oscillatory activities in the regions of the brain. Further, the proposed models did not account for the temporal structure of spontaneous fluctuations.

Deco et al. (submitted) proposed a model that can reconcile noise-based and oscillation-based approaches using the normal form of supercritical Hopf bifurcation (Figure I.20). The advantage of this model is that it allows transitions between asynchronous noise activity and oscillations. Where ω is the intrinsic frequency of each node, a is the local bifurcation parameter, η is additive Gaussian noise with standard deviation β, and the temporal evolution of the activity z in node j is given in the complex domain as:

$$\frac{dz_j}{dt} = \left[a_j + i\omega_j - \left|z_j^2\right|\right] + \beta\eta_j(t)$$

and,

$$z_j = \rho_j e^{i\theta_j} = x_j + iy_j$$

This system above shows a supercritical bifurcation at $a_j = 0$. Specifically, if a_j is smaller than 0, the local dynamic has a stable fixed point at $z_j = 0$, while for a_j values larger than 0 there exists a stable limit-cycle oscillation with the frequency $f = \omega/2\pi$. Finally, the whole-brain dynamics is described by the following coupled equations:

$$\frac{dx_j}{dt} = [a_j - x_j^2 - y_j^2]x_j - \omega_j y_j + G\sum_i C_{ij}(x_i - x_j) + \beta\eta_{xj}(t)$$

$$\frac{dy_j}{dt} = [a_j - x_j^2 - y_j^2]y_j + \omega_j x_j + G\sum_i C_{ij}(y_i - y_j) + \beta\eta_{yj}(t)$$

Where C_{ij} is the structural connectivity (SC) between nodes *i* and *j*, *G* is the global coupling factor and the standard deviation of Gaussian noise is $\beta = 0.02$. In this model the simulated activity corresponds to the BOLD signal of each node. The intrinsic frequency of each node was estimated as the peak frequency in the associated narrowband (i.e., 0.04 - 0.07 Hz) of the empirical BOLD signals of each brain region. Then, they optimized the local bifurcation parameter of each node based on the proportion of point in 0.04 - 0.07 Hz narrowband with respect to 0.04 - 0.25 Hz band (i.e., up to the Nyquist frequency).

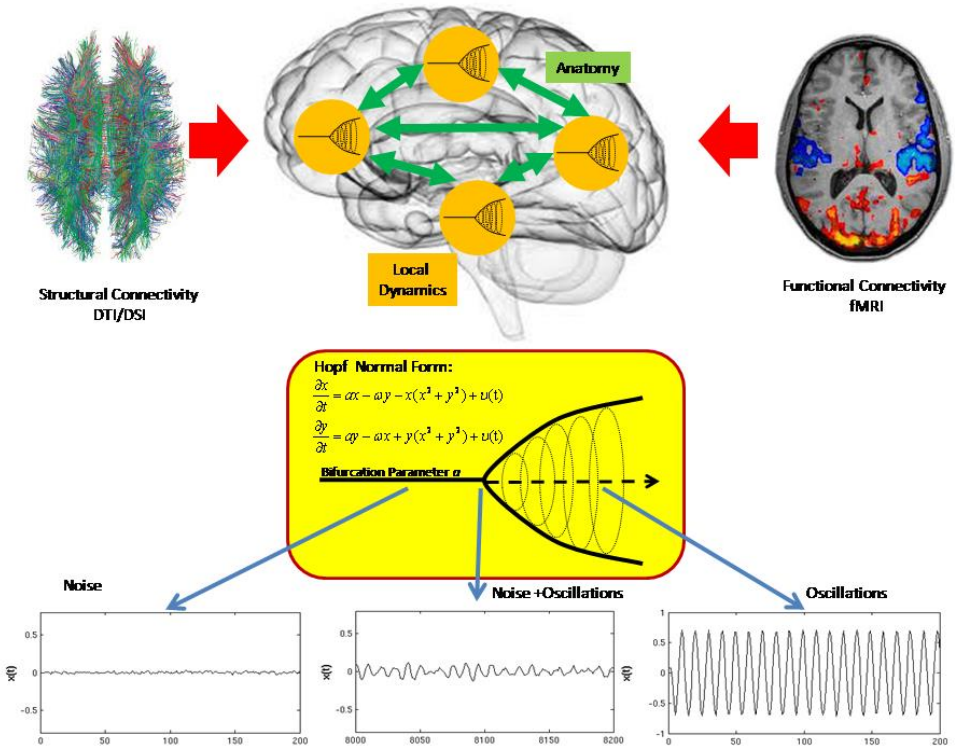

Figure I.20. The overview of Hopf model. Bottom: The panels show the transition between states for different local bifurcation parameters (adapted from Deco et al., submitted).

They showed that the similarity between empirical and simulated FC was higher when the local bifurcations parameters were set to critical point (*a=0*) compared to sub- (*a=-0.2*) and super-critical points (*a=0.2*). Moreover, they studied the spatiotemporal structure in dynamic FC, which was quantified as the correlation coefficients between functional states at different time instances (i.e., functional connectivity dynamics, or FCD). They showed that the Kolmogorov-Smirnov distance between empirical and simulated FCD distributions is not only optimal at critical point but is also more sensitive to deviations from the critical point (Figure I.21).

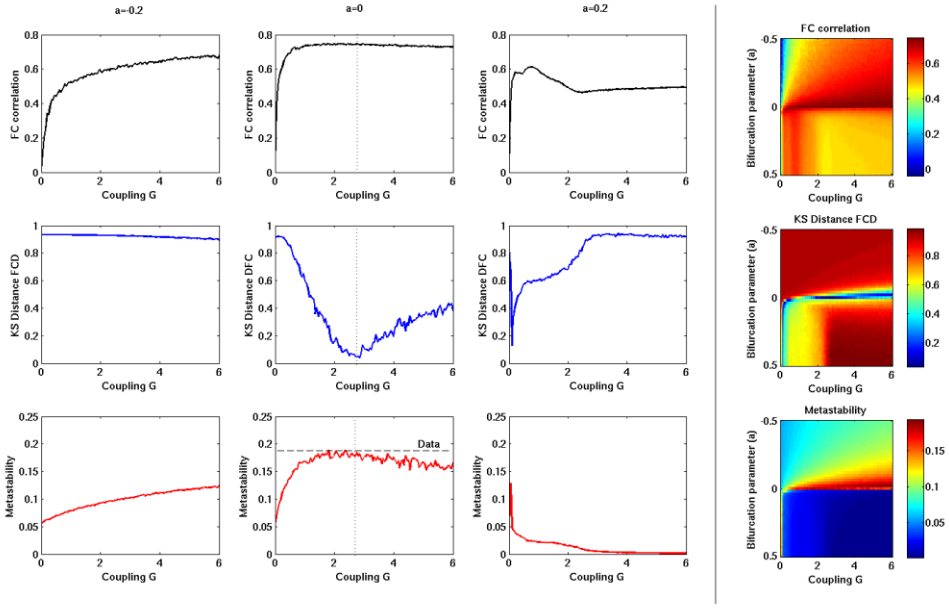

Figure I.21. The similarity between empirical and simulated time series. The first three columns correspond to different local bifurcation parameters (-0.2, 0, 0.2). The fourth column shows the parameter space. The first row shows the similarity between eFC and sFC. The second row shows the KS-distance between empirical and simulated FCD. The last row shows the metastability (adapted from Deco et al., submitted).

The final implication of Hopf model was that, by means of local bifurcation parameters, it illustrated the regions that might feed the whole-brain activity (i.e., a > 0).

I.III.x . Effective Connectivity

Many studies have shown the relationship between SC and FC. Computational models refined this relationship by demonstrating that the FC between unconnected cortical regions can be explained by indirect connections in SC. However, SC only accounts for the physical characteristics of the fibers. Furthermore, although fiber-tracking methods can measure the weights of the connections, they do not carry any information on the causality of the connections. The issue is further complicated when the biophysical properties of the neural fibers and the cortical regions are considered. The problem becomes even more complicated for FC. Functional connectivity in resting-state fMRI measures overall dependence between the BOLD time series of brain regions. Therefore, besides being undirected, FC between two regions may depend on the whole-brain activity. To address this problem, Friston et al. (Friston et al., 1995) introduced the effective connectivity (EC) describing the modulatory interactions between visual processing regions, later extended as "psychophysiological interaction analysis" (PPI) (Friston et al., 1997). Likewise, a structural equation modeling (SEM) approach was proposed based on minimization of predicted and observed dependent variables (Büchel and Friston, 1997). Effective connectivity has potential implications in uncovering the neural mechanisms behind clinical disorders (Dauwels et al., 2010) and consciousness (Boly et al., 2011; Denis Jordan, 2013).

Briefly, EC refers to a broader definition of structural connectivity, which captures all the features that shape connectivity, such as synaptic strengths, concentration of neurotransmitter, neural excitability, causal structure of the links, etc. Various techniques have been proposed to estimate EC from fMRI BOLD signals, but the applications of these techniques were often overlooked due to the complexity of the methods (Stephan and Roebroeck, 2012). Furthermore, in the review article of Stephan and Roebroeck, they underline the fact that resting-state studies in particular are exploratory in nature and "the richness and complexity of their results can invite unconstrained interpretations and post-hoc injection of meaning" (Stephan and Roebroeck, 2012).

There are two fundamental approaches to estimate EC: model-driven and data-driven. The model-driven approaches rely on the generation of BOLD signals under some assumptions. The most widely used approach is dynamic causal modeling (DCM) as proposed by Friston et al. (2003). In DCM the hidden states of neuronal origin are simulated through generative models (i.e., neuronal state equations). Then, the neuronal state equations are linked to the observed data using hemodynamic models (Figure I.22). Finally, given the experimental constraints, the most likely model is inferred from the observed data through Bayesian techniques (Stephan and Roebroeck, 2012).

One of two important aspects of DCM that were emphasized in the literature was the hemodynamic response model. The most widely used hemodynamic response functions are based on "Balloon" model proposed by (Buxton et al., 1998). Later, various modifications were done for the hemodynamic models (Havlicek et al., 2015; Stephan et al., 2007). However, there are also some regional differences in hemodynamic responses (Huettel and McCarthy, 2001), which increase the free parameters in the DCM model.

Another key aspect of DCM is the selection and verification of the model. The decision regarding an optimal model requires the assessment of the trade-off between fit and complexity. Bayesian model selection (BMS) provides an ideal framework for this purpose. The estimated parameters are assessed through methodologies such as AIC/BIC (Penny et al., 2004) and the more widely used free energy principle (Friston et al., 2007).

The verification of DCMs involves two stages. First, the validity of parameter assessment, namely face validity, is performed using *in silico* models (Friston et al., 2003; Razi et al., 2015). Specifically, in this approach the model's validity is tested using artificial networks. A more challenging problem for DCM is the predictive validity, which accounts for the performance of the model given different settings. One approach to this question is to test the performance of model for test data given parameter estimates for training data (Smith et al., 2010). Another approach is to compare the model with respect to known independent states, such as the classification of clinical populations (Brodersen et al., 2011). The most convenient approach, however, is to use invasive

techniques that assess the validity of the model by simultaneous electrophysiological measurements (Moran et al., 2011).

An alternative approach is to characterize dependencies in the BOLD signals using multivariate (or vector) autoregressive (MAR) models (Harrison et al., 2003). The major difference in MAR models is that they reduce the model's complexity by bypassing the hemodynamic response compromising the accuracy of the estimates given the non-neuronal hemodynamic confounds (Rogers et al., 2010). To address this problem, the MAR approach requires estimation of the model order (Penny and Roberts, 2002).

In contrast to the model-based estimates of EC, data-driven approaches were also considered in the literature. These approaches rely on higher-order statistics, information theoretical measures or phase relationships in the BOLD signals. The most widely used method by which to extract EC from BOLD signals is Granger causality modeling (Goebel et al., 2003), which quantifies how well the past behavior of a signal can predict the second signal with respect to the past of the second one alone. Other approaches comprise mutual information and transfer entropy (Lizier et al., 2010), Bayesian networks (Ramsey et al., 2010), LiNGAM (Shimizu et al., 2006), Patel's tau (Patel et al., 2006), or non-linear synchronization (Quian Quiroga et al., 2002). Smith et al., (2011) compared the performance of these measures (Smith et al., 2011) and found that only correlation-based measures and Bayesian networks approach could accurately reflect the presence of the connections. Furthermore, they showed that all of the measures perform poorly in detecting the directionality of the connections, although Patel's tau performed slightly better than the other approaches. Other studies using simultaneous EEG recordings showed that regional variations in HRF might confound the causal relationships reflected in data-driven approaches (David et al., 2008). Recent studies proposed an alternative approach to overcome this problem, which involves de-convolution of BOLD signal prior to analysis (Bush et al., 2015). Nevertheless, as suggested by (Friston et al., 2014a) the EC is naturally model-based.

The techniques inferring that EC performs well are dependent on the context in which the data has been acquired. Crucially, they require experimentally controlled stimula-

tion, such as transmagnetic or deep-brain stimulation. A serious problem arises when the origin of the stimulation is not known, such as resting-state fMRI. The extensions of DCM addressed this problem by using stochastic (Daunizeau et al., 2009), Fourier series (Di and Biswal, 2014) and cross-spectrum-based approaches (Friston et al., 2014a).

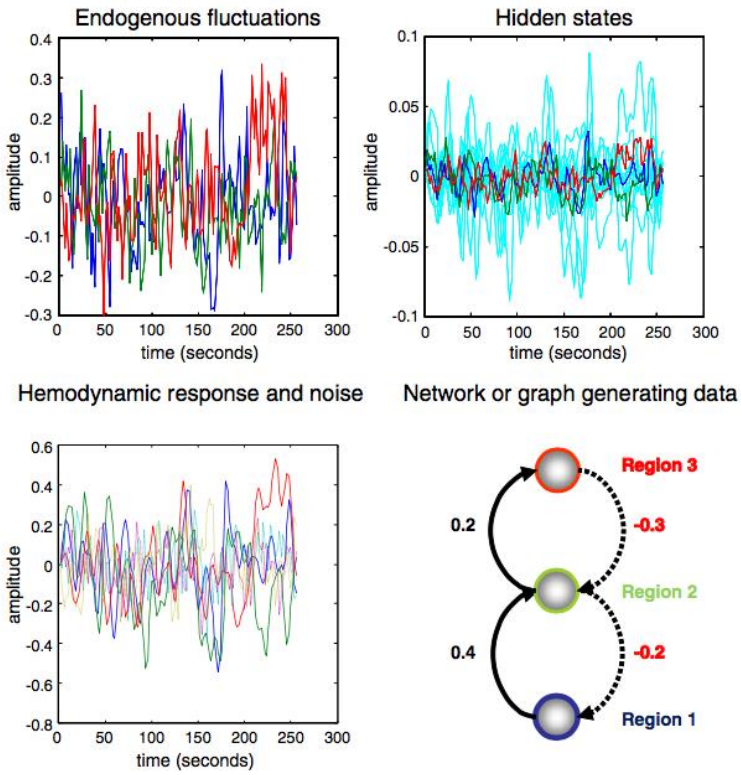

Figure I.22. Overview of Dynamic Causal Modeling (DCM) (adapted from Friston et al., 2014a).

Another important problem arises as the number of brain regions increases. The current frameworks to infer EC from fMRI BOLD signals are computationally expensive, and the computation time increases exponentially with the number of nodes. For this reason the analysis of EC could cover only small sets of regions in the cortex. Critically, the resting-state research showed that interactions between regions are non-trivial: The entire cortex is coordinated to generate rich, dynamic patterns of activity. Therefore, whole-brain based models are essential for the study of EC.

Inspired by the relationship between structure and function in the resting-state signals revealed by computational models Deco et al. (2014a) proposed a whole-brain computa-

tional model based on dynamic mean-field approximation of a biophysical model to infer EC using observed FC. They illustrated that the analytical approximation of covariance in simulated time series might make it possible to heuristically estimate optimal SC (i.e., EC) (Figure I.23). The disadvantage of this approach, however, was that the directionality of the connections could not be incorporated. A recent study extended this approach to construct a framework that can account for causal interactions (Gilson et al., submitted).

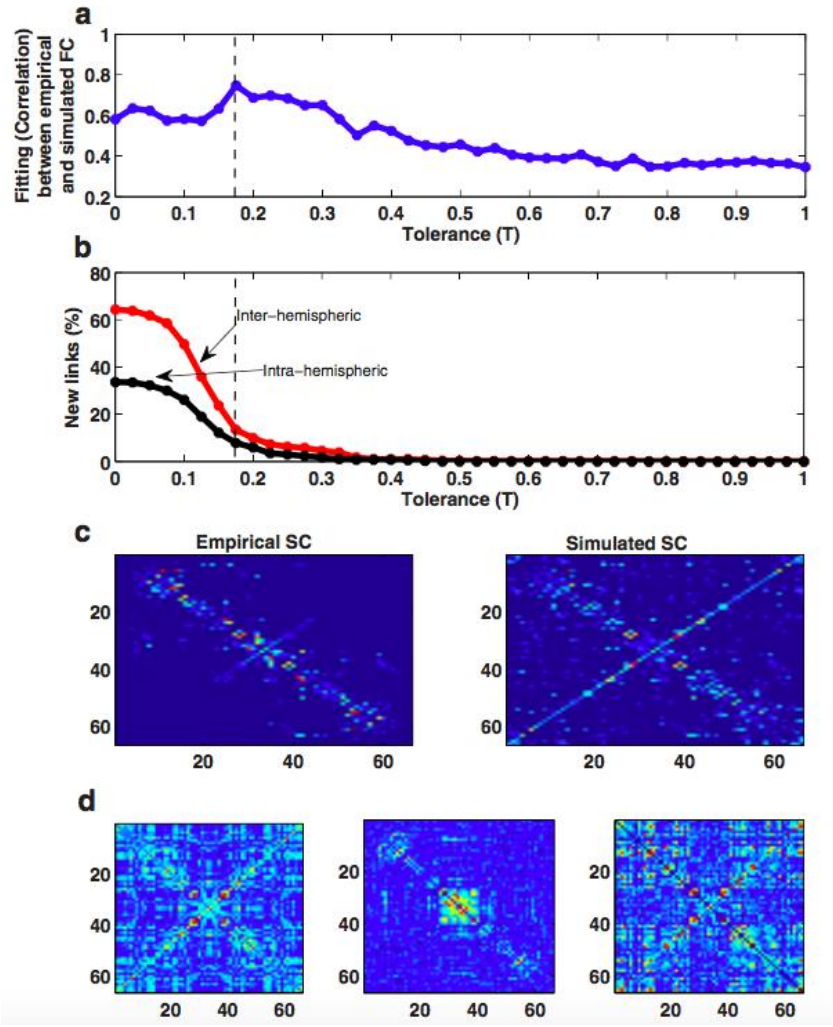

Figure I.23. Finding optimal SC using whole-brain computational model (adapted from Deco et al., 2014).

I.IV. Motivation

Subsequent to the seminal study by Biswal et al. (1995), thousands of research studies contributed to the understanding of resting-state fMRI BOLD signals. The research was regarded as a promising tool for the understanding of brain disorders, and most of the efforts were made in this direction. However, as it was reviewed in this chapter, it was not a straightforward problem. Most of all, the data analysis approaches using current neuroimaging methods rely on the observed connectivity measures that yield cumulative and interdependent interactions between brain regions. Moreover, most of the research on clinical applications of the resting-state fMRI can be considered as exploratory based on statistical comparisons between groups. It is important to note that the dominant approach in our study was exploratory in a similar way, although we intended to go beyond this border as much as we could.

We focused on two major problems in the field, the first of which is the conventional approaches to the characterization of FC present problems in interpretation. Recent evidence consistently suggests the FC is not a static measure but is instead composed of complex, spatiotemporal interactions between networks. It is crucial to develop methods by which to study time-dependent changes in rs-FC in clinical populations. The second problem is that current approaches cannot account for the possible origins of the alterations in the connectivity structure. Consequently, they cannot provide mechanistic explanations for the brain disorders.

The goal of this study is to address some of these problems. Using different clinical populations, we investigated the role of the dynamic changes in FC. To begin with, the whole-brain connectivity comparisons were implemented. We then proposed several high-level computational models as the means to understand the emergence of resting-state BOLD time series. These models were then used to infer effective connectivity that might reflect the hidden connectivity patterns underlying each clinical condition. In chapter III and chapter IV we focused on two major affective disorders: Major depressive disorder (MDD) and bipolar disorder (BP). In both cases the clinical populations were compared the static and dynamic FC measures along with the global characteriza-

tion of the connectivity differences. In the BP study we aimed to infer the EC using a linear model. This study tried to propose a mechanistic model for the alterations in connectivity patterns. The next two chapters studied the clinical populations at the two opposite edges of the human lifespan. At one end we studied newborns and infants with intrauterine growth restriction (IUGR). At the other end we investigated the progression of Alzheimer's disease (AD). Using a similar approach, we characterized various connectivity metrics in the global and nodal scales. Those metrics were then compared in terms of their static and dynamic properties. Finally, we used EC to understand the mechanics behind these alterations.

In summary, we aimed to build a computational framework to investigate resting state FC in neuropsychiatric disorders.

II. Insights From Nonclinical rs-fMRI

Before investigating the connectivity dynamics in clinical populations, we present preliminary analyses of non-clinical rs-fMRI data. The contents of this chapter are unpublished pilot studies that are aimed to serve as a benchmark for the studies presented in the remaining chapters.

The fundamental hypothesis in rs-fMRI studies in disease is that alterations in functional connections between regions reflect the impairments in the links. Therefore, the findings are usually interpreted in a straightforward way: Decreased FC between regions indicates disconnection, while increased FC indicates enhanced communication. However, this view is quite naïve considering the recent research on rs-fMRI. First, the functional connections are not operating in an isolated way. They are highly interdependent. Second, the FC between regions emerges as a result of highly complex interactions. Despite advanced statistical techniques alleviate these problems; it is very difficult to build a proper framework to consider all these aspects in a reliable way.

The purpose of this chapter is to investigate how the whole-brain activation patterns might be related to the connectivity alterations. In addition, this chapter discusses the major concerns in connectivity analyses, such as global average signal fluctuations.

II.I. Task as a benchmark

The idea behind the clinical investigations of connectivity is that the abnormal functioning of brain is associated to the disconnection between certain regions. The foundations behind this idea are presented in chapter I. Clinical neuroscience focuses on discriminating the disease-specific alteration patterns hoping to find their neural correlates. As we discussed earlier, the motivation of this approach comes from seminal historical case studies showing the dramatic effects of brain disconnection. Nevertheless, the complex disorders such as major depression or Alzheimer's disease might not show straightforward disconnection patterns. The "dysconnexion syndromes" involves the loss of a

mental skill after a devastating lesion in some part of the brain, which provides direct evidence for functional localization. On the other hand, the widespread mental disorders manifest themselves as alterations in mental and behavioral patterns, which are highly complex and heterogeneous. We believe that investigating the variations in connectivity during task might provide insights. The details of the methods that are used in this chapter are covered in the chapters III, V, and VI.

We investigated the relationship between resting-state and task FC. Our motivation is to understand how the whole-brain FC adapts to the external stimuli. We used the 2 sessions of 10 minutes fMRI BOLD time series of 22 healthy subjects recorded at rest and while watching natural images (see Appendix 7. Materials and Methods: Movie vs. Rest). We computed dynamic FC using the instantaneous phases of the time series that were extracted using Hilbert transform (for details see chapter III and chapter V). In brief, we quantified the functional relationship between regions using the phase coupling at each time point. This way, we obtained a dynamic FC tensor varying in the same temporal resolution with the BOLD time series. The BOLD time series were band-pass filtered between 0.04 – 0.07 Hz (for details see chapter III and chapter V). Static (grand average) FC was defined as the average synchronization between regions over time. We computed the variability of each connection, using index of dispersion (i.e. variance divided by mean) of phase-lock values. Finally, we compared the network alterations using NBS approach (the details of this procedure are presented in the appendices).

We found significantly different static FC networks in the movie group compared to the resting group. We found hyper-synchronized networks comprising fronto-temporal regions in the movie group compared to the resting group (Figure II.1-A). The core of the alteration was located in the orbital frontal cortex. In contrast, movie group was subjected to a network of decreased FCs between fronto-parietal regions, especially in the connections of supramarginal gyrus and caudal anterior cingulate (Figure II.1-B). This network was extended toward medial and superior parts of the frontal cortex and precentral gyrus. The results suggest that there is a decreased connectivity in somatosensory association areas while watching movie.

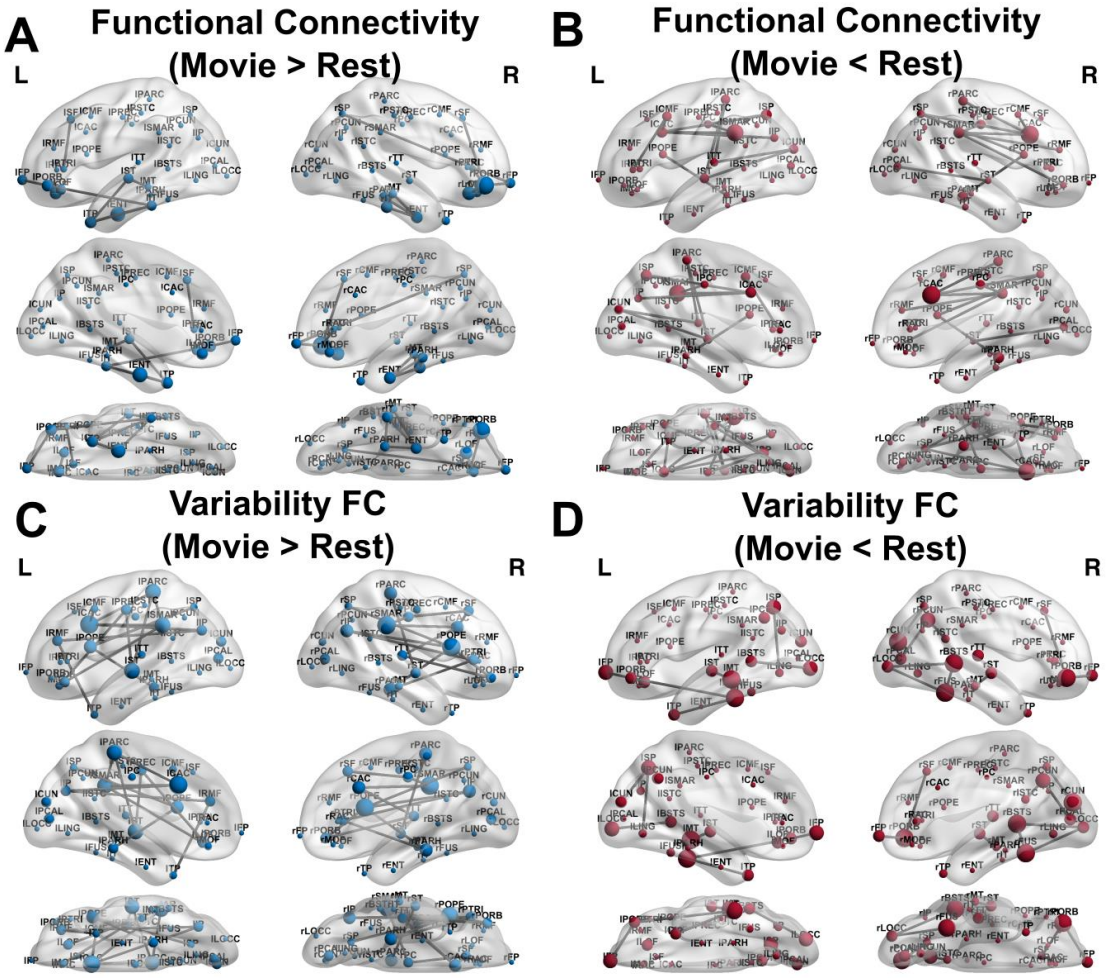

Figure II.1. NBS comparisons for FC and variability of FC between rest and movie. Top panel shows static FC, bottom panel shows variability of FC.

We repeated the same analysis for the second session. The correlation coefficient between the test statistics (T-statistic) obtained from the permutation tests in the first session and that in the second session was highly correlated ($r = 0.83$, p-value < 0.001). Hence, the altered networks were robust between sessions.

The brain regions showing altered FC variability were highly overlapping with those that were found in the static FC. However, there were important differences in the network topology. The network of increased variability of FCs was extended towards middle and superior parts of the temporal lobe and the parietal regions (Figure II.1-C). Furthermore, we found decreased variability of FC in the occipital lobe and in its connections with posterior parts of the parietal and temporal lobes (Figure II.1-D).

In summary, the static FC was increased in the orbital frontal and the temporal regions and decreased in the parietal regions while the subjects were watching movie. However, there were also alterations in the variability of FC. The variability of FC was increased between the temporal lobe and the parietal regions, and decreased between the temporal lobe and the occipital and orbital frontal cortices in the movie group.

There is a dramatic task-induced change in the whole-brain network topology that has never been investigated before. Furthermore, these results suggest that the connectivity alterations cannot be interpreted as an implication of straightforward mechanisms. For example, decreased FC might reflect modulatory role of the associated regions. Being specific, these regions might be interacting with distinct networks during task, which might cause enhanced FC variability and attenuated static FC.

II.I.i . Implications of the whole-brain connectivity

We computed the grand average FC of each subject, and then we implemented a clustering algorithm based on the correlation distance (1 – Pearson's correlation) to see how well the global functional states can distinguish whether a subject is at rest or watching movie. Surprisingly, the algorithm clustered the resting and movie groups with 100% accuracy (Figure II.2). We further verified this finding by using Support Vector Machine (SVM) classification. Here, we used the first session as the training set for SVM, and then predicted whether the subjects in the second session are resting or watching movie. SVM classification also confirmed that the whole-brain FC could distinguish the state of the subjects with 100% accuracy.

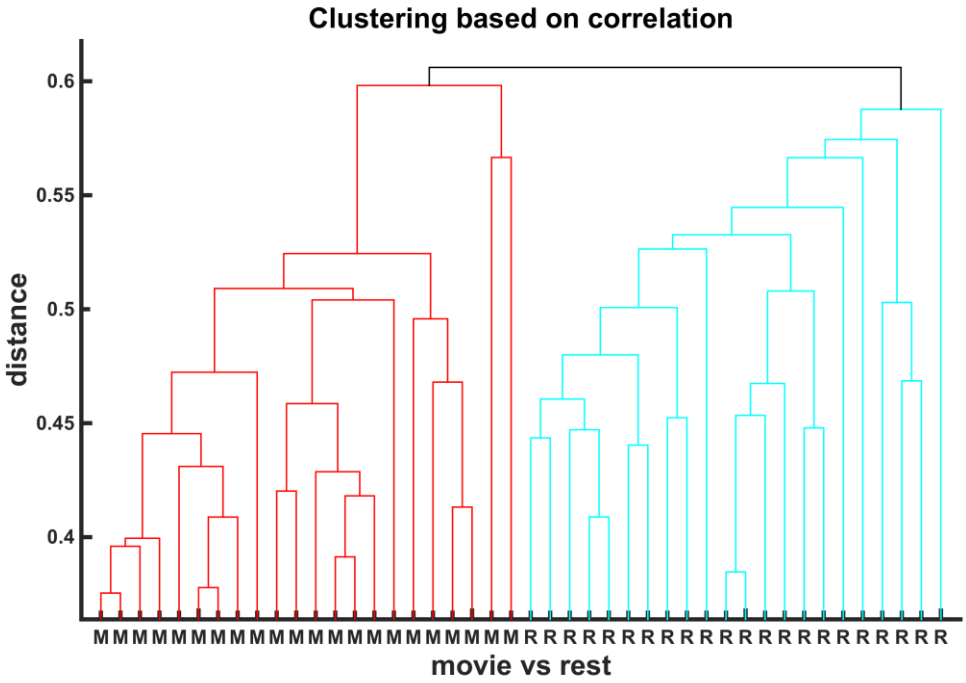

Figure II.2. Clustering based on correlation distance between whole-brain FCs. M stands for movie, R stands for rest. The subjects are classified 100%.

We also checked how often these global brain states were appeared in dynamic FC. First, we defined whole-brain connectivity masks of the "rest" and "movie" states based on the grand average FCs of each group using the first recording session. Later, using the dynamic FC tensors, we computed how well these masks fitted to the whole-brain connectivity states at each time step for the second recording session. We found that for each subject the temporal FC patterns showed preference to a particular mask in accordance with whether they are at rest or watching movie (Figure II.3). However, this preference for the similarities was fluctuating slightly (i.e. a movie subject could switch to a resting-like state for a very short period of time).

We quantified this preferences by computing the probability of being at "rest" or "movie" by counting the times that a subject's temporal FCs showed higher similarity for a particular mask, and dividing it to the total time steps (Figure II.4). Moreover, we showed that the probability of being at "rest" or "movie" correctly predicted the state of each subject.

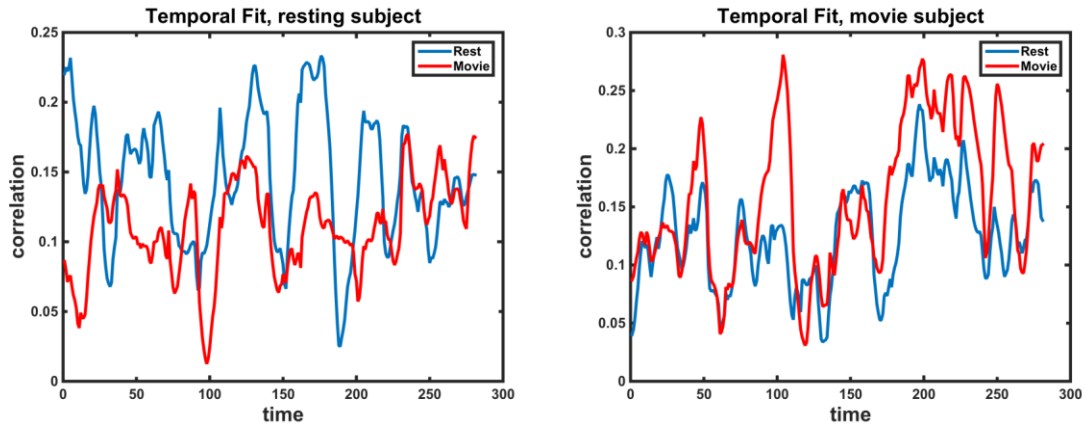

Figure II.3. Similarity between instantaneous FC matrices in time and average FC at rest and movie. Similarity of resting FC is higher for most of the time in resting subject (right), and vice versa (left).

The whole-brain connectivity patterns are one of the promising tools that might have clinical significance. Zeng et al., (2012) showed that the whole-brain FC multivariate pattern analysis might classify major depressive disorder (MDD) patients with 94.3 % accuracy. This is also consistent with our observations on the clinical population of MDD patients. We measured how well each subject fit to the average FC mask of each group. Despite the short fMRI recording time, this simple measure could classify MDD patients with 85% sensitivity and 67% specificity (Figure II.5)(the analysis of MDD patients is discussed in more detail in chapter III).

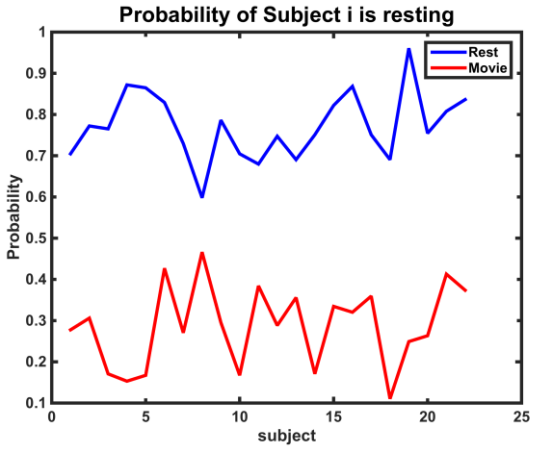

Figure II.4. Probability of subjects being at rest or watching movie based on the time points in dFC in which an instantaneous state is closer to rest or movie FCs of the first session.

In conclusion, we found that the global connectivity patterns may alter dramatically in distinct conditions. However, even if these patterns can provide perfect classification, they don't explain the underlying mechanisms. Conventional FC analyses are useful, but they are insufficient. We showed that temporal variations of FC could provide additional information to identify the mechanisms behind the connectivity changes. However, the most convenient approach is the computational modeling of whole-brain activity.

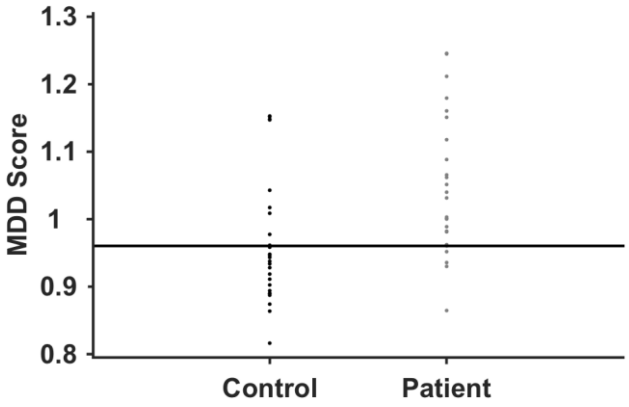

Figure II.5. The similarity scores (indicating how much each subject is closer to MDD grand average FC than that of HCs). The similarities were estimated using one-leave-out procedure.

II.I.ii . Can we trace the origins?

Dynamic FC provides a better understanding of the mechanisms underlying whole-brain connectivity alterations. However, as the results suggested, these mechanisms are extremely complex and interdependent. Being specific, using data-driven approaches we capture the cumulative alterations in the connectivity, but not the origins. We believe that the only way to propose mechanistic explanations is to use computational modeling at the whole-brain level.

Using the same dataset, we simulated the BOLD time series of the subjects using Hopf normal model (see chapter VI.II.iv . for details).

As a summary, the time evolution of the whole-brain dynamics is described by the following coupled differential equations:

$$\frac{dx_j}{dt} = \left[a_j - x_j^2 - y_j^2\right]x_j - \omega_j y_j + G\sum_i C_{ij}\left(x_i - x_j\right) + \beta\eta_{xj}(t)$$

$$\frac{dy_j}{dt} = \left[a_j - x_j^2 - y_j^2\right]y_j + \omega_j x_j + G\sum_i C_{ij}\left(y_i - y_j\right) + \beta\eta_{yj}(t)$$

Where C_{ij} is the Effective Connectivity (EC) between nodes *i* and *j*, *G* is the global coupling factor, and $\beta = 0.02$ is the standard deviation of the Gaussian noise. The simulated activity, *x*, corresponds to the BOLD signal of each node. The system shows a supercritical bifurcation at $a_j = 0$. If a_j is smaller than 0, the local dynamics has a stable fixed point at $z_j = 0$, and for a_j values larger than 0, there exists a stable limit cycle oscillation with a frequency $f = \omega/2\pi$. The model is discussed in more detail in chapter I.III.ix . and in chapter VI. Following the procedure presented in chapter VI, we estimated the underlying EC from observed FC at rest. Then, we used the estimated EC of each subject to predict the FC while the subject is watching movie. Here, we fixed the ECs (along with the other parameters), but modified the local bifurcation parameter of each region.

Iteratively, we increased and decreased the local bifurcation parameter, *a*, by 0.01, for each region separately (i.e. we kept the remaining bifurcation parameters at their original value). After computing the updated simulated FCs, we accepted the modifications if the Euclidean Distance between simulated and empirical FC decreased as a result of corresponding modification. We used 100 iterations, which was enough to reach a global minimum.

We tested whether the mean bifurcation parameter of a particular region was significantly different than 0 using t-test. Since we did multiple comparisons, we used False Discovery Rate (FDR) correction for the acquired p-values. We found that the bifurcation parameter of 3 regions was significantly altered: right inferior temporal, left lingual gyrus, and left temporal pole (Figure II.6).

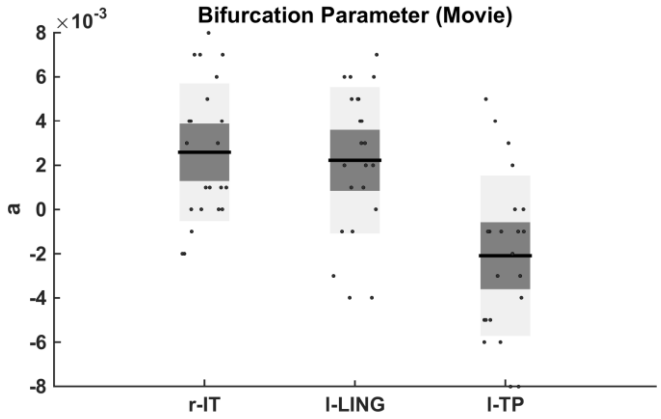

Figure II.6. The regions with optimal bifurcation parameters during movie session significantly different than zero.

We found that the bifurcation parameters of right inferior temporal and left lingual gyrus were significantly higher than 0, which suggest that these regions became a source that orchestrates the dynamics. These results indicate that integration and memorization related brain regions dominate the whole-brain activity while watching natural scenes. On the other hand, for left temporal pole, we found a negative bifurcation parameter suggesting that the region shifted toward noisy regime, and it lost its influence on the whole-brain dynamics.

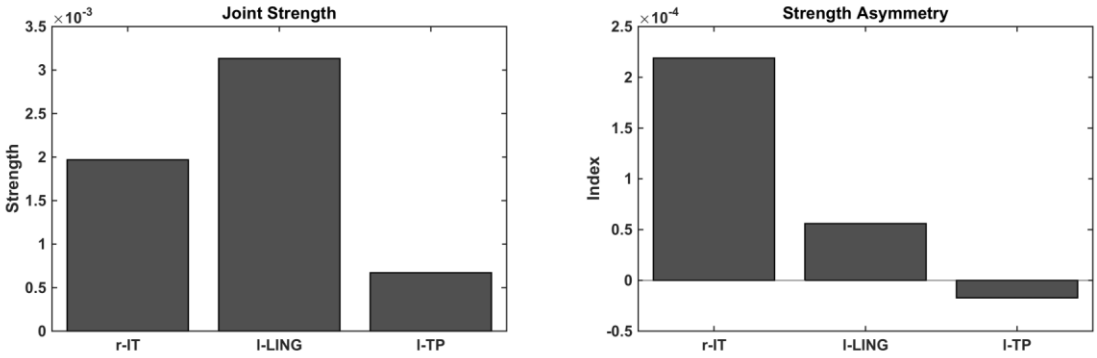

Figure II.7. Joint strength (out-strength plus in-strength) of significantly different regions (left) and strength asymmetry (out-strength minus in-strength) of significantly different regions (right).

We analyzed two basic graph metrics of EC's of the nodes with altered bifurcation parameters. These metrics are the joint strength (i.e. the sum of mean out- and in-strengths), and the strength asymmetry (i.e. the difference between mean out- and in-

strengths) of each region. The second measure quantifies the directedness of the nodes. Positive values indicate higher out-strength (source), while negative values indicate higher in-strength (sink). The results showed a distinct topology for each region (Figure II.7). Inferior temporal cortex is a high strength node with high output preference. The lingual gyrus had very high strength, but its in- and out-strengths were relatively balancing each other. Finally, temporal pole was low in strength and it was a balanced node (but the asymmetry index was slightly negative).

We speculate that r-IT acts like a source hub that modulates the whole-brain activity while watching natural scenes. l-LING might be considered as a different kind of hub because of its high strength that is fairly distributed on both directions unlike r-IT. On the other hand, l-TP lost its influence while the subjects were watching movie. We emphasize that temporal pole was consistently altered also in different clinical populations (see following chapters). This region is usually omitted during the analyses, and considered to be enigmatic (Olson et al., 2007)**.** We believe that temporal pole needs more attention in resting state research.

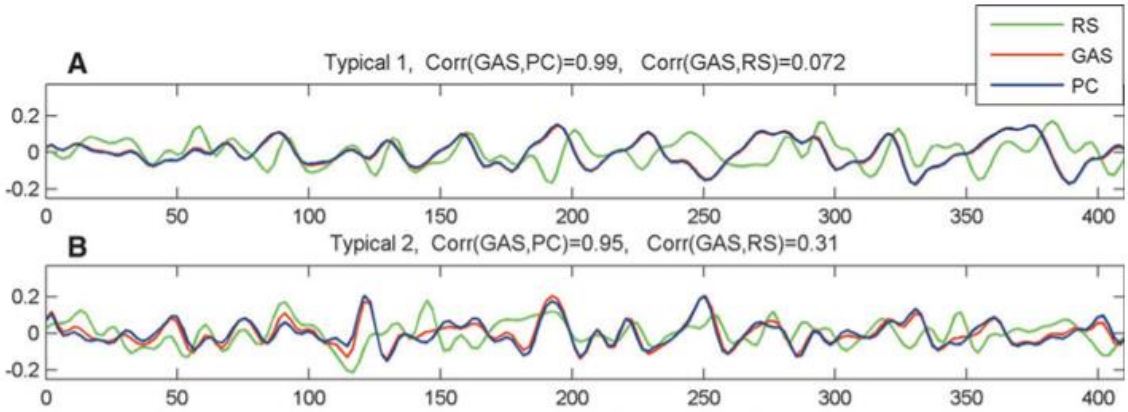

Figure II.8. Relationship between PCA and GAS. First principal component is perfectly correlated with GAS. (adapted from Carbonell et al., 2011)

II.II. Global Average Signal

The removal of global average signal (GAS) is a controversial procedure in rs-fMRI studies (see chapter I). Most of the studies considered GAS as a consequence of physio-

logical noise, which confounds the temporal correlations between the brain regions. However, this procedure can also induce artificial temporal correlations (see chapter I). One study showed that the time course of the GAS is almost identical to the first principal component of the BOLD time series (Carbonell et al., 2011) (Figure II.8). Furthermore, Yang et al., (2014) illustrated the clinical relevance of GAS in schizophrenia and bipolar disorder. They verified this further through large-scale computational modeling.

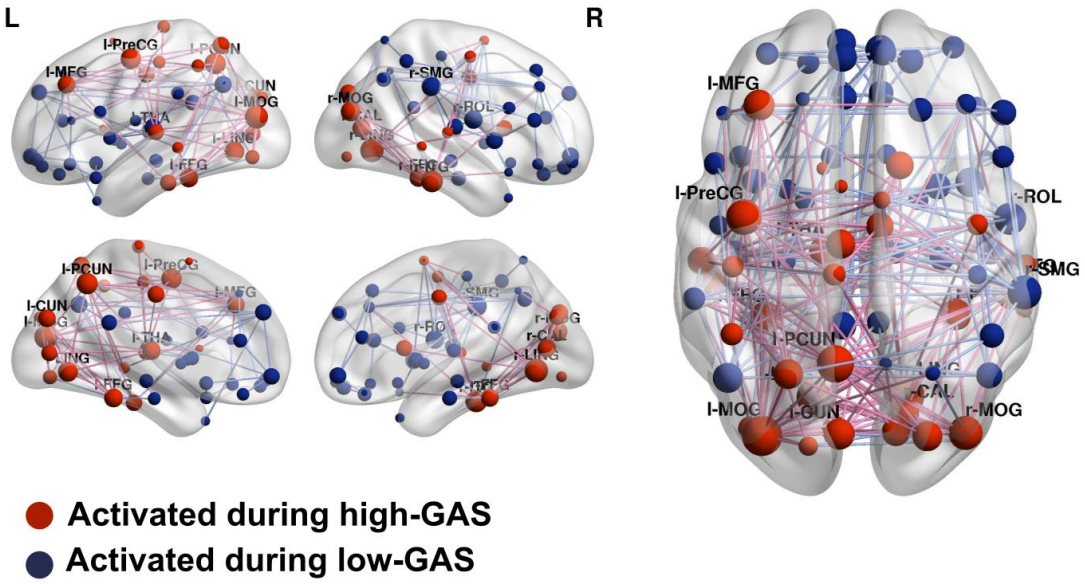

Figure II.9. Changes in FC patterns during high- and low-GAS states. Red nodes and links indicate higher synchronization during high-GAS state, while blue nodes and links indicate higher synchronization during low-GAS state.

In this subchapter, we investigated the relationship between GAS and FC. We used the 27 healthy controls subjects' rs-fMRI BOLD signals, which were the part of the Major Depression Disorder (MDD) project (the details are presented in Chapter III). Following a similar approach to Tagliazucchi et al., (2012a), we constructed the time courses of the BOLD signals as a point-process. However, instead of using the BOLD time-series of the rain regions, we focused on the time course of the GAS. First, we transformed the GAS for each subject to z-scores. Then, we defined the high-GAS and low-GAS states as the time points in which the z-scores of the GAS exceeded a predefined threshold (i.e. $|z| > 1$). In parallel; we extracted the dynamic FC using Hilbert transform (see

Chapter III). Then, we computed the average FC in dynamic FC tensor at the time points corresponding high- and low-GAS states separately. Finally, we measured the differences between the FC at high-GAS and low-GAS states (i.e. the difference between mean FC at high-GAS state and that at the low-GAS state).

The results showed very particular patterns at two extreme GAS states. High-GAS was associated to hyperconnectivity with in occipital lobe. Furthermore, this network was extended toward parietal regions, notably precuneus and other default mode network (DMN) regions such as thalamus, anterior cingulate and medial frontal gyrus. In contrast, fronto-parietal formed a network during low-GAS state (Figure II.9). Based on these results, we speculate that GAS is functionally relevant, and removal of it via global signal regression (GSR) might affect the interpretation of the results. We further explored the relationship between GAS variability and metastability (standard deviation of Kuramoto order parameter. See chapter IV). We found a strong correlation between these two quantities (Figure II.10).

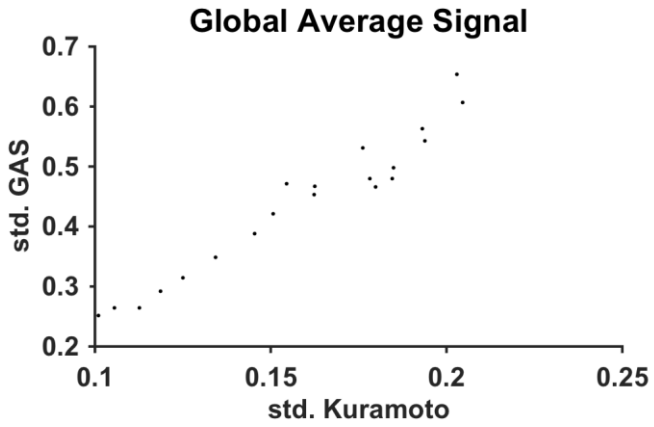

Figure II.10. The relationship between GAS and Kuramoto order parameter variability. (r = 0.97)

III. Major Depressive Disorder

Don't let us forget that the causes of human actions are usually immeasurably more complex and varied than our subsequent explanations of them

Fyodor Dostoyevsky, The Idiot

Abstract

Resting-State fMRI (RS-fMRI) has become a useful tool to investigate the connectivity structure of mental disorders. In the case of Major Depressive Disorder (MDD), recent studies regarding the RS-fMRI have found abnormal connectivity in several regions of the brain, particularly in the Default Mode Network (DMN). Thus, the relevance of the DMN to self-referential thoughts and ruminations has made the use of the resting-state approach particularly important for MDD. The majority of such research has relied on the grand averaged functional connectivity measures based on the temporal correlations between the BOLD time series of various brain regions. We, in our study, investigated the variations in the functional connectivity over time (i.e., dynamic functional connectivity) at global and local level using RS-fMRI BOLD time series of 27 MDD patients and 27 healthy control subjects. We found that global synchronization and temporal stability were significantly increased in the MDD patients. Furthermore, the depressive patients showed significantly increased overall average (static) functional connectivity (sFC) but decreased variability of functional connectivity (vFC) within specific networks. Static FC increased to predominance among the regions pertaining to the default mode network (DMN), while the decreased variability of FC was observed in the connections between the DMN and the fronto-parietal network.

III.I. Introduction

Major depressive disorder (MDD) is among the world's most prevalent mental disorders. Annually, it affects nearly 7% of the European Union's population (Wittchen et al., 2011), and in 2010 it was cited as the second-most prevalent cause of disability worldwide (Ferrari et al., 2013). Research on the complex mechanisms underlying MDD is crucial as a means to ensure effective measures for diagnosis, treatment and prevention as well as for understanding function in the diseased brain as compared to

the healthy one. The current evidence supports the assertion that the development of MDD depends on alterations in distributed neural networks involving cortical and subcortical structures. In that respect, the development of analysis approaches for resting-state fMRI (rs-fMRI) represents a major step forward in the evaluation of brain function at the network level.

Studies based on rs-fMRI have, with respect to MDD samples, reported significant decreases in functional connectivity among the cortical, limbic and thalamic regions (Anand et al., 2005; Cullen et al., 2009; Lui et al., 2011; Bluhm et al., 2009; Ramasubbu et al., 2014) (for review, see L. Wang et al., 2012). Likewise, rs-fMRI studies have highlighted the alterations in different resting-state functional networks (RSNs). Particularly, research focusing on the default mode network (DMN), typically being associated with introspection and inward attention, has shown that depressive patients exhibit increased functional connectivity within this network (Sheline et al., 2010; Zhou et al., 2010; Alexopoulos et al., 2012; Grecius et al., 2007; Berman et al., 2014), which is normalized after anti-depressant treatment (Li et al., 2013; Liston et al., 2014). Other authors have reported that, MDD patients in the resting state display an increased anti-correlation between task-positive and task-negative (akin to the DMN) networks (Zhou et al., 2010) but a failure to down-regulate the DMN during tasks involving emotional judgment (Grimm et al., 2011). Contrastingly, significant disconnections between posterior and anterior components of the DMN have been also described (Grimm et al., 2011), showing these components a differential response to anti-depressant treatment (Li et al., 2013). In any case, alterations within the DMN have been shown to be related to specific MDD clinical features such as exaggerated self-focus and depressive maladaptive ruminations (Hamilton et al., 2011; Berman et al., 2011). Concurrently, results regarding other RSNs also remain controversial. For example, while some studies have reported increased functional connectivity within cognitive control and affective networks (Sheline et al., 2010; Connolly et al., 2013; Avery et al., 2014), others have, in regard to those regions, offered diametrically opposite findings (Alexopoulos et al., 2012; Veer et al., 2010).

Research on resting-state FC, in addition to providing relevant information on the pattern of regional connectivity in specific brain networks, has made it possible to examine functional connectivity patterns in the context of the entire brain. This whole-brain approach has been applied to the study of different samples of MDD patients using a broad range of FC measurements (Gong and He, 2015). However, disparate results have been reported in regard to whole-brain functional connectivity decreases (Berman et al., 2014), reductions in inter-hemispheric connectivity (Guo et al., 2011; Li Wang et al., 2013) and increases in global patterns of functional connectivity (Bohr et al., 2013). Different explanations for the inconsistencies of the results have been proposed, including the clinical heterogeneity of MDD samples; the use of different definitions for network nodes and edges; changes in arousal; and cardiorespiratory and/or motion artifacts, all of which might be correlated with the global properties of brain networks (Gong and He, 2015).

Nearly all of the resting-state literature has considered FC measurement as the average connectivity between different regions during a resting period (i.e., static FC), thus assuming that functional connectivity remains constant while the brain is in the resting state. Recently, however, we have seen the emergence of interest in the temporal properties of FC (i.e., dynamic FC), which may be defined as the time-varying functional connectivity between brain regions, whether assessed at rest or during task performance. Given the disparities among the findings regarding the static measures of FC in MDD, an investigation of the temporal dynamics of the FC during rest might provide new insights into the alterations of functional connections in MDD. As of this writing, few studies have been conducted with the use of this approach and the findings have been controversial, with null (Hamilton et al., 2011) and positive findings reported. Regarding the latter, two recent studies by Wei et al. (2013 and 2015) found alterations in the Hurst exponent of the time series in MDD patients. The Hurst exponent indicates the self-similarity or regularity of a time series, where a greater Hurst exponent value signifies highly regular fluctuations over time, suggesting a tendency toward coordinated signal organization within a network (Wei et al., 2015). In depressed patients, a low Hurst exponent was detected within the DMN, thus indicating uneven signal oscillation over time. Nevertheless, in this same sample the fronto-parietal, ventromedial prefrontal

and salience networks showed increased Hurst exponent values (Wei et al., 2013; Wei et al., 2015). In summary, although still in the emergent stage, the dynamic analysis of rsFC appears to be useful as a means to obtain additional measurements with which to better characterize the underlying neuropathological mechanisms of MDD.

This study is intended to examine the relationship between static and dynamic measures on the global level, as well as the local level, in a sample of MDD patients. Accordingly, we have employed whole-brain connectivity analysis based on static and dynamic functional connectivity in 27 MDD patients and 27 controls. We checked the global stability of dynamic functional connectivity in each MDD patient during the scan using the average global synchronization and examined the similarities among the temporal states of the subjects. We then compared the differences at the local level using the overall average FC and the variability of FC among the MDD patients and the controls. Finally, through a process of machine-learning classification we tested the clinical significance of the results.

III.II. Materials and Methods

Preprocessed time series were band-pass filtered in 0.04-0.07 Hz range in order to reduce the effects of low-frequency drift and high-frequency noise (Glerean et al., 2012). The global average functional connectivity (sFC) was defined as the Pearson's correlation coefficient (r) between the time series of each ROI. The resulting correlation coefficients were approximated as a normal distribution using Fisher's z-transformation ($z = \arctan(r)\sqrt{r - 3}$), where T is the total number of time points). The same narrow-band signal was used for both analyses in order to justify the comparison. One healthy control subject was excluded from the analysis due to segmentation error in any single ROI. However, no difference was observed in the results between 26 of the MDD subjects and the 27 healthy control subjects.

The Hilbert transform (Glerean et al., 2012) was used for the assurance of dynamic functional connectivity. This approach allowed us to extract dFC with a higher temporal resolution given the short length of the resting-state fMRI session. The Hilbert

transform, $S(t) = A\cos(j(t))$S(t) = Acos(φ(t)) of the preprocessed BOLD time series broke the signal down to an analytical signal *S(t)* with an instantaneous phase *φ(t)* and amplitude *A*. For each time instance *t*, the difference between the phases of the respective ROIs was calculated as $Dj_{ij}(t) = j_i(t) - j_j(t)$, where *i* and *j* are the indices of each ROI. Then, instantaneous coupling matrices (ICMs), *C(t)*C(t) were constructed using the phase differences normalized between 0 and 1, thereby representing perfect synchronization and perfect synchronization respectively, such that: $C_{ij}(t) = 2\pi / \Delta\varphi_{ij}(t)$.

Global synchronization *G(t)* G(t) was calculated using binarized ICMs (i.e., binary connectivity matrix comprising phase differences less than *π/8*). The percentage of existing connections at each binary ICM was defined as global synchronization (see Appendix 1. Materials and Methods: MDD).

The similarities between the ICMs with the given time lag (0-20 sec.) were quantified for each subject as the correlation coefficient between two matrices at each instance. Moreover, because global synchronization also affects the similarity between ICMs, the similarity of each ICM to the overall average dFC was taken as a reference (see supplementary materials). Similarity to the reference was calculated as the correlation coefficient between each ICM and the average dFC. Thus, the intertemporal closeness (*ITC)* was defined as the proportion of similarities between ICMs that were smaller than the average similarity to the reference (i.e., the probability of observing greater similarity between instances than their similarity to the global phase-coupling matrix).

The global synchronization and intertemporal closeness measures were used to quantify the overall spatiotemporal stability of the dynamic FCs. A high *G(t)* indicates that the subject has a tendency to linger in a state where the overall phase-coupling between each ROI is persistently high. Contrastingly, ITC takes into account the spatial similarity between each temporal state, characterized by ICMs. Furthermore, while the correlation coefficients among the ICMs decreased monotonously over time, generally the correlation coefficients to the reference were normally distributed around a moderate value (Figure III.1). Accordingly, a lower ITC suggests that the fluctuations in temporal states around the global average FC are higher, while a higher ITC indicates a

more stable temporal dynamic.

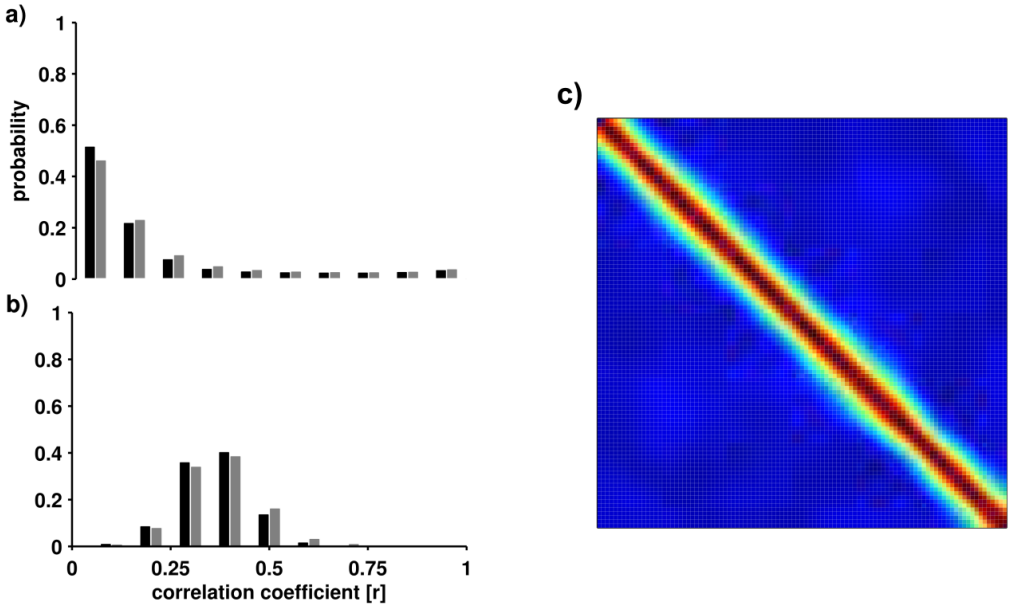

Figure III.1. The histograms of correlation coefficients between instantaneous states (i.e. the correlation coefficient between the whole-brain FC at time t1 and t2 in dFC. The correlation matrix, also called functional connectivity dynamics (FCD) matrix.

The variability in each pair in ICMs, $C_{ij}(t)$ was considered at the nodal level. The variability of functional connectivity (vFC) was computed as the index of dispersion (variance/mean) of the coupling between each pair, and this was calculated for each subject. Figure III.2 illustrates the process.

III.III. Results

III.III.i . Global Stability of Dynamic Functional Connectivity

We first compared the distributions of global synchronization of the MDD patients and healthy controls using the Kolmogorov-Smirnov distance between cumulative distribution functions. We found that the global synchrony distribution of MDD patients had shifted toward high synchrony as compared to the healthy controls, showing a significant difference (Kolmogorov-Smirnov test, $p < 0.001$, $D = 0.12$). However, we

found no significant difference between the means of global synchronization of the respective groups, despite a tendency toward significance (p = 0.0554, permutation test). (Figure III.3).

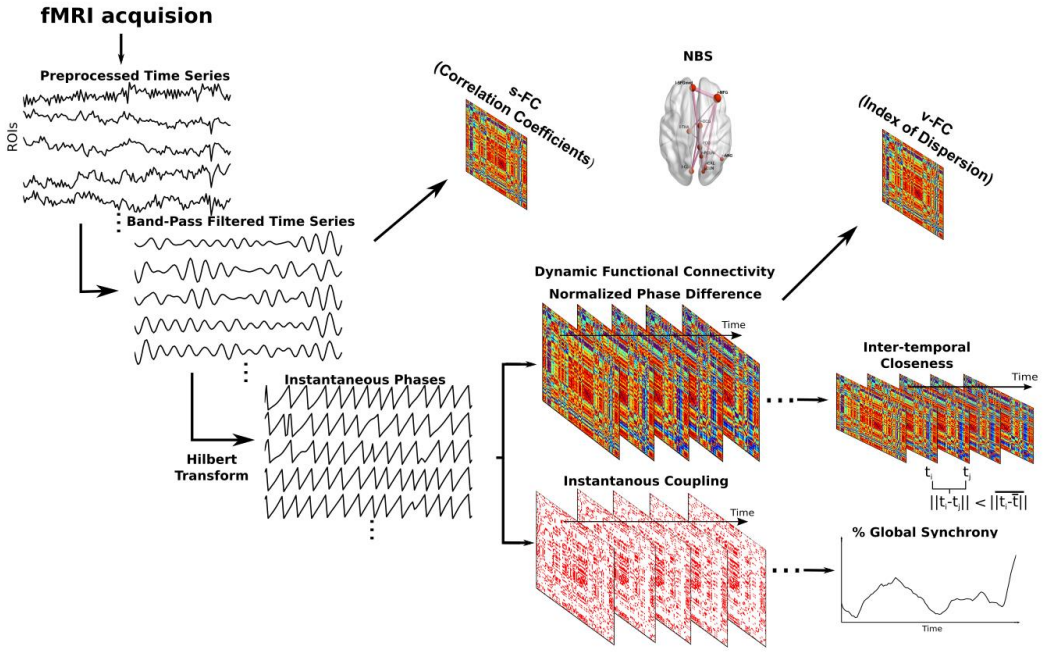

Figure III.2. The static and dynamic analysis of rsFC. Following the fMRI acquisition and preprocessing, the BOLD time series results were band-pass filtered in the 0.04-0.07Hz frequency range. The instantaneous phases of resulting time series at each time step were then calculated using the Hilbert transform (left). The phase difference between each ROI was normalized between 0 and 1, indicating perfect synchrony and asynchrony, respectively. Consequently, the resulting matrix of dynamic functional connectivity (dFC) comprised an instantaneous coupling matrix (ICM) at each time step. The global synchrony, i.e., the percentage of synchronized pairs at each instance, was calculated using binarized ICMs (connection pairs greater than $\pi/8$). Intertemporal closeness (hereinafter "ITC") was defined as the probability of detecting two ICMs having greater-than-average similarity to the grand average of dFC. Connectivity analysis was performed through use of the Network Based Statistics (NBS) toolbox. The global average FC (sFC) was calculated as Fisher's z-transformed correlation coefficient of the BOLD time series. The variability of FC (vFC) was quantified as the index of dispersion (variance/mean) of the dFC.

Subsequently, we defined the measure of intertemporal closeness (ITC) to quantify the stability of FC over time. ITC was calculated as the probability of detecting a pair of

instantaneous coupling matrices (ICMs) having a similarity greater than the average similarity of each instance to the mean coupling between pairs over time. The reason behind this metric is that while the similarity between two ICMs decays over time, each of these matrices shows a stable correlation with the global mean FC. For the same reason we checked ITC for different time lags τ. The MDD group showed significantly greater intertemporal closeness than did the HC group ($p = 0.013$, permutation test) (Figure III.4): In the former group, ITC fell below the 5% chance level at a lag of 11.7 seconds, while for the HCs the time lag was approximately 10.3 seconds (Figure III.4), suggesting the greater stability of dynamic functional connectivity in the MDD group.

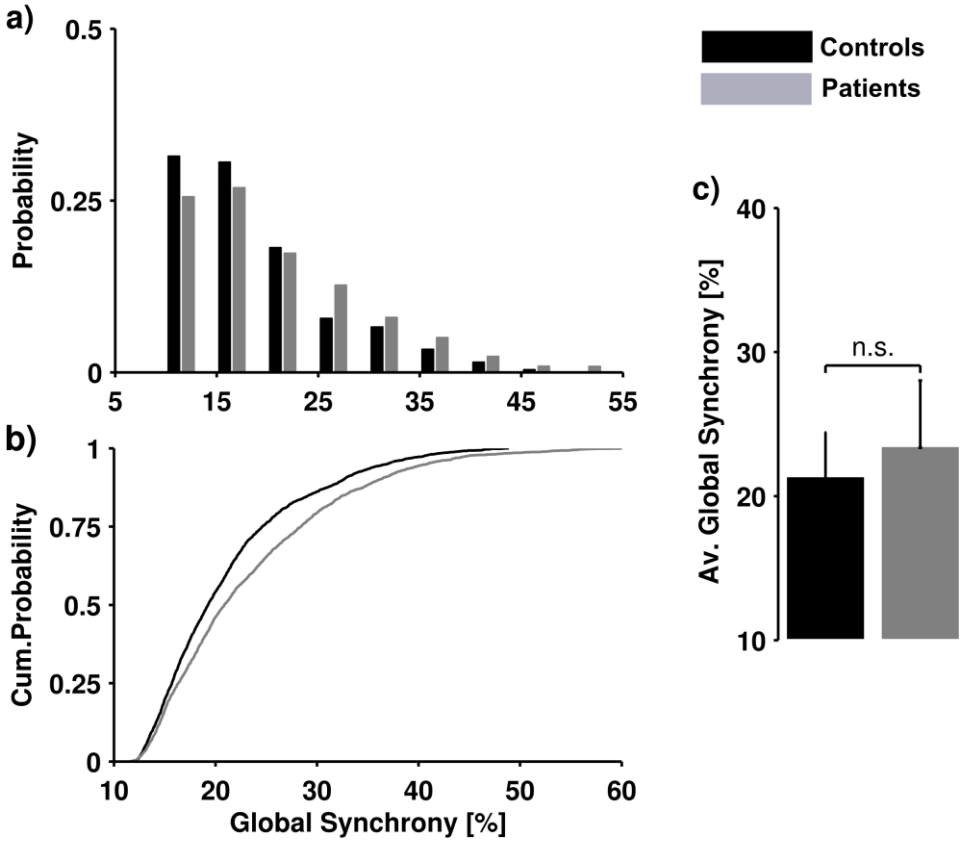

Figure III.3. Global synchrony. a) Probability distribution histograms of global synchronization in MDD patients and HCs; b) cumulative distribution function: the distance between two distributions is statistically different (Kolmogorov-Smirnov test, $p < 0.001$); and c) comparison of means of global synchronization (tendency toward significance, $p = 0.0554$). (In all figures, black represents healthy controls and gray represents MDD patients.)

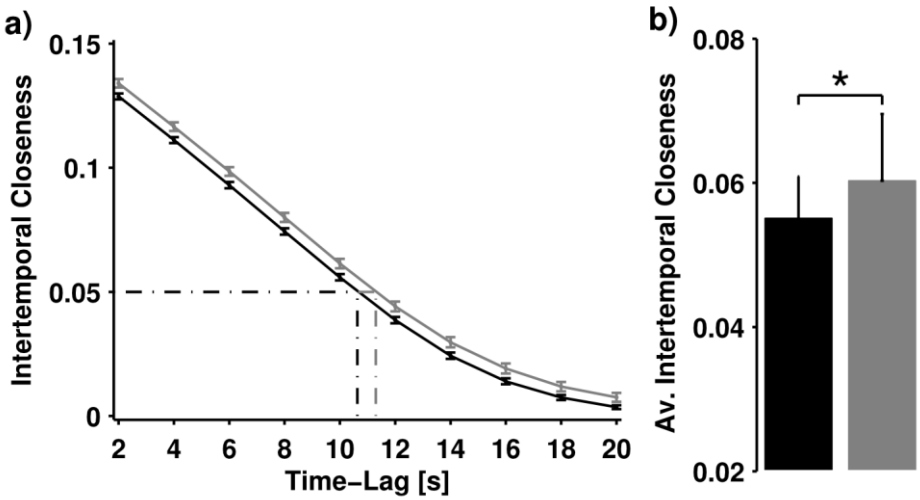

Figure III.4. Intertemporal Closeness. a) Probability of finding two temporal states (characterized by ICMs) having a similarity (correlation coefficient) greater than the overall similarity to the average coupling matrix using different time-lags (i.e., excluding nearby τ time points). Chance level closeness ($p < 0.05$) is 10.3 seconds for healthy controls, 11.7 seconds for MDD patients. b) Comparison of mean intertemporal closeness without time-lag (permutation test with 10000 permutations, $p = 0.013$).

III.III.ii . Whole-Brain Connectivity Analysis Based on s-FC (Static) and v-FC (Non-static) Connectivity

We used the Network Based Statistics (NBS) approach to study local alterations in whole-brain functional connectivity. We compared static and non-static connectivity measures, namely sFC (Fisher's z-transformed correlation coefficients between the time series of each ROI) and vFC (index of dispersion of the coupling between each pair), respectively. The index of dispersion was used to distinguish the variability of the coupled pairs from the uncoupled pairs. MDD patients showed a significant, widespread increase in sFC and a decrease in vFC. With respect to both measures, the altered connections were observed among the right dorsal and posterior cingulate, the precuneus, and the right medial and left superior frontal gyri, forming a network associated with the default mode network (DMN) (Figure III.5). However, while the increase in sFC was extended further to other DMN-related regions such as the right cuneus, left thalamus and right angular gyrus, the decrease in vFC suggested an impaired variability between the core DMN components and the fronto-parietal network

comprising the right paracentral and inferior parietal lobules, the dorsal part of the left superior frontal gyrus, the right inferior frontal gyrus and the post-central gyrus (Table III.1). In brief, MDD was manifested as hyperconnectivity within the regions of the DMN accompanied by decreased variability with DMN and the regions related to executive function and sensory information integration.

Table III.1. Significantly Different Connections Based on Static FC (sFC) and Variability of FC (vFC)

Static Functional Connectivity (sFC)			Variability of Functional Connectivity (vFC)		
Pair	**T-statistic**	**p-value**	**Pair**	**T-statistic**	**p-value**
IFGoperc (right) - FFG (left)	4.1412	0.0001	MFG (right) - PoCG (right)	4.3769	0.0001
MFG (right) - SFGmed (left)	3.6813	0.0006	IFGoperc (right) - PCG (right)	4.3620	0.0001
DCG (right) - PCG (right)	3.6159	0.0007	CAL (right) - IPL (right)	4.0979	0.0001
MFG (right) - CAL (right)	3.5159	0.0009	IFGoperc (right) - PCL (right)	4.0553	0.0002
SFGmed (left) - CUN (right)	3.5116	0.0009	DCG (right) - PCG (right)	4.0228	0.0002
MFG (right) - CAL (left)	3.4895	0.001	MFG (right) - SFGmed (left)	3.9779	0.0002
DCG (right) - CAL (left)	3.4439	0.0011	SFGdor (left) - MFG (right)	3.4431	0.0011
IFGoperc (right) - LING (right)	3.4224	0.0012	IPL (right) - PCUN (left)	3.3909	0.0013
IFGoperc (right) - LING (left)	3.3994	0.0013	MFG (right) - PCL (right)	3.3567	0.0015
MFG (right) - THA (left)	3.3911	0.0013	SFGdor (left) - IPL (right)	3.3203	0.0016
ANG (right) - THA (left)	3.3882	0.0013			
LING (right) - SMG (right)	3.3164	0.0017			
PCG (right) - CAL (right)	3.3068	0.0017			
SOG (right) - SMG (right)	3.3040	0.0017			
SFGmed (left) - PCUN (right)	3.3019	0.0017			
PCG (right) - PUT (left)	3.2903	0.0018			
PreCG (right) - ANG (right)	3.2415	0.0021			
MFG (right) - LING (right)	3.2412	0.0021			

III.III.iii . Classification and the Linear Model

Two widely accepted machine learning tools, SVM and LDA, were applied in the classification study. SVM demonstrated greater accuracy than LDA (Table III.2). Using SVM, global spatiotemporal measures correctly classified 72% of the subjects (sensitivity: 70%; specificity: 74%). The connections in sFC classified each subject

correctly with 75% accuracy (sensitivity: 78%; specificity: 73%), while in v-FC the accuracy was 73% (sensitivity: 78%; specificity: 69%). Taken together, sFC and vFC classified each subject with 81% accuracy (sensitivity: 81%; specificity: 81%). Finally, the global and nodal parameters together classified each subject with 83% accuracy (sensitivity: 81%; specificity: 85%).

Table III.2. Classification Results

	Linear Discriminant Analysis (LDA)			**Support Vector Machines (SVM)**		
	Accuracy	**Sensitivity**	**Specificity**	**Accuracy**	**Sensitivity**	**Specificity**
Global	68.52%	62.96%	74.07%	72.22%	70.37%	74.07%
sFC	64.15%	62.97%	65.38%	75.47%	77.78%	73.08%
vFC	75.47%	77.78%	73.08%	73.58%	77.78%	69.23%
sFC-vFC comb.	60.15%	59.26%	61.54%	81.13%	81.48%	80.77%
All	71.70%	70.37%	73.08%	83.02%	81.48%	84.62%

Additionally, partial correlations of each feature with clinical indicators (gender, duration of disease, HDRS, episode duration, drug washout) were calculated. No significant correlation was found between clinical indicators and global synchronization with respect to ITC. Nevertheless, there was a significant correlation of raw global MDD-HC FC distance to disease duration (rho = 0.47, $p < 0.05$), suggesting a global spatial alteration in MDD during the course of the disease.

III.IV. Discussion

We studied the rsfMRI of depressive patients using static and dynamic measures on the global and local levels. Our results showed increased global synchronization and temporal stability in the MDD patient group. Furthermore, we found alterations in static FC and the variability of FC in MDD patients relative to the healthy control group. Generally, those alterations occurred in the right hemisphere but also occurred, albeit to

a lesser extent, in the interhemispheric static and dynamic connections. Thus, our findings on widespread global synchronization and increased temporal stability in MDD contradict the results of (Berman et al., 2014). This might be due to the differences in preprocessing steps, particularly in band-pass filtering (as discussed below).

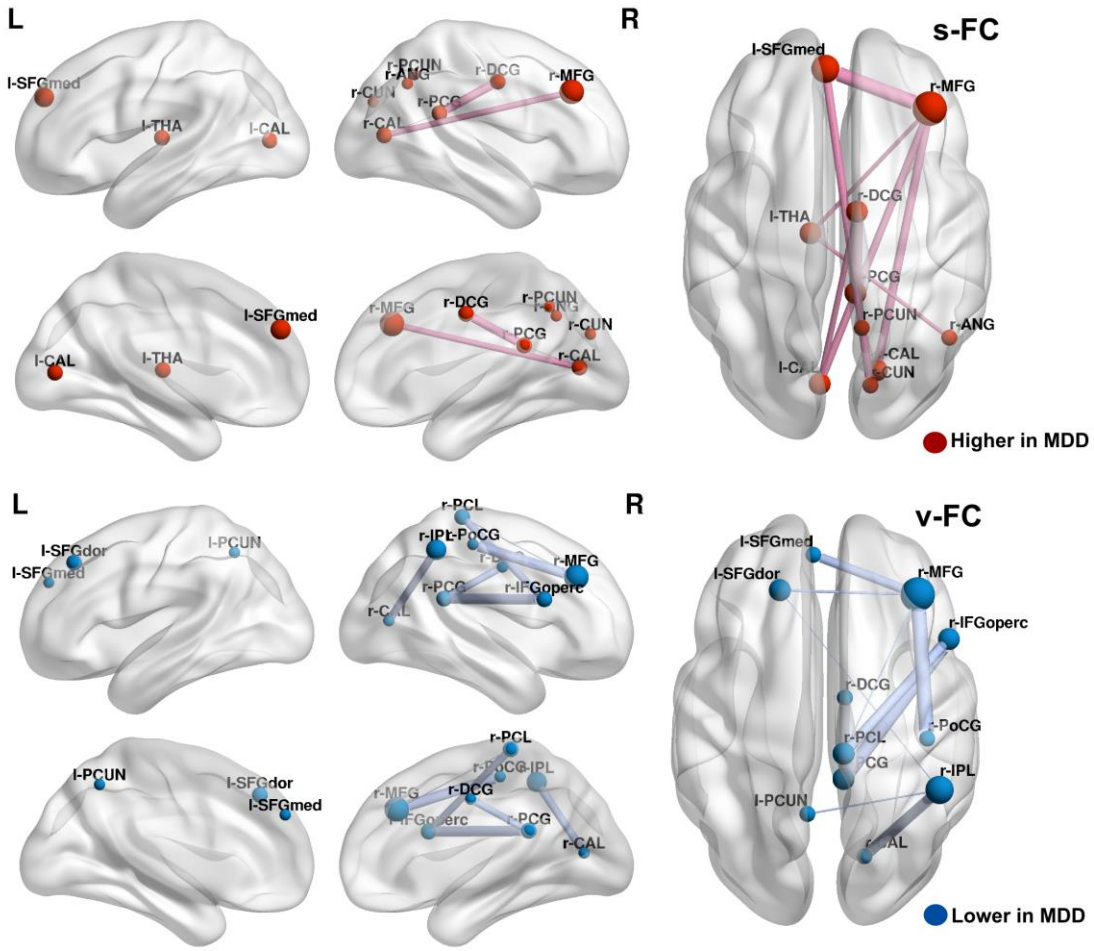

Figure III.5. Whole-Brain Connectivity Analysis of sFC (Top) and vFC (Bottom). Herein, sFC refers to static functional connectivity (i.e., Fisher's z-transformed Pearson's correlation coefficients), while vFC refers to variability of functional connectivity (i.e., Index of Dispersion of phase-coupling between two-ROI). The results are based on NBS using 5,000 permutations, corrected p-value <0.05 and maximum component threshold t>3.3 (vFC) t>3.2 (sFC). The red nodes and edges indicate higher values in MDD patients, while the blue nodes and edges indicate lower values in MDD patients.

We found that, in depressive patients, static FC was increased dominantly in the regions related to the DMN and variability of FC decreased within an extended network of the DMN and fronto-parietal regions. This result is consistent with the previous findings

that showed reduced irregularity (increased memory) in the fronto-parietal network using the Hurst exponent (Wei et al., 2013). A similar approach was previously applied to rs-fMRI signals of healthy controls subjects while they were daydreaming (Kucyi and Davis, 2014)(Figure III.6). Furthermore, we showed that these measures might function as predictors in discriminating patients from healthy controls. Collectively, the results suggest that dynamic functional connectivity can reveal different aspects of brain connectivity in MDD patients. Therefore, we claim that attenuated variability in the fronto-parietal region might influence widespread global synchronization and the difficulty of down-regulating the DMN. This conclusion is consistent with the existing neuropsychological models of MDD and most of the recent findings regarding the role of the DMN in the disorder. The novelty is that we have shown that the changes in modulatory networks (dynamical/binding hubs) could be more effectively characterized by dynamic FC than with static FC, and that the converse is true for structural networks (static hubs). In our study, these potential modulatory networks were consistently the regions related to executive function and the integration of sensory information.

The relationship involving increased global synchronization, increased temporal stability and decreased variability might seem trivial or possibly as an artifact due to the influence of physiological noise. However, the occurrence of local alterations in variability within specific, clinically relevant networks suggests that variations in global and local spatiotemporal patterns might be linked. In other words, the results might be interpreted such that the local alterations in sFC (increased connectivity) and vFC (decreased variability) might also manifest as increased global synchronization and temporal stability in MDD, or the other way around. Moreover, we found that the average BOLD signal in the fronto-parietal and temporal regions would fluctuate with the global average signal (Figure II.9). Additionally, one study reported that DMN is correlated with autonomic arousal (Fan et al., 2012). Thus, the relationship between global and local variations might also be relevant to the bottom-up modulation of binding hubs via subcortical circuits and/or whole-brain global modulation by autonomic arousal. Nevertheless, the evidence cannot rule out the indirect involvement of physiological noise in the signal and its ability to bias the results. Further research is needed in order to clarify the mechanisms that underlie the global average signal.

Moreover, we found that the raw distance between the average FC of depressive patients and grand average FC of healthy subjects has a significant correlation with illness duration and a moderate correlation with HDRS. This might be interpreted as a gradual alteration of global static functional connectivity (or anatomical connectivity) as the disease progresses.

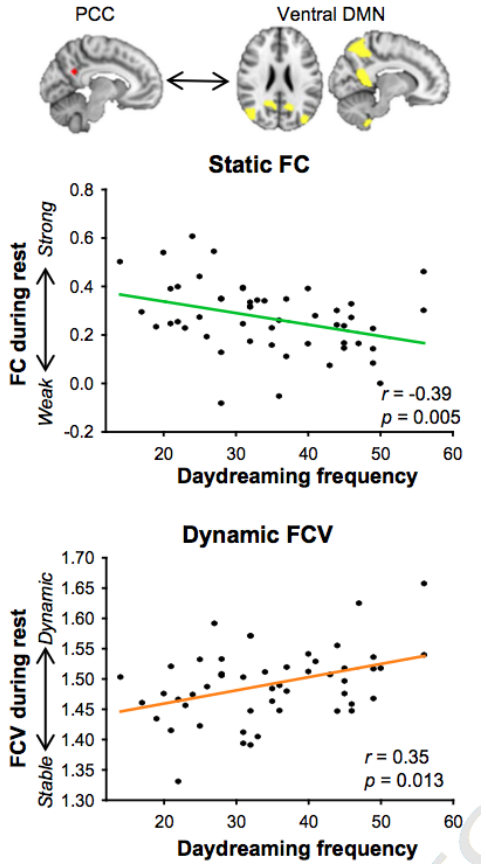

Figure III.6. Changes in static FC and variability of FC with respect to daydreaming frequency (adapted from Kucyi and Davis, 2014)

Our study was subject to various considerations and limitations. We underscore the fact that these results are very specific to the 0.04-0.07Hz narrow band, which is essential for the Hilbert transform. First, the global synchronization of each region was correlated with the power in the narrow band. Secondly, the average 0.04-0.07Hz bandwidth power of related regions (such as the medial frontal gyrus and precuneus) was significantly different in the MDD patients (Figure III.7). Accordingly, we suggest that

the widespread increase (or decrease) found in connectivity might be related to the changes in the power of ROIs in various frequency bands. It was also observed that the MDD patients had increased power in this narrow bandwidth despite their reduced power in wider bandwidths. Additional research is needed in order to clarify the role of the spectral properties of RSNs. In any case, the major limitation of this study was the short scan duration (four minutes), which might be insufficient for the stabilization of resting-state functional connectivity (rsFC). In addition to the reliable stabilization of FCs, the short scan duration prevented us from using extensive analyses such as sliding-window analysis, the Fano factor of dynamic connectivity in time, and wavelet analysis. Multiple comparisons constituted another problem encountered during the study. Although the NBS approach provides a reliable way to correct for multiple comparisons without compromising with regard to type-II error, it might mask the local alterations. An ICA-based approach might resolve this issue. Because it partitions the entire network into independent sub-networks, it facilitates an increase in the power of multiple comparisons.

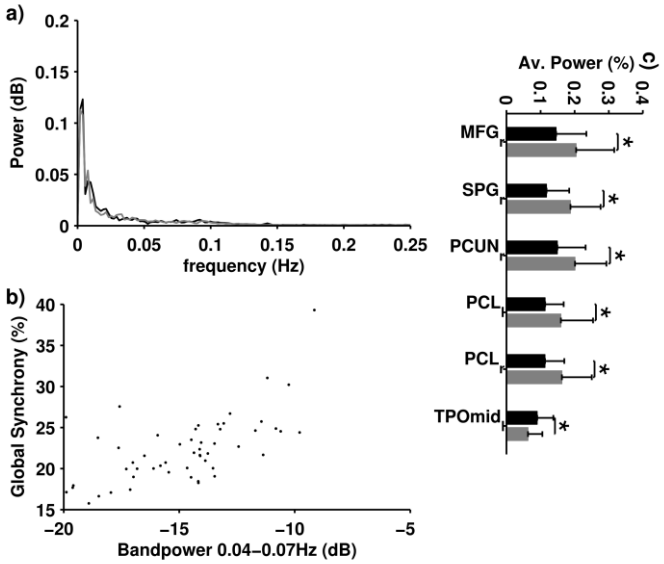

Figure III.7. a-b. The relationship between frequency power and GAS. c. Regions that showed significantly different power at 0.04-0.07 Hz between MDD and HC.

This study provides new insights with which to better our understanding of the

anomalous pattern of brain activity during the resting state in MDD (Major Depressive Disorder). The analysis of dynamic functional connectivity reveals that the depressed brain shows an abnormally stable, synchronous pattern of activity, whereby it mimics the various core features of depressive patients, such as ruminative, slow and monotonous thinking. Our novel approach has confirmed the presence of static hyperconnnectivity in MDD within the DMN, along with a reduction in the variability of dynamic functional connectivity in the DMN and fronto-parietal networks. This has in turn allowed us to accurately classify depressed patients and distinguish them from healthy controls. Future examination of the complex relationship between dynamic and static connectivity can provide adequate measurements with which to deepen characterization in the pathophysiology of depression.

IV. Bipolar Disorder

Abstract

Advancements in resting-state functional magnetic resonance imaging (rs-fMRI) and diffusion weight imaging (DWI) provide useful tools to study connectivity structure in healthy and diseased brain. In parallel, various computational models were proposed as the means to understand the mechanisms behind the emergence of connectivity patterns in spontaneous brain activity. However, the widely used measures of functional connectivity do not reflect the dynamic interactions between brain regions. Our study introduces a whole-brain model to estimate the effective connectivity underlying rs-fMRI signals based on the functional and structural connectivity of bipolar patients suffering a depressive relapse and healthy controls. We show that the dynamic features in rs-fMRI time series can be explained by the causal interactions between brain regions. Additionally, we show that a model-based estimate of the effective connectivity provides a mechanistic explanation for the widespread alterations in connectivity and vulnerability to psychosis in bipolar patients.

IV.I. Introduction

The observation of coordinated spontaneous low-frequency fluctuations in motor cortex (Biswal et al., 1995) encouraged interest in the task-free experimental paradigm of fMRI research. Subsequently, there has been an explosion in research on the clinical applications of resting-state functional MRI (rs-fMRI) (Fox and Greicius, 2010; Greicius, 2008; Whitfield-Gabrieli and Ford, 2012). Collectively, the literature on clinical rs-fMRI has been intended to make statistical inferences on the temporal correlations between the regional BOLD time series (functional connectivity - FC) and the characteristics of anatomical and functional network topology (structural connectivity - SC) or the analysis of resting-state networks (RSNs). However, these approaches do not address the causal interactions between brain regions (i.e., effective connectivity, or EC).

Furthermore, recent studies on rs-fMRI in clinical populations have shown that abnormal synchronization on the global level impeded the interpretation of alterations in whole-brain connectivity. As a result, despite tremendous effort, rs-fMRI studies are still challenged in their ability to provide mechanistic explanations underlying clinical conditions.

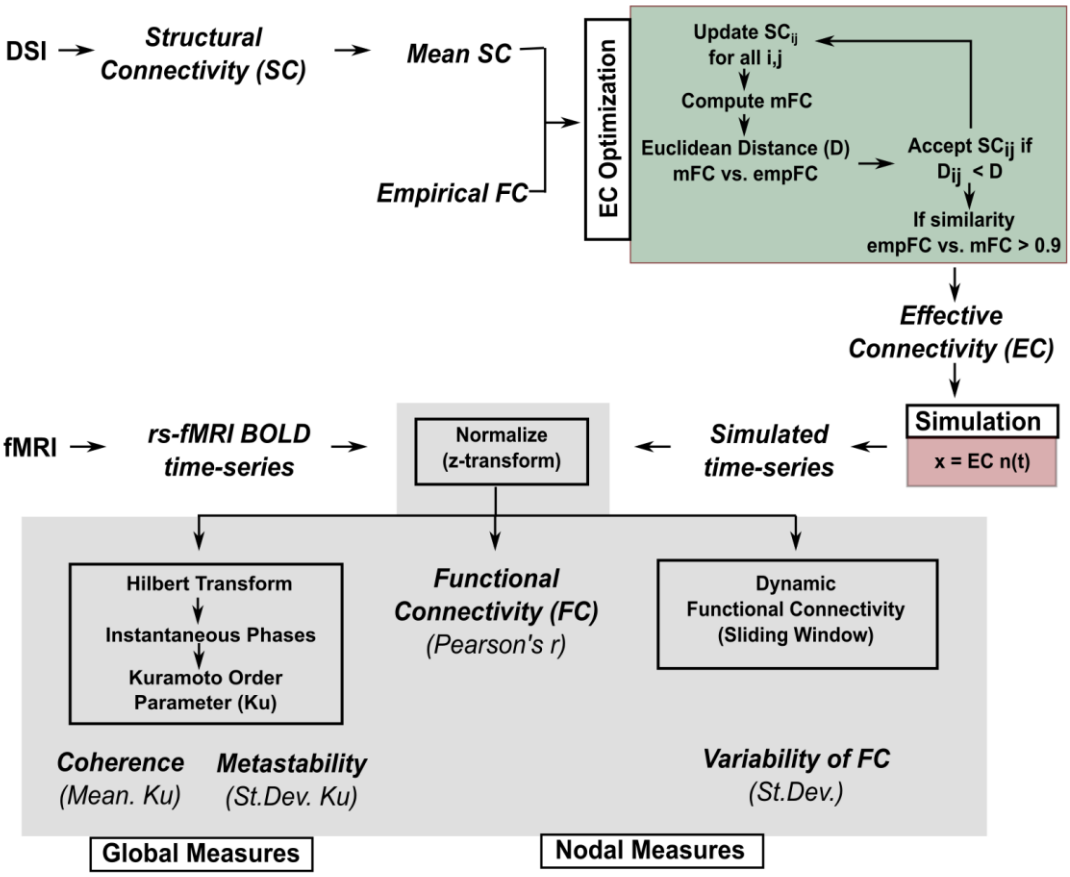

Figure IV.1. The summary of the procedure. Top part shows the optimization procedure of EC. SC matrices obtained from Diffusion Weighted Imaging (DWI) were averaged across all subjects. Then using an evolutionary algorithm the EC matrices that optimally fit to the empirical FC were computed. Bottom part shows the comparison of empirical and simulated time series. Both empirical rs-fMRI and simulated time-series were processed in the same way to obtain global and nodal measures of connectivity (gray region).

A structural basis for interactions between brain regions can be obtained through DWI techniques such as Diffusion Tensor Imaging (DTI) and Diffusion Spectrum Imaging (DSI), among others. However, although structural and functional connectivity have

been shown to have certain features in common, there is no direct correspondence between SC and FC due to the differences in biophysical properties of the brain (i.e., synaptic conductance, neuronal excitability and time-scale, etc.). EC aggregates the biophysical features and directed connectivity in the brain, thus yielding a richer description of the dynamic interactions of the brain (Friston, 2011; Razi et al., 2015). Nevertheless, most of the research on EC has been based on the experimental manipulation of underlying neuronal process.

Various computational models have been proposed to simulate spontaneous fluctuations during rest that were constrained by SC (Cabral, Kringelbach and Deco 2014). These studies explored resting-state FC through the use of models ranging from simple rate models to spiking neural network simulations (Christopher J. Honey et al. 2007; C. J. Honey et al. 2009; Ghosh et al. 2008; Deco et al. 2009; Deco and Jirsa 2012; Messé, Benali and Marrelec 2015). Furthermore, computational modeling of resting-state activity facilitated the inference of EC from observed FC (Friston et al. 2011; Friston et al. 2014) (Deco et al., 2014a).

This chapter proposes a counter-intuitive approach to the inference of whole-brain EC using a linear model with stationary higher-order statistics. Our aim is to provide a mechanistic model of resting-state FC dynamics and apply it to the specific case of Bipolar Disorder (BP). Briefly, we introduce the use of the Kuramoto Order Parameter as a measure of global coherence and metastability. We then propose a simple linear noise-propagation model that could be solved analytically in order to infer EC from FC. In this manner, we extracted the directed connectivity structure that underlies the rs-FC. Using a sample comprising healthy controls and bipolar patients suffering acute depressive episode, we showed that the EC can accurately replicate the spatiotemporal characteristics of rs-fMRI time series. Furthermore, we provided a mechanistic explanation for the alterations in whole-brain connectivity as presented in the data. Figure IV.1 summarizes the process. The materials and methods are covered in Appendix 3. Materials and Methods: Bipolar.

IV.II. Simulations

The BOLD signals can be modeled either through descriptive approaches such as structural equation modeling (SEM) and auto-regressive models (Messé, Benali and Marrelec 2015) or through the hemodynamic transformation of generative models. We simulated the BOLD signals using an auto-regressive model based on linear diffusion of noise. Where x_i is the BOLD signal of node *i*, C_{ij} is the effective connectivity with zero-diagonal (C_{ii} = 0), and $\eta(t)$ is the Gaussian random variable ($\mu = 0, \sigma = 0.01$):

$$x_i(t) = kx_i(t) + \sum_{j \neq i} C_{ij}\eta_i(t)$$

The noise term represents the spontaneous neuronal fluctuations in each node with negligible time scale with respect to the BOLD signal. Auto-regression coefficient k was taken as 0.5. We used 10 trials of 240,000 time points (sampled at two-second intervals). The resulting signals were z-transformed and band-pass filtered (0.001-0.25 Hz).
We optimized EC using an evolutionary algorithm that minimizes the Euclidean distance (D) between empirical and model FC (*mFC*). First, we estimated the variance-covariance matrix (Σ^x) of the diffusion process analytically such that: $\Sigma^x = (I - k)C\,\Sigma^\eta C^T$, where Σ^η is the input noise. The correlation coefficients (*mFC*) were computed as covariance divided by the standard deviation of corresponding nodes. Then, we sequentially increased and decreased each non-zero connection weight by 5% and updated the EC if the modification decreased the distance (D). The weights of the connections were within the range of 0 to 1.

To avoid over-fitting, the procedure was repeated until the Pearson's Correlation between eFC-mFC exceed desired value ($r>0.9$), or the number of iterations exceeded 250. As an initial guess for the EC, we used the average SC matrix over all subjects.

Effective Connectivity (EC) matrices were compared using the permutation t-test (10,000 permutations). The correction for multiple comparisons for the connections

were performed using Benjamini & Yakutieli False Discovery Rate (FDR) correction (Benjamini and Yekutieli, 2001) with p-value threshold $p < 0.05$.

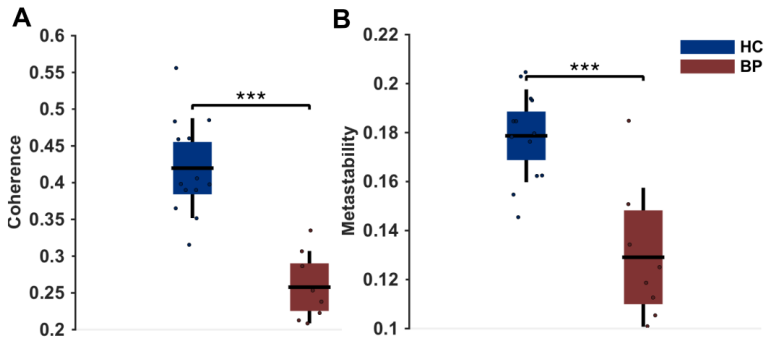

Figure IV.2. Group comparison of (A) Coherence (Average Kuramoto Order Parameter) and (B) Metastability (standard deviation Kuramoto Order Parameter). The comparisons were done using permutation t-test (10000 permuations, p-valus < 0.001). Kuramoto Order Parameter of each subject was computed using Hilbert Transform of the time-series (see materials and methods).

IV.III. Results

We compared the whole-brain FC of the BP patients and the healthy controls. In order to quantify the global coherence and metastability of time series, we used the Kuramoto Order Parameter (K) (Cabral et al., 2012a; Hellyer et al., 2014; Kuramoto, 1986; Shanahan, 2010): $K_t = \frac{1}{N}\sum_{j=1}^{N} \exp(i\theta_j(t))$, where N is the number of ROIs and $\theta(t)$ is the instantaneous phase of each ROI estimated using Hilbert Transform. The temporal average of the Kuramoto Order Parameter quantified the coherence (synchronization index) of the ROIs over time. However, the standard deviation of the Kuramoto Order Parameter defined the metastability of time series (i.e., the variation in synchronization over time). The results showed widespread decrease of connectivity in BP patients suggesting impairments in the overall network topology. Correspondingly, we found significant decrease in both the average and the standard deviation of the Kuramoto Order Parameter (permutation t-test, $p < 0.001$; Figure IV.2). Together, these results suggest that impairment of connectivity between different regions might be interdependent, resulting from a global network effect. However, whole-brain FC reflects the cumulative

effect but does not provide useful information to understand the actual disturbances in the network.

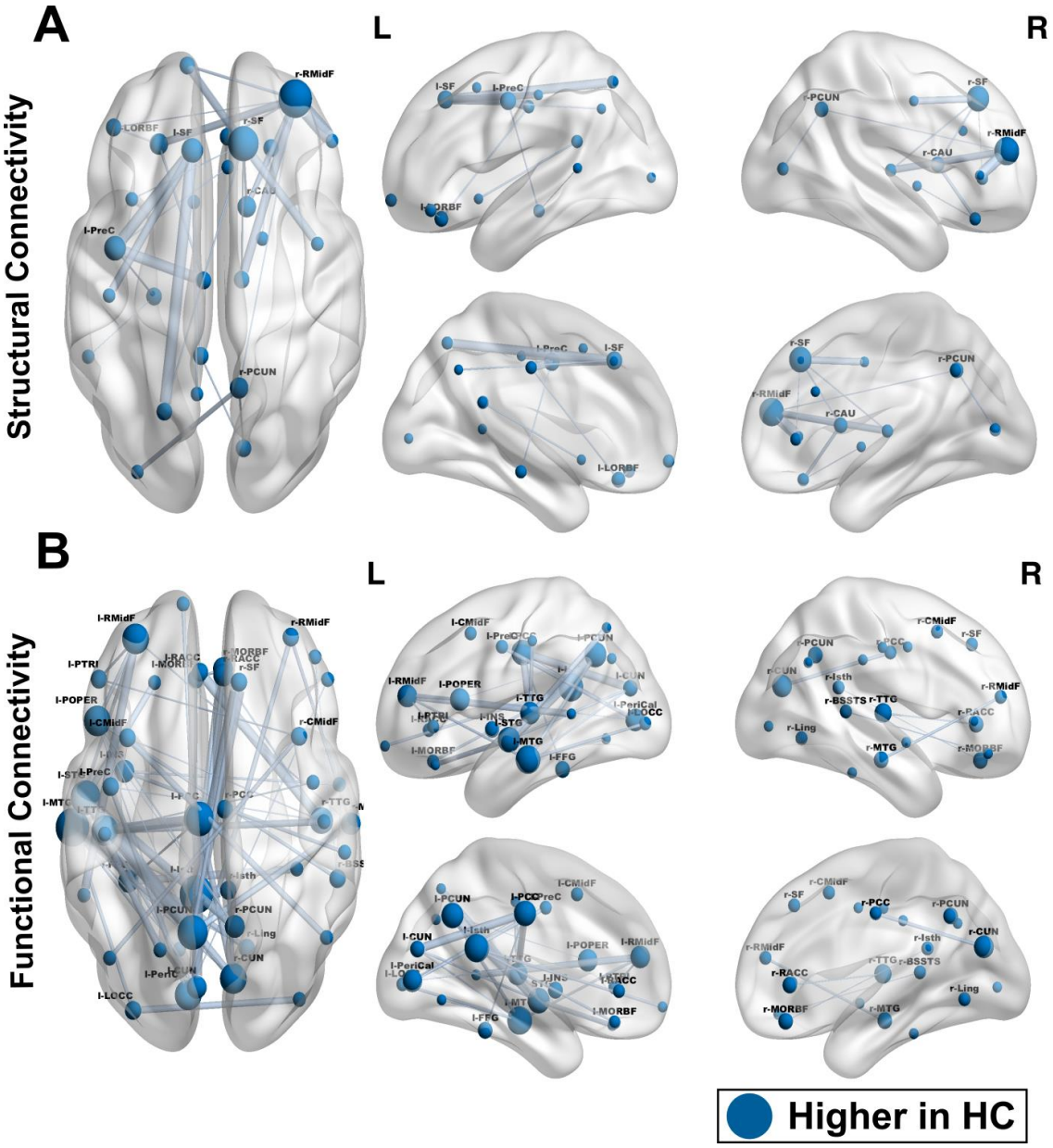

Figure IV.3. Whole-Brain Group Comparison of (A) Structural Connectivity, (B) Functional Connectivity. Size of the nodes shows the number of significant connections and size of the edges shows the t-statistic. The group comparisons were done in NBS toolbox (5000 permutations, p-value < 0.05). The thresholds for connected components were arbitrarily selected to report 1-2% of the connections that have the highest t-statistic. No significant increase in SC and FC was detected in bipolar patients.

IV.III.i . Static and dynamic functional connectivity

We compared the whole-brain SC and FC of BP patients and healthy controls (see appendix 3). We also investigated the variability of FC in temporal and spectral domains. We found widespread decreases in SC and FC, and increases of variability in BP patients. The core of the alterations in SC was observed in frontal and sensory regions. Particularly, anatomical connections of right rostral middle frontal and the bilateral superior frontal cortex were significantly reduced in bipolar group (Figure IV.3A).

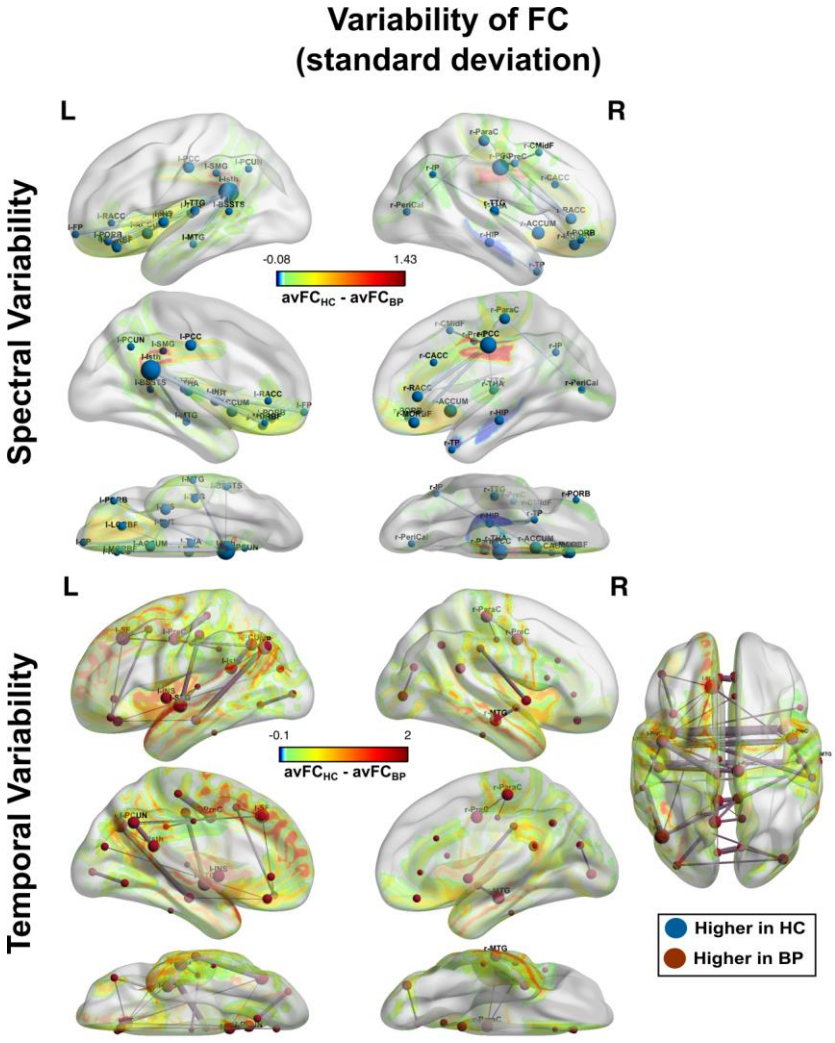

Figure IV.4. The alterations in spectral (top) and temporal (bottom) variability of FC.

Regarding FC, the decreases in BP patients were observed virtually in the entire brain. For this reason, we set the threshold for the connected components in NBS in order to focus to the most significant alterations. FC of BP patients was mostly decreased in left hemisphere, and in inter-hemispheric connections (Figure IV.3B). Unlike SC, the regions that were decreased in FC were related to the default mode network as well as auditory-visual networks. Isthmus of Cingulate, Anterior and Posterior Cingulate, Superior Temporal Gyrus, Medial and Orbital Frontal connections showed the highest attenuation.

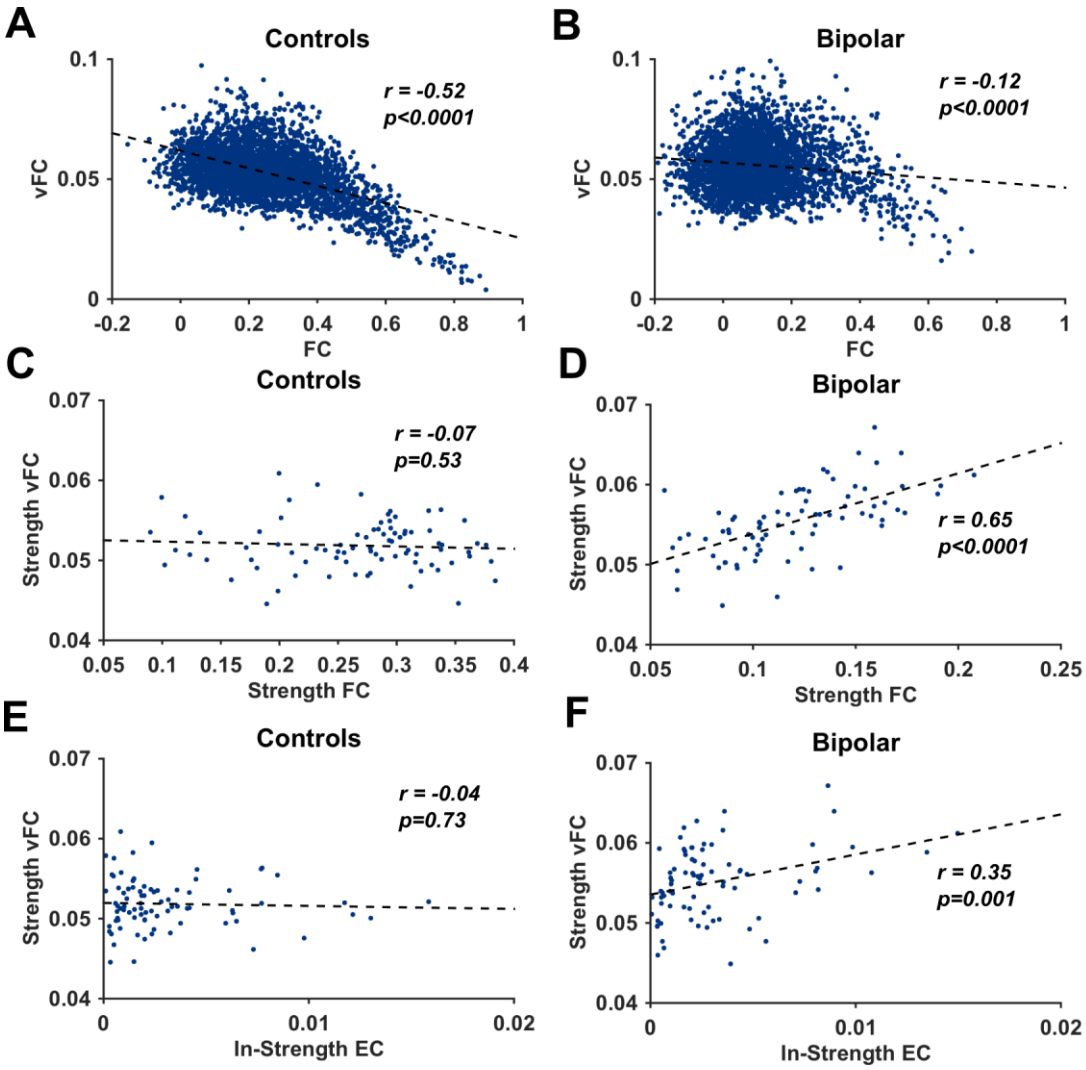

Figure IV.5. The relationship between FC and variability of FC (HC-left, Bipolar-right). A-B. Relationship between FC and variability of FC for average connectivity. C-D. Relationship between strength of FC and strength of variability of FC. E-F. Relationship between strength of FC and input strength of EC.

The temporal variability of FC was significantly increased in BP group (Figure IV.4-bottom). Almost all of the alterations were found in inter-hemispheric connections. Furthermore, the differences in variability were mostly in the homologous inter-hemispheric connections, especially in temporal and sensory-motor regions. Among the homologous inter-hemispheric connections, insula and rostral anterior cingulate cortex showed the highest increase in variability, suggesting abnormal activity in salience network. In contrast, spectral variability was significantly decreased in BP group. The decreased spectral variability observed along the cingulate cortex and the orbital frontal cortex (Figure IV.4-top).

The increases in temporal variability of FC were consistent with the decreases in FC. In order to check the possible mechanism underlying these differences, we compared the relationship between the FC and the temporal variability of FC (Figure IV.5). We found a strong negative correlation between FC and the variability of FC for each individual connection. However, the strength of the negative correlation between the FC and the variability of FC in healthy controls was much stronger than in BP group ($r = -0.52$ for FC, $r = -0.12$ for BP). On the other hand, the strength of FC of each node was strongly correlated with the strength of vFC in bipolar group ($r = 0.64$, $p < 0.0001$), but no such relation was observed in healthy controls ($r = -0.07$, $p = 0.53$).

IV.III.ii . Effective connectivity

We simulated the rs-fMRI time series using auto-regressive noise diffusion model based on the EC matrices. The average correlation coefficient between simulated and empirical FC was estimated at 0.9. The correlation between the scores of the first principal components of the simulated and empirical time series was estimated to be 0.96. In addition to static FC, we found a modest but significant correlation between simulated and empirical variability of FC ($r = 0.27$). The model also showed great similarity between empirical and simulated mean Kuramoto Order Parameter and metastability, 0.96 ($p < 0.0001$) and 0.97 ($p < 0.0001$), respectively (Figure IV.6).

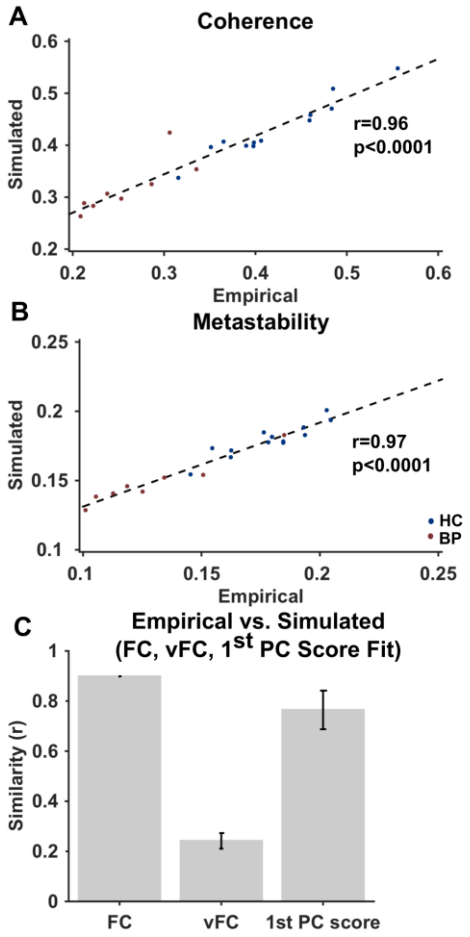

Figure IV.6. Relationship between the empirical and simulated measures. A. Simulated vs. empirical Coherence ($r = 0.96$, $p < 0.001$). B. Simulated vs. empirical Metastability ($r = 0.97$, $p < 0.001$). The dashed line shows the linear model. Red dots indice bipolar patients, while blue dots indicate healthy controls. C. Correlation coefficient between empirical and simulated FC, variability of FC and the score of 1st principal components. Error bars indicate SEM.

We compared the EC between groups, using the permutation t-test (10,000 permutations) and then corrected for multiple comparisons by FDR (corrected $p < 0.05$). In contrast to the FC, we found both increased and decreased ECs in BP group (Figure IV.7). Furthermore, the impaired ECin BP originated from fronto-parietal regions. Contrastingly, BP group showed increase EC among the inter-hemispheric connections between limbic and sensory networks. To refine the findings, we studied the output and input strengths of the effective connectivity of each node. First, we quantified the balance between output and input strength of each region as the difference between output

strength and input strength of the EC. A positive index indicated that the region had higher output strength than input strength, but a negative index indicated the inverse.

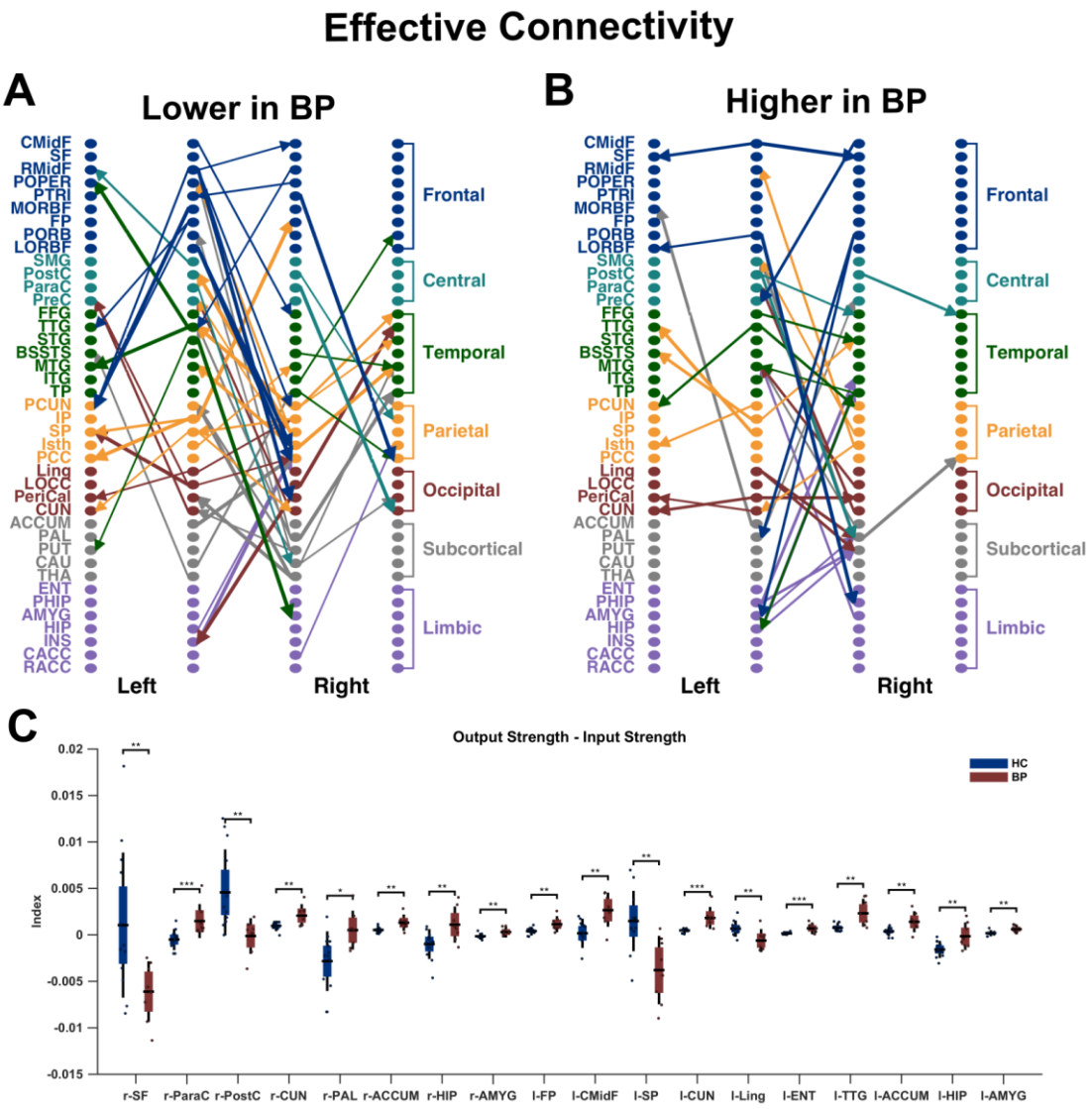

Figure IV.7. Comparison of Effective Connectivity (EC) of bipolar patients and healthy controls. A. Decreased effective connectivity in bipolar patients (top 1% of the connections). B. Increased connectivity in bipolar patients. Comparisons were performed using permutation t-test (10000 permutations) corrected with FDR ($p < 0.05$). Size of the arrows shows t-statistic. C. Group comparison of the output-input balance (the difference between output strength and input strength) of each ROI. The comparisons were done using permutation t-test (1000 permutations) corrected with FDR ($p < 0.05$). Positive values indicate the regions with higher output strength, while negative values indicate higher input strength.

Table IV.1. Out- and In-Strength vs. Metastability

Out-Strength vs. Metastability			**In-Strength vs. Metastability**		
ROI	*Pearson's r*	*p-value*	*ROI*	*Pearson's r*	*p-value*
l-ENT	-0.8307	<0.0001	l-CUN	-0.6225	0.0026
l-AMYG	-0.8090	<0.0001	l-MORBF	-0.6060	0.0036
l-TTG	-0.7789	<0.0001	l-LORBF	-0.5824	0.0056
l-PORB	-0.7633	0.0001	l-PeriCal	-0.5453	0.0106
r-TTG	-0.7256	0.0002	r-LORBF	-0.5372	0.0120
l-CUN	-0.7151	0.0003	l-Ling	-0.5192	0.0159
l-Isth	-0.6935	0.0005	l-PreC	-0.4665	0.0330
l-FP	-0.6436	0.0016	l-IP	-0.4594	0.0361
r-ParaC	-0.6185	0.0028	r-MORBF	-0.4535	0.0390
r-ACCUM	-0.6165	0.0029	l-RMidF	-0.4465	0.0425
r-STG	-0.6131	0.0031	r-RMidF	-0.4332	0.0498
r-AMYG	-0.6109	0.0033	r-THA	0.5026	0.0202
l-BSSTS	-0.5603	0.0083	r-POPER	0.5950	0.0044
r-PHIP	-0.5534	0.0093			
l-PeriCal	-0.5528	0.0094			
l-PHIP	-0.5435	0.0109			
r-ENT	-0.5397	0.0116			
l-ACCUM	-0.5397	0.0116			
l-TP	-0.5379	0.0119			
r-CUN	-0.5366	0.0121			
l-RACC	-0.5283	0.0138			
l-PCC	-0.5234	0.0149			
r-Isth	-0.5148	0.0169			
r-INS	-0.4821	0.0269			
l-PAL	-0.4788	0.0281			
l-ITG	-0.4709	0.0312			
r-BSSTS	-0.4672	0.0327			
l-CMidF	-0.4612	0.0353			
r-HIP	-0.4611	0.0354			
r-PUT	0.4721	0.0307			
l-SP	0.5341	0.0126			
r-SP	0.6535	0.0013			

When we compared the difference between output and input strengths between groups, the BP patients showed increased output tendency in the bilateral amygdala, hippocampus, accumbens and cuneus as well as the right paracentral, pallidum and left frontal pole, caudal middle frontal, enthorinal and transverse temporal gyrus. Contrastingly, the output tendency was decreased in the right superior frontal and postcentral cortex as well as in the left superior parietal and lingual cortex (Figure IV.7C).

We checked the relationship between output-input strength of EC and the global metastability for all subjects. We found strong negative correlations between the output strength of the limbic regions (particularly amygdala and hippocampus) and metastability. However, output strength of bilateral superior parietal cortex was positively correlated to the metastability suggesting a modulatory role of this region. Contrastingly, while the input strength of the medial and orbital frontal regions were negatively correlated to the metastability, the input strength of right pars opercularis and thalamus showed a positive correlation with metastability (Table IV.1).

IV.III.iii . Predictive model

Based on the model, we attempted to make some predictions for the possible mechanism underlying the vulnerability of BP patients to psychosis. We hypothesized that most of the abnormal effective connectivity patterns in the BP patients in depressive episode would not adapt fast enough to a sudden change in the global connectivity (for example, an increase in baseline spontaneous activity). To check this hypothesis, we increased the global coupling of EC of each patient by adding a constant global coupling parameter (k), between 0 and 0.001. Then, we estimated the simulated FC using the modified ECs. The rate of change of the resulting FCs ($\partial FC_{ij}/\partial k$) was computed, and averaged across all patients. Finally, we evaluated the rate of change of each connection relative to each other using the z-score of the average rate of change of each connection ($(\partial FC_{ij} - \mu_{\delta FC})/\sigma_{\partial FC}$). Furthermore, we computed the change in mean Kuramoto Order Parameter and metastability with increasing global coupling. Our model

predicted that the increase in metastability would be slower than mean Kuramoto Order Parameter (Figure IV.8).

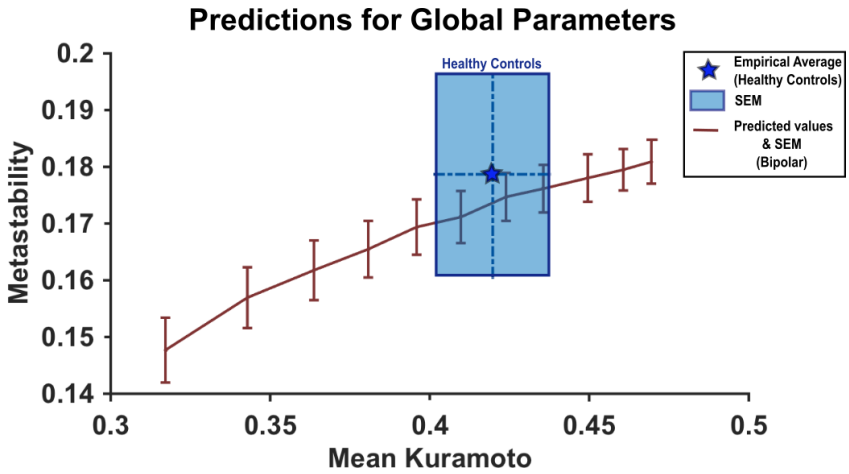

Figure IV.8. Global predictions of the model. Increases in metastability and coherence with the global coupling. Blue area indicate the mean and SEM estimated for healthy controls.

At the nodal level, our model predicted that the FC change rate would be different for distinct networks (Figure IV.9). We found that the temporo-limbic was the most reactive, and striatal-thalamo-cortical was the least reactive networks. In other words, the FC of temporo-limbic regions was sensitive to the changes in the global coupling strength. Furthermore, we found there the reactivity in BP patients would be located in single hemisphere, and would be pronounced in frontal pole rather than medial and orbital frontal regions as observed in the healthy controls. In addition, we observed that while the sensory-motor connections of thalamus pallidum and putamen were less reactive in healthy controls, in bipolar patients caudate, superior and medial frontal and thalamus were less reactive. These results are consistent with the research on the effects of psychoactive agents. A recent research found decreased cerebral blood flow and abnormal connectivity in striatum, thalamus, somatosensory, and temporal regions after administration of MDMA (Carhart-Harris et al., 2014). Furthermore, another study investigating the psychosis-like effects of ketamine found abnormal connectivity in striatal-thalamic regions (Dandash et al., 2015). They also found that the connectivity between dorsal caudate and thalamus was inversely correlated with the intensity of the symptoms suggesting a possible role of this connection in regulating psychotic experi-

ence. Therefore, we speculate that BP patients might fail to regulate the high arousal state efficiently, which increases their vulnerability to psychotic experience.

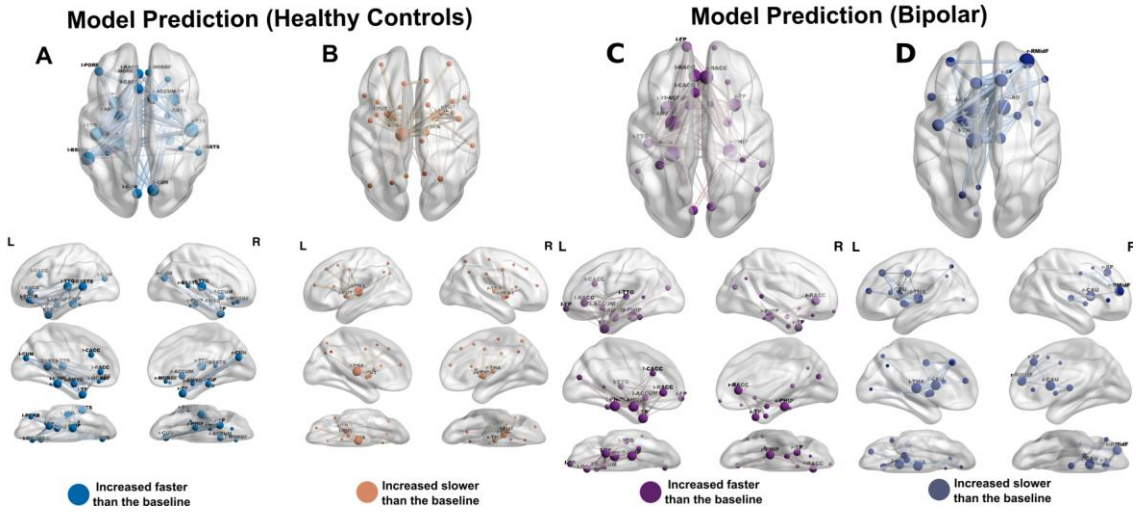

Figure IV.9. Predictive model. Rate of FC change with respect to the global coupling strength. A-C illustrate the links with the highest reactivity (high rate of change). B-D illustrate the links with the lowest reactivity (low rate of change).

IV.IV. Discussion

The majority of rs-fMRI studies have relied on hypothesis-driven (e.g., seed-correlations), data-driven (e.g., ICA) or whole-brain connectivity analysis approaches. However, evidence from any such approach suggests abnormal global connectivity in various disorders, thereby complicating the interpretation of the results. Furthermore, functional connectivity (FC) accounts for the cumulative interactions in the brain underestimating the dynamics of these interactions. Structural connectivity (SC), however, tracks the anatomical links between the brain regions using DWI methods. However, SC does not provide any information on the biological properties of the connections (i.e., synaptic conductance, neuronal excitability…etc.) but performs poorly in the detection of inter-hemispheric connections (Ajilore et al. 2013; Horwitz, Hwang and Alstott 2013; Rodrigues et al. 2013). Moreover, both quantities yield a symmetric measure for the connectivity, and they suffer from high inter-subject variability and dependence

to preprocessing procedure. Thus the current approach to rs-fMRI fails to provide mechanistic explanation underlying dynamic interactions in the brain.

Our study has proposed a simple noise-propagation model that predicts the EC underlying the FC for the entire brain. Unlike previously proposed models, the simplicity of the model allowed us to use evolutionary algorithm that blindly modifies the unknown connectivity and finds the fittest solution to the FC. Surprisingly, the model not only predicted the FC accurately but also replicated the dynamical properties of the time series (such as global metastability, variability of FC and the spatial principal components). Given an identical hemodynamic transformation for each node, the approach presented here could also be adapted as a generative model.

We demonstrated the utility of the model in a clinical population of BP patients and healthy controls. We quantified the global spatiotemporal characteristics of the time series using the Kuramoto Order Parameter. The average Kuramoto Order Parameter described the overall coherence between the regions, while the standard deviation of the Kuramoto Order Parameter quantified the metastability of the system. Global coherence and metastability alone could provide information on the tendency of hyper- or hypo-connectivity and the richness of dynamic repertoire of the resting-state networks (Hellyer et al., 2014). In contrast to the burden of statistically significant differences in the whole-brain FC analysis, coherence and metastability provided a simple but effective measure with which to characterize the dynamic repertoire of the spontaneous brain activity. We found that both coherence and metastability are decreased in BP patients suggesting the presence of a global network effect. This is consistent with the recent studies that found an overall decrease in connectivity in BP disorder (Kim et al., 2013) and impaired interhemispheric communication (Y. Wang et al., 2015).

The research on BP disorder suggests impaired cortico-limbic connectivity in BP patients (Vargas, López-Jaramillo and Vieta 2013). Additionally, there is a consensus among the research that the most significant clinical features of BP disorder is the defective anatomical connectivity in prefrontal cortex and abnormal functional connectivity in ventral prefrontal cortex and limbic structures in the brain (Strakowski et al.,

2012). However, the implications and the mechanisms behind these changes remain controversial. The use of a model-based approach allowed us to propose a mechanistic explanation for the alterations in the global network. We showed that EC from frontal and parietal regions to the posterior parts of the default network and sensory motor regions were significantly reduced in BP patients. Contrastingly, BP patients showed increased EC in interhemispheric connections among the limbic and sensory motor regions. Briefly, our model suggests that the reduced widespread decreases observed in FC of BP patients originates from impaired top-down modulation of sensory motor integration by fronto-parietal regions and abnormal interference of limbic regions to the rest of the cortex.

We further refined the analysis of EC regarding the input-output relationship of each region. We showed that the restricted dynamic repertoire (metastability) in rs-FC was strongly associated with the disturbance in output-input strength balances in the network. Specifically, impaired metastability was associated with the high output strength in the limbic regions and high input strength in the frontal regions. Contrastingly, the increase in global metastability was related to increased output strength in the bilateral superior parietal and right putamen, and to increased input strength in the right pars opercularis and thalamus.

The model showed that the dynamics of rs-fMRI time series are dominated by the directionality of the connections in such a way that the clusters of regions in which the input from distinct regions converge tend to be activated by global signal increases. In the healthy control subjects, the frontal and parietal regions were characterized by high output strength while the regions in the default network showed the inverse pattern. Therefore, we speculate that the convergence and divergence of distinct clusters of regions due to preferred causal interactions and the global fluctuations might account for the dynamics of FC (e.g., a negative relationship between the fronto-parietal control network and the default network).

Despite pharmacological advancements, BP continues to be difficult to treat, and there is accumulating evidence for the role of brain stimulation techniques (Loo et al., 2011).

This model, which contributes to a better understanding of the exact localization of alterations in connectivity in BP patients, can potentially contribute to a better understanding of this severe, debilitating pathology and facilitate identification of the optimal position for stimulation in order to improve the currently available physical treatments of BP.

We also introduced the variability of FC in temporal and spectral domains. The results suggested that spectral variability of FC comprises relevant information. Temporal variability of FC was impaired in interhemispheric connections in BP patients. Moreover, temporal v-FC was inversely correlated with grand average FC. On the other hand, spectral FC variability was altered in cingulate cortex, which was one of the most affected regions in BP disorder. However, further investigation is needed to understand the clinical relevance of spectral variability of FC.

Finally, we proposed a predictive model for the vulnerability of bipolar patients to psychosis. We hypothesized that the modulation of the global coupling strength in the network might be related to the psychotic experience. We illustrated this using the computational framework provided in this chapter. Furthermore, we showed that the altered EC in BP patients might explain their vulnerability to psychosis.

The disadvantage of the model is that it does not account for the nuisance of local neuronal dynamics but instead encodes all the information in the EC. The dramatic changes in effective connectivity are unlikely to be explained solely by the differences in synaptic conductance. Nevertheless, explanatory power of this minimalistic model provides a refined perspective to build realistic models that account for the complex interactions in the brain. The limitation of this study is that the small sample size of the clinical population and the lack of correspondence of age between groups reduce the clinical validity of the group comparisons. However, these limitations are unlikely to affect the outcomes of the proposed model (e.g., the correspondence between EC, simulations and empirical observations).

V. Intrauterine Growth Restriction

Abstract

Intrauterine Growth Restriction (IUGR) is a major public health concern due to its high prevalence and consequences in children neurodevelopment. Recent advances in resting-state fMRI and diffusion imaging allow researchers to investigate the connectivity structure associated to various clinical conditions. Furthermore, over last decade diverse applications of these image modalities shed light on the neurodevelopmental process becoming a promising candidate to detect and prevent developmental and psychiatric disorders. However, currently these applications are limited to statistical inferences based on hypothesis- or data-driven analyses of grand average resting state functional connectivity (rs-FC), and topological measures of anatomical connectivity. In this chapter, we analyzed average and time-dependent dynamics of rs-FC based on phase coupling between regions across time. Furthermore, we modeled the connectivity dynamics using Kuramoto Model to infer whole-brain effective connectivity (EC) from observed functional connectivity (FC). Using populations of newborns and one-year-old infants with IUGR and corresponding controls, we showed distinct networks that were involved in the FC dynamics. In addition, whole-brain modeling approach revealed alterations in EC that extends the scope of traditional methods. We found hyper-synchronization of brain activity coupled with impaired variability in neonates with IUGR. These alterations were associated to decreased EC. The infants with IUGR showed no significant differences in observed connectivity measure, but EC revealed increased connectivity.

V.I. Introduction

Intrauterine Growth Restriction (IUGR) is characterized by abnormally restrained development of the fetus caused by impaired placental blood flow during the pregnancy (Baschat, 2004). IUGR is a major concern in pediatrics due to its high prevalence, and its association to perinatal mortality (M. Kady and Gardosi, 2004), lifelong disability (Jarvis et al., 2003), and developmental and psychiatric disorders (Bassan et al., 2011; Eixarch et al., 2008; McCarton et al., 1996; Murray et al., 2015). Previous research on structural alterations in IUGR showed decreased cortical and subcortical gray matter

volume (Padilla et al., 2011; Tolsa et al., 2004), abnormal gyrification (Dubois et al., 2008) in infants, and impaired cortical thickness (De Bie et al., 2011), thalamus volume (Martinussen et al., 2009) and white matter (Skranes et al., 2009, 2005) during childhood. Recent studies on the brain connectivity of IUGR showed alteration in graph theoretical measures in structural connectivity (Batalle et al., 2013, 2012). Moreover, resting-state fMRI approach revealed the development of functional networks in term and pre-term infants (Fransson et al., 2009, 2007; Gao et al., 2009). A recent study found that in premature infants the thalamic resting state functional connectivity (rs-FC) was increased with primary sensory cortex and decreased with heteromodal cortex (Toulmin et al., 2015). Overall, the evidence suggests that rs-FC might be useful in understanding normal and abnormal maturation of the brain.

Although the hypothesis- or data-driven analyses of rs-fMRI and the tracking of anatomical links,i.e. diffusion tensor imaging (DTI)/ diffusion spectrum imaging (DSI), provided powerful insights on the connectivity underlying observed pathologies, the utility of these approaches is limited in explaining the dynamic interactions between brain regions. First, the traditional measurement of FC during resting state relies on the grand average of the temporal correlation between brain regions. Recent studies emphasized the importance of the time-varying functional connectivity between brain regions (i.e. dynamic functional connectivity) (Hutchison et al., 2013). A common approach to study dynamic FC is the sliding window analysis that computes the FC in time using smaller temporal windows (Allen et al., 2014; Chang and Glover, 2010). However, this approach has some limitations, such as choosing an appropriate time window (Hutchison et al., 2013).

Another limitation of the conventional connectivity analyses is that the observed FC reflects the ultimate consequences on the dynamic interactions between regions. Furthermore, DTI/DSI-based structural connectivity (SC) analyses do not take into account the biophysical properties of the link that shapes the dynamics. Another evident problem is that neither rs-FC nor SC analyses provide any information on the causality of the interactions. Effective connectivity (EC), on the other hand, aggregating the biophysical features (i.e. synaptic conductance, neuronal excitability and time-scale…etc.)

and the directed connectivity in the brain, might reinforce our understanding of dynamic interactions in the brain (Friston, 2011; Goldenberg and Galván, 2015; Razi et al., 2015). However, most of the research on EC was based on the experimental manipulation of underlying neuronal process and rarely implemented on whole-brain level. Furthermore, a variety of recent computational models successfully have been implemented on the spontaneous fluctuations during rest (Joana Cabral et al., 2014). All these computational models provide different perspective to understand the neuronal activity underlying resting state activity, and allow making inferences on connectivity structure hidden in the data (Deco et al., 2014a; Friston, 2011; Friston et al., 2014b).

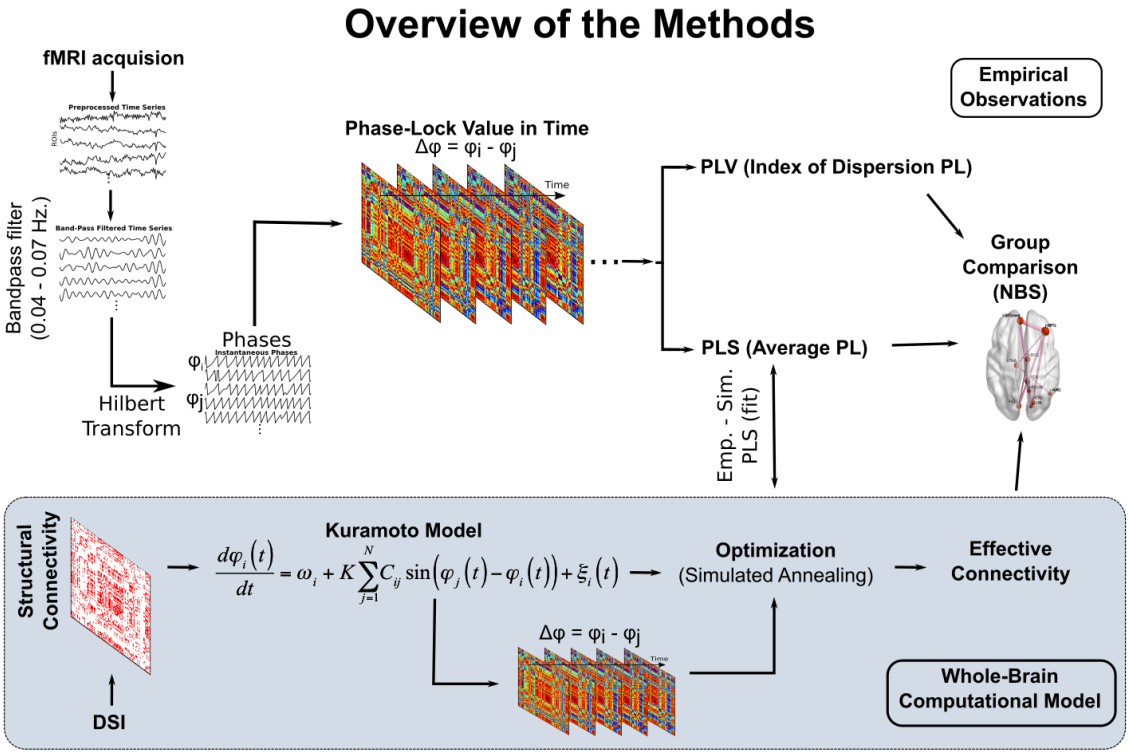

Figure V.1. The summary of the methodology. Upper panel describes the empirical data analysis. Lower panel describes the modeling and the optimization of effective connectivity.

The purpose of this chapter is to explore the static (grand average) and dynamic (variability) alterations in the networks of newborns and infants with IUGR, and to investigate possible origins of these alterations by revealing the EC based on a whole-brain model. As an alternative to functional connectivity measures based on Pearson's correlation coefficient, we used the phase coupling between brain regions (Ponce-Alvarez et

al., 2015). This way, we quantified both static (grand average phase coupling) and dynamic (variability in phase coupling) information. Finally, we used Kuramoto model of coupled oscillators via EC to simulate the phase dynamics, and to infer EC from observed data. For the overview of the methodology see Figure V.1.

We found widespread increase in synchronization within various cortical regions in neonates with IUGR. Caudate and putamen were found to be the central regions of the altered network. When we considered the variability in the synchronized networks, we found decreased variability in similar networks but these networks were extended toward fronto-parietal regions. The inferred EC, on the other hand, revealed a different network topology between IUGR and control groups. Counter intuitively, we found decreased EC among the regions that were related to Default Mode Network (DMN) and fronto-parietal control networks. Moreover, we found no alterations in the synchronization dynamics in one-year-old infants with IUGR. Nevertheless, the model showed increased EC in IUGR infants within temporal, occipital and parietal regions with a particular role of precuneus. Finally, we check the association between these alterations and behavioral assessments of neonatal and one-year-old cohorts.

V.II. Materials and Methods

The materials and methods of this chapter are presented in Appendix 4. Materials and Methods: IUGR.

V.II.i . Dynamic Functional Connectivity

We used phase-lock (PL) values to characterize the synchronization level between brain regions. PL values were extracted using Hilbert transform of the time series following (Glerean et al., 2012). Since, Hilbert transform operates in a narrow frequency band, we first band-pass filtered the time series. Previous studies showed that 0.04 – 0.07 Hz. frequency band contains the most reliable signal in resting state fMRI signals (Glerean et al., 2012), so we focused our attention to this specific frequency band (see chapter I). We also checked the differences in global coherence between groups in various fre-

quency bands with 0.03 Hz. window, and 0.001 Hz. step size (the onsets ranging from 0.001 Hz to 0.07 Hz). Our analysis confirmed that the differences between groups (for neonatal cohort) were maximized around 0.04 – 0.07 Hz. narrowband (Figure V.2).

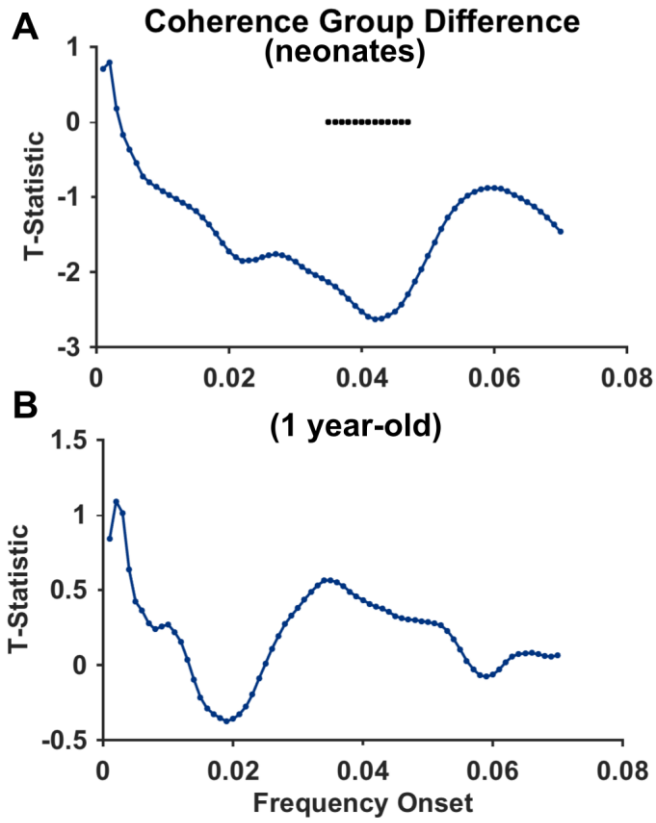

Figure V.2. Group differences in coherence (average Kuramoto order parameter) between IUGR and healthy controls in 70 different narrow frequency bands (0.03 Hz. width). A. Neonatal cohort. B. One-year-old cohort. The groups were compared using permutation t-test (10000 permutations). The group differences were maximal around 0.04 – 0.07 Hz. frequency band.

Hilbert transform represents a narrowband signal, $a(t) = A(t)\cos(\varphi(t))$, with an instantaneous amplitude, $A(t)$, and an instantaneous phase, $\varphi(t)$. Therefore, using the instantaneous phase information dynamic PL values can be estimated as the phase difference, $\Delta\varphi_{ij} = \varphi_j - \varphi_i$, between brain regions. We normalized the phase difference between 0 and 1, such that the values 0, 0.5 and 1 referred perfect anti-synchrony, asynchrony, and perfect synchrony, respectively. Finally, static (PLS) and dynamic (PLV) information regarding functional coupling between regions were estimated as the average and index of dispersion (variance divided by mean) of the phase-lock values for each subject. The

abbreviations PLS and PLV stand for phase-lock (static) and phase-lock (variability), respectively. The index of dispersion was chosen because of the inverse relationship between the mean and variance of the PL values pronouncing the variability in the asynchronous connections (PLS ≈ 0.5). Normalizing the variance by PLS allowed us to contrast the variability in intermediately phase-locked connections.

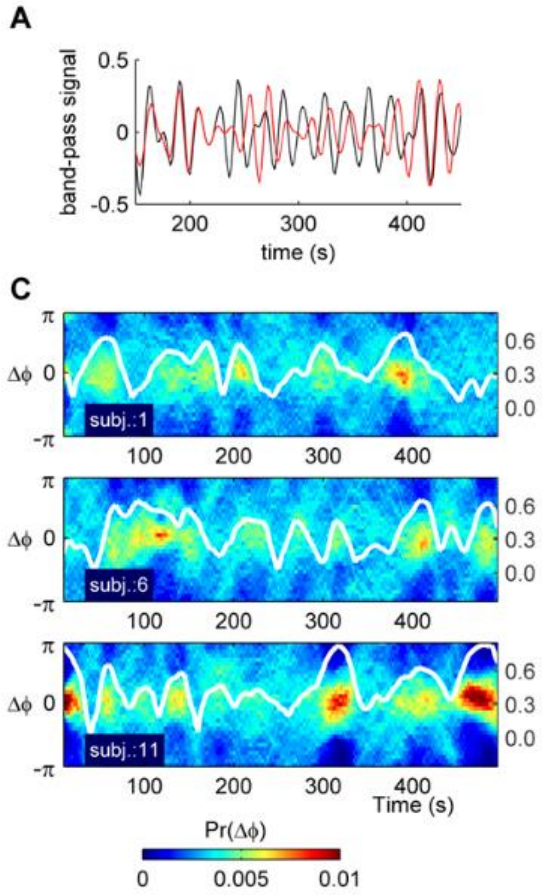

Figure V.3. A. Example band-pass filtered BOLD time series of two regions. C. Temporal evolution of the phase differences between two regions. (adapted from Ponce-Alvarez et al., 2015)

In addition to the nodal phase-lock values, we computed Kuramoto order parameter (KOP) as an indicator of global synchronization, or coherence: $H(t) = \frac{1}{N}\sum_{j=1}^{N} exp\left(i\varphi_j(t)\right), i = \sqrt{-1}$. (Cabral et al., 2012a; Hellyer et al., 2014; Kuramoto, 1986; Shanahan, 2010).

V.II.ii . Kuramoto Model

We used Kuramoto Network Model with N coupled phase oscillators (N is the number of regions) to simulate BOLD time series (Ponce-Alvarez et al., 2015)(Figure V.3). Where the phase of the oscillator i $(i = 1,\ldots,N)$ at time t is denoted by φ_i, the time evolution of the phases are defined by:

$$\frac{d\varphi_i(t)}{dt} = \omega_i + \xi_i(t) + K\sum_{j=1}^{N} C_{ij} sin\left(\varphi_j(t) - \varphi_i(t)\right)$$

Here ω_i is the natural frequency of each oscillator, K is the global coupling parameter, C_{ij} is the effective connectivity between nodes i and j, and ζ_i is uncorrelated white noise with zero mean and standard deviation σ. The natural frequencies of the regions were extracted from the original time series as the higher power frequency. We run the simulations using Euler's Method ($dt = 0.1$), 1000 seconds sampled at 2 seconds, considering the trade-off between the convergence of the solution and computational expense. The average PL (simulated PLS) and the coherence (average H) were then computed using the phase information in each time step.

V.II.iii . Optimization of Effective Connectivity

The goal of the optimization procedure was to infer the most likely connectivity matrix (i.e. EC) that explains the empirical functional connectivity. To achieve this, we used simulated annealing approach with a deterministic guidance term. As an initial guess for the EC, we used the average structural connectivity matrices based on Fractional Anisotropy (FA) of the corresponding cohort. Then, at each iteration we run the Kuramoto simulation, and computed the simulated PLS and coherence values (H).

In the beginning of the each iteration, first, we adjusted the global coupling (K) to ensure the stability of the simulations. Where H^{sim} and H^{emp} are simulated and empirical coherences, we updated global coupling as: $K_{update} = Kexp\left(H^{sim} - H^{emp}\right)$, until

$\left|H^{sim} - H^{emp}\right| < 0.1$.

Then, we updated the effective connectivity matrix (C), using:

$$C_{ij}^{update} = C_{ij}^{current} + T\left(P_{ij}^{sim} - P_{ij}^{emp}\right) + \eta_{ij}$$

Where *i* and *j = (1, ..., N)*, *N* is the number of regions, *T* is the temperature, P^{sim} and P^{emp} are the simulated and empirical PLS, and η_{ij} is a Gaussian random noise ($\mu=0$ and $\sigma=0.01$). The term $T\left(P_{ij}^{sim} - P_{ij}^{emp}\right)$, decaying with the temperature, was aimed to guide the Metropolis-Hastings algorithm to facilitate the convergence given the high dimensional space and the non-linear model. Furthermore, we updated only the non-zero connections in the structural connectivity matrix, and inter-hemispheric links.

For both current and updated effective connectivity, we compared the similarity between simulated and empirical PLS values using Euclidean distance:

$D = \sqrt{\sum_{i=1}^{N}\left(P_{ij}^{sim} - P_{ij}^{emp}\right)^2}$. Then, the cost function was defined as:

$$Cost = exp\left(\frac{D^{current} - D^{update}}{T}\right)$$

We accepted the updated effective connectivity matrix if the *Cost* is lower than a random threshold *v*, which is uniformly distributed between 0 and 1. Then, temperature *T* was reduced 10%. In brief, a closer solution (*Cost > 1*) will be accepted with certainty, and to avoid being stuck in local minima, worse solutions will be accepted with some probability depending on the distance and temperature. This procedure was repeated until $T < 3x10^{-5}$, where it is unlikely to find a new solution. Finally, the *C* that gave the best fit was kept as the optimal EC. Here, we used Pearson's correlation coefficient instead of Euclidean distance as it provides a normalized measure that can be easily compared and interpreted. We repeated this procedure for the standard deviation of the noise in Kuramoto model (ζ_i), ranging between 0.1 and 1.

V.III. Results

First, we compared the Pearson's correlation coefficient based FC networks of neonates and infants with IUGR and healthy controls. We found no significant differences between groups. Then, we investigated the connectivity differences in average phase-lock (PLS), and variability of phase-lock (PLV). In neonatal cohort, we found altered networks of PLS and PLV. We found no significant differences between groups in PLS and PLV networks in 1 year-old cohort. In contrast, model based estimate of EC revealed impaired connectivity in both cohorts. We used NBS approach to compare whole-brain networks between groups (see Appendix 4. Materials and Methods: IUGR).

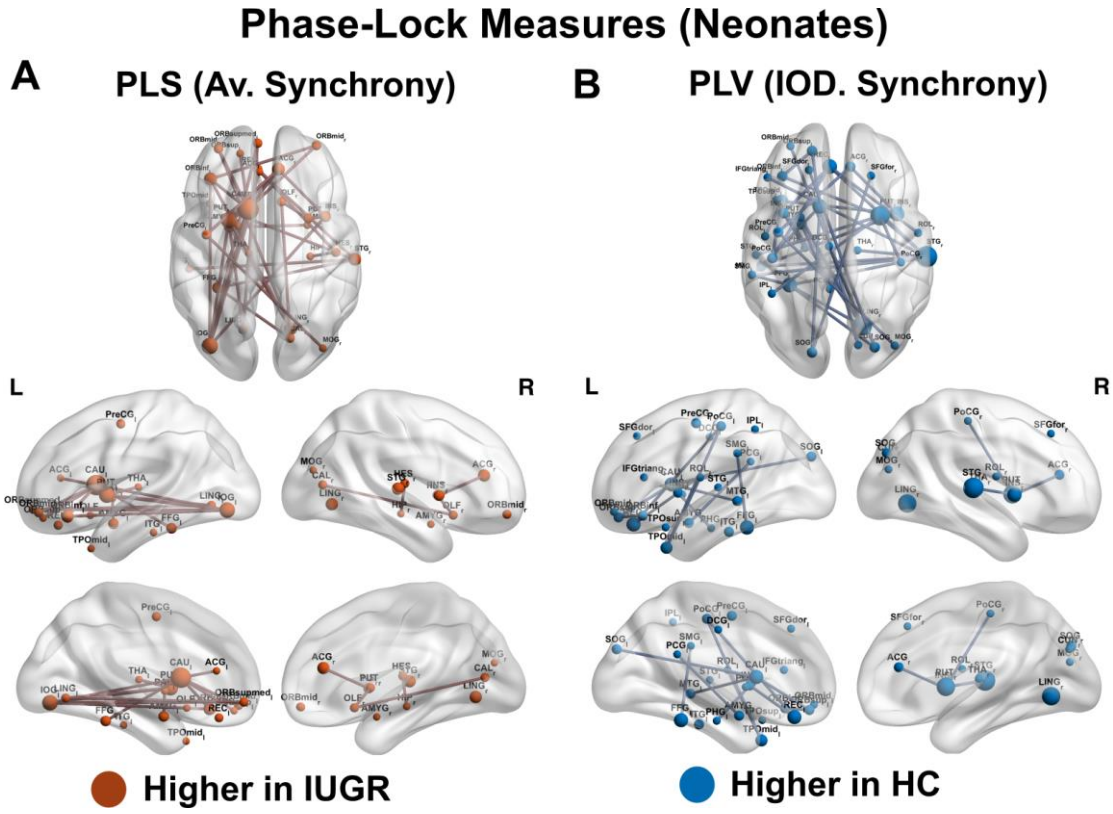

Figure V.4. Phase-lock (PL) measures group comparisons between IUGR and healthy controls for neonatal cohort. A. Average PL (higher in IUGR). B. Variability in PL (lower in IUGR). The comparisons were done using NBS (permutation t-test, 5000 permutations, p-value < 0.05). The thresholds for component size were set to report the network with at most top 1% of the connections.

V.III.i . Alterations in Synchronization Patterns in the Networks

We found a significantly hypersynchronized network ($p < 0.05$) in neonates with IUGR in which left caudate and putamen played the central role (Figure V.4). The network comprised increased synchronization between striato-thalamic network (left caudate and putamen, bilateral thalamus), orbital frontal cortex, limbic network (bilateral amygdala and anterior cingulate, olfactory cortex, right insula), temporal cortex (left temporal pole, inferior temporal gyrus and fusiform gyrus, and right hippocampus, Heschl gyrus and superior temporal gyrus), occipital cortex (bilateral lingual gyrus, left inferior occipital gyrus, and right medial occipital gyrus and calcarine), and precentral gyrus. In contrast, the variability of synchronization (PLV) was significantly decreased ($p < 0.05$) in neonates with IUGR with respect to healthy controls. The network of low variability connections showed a similar topology with the hypersyncronized network. This was an expected result since there is a inverse relationship between average synchronization (PLS) and variability of synchronization (PLV). However, we observed some important differences between altered PLS and PLV networks. First, the epicenter of the altered network shifted towards right putamen, superior temporal gyrus, and interhemispheric connections of lingual gyrus. Furthermore, the altered PLV network was extended toward posterior and superior parts of the brain (e.g. bilateral superior frontal gyrus and postcentral gyrus, left inferior parietal, supramarginal gyrus, dorsal and posterior cingulate). This suggests that the hypersynchronization in the network might be related to the impaired variability in fronto-parietal network, and the connections of the regions that are associated with task-negative and task-positive networks. No significant differences were observed in one-year-old cohort.

We also compared the perturbation integration level in PLS networks (Figure V.5). Consistent with the aforementioned results, we found a significant increase in neonates with IUGR compared to healthy controls (T-statistic = -2.643, $p = 0.0195$, d.o.f. = 38; permutation t-test), but no significant differences one-year-old cohort (T-statistic = -0.1612, $p = 0.874$, d.o.f. = 39; permutation t-test).

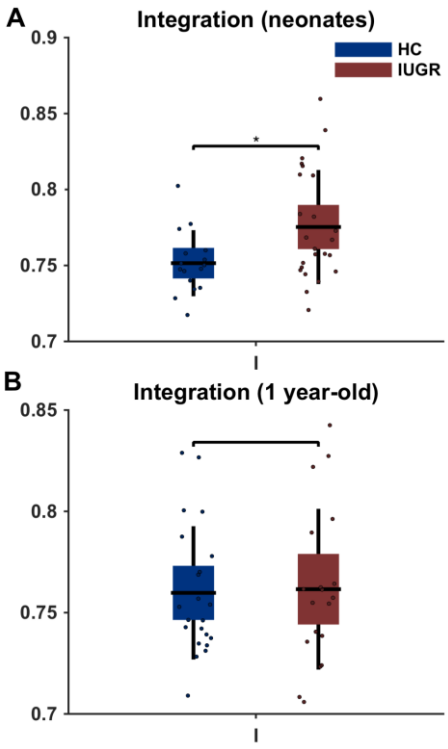

Figure V.5. Perturbational integration group comparison. A. Neonatal cohort. B. One-year-old cohort. The groups were compared using permutation t-test (10000 permutations).

V.III.ii . Alteration in Effective Connectivity Networks

We simulated the resting state fMRI BOLD time series using Kuramoto Model (see materials and methods). Kuramoto Model allowed us to represent the dynamics of the phase-lock values directly. Based on the simulated PLS matrices, using a simulated annealing approach, we inferred the EC underlying observed PLS. The similarity between simulated and empirical PLS was estimated as Pearson's correlation coefficients r = 0.6734 (std = 0.069) for neonates cohort, and r = 0.6731 (std = 0.079) for one-year-old cohort. Apart from EC, we also adjusted the global coupling parameter (K) and internal noise of each oscillator (σ). We found no significant differences between groups regarding global coupling parameter (permutation t-test: Neonates cohort, T-statistic = 1.65, p-value = 0.10, d.o.f. = 38; One-year-old cohort, T-statistic = -1.78, p-value = 0.09, d.o.f.

= 39) and internal noise (permutation t-test: Neonates cohort, T-statistic = 0.30, p-value = 0.78, d.o.f. = 38; One-year-old cohort, T-statistic = 0.68, p-value = 0.47, d.o.f. = 39).

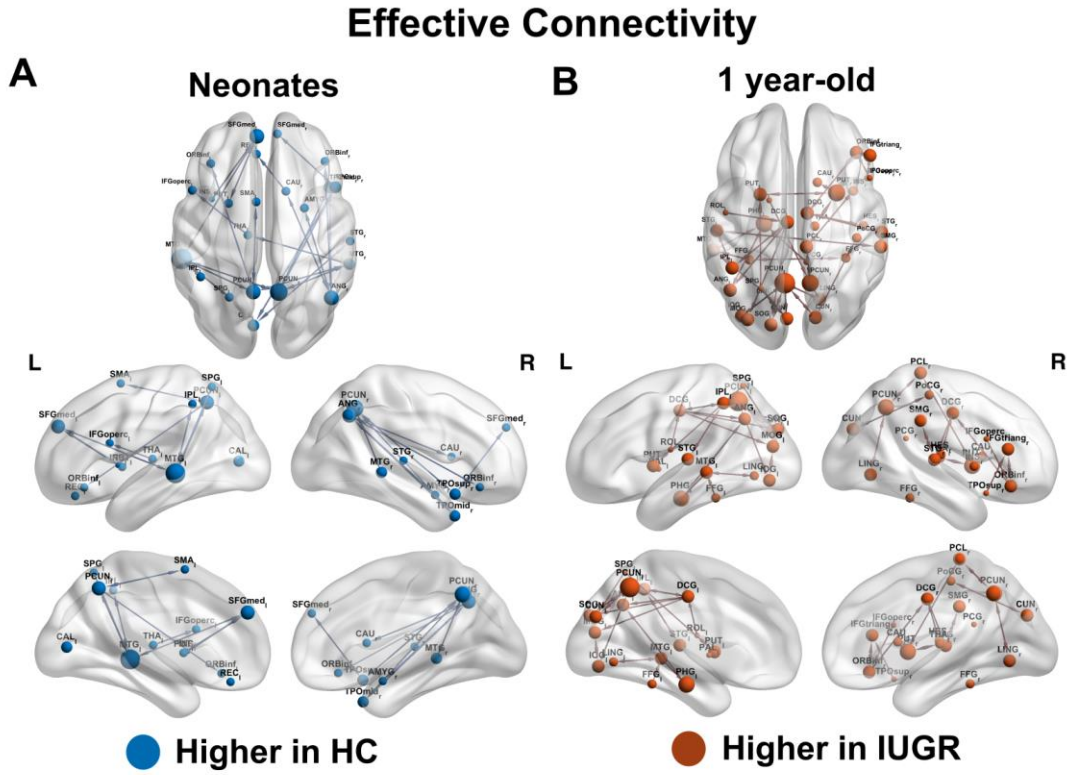

Figure V.6. Effective Connectivity group comparisons between IUGR and healthy controls measure for neonatal cohort (A) and one-year-old cohort (B). The comparisons were done using NBS for directed networks (permutation t-test, 5000 permutations, p-value < 0.05). The thresholds for component size were set to report the network with at most top 1% of the connections.

V.III.ii.a) Effective Connectivity of Neonates Cohort

In contrast to the hypersynchronized networks that we found in neonates in IUGR, the Effective Connectivity (EC) analysis revealed only significantly disconnected networks in IUGR compared to healthy controls (Figure V.6). Furthermore, the regions that were involved in altered EC were different than PLS and PLV networks. The core of the alterations was the connections of right medial temporal and superior frontal gyri, and bilateral precuneus. We found decreased EC between precuneus, and orbital frontal and medial temporal gyrus in both hemispheres. In left hemisphere, precuneus was further

disconnected with supplementary motor area, while in right hemisphere it was disconnected with temporal pole. Left medial temporal gyrus EC, and superior frontal gyrus, and superior and inferior parietal lobe were also decreased in neonates with IUGR. Thalamic afferent towards inferior frontal gyrus, and interhemispheric EC between calcarine and temporal lobe were also impaired in left hemisphere. Moreover, we found decreased EC between right angular gyrus and right amygdala, caudate and left rectus gyrus. Despite the differences in the strength of the test statistic, most of the altered connectivity was bidirectional.

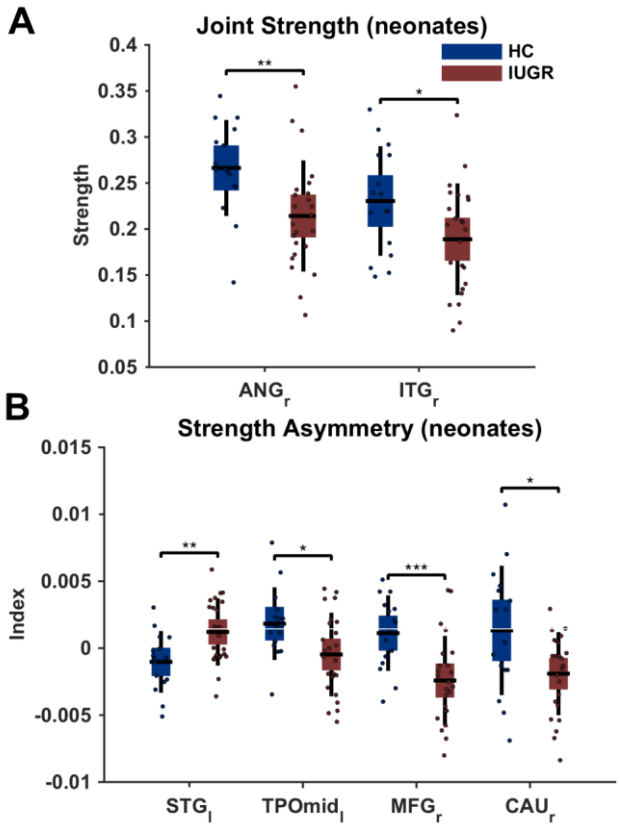

Figure V.7. Comparison of nodal metrics for neonatal cohort. A. Joint Strength (the sum of in- and out-strength of a particular node). B. Strength asymmetry (the difference between out- and in-strength of a particular node. Negative values indicate input dominated nodes, while positive values indicate output dominated nodes. The groups were compared using permutation t-test (10000 permutations), corrected for multiple comparisons using FDR.

We also compared the nodal strengths of EC between groups. The joint strength of right angular gyrus and right inferior temporal gyrus was significantly lower in IUGR group

than in healthy control group. The strength asymmetry, however, was significantly shifted towards high input tendency in left temporal pole, right medial frontal gyrus, and right caudate, but shifted towards high output tendency in left superior temporal gyrus (Figure V.7).

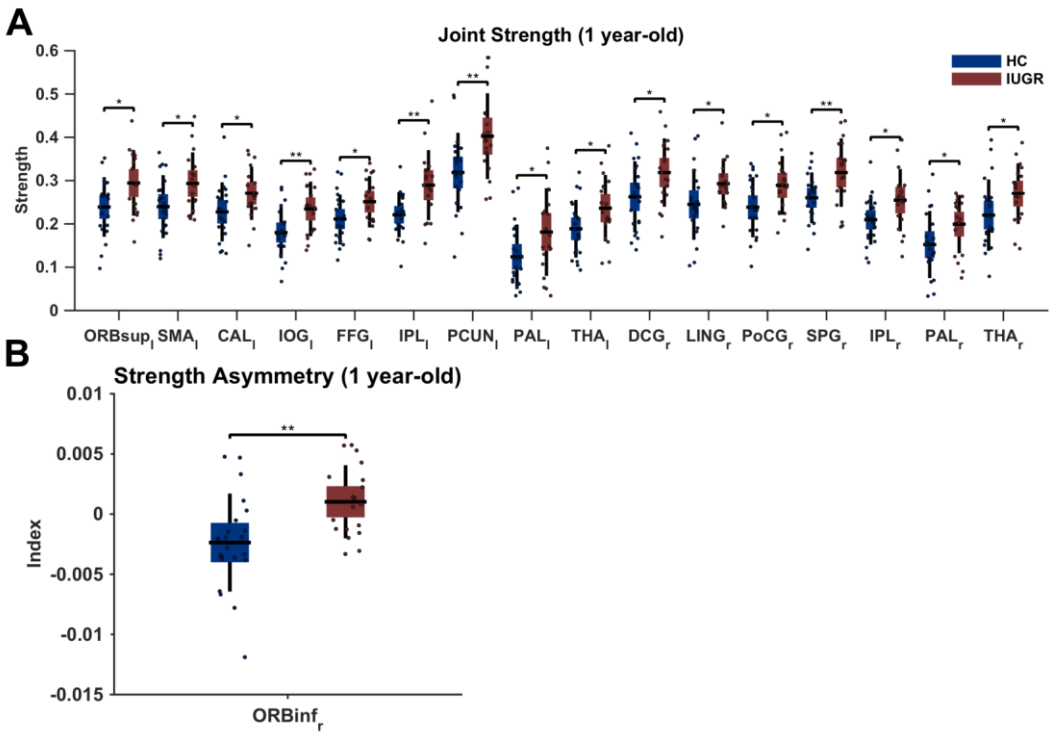

Figure V.8. Comparison of nodal metrics for one-year-old cohort. A. Joint Strength (the sum of in- and out-strength of a particular node). B. Strength asymmetry (the difference between out- and in-strength of a particular node. Negative values indicate input dominated nodes, while positive values indicate output dominated nodes. The groups were compared using permutation t-test (10000 permutations), corrected for multiple comparisons using FDR.

V.III.ii.b) Effective Connectivity of One-year-old Cohort

Although no significant differences were found in PLS and PLV of one-year-old cohort, we found increased EC in one-year-old infants with IUGR. Interestingly, the most influential regions in the altered network were also left and right precuneus as observed in neonates cohort, but in IUGR group in one-year-old cohort showed increased EC (Figure V.6). Furthermore, the altered network in one-year-old cohort was dominantly

in parietal, occipital and temporal lobes of the brain, with an exception of right inferior and orbital frontal gyri. The altered network was extended towards temporal lobes (right medial temporal, parahippocampus, right Heschl, bilateral superior temporal and fusiform gyri), thalamo-striatal regions (bilateral putamen, left pallidum, and right caudate), occipital lobe (left superior, medial and inferior occipital gyrus, and right cuneus and lingual gyrus), sensory-motor regions (right paracentral lobe, postcentral gyrus, supramarginal gyrus). Particularly, the alterations were observed among the regions that were associated to default model network (DMN) (e.g. precuneus, dorsal and posterior cingulate, medial frontal, parahippocampus). Moreover, increased EC among insula, orbital frontal, and temporal pole in right hemisphere suggests hyperconnected limbic network in one-year-old infants with IUGR.

The joint strength of IUGR infants showed widespread increases with respect to healthy controls, particularly in left precuneus and right superior parietal gyrus (Figure V.8). The strength asymmetry became output oriented in right inferior orbital frontal compared to healthy controls.

V.III.iii . The Relationship Between Altered Connectivity and Behavioral Assessments

We evaluated the relationship between alterations in connectivity (PLS, PLV, and EC) and behavioral assessments using partial correlation between significantly altered connections and behavioral assessment scores. For both cohorts we used birth percentile as a cofactor, and the partial correlations were controlled for sex, gestional age (GA), and mother's education and smoking status for both cohorts, and additionally controlled for breast feeding for one-year-old cohort. We found that percentile was significantly correlated with connectivity alterations in both cohorts.

Table V.1. PLS-PLV vs. behavioral measures (neonates). (* p < 0.05, ** p < 0.01)

Average Phase-Lock Synchronization in Neonates

Pair	Social-Interactive	Organization of State	Regulation of State	Autonomic Nervous System	Attention	Percentile
PreCG_l-ACG_r	-0.0041	0.1211	0.0090	-0.4258*	0.1254	-0.6407**
PreCG_l-MOG_r	0.0028	0.0424	0.1612	-0.4425*	0.0532	-0.4973**
ORBinf_l -IOG_l	-0.0469	-0.1355	0.0023	-0.4354*	0.0575	-0.4225*
ORBinf_l -LING_r	-0.0035	0.2040	0.1354	-0.5220**	0.0162	-0.3447
ORBsupmed_l -IOG_l	-0.1410	-0.0610	0.0127	-0.4483*	-0.0394	-0.3522
AMYG_l -LING_r	-0.2608	0.2292	-0.0360	-0.4795**	-0.0638	-0.4807**
LING_l -PUT_l	-0.3797*	-0.0160	-0.0629	-0.3605	-0.2666	-0.2337
FFG_l-CAU_l	-0.2027	-0.0048	0.1295	-0.5425**	-0.2066	-0.4155*
FFG_l-STG_r	0.0044	0.4227*	-0.1317	-0.3420	-0.0390	-0.4946**
PUT_l-ACG_r	-0.2356	-0.0826	-0.1870	-0.3749*	-0.1584	-0.4192*
PUT_l-LING_r	-0.4186*	0.2337	-0.0269	-0.4235*	-0.4187*	-0.2933
ITG_l-STG_r	-0.0741	0.3984*	0.0442	-0.4201*	-0.0679	-0.4351*
INS_r-ACG_r	-0.2686	0.1211	-0.1529	-0.4592*	-0.1499	-0.5031**
INS_r-PUT_r	-0.3875*	0.1768	-0.0337	-0.4616*	-0.2653	-0.3525
HIP_r-HES_r	-0.3351	0.1839	-0.2104	-0.6162**	-0.3881*	-0.4010*

Index of Dispersion of Phase-Lock Synchronization in Neonates

Pair	Social-Interactive	Organization of State	Regulation of State	Autonomic Nervous System	Attention	Percentile
SFGdor_l -SOG_r	0.2010	0.0815	0.0918	0.3750*	0.0318	0.2618
IFGtriang_l -STG_r	0.0389	-0.3470	0.0352	0.4178*	-0.0415	0.4568*
ROL_l-TPOmid_l	0.4481*	0.0171	0.2705	0.2938	0.2380	0.4752**
REC_l-INS_l	0.3663	-0.0545	0.0786	0.4159*	0.3486	0.3300
DCG_l-LING_r	-0.0558	-0.1479	0.0612	0.4183*	-0.0962	0.5499**
AMYG_l -LING_r	0.2198	-0.1208	-0.1743	0.4800**	-0.0010	0.4207*
SOG_l-CAU_l	0.0618	-0.0548	0.0471	0.5444**	0.0921	0.2087
FFG_l-STG_r	-0.0464	-0.4399*	-0.0665	0.4305*	-0.0027	0.7026**
PoCG_l -TPOmid_l	0.3468	-0.0312	0.2009	0.4278*	0.2738	0.2998
CAU_l-MTG_l	-0.0178	0.0567	-0.2785	0.3931*	0.0249	0.3857*
CAU_l-CUN_r	-0.0295	-0.2551	0.0582	0.5931**	-0.0042	0.5037**
PUT_l-LING_r	0.2473	-0.3783*	0.0333	0.3107	0.2507	0.2985
STG_l-PUT_r	0.4065*	-0.1633	0.2060	0.3556	0.3206	0.4018*
TPOsup_l -LING_r	0.2558	-0.2219	-0.0424	0.4597*	0.1399	0.4096*
MTG_l-STG_r	0.1625	-0.3966*	0.3321	0.3803*	0.1938	0.3100
TPOmid_l -INS_r	0.4374*	-0.0920	0.3822*	0.1636	0.2945	0.3155
ITG_l-INS_r	0.0866	-0.4195*	-0.0315	0.3459	-0.0045	0.5464**
ITG_l-STG_r	0.0147	-0.5077**	-0.1160	0.4688*	0.1377	0.4380*
INS_r-ACG_r	0.3486	-0.1689	0.2865	0.4949**	0.2357	0.4033*
INS_r-PUT_r	0.2821	-0.1999	0.0810	0.3871*	0.1325	0.3532
PUT_r-STG_r	0.2562	-0.2551	0.1001	0.3775*	0.1944	0.3996*
THA_r-STG_r	0.2506	-0.2276	0.2236	0.3514	0.2656	0.2741

V.III.iii.a) Neonates Cohort

Social-interactive cluster was negatively correlated with average synchronization in putamen, and positively correlated with the variability of connections of putamen and temporal pole (Table V.1)(for complete tables see Appendix 5. Supplementary Tables: IUGR). Variability of left temporal pole and right insula connectivity was also positively correlated with regulation of state cluster. However, no significant correlations were found between regulation of state cluster and PLS alterations. The autonomic nervous system cluster was associated to the alterations in the connectivity dominantly in temporal and occipital lobes, and limbic regions (orbital frontal, insula). The highest negative correlation observed in PLS between right hippocampus and right Heschl gyrus (rho = -0.6162, p-value < 0.01). This link was also played role in attention cluster. Attention cluster also showed an inverse relationship with the PLS between left putamen and right lingual gyrus, but no significant correlations with PLV alterations. Interestingly, organization of state cluster showed positive correlations with PLS between right superior temporal gyri and left fusiform and inferior temporal gyri. Similarly, the variability of the connections between inferior and superior temporal gyri, and fusiform gyrus, and left putamen and right lingual gyrus was negatively correlated with organization of state cluster. Finally, most of the alterations in connectivity were significantly correlated with birth percentile.

Regarding EC alterations, autonomic nervous system cluster was positively correlated with the connections between precuneus and supplementary motor area, temporal role and medial temporal gyrus, as well as left medial temporal gyrus and inferior parietal lobe (Table V.2). Regulation of state cluster was positively correlated with right amygdala – right angular gyrus EC. However, the rest of the behavioral measures showed inverse relationship with the alterations in EC. Left insula and superior frontal gyrus connectivity was negatively correlated with social-interactive, regulation of state and attention clusters. The EC between left precuneus and supplementary motor area was negatively correlated with organization of state cluster.

Table V.2. EC vs. behavioral measures (neonates)

Effective Connectivity of Neonates

Pair	Social-Interactive	Organization of State	Regulation of State	Autonomic Nervous System	Attention	Percentile
SMA_l-PCUN_l	-0.0568	-0.4586*	-0.0601	0.4909**	-0.1405	0.4789**
INS_l-SFGmed_l	-0.4386*	-0.1460	-0.5548**	0.0033	-0.4734**	0.1718
IPL_l-MTG_l	0.0718	-0.1207	-0.0640	0.4458*	0.2087	0.2271
PCUN_l-SMA_l	-0.0557	-0.4279*	-0.0520	0.4722**	-0.1295	0.4573*
MTG_l-IPL_l	0.0631	-0.1081	-0.0583	0.4828**	0.1974	0.2334
AMYG_r-ANG_r	0.2403	-0.1217	0.3733*	0.1022	0.2420	0.4145*
ANG_r-ORBinf_r	0.2190	-0.0106	-0.0682	0.4017*	0.2020	0.2671
PCUN_r-TPOsup_r	-0.0743	-0.2231	-0.0888	0.3953*	-0.1714	0.6675**
PCUN_r-MTG_r	0.2509	-0.1091	0.1447	0.3822*	0.1848	0.5918**
TPOsup_r-PCUN_r	-0.0040	-0.2310	-0.0776	0.4314*	-0.1208	0.6821**

* p < 0.05, ** p < 0.01

Table V.3. EC vs. behavioral measures (infants)

Effective Connectivity of Infants

Pair	Adaptation	Cognitive	Language	Motor	Social	Percentile
DCG_l-ANG_l	0.1613	-0.0631	0.0862	-0.1922	0.4825*	-0.1395
SOG_l-PCUN_l	0.5319*	-0.2894	-0.1617	-0.3625	0.4652*	-0.3244
MOG_l-IOG_l	-0.1579	-0.5370*	-0.2314	-0.1443	-0.2840	-0.5317*
IOG_l-MOG_l	-0.1954	-0.5462*	-0.2285	-0.1415	-0.2906	-0.5006*
FFG_l-MTG_l	-0.0785	-0.5318*	-0.3066	-0.2459	-0.1952	-0.2633
FFG_l-FFG_r	-0.4681*	-0.2352	-0.2212	-0.0247	-0.3289	-0.2157
SPG_l-PUT_l	0.2666	-0.4671*	-0.1723	-0.4832*	0.1586	-0.4908*
PCUN_l-SOG_l	0.4898*	-0.2728	-0.1372	-0.3232	0.4823*	-0.2913
PAL_l-PCUN_r	0.2966	-0.1803	0.1949	-0.1298	0.5290*	-0.3405
DCG_r-HES_r	0.6152**	-0.1731	-0.2427	-0.4107	0.1486	-0.4362
HES_r-DCG_r	0.5591*	-0.1590	-0.2542	-0.4394	0.1740	-0.4311

* p < 0.05, ** p < 0.01

V.III.iii.b) One-year-old Cohort

We found negative correlations between cognitive scores of one-year-old infants and EC between medial and superior occipital gyri, fusiform and medial temporal gyri, and superior parietal gyrus and putamen in left hemisphere (Table V.3). Moreover, adaptation scores were negatively correlated with left and right fusiform gyri connectivity. Similar to the neonate cohort, several EC alterations showed positive correlations with

behavioral assessment scores: Right dorsal cingulate – Heschl gyri and left precuneus – superior occipital connectivity was positively correlated with adaptation scores. Motor scores were correlated with left superior parietal gyrus – left cuneus EC. Finally, social scores were positively correlated with the EC between left precuneus and left superior occipital gyrus, right precuneus and left pallidum, and left dorsal cingulate and left angular gyri.

V.IV. Discussion

In this paper we proposed a whole-brain model based approach to analyze underlying connectivity structure of neonates and infants with IUGR. Instead of using correlation based functional connectivity (FC) measures, we used the temporal dynamics of phase-lock values based on instantaneous phases of each region in a narrow-band between 0.04 and 0.07 Hz.. The proposed methodology in this paper allowed us to characterize both static (grand average) and dynamic (variability) properties of the synchronization between regions in the same temporal resolution. This was, we avoided the problems discussed in sliding-window approach in dynamic functional connectivity. Furthermore, this approach allowed us to model the phase dynamics of the brain regions directly using Kuramoto model.

We defined static and dynamic connectivity metrics as average phase-lock (PLS) and variability of phase-lock (PLV), respectively. Then, we compared the altered networks between IUGR and healthy control groups for both neonate and one-year-old cohorts. Finally, we used the Kuramoto model to infer whole-brain effective connectivity (EC) of each subject to reveal the connectivity patterns underlying observed interactions between brain regions.

We found no significant differences in PLS and PLV networks of one-year-old cohorts. However, we found hypersynchronized and less variable networks in neonates with IUGR. The increased synchronization in IUGR neonates was observed in cortical connections of left caudate and putamen. However, the results showed that the hypersynchronization was closely related to impaired variability in associated networks. Specifically, the altered PLV in IUGR neonates was extended towards the regions that are re-

lated to both Default Mode Network (DMN) and fronto-parietal control networks. An immediate consequence of this finding is that altered connectivity in resting state might not necessarily match to the underlying connectivity changes between the same regions. Instead, much complex patterns of alterations might lead to observed FC, due to abnormal temporal dynamics in the connectivity.

When we estimate whole-brain EC based on observed connectivity, we found significantly different networks both in neonates and one-year-old cohorts. Furthermore, the altered EC networks showed related but very different topologies compared to PLS and PLV. First, although we observed increased synchronization in neonates with IUGR, the inferred EC showed an opposite pattern. We found widespread decreases in EC, instead of increases, and the epicenter of these decreases were the core regions in Default Mode Network (DMN) such as precuneus, superior and medial frontal, and temporal regions. In brief, the results suggest that DMN connectivity is relatively immature in the neonates with IUGR, leading to abnormal coordination of whole-brain dynamics.

Interestingly, the one-year-old IUGR infants showed increased EC, compared to healthy controls, in occipital, temporal and parietal regions especially in precuneus. A possible interpretation of these results might be that the brains of the infants with IUGR try to compensate the immature connectivity in DMN in order to adapt to the environmental demands.

VI. Alzheimer's Disease

Abstract

The neuronal mechanisms behind the Alzheimer's disease (AD) are still one of the most important problems in neuroscience. Recent efforts provided valuable insights on the genetic, biochemical and neuronal correlates of AD. The advances in structural and functional neuroimaging provided massive evidence for the AD related alterations in brain function. In this chapter, we contributed to these efforts by investigating the alterations in whole-brain structural (SC) and resting state functional connectivity (FC) in AD patients and preclinical individuals (PCs) compared to healthy controls (HC). However, we extended the scope the analysis by introducing global and nodal measures of FC dynamics. We found that altered SC and FC networks that are consistent in both groups compared to HCs. Nevertheless, dynamic FC revealed that the origins of these alterations might be different for PC and AD groups. We showed that the variability in FC was significantly altered in PC, but not in AD groups. Furthermore, we deepened the analysis using whole-brain computational model that allows estimating the underlying Effective Connectivity (EC) of each subject. Reinforcing our findings, we showed differences in EC networks in AD group, but found no significant differences in PCs compared to HCs. We also investigated the relationship between the connectivity structure and biomarkers. The analysis showed that Amyloid-β was associated to widespread FC measures, while tau tangles were correlated with the metastability of the FC dynamics. Finally, we proposed a noise-induced model for AD progression by disrupting the spontaneous activity in healthy controls using the computational model.

VI.I. Introduction

Alzheimer's disease (AD), being the most prevalent dementia, became a major concern in developed countries as a consequence of increasing life expectancy (Blennow et al., 2006; Plassman et al., 2007). During the past two decades advancements in genetics, neurobiology and neuroimaging techniques allowed researchers to study the mechanisms behind the underlying causes of AD. In particular, resting state fMRI (rs-fMRI) became a useful tool to study the alterations in brain activity of AD patients as well as many other clinical conditions.

Based on two widely accepted approaches (i.e. seed-based approach and independent component analysis (ICA)), recent research on functional connectivity (FC) in AD revealed specific patterns of connectivity associated to the disease (Brier et al., 2014; Dennis and Thompson, 2014; Filippi and Agosta, 2011). The studies that used seed-based approach showed widespread decreases in connectivity between various brain regions and hippocampus (Allen et al., 2007; Li et al., 2012; Wang et al., 2006) as well as posterior cingulate (Bai et al., 2011; Zhang et al., 2009) in AD. In contrast, an increased FC between prefrontal cortex and hippocampus (Wang et al., 2006), and posterior cingulate (Bai et al., 2011; Zhang et al., 2009) were associated with AD. The increased connectivity regarding prefrontal cortex was interpreted as a compensation mechanism during the initial stages of the disease (Dickerson et al., 2004; Filippi and Agosta, 2011; Sanz-Arigita et al., 2010). In addition, ICA of rs-fMRI showed decreased activation of default mode network (DMN) (Agosta et al., 2012; Koch et al., 2010; Qi et al., 2010; Sorg et al., 2007) and increased activation of fronto-parietal network (FPN) (Agosta et al., 2012).

Furthermore, various studies found impaired deactivation of DMN during task in AD and dementia (Celone et al., 2006; Greicius et al., 2004; Lustig et al., 2003; Petrella et al., 2007; Rombouts et al., 2009, 2005). The relationship between DMN and AD was further confirmed by the overlap between Aβ deposition and DMN (Buckner et al., 2008; Hedden et al., 2009) and other biomarkers (Sperling et al., 2011; L. Wang et al., 2015).

Overall, recent research suggests that the most robust characteristics of AD are decreased DMN connectivity (particularly in hippocampus and posterior cingulate), disconnection between anterior and posterior regions, and increased prefrontal connectivity. However, a recent review emphasized that the consequences of AD related atrophy in brain connectivity could one be identified during symptomatic stage of the disease and that an integrative approach between connectivity and biomarkers is needed (Ramirez et al., 2014). Furthermore, the structure-function relationship is more complex that it appears (Filippi and Agosta, 2011). Brier et al., (2014) suggests that the disconnection in several regions spread following a Hebbian kind of mechanism.

In this chapter, we studied the alterations in static (grand average) and dynamic FC in Alzheimer's disease, and proposed a whole-brain computational model that provided a mechanistic model for the neuronal manifestation of the disease. We first studied the global connectivity measures reflecting the average level of synchronization (coherence) and the metastability of the rs-BOLD signals. Then, we compared the structural, static and dynamic functional connectivity of the healthy controls (HC) to the preclinical individuals (PC) and the Alzheimer's disease patients (AD). Finally, using a whole-brain computational model, we inferred effective connectivity (EC) underlying observed FC, and proposed a mechanistic model for the progression of the disease. The results showed a monotonous decrease in coherence and metastability during the progression of the disease. Furthermore, we found that while amyloid-beta (Aβ-42) was significant associated with coherence, tau tangles were associated with the metastability.

We found altered SC and FC in both PC and AD groups. Consistent with the previous studies, we found disconnection between anterior and posterior parts of the brain in both PC and AD groups, and increased FC in a cluster of regions in AD patients. We compared the variability in FC (vFC), as a measure that reflects dynamical characteristics of the connectivity, and found that only in PC group there were alterations in vFC networks. Based on these findings, we hypothesized that the FC alterations observed in PC group are related to abnormal neuronal dynamics rather than the connectivity itself. Computational modeling, supercritical Hopf Normal Model, allowed us to infer whole-brain EC that gave rise to the observed rs-BOLD signals. Supporting our hypothesis, we found no significant EC differences in PC group, but found alterations in AD patients compared to HCs.

Beyond the statistical comparisons, we predict the alterations in the FC and v-FC in clinical groups by modifying the neuronal dynamics of the HCs in the model. Specifically, we gradually shifted the bifurcation parameter away from the critical point, producing noise driven dynamics. We found FC and vFC alterations in the model consistent with the empirical observations. Moreover, the maximum similarity between the empirical FC of severe AD group and the simulated FC of disrupted HC group were

significantly farther away from the critical point than preclinical and milder AD groups.

VI.II. Materials and Methods

We investigated 4 groups of subjects: Healthy controls, preclinical individuals (i.e. subjects having plaque formation without dementia), mild Alzheimer's disease (i.e. global deterioration scale 3), and severe Alzheimer's disease (i.e. global deterioration scale 4). The details of the materials and methods of this chapter are presented in Appendix 6. Materials and Methods: AD.

VI.II.i . Global Measures of Connectivity

We quantified the measures of connectivity based on level of synchronization in the BOLD time series. After defining a narrowband frequency with 0.03 Hz. window sizze, we computed Hilbert transform of the narrowband signal. Hilbert transform converts the narrowband signal as $a(t) = A(t)cos(\varphi(t))$, where $A(t)$ is the instantaneous amplitude (or envelope), and A(t), and $\varphi(t)$ is the instantaneous phase. The first and last 20 seconds (10 TR) of the transformed BOLD signal was then removed. The global coherence and metastability of time-series were computed based on the Kuramoto Order Parameter (KOP)(Cabral et al., 2012a; Hellyer et al., 2014; Kuramoto, 1986; Shanahan, 2010): $K(t) = \frac{1}{N} \sum_{j=1}^{N} \exp(i\varphi_j(t))$, where N is the number of ROIs and $\varphi(t)$ is the instantaneous phase of each region estimated using Hilbert Transform. The temporal average of Kuramoto Order Parameter defined as the coherence (or synchronization index), while the standard deviation of Kuramoto Order Parameter defined the metastability (i.e. the variation in synchronization over time).

VI.II.ii . Dynamic Functional Connectivity

Dynamic Functional Connectivity was computed using a sliding-window analysis approach. We used 2 minutes (60 TR) window size with 20 seconds sliding step size (10

TR). Then, we variability in FC was estimated as the standard deviation of each connection across time.

VI.II.iii . Statistical Analyses

The group comparisons for the networks were performed using Network Based Statistics (NBS) toolbox (Zalesky et al., 2010). For the comparisons between connections, we used permutation t-test with 5000 permutations, and defined p-value threshold as $p < 0.05$. Effective Connectivity matrices were compared using the directed version of NBS. To define connected component size, we iterated over the thresholds between the values 1 and 5 using a step size of 0.05. For the ease of interpretation, we chose the threshold that gives the networks comprising at most 1-2% of the connections with the highest t-statistic. The networks were visualized using BrainNet Viewer toolbox in Matlab (Xia et al., 2013).

The rest of the statistical comparisons were done using permutation t-test (1000 permutations), and multiple comparisons were corrected using FDR approach with Benjamini&Hochberg algorithm if necessary (Hochberg and Benjamini, 1990).

Correlations between measures were estimated as partial correlations controlled for age, gender and education level.

VI.II.iv . Computational Model

We modeled the whole-brain spontaneous activity using 78 nodes, excluding striatothalamic subcortical regions. Each node was coupled with each other via effective connectivity (EC) matrix. We described the local dynamics of each individual node using normal form of a supercritical Hopf bifurcation. The advantage of this model is that it allows transitions between asynchronous noise activity and oscillations. Where ω is the intrinsic frequency of each node, a is the local bifurcation parameter, η is additive

Gaussian noise with standard deviation β, the temporal evolution of the activity, z, in node j is given in complex domain as:

$$\frac{dz_j}{dt} = [a_j + i\omega_j - |z_j^2|] + \beta\eta_j(t)$$

and,

$$z_j = \rho_j e^{i\theta_j} = x_j + iy_j$$

This system shows a supercritical bifurcation at $a_j = 0$. Being specific, if a_j is smaller than 0, the local dynamics has a stable fixed point at $z_j = 0$, and for a_j values larger than 0, there exists a stable limit cycle oscillation with a frequency $f = \omega/2\pi$. Finally, the whole-brain dynamics is described by the following coupled equations:

$$\frac{dx_j}{dt} = [a_j - x_j^2 - y_j^2]x_j - \omega_j y_j + G\sum_i C_{ij}(x_i - x_j) + \beta\eta_{xj}(t)$$

$$\frac{dy_j}{dt} = [a_j - x_j^2 - y_j^2]y_j + \omega_j x_j + G\sum_i C_{ij}(y_i - y_j) + \beta\eta_{yj}(t)$$

Where C_{ij} is the Effective Connectivity (EC) between nodes i and j, G is the global coupling factor, and the standard deviation of Gaussian noise, $\beta = 0.02$. The simulated activity corresponds to the BOLD signal of each node. The simulations were run for 30000 s., sampled at 2 s., if not stated otherwise. Both the empirical and simulated BOLD signals were band-pass filtered in narrowband 0.06–0.09 Hz., since the group differences in coherence and metastability were optimal in this narrowband. The intrinsic frequency of each node was estimated as the peak frequency in the associated narrowband of the empirical BOLD signals of each brain region.

VI.II.v . Optimization of Effective Connectivity

We implemented a heuristic approach to infer the most likely connectivity matrix (i.e. Effective Connectivity) that explains the empirical functional connectivity. As an initial

guess, we started with the anatomical connectivity matrices.

First, we adjusted the global coupling parameter (G) to prevent overflow during the optimization procedure, and to ensure the stability of the system of equations. Where K^{sim} and K^{emp} are simulated and empirical coherences (average Kuramoto order parameter), we updated global coupling parameter as: $G = G\ exp(K^{sim} - K^{emp})$, until the desired condition, $\left|K^{sim} - K^{emp}\right| < 0.1$, was satisfied.

We evaluated both zero-time-lag Functional Connectivity (FC^0) and time-lagged FC (FC^τ) for both empirical and simulated BOLD signals. Time-lagged FC measure was chosen for two reasons. First, it provides an additional constraint ensuring that the optimal solution is unique. Second, time-lagged correlations allow inference on the directionality of the connections. The defined the distance metric as Euclidean Distance between simulated and empirical FC values for both FC^0 and FC^τ:

$$D^l = \sqrt{\sum_{i,j=1}^{N} (FC_{ij}^{sim,l} - FC_{ij}^{emp,l})^2}, l \in \{0, \tau\}$$

Then, where E is the average error between empirical and simulated FC measures;

$$E = \frac{\left(FC_{emp}^0 - FC_{sim}^0\right) + (FC_{emp}^\tau - FC_{sim}^\tau)}{2}$$

And where S_{ij} is the anatomical connectivity matrix, N is the number of regions, and Λ denoted inter-hemispheric links; we updated the effective connectivity between i and j $= (1, \ldots, N)$ according to:

$$C_{ij}^{update} = C_{ij}^{current} + 0.01E_{ij}, \quad if\ S_{ij} > 0, or\ S_{ij} \in \{\Lambda\}$$
$$C_{ij}^{update} = 0, \quad if\ S_{ij} = 0, or\ C_{ij}^{current} + 0.01E_{ij} < 0$$

In other words, we updated the EC based on the average error between empirical and

simulated FC measures for non-zero connections and inter-hemispheric connections. Negative weights were not allowed, and they all set to zero during the update procedure.

We accepted the total distance between empirical and simulated FC measures, $D^T=D^0+D^\tau$, for updated EC is lower than the minimum total distance observed during the procedure. We repeated this procedure using 100 iterations, and the best solution (minimum D) was considered as EC for a given subject. The entire procedure was also repeated for bifurcation parameter $a = \{-0.1, -0.05, 0, 0.05, 1\}$.

VI.II.vi . Artificial Disruption of The Dynamics in Healthy Controls

Given the inferred EC matrices, we disrupted the dynamics in healthy controls based on the bifurcation parameter, *a*, of the supercritical Hopf Normal Model. First, we computed the FC of the healthy controls at $a = -0.05$, where the optimal similarity between simulated and empirical values was observed. Then, we decreased the bifurcation parameter by 0.001 at each iteration, spanning values between -0.05 and -0.15. The FC and the variability of FC were computed for each value and quantified the alterations as $FC^a - FC^{-0.05}$. Specifically, we measured the changes in FC and vFC with respect to the reference point ($a = -0.05$).

The predicted alterations in healthy controls were then compared to the empirical alterations observed in clinical populations as $FC^{disease} - FC^{HC}$. For the nodal alterations (i.e. ΔFC_{ij}) we binarized the difference matrices using a threshold to give the highest 25% altered connections. Then, we compared the overlap between predicted and empirical alterations using Jaccard similarity (1 – Percentage of Overlap). In order to test the significance of the overlap, we compared 1000 random surrogate matrices having the same number of links, and computed the 95% confidence intervals for the surrogate data. We also compared the alterations for the strength of alterations (both for FC and vFC) in each node. The similarity between alteration strengths was quantified as Pearson's correlation coefficients between predicted and empirical alteration strengths.

VI.III. Results

VI.III.i . Global Measures of Connectivity

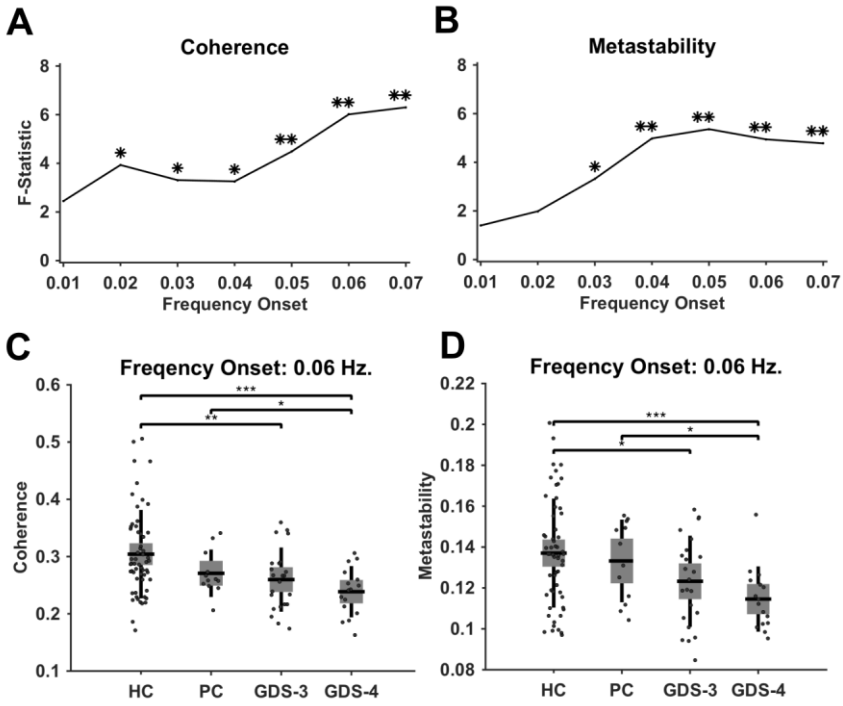

Figure VI.1. Comparison of global connectivity measures. A. Coherence One-way ANOVA between groups (HC, PC, GDS-3, GDS-4) across frequency narrowbands. B. Metastability One-way ANOVA between groups across frequency narrowbands. C. Coherence T-test between each group (permutation test, 10000 permutations). D. Metastability T-test between each group (permutation test, 10000 permutations). "*" indicates the level of significance.

We defined two global connectivity measures based on instantaneous phases that were obtained using Hilbert transform of the rs-fMRI BOLD time-series: Coherence and metastability. Both measures were computed using Kuramoto order parameter (KOP), that is the dispersion of the distribution instantaneous phases of each region in a particular time (where 0 indicates perfect asynchronization and 1 indicates perfect synchronization). Coherence (mean KOP) reflects the average level of synchronization, and metastability (standard deviation of KOP) quantifies the variability in synchronization between the brain regions across time. Being specific, higher metastability indicates how flexibly the spontaneous brain activity alternates between synchronous and asynchro-

nous states. Since Hilbert transform of a signal is the most reliable in a narrow frequency band, first identified 7 frequency bins between 0.01 and 0.07 Hz. with a window size of 0.03 Hz. and a step size of 0.01 Hz. Then we compared coherence and metastability between 4 groups using one-way ANOVA. We found that the group differences were optimal in the narrow-band between 0.06 – 0.09 Hz for both coherence and metastability (Figure VI.1 A-B). Therefore, we focused our analysis in this specific narrow-band. First, we compared coherence and metastability between each group using permutation t-test (10000 permutations, p-value < 0.05). The results showed a monotonous decrease in both coherence and metastability along with the progression of the disease (Figure VI.1 C-D). The differences between healthy controls (HC) and Alzheimer's disease groups (GDS-3 and GDS-4) were highly significant. However, we found no significant difference between HCs and preclinical (PC) groups. Moreover, although coherence and metastability of PC group was not significantly different than GDS-3 group, there was a significant difference between PC group and GDS-4 group.

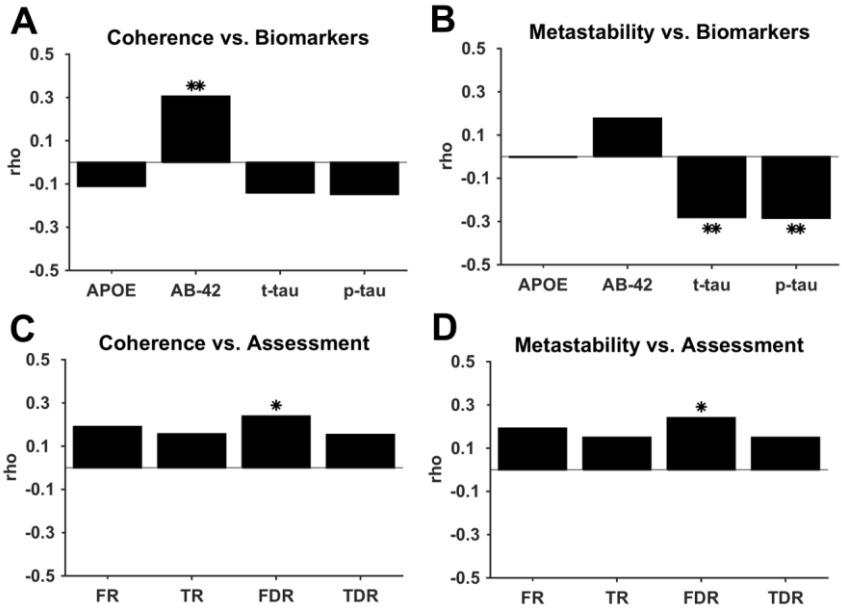

Figure VI.2. Relationship between global connectivity measures, biomarkers and behavioral assessment score. A. Partial correlations between coherence and biomarkers. B. Partial correlations between metastability and biomarkers. C. Partial correlations between coherence and behavioral assessment scores. D. Partial correlations between metastability and behavioral assessment scores. Partial correlations were computed by controlling age, gender and education level. FR: free-recall, TR: total recall, FDR: free-delayed recall, TDR: total-delayed recall.

Then, we checked the relationship between global connectivity measures (coherence and metastability) and clinical indicators, namely number of APOE E4 alleles, biomarkers (Aβ-42, t-tau, p-tau) and behavioral assessment scores (Buschke selective recall test). We used partial correlations between variables controlling confounding factors such as age, gender and education. We found that coherence was significantly correlated with Aβ-42, while metastability was significantly correlated with t-tau and p-tau (Figure VI.2 A-B). When the analysis was repeated for only PC and AD groups, the correlations in tau tangles survived, but in Aβ-42 they were disappeared. Moreover, both coherence and metastability was only significantly correlated with free delayed recall scores (Figure VI.2 C-D). These results suggest that Aβ-42 affects the overall connectivity level, while tau pathologies are associated to the dynamics of the connectivity.

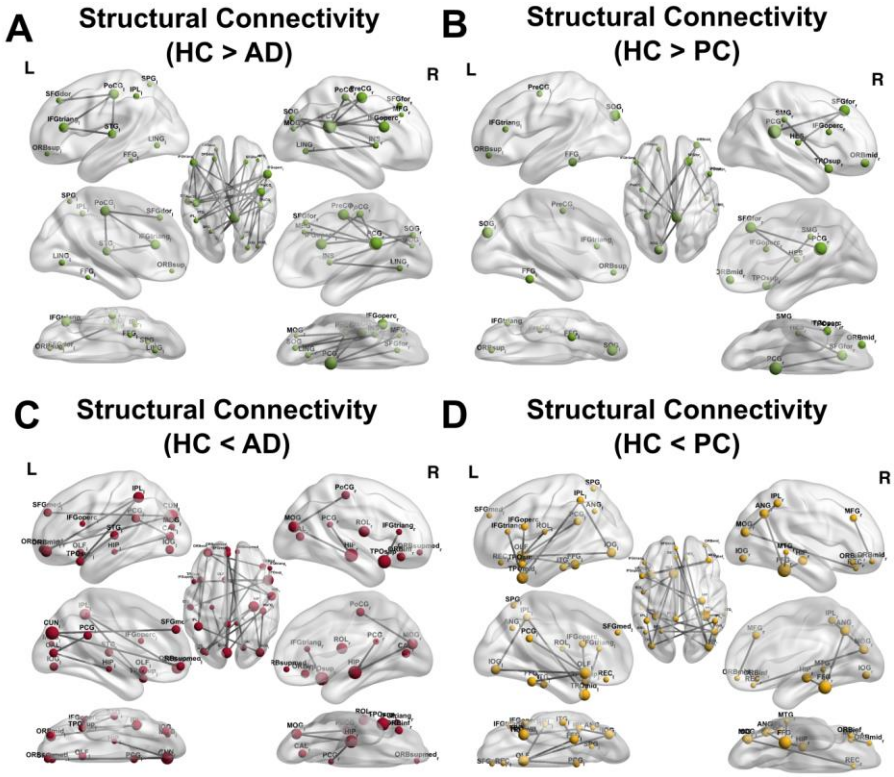

Figure VI.3. Significantly altered SC networks in preclinical (PC) and Alzheimer's disease (AD) groups. A. Decreased SC in AD. B. Increased SC in AD. C. Decreased SC in PC. D. Increased SC in PC. The comparisons were done in NBS (permutation t-test, 5000 permutation, p-value < 0.05), adjusted connected components threshold to report top 1-2% of the connections. Green nodes indicate HCs have higher values, red nodes indicate ADs have higher values, yellow nodes indicate PCs have higher values.

Table VI.1. Highest 10 Alterations in SC

Preclinical Group				Alzheimer's Disease Group			
Altered SC in Preclinical Group (HC > PC)				Altered SC in Alzheimer's Group (HC > AD)			
ROI-1	ROI-2	T-statistic	p-value	ROI-1	ROI-2	T-statistic	p-value
r-MOG	r-REC	4.52	<0.001	l-CUN	l-ORBsupmed	4.37	<0.001
r-ANG	r-FFG	4.44	<0.001	r-TPOsup	l-OLF	4.25	<0.001
l-MFG	l-PreCG	4.00	<0.001	l-IFGtriang	l-MFG	4.21	<0.001
r-MFG	l-TPOsup	3.96	<0.001	r-HIP	r-PCG	4.14	<0.001
l-TPOmid	l-IPL	3.93	<0.001	r-TPOsup	l-STG	3.82	<0.001
r-FFG	l-ANG	3.87	<0.001	r-ITG	r-PCL	3.79	<0.001
r-HIP	l-PCG	3.86	<0.001	r-PoCG	r-MOG	3.62	<0.001
l-ACG	l-INS	3.86	<0.001	r-MOG	l-IPL	3.61	<0.001
l-IPL	l-IOG	3.80	<0.001	r-ORBsupmed	l-CUN	3.56	<0.001
r-ANG	l-FFG	3.80	<0.001	r-TPOsup	l-IFGoperc	3.51	<0.001
Altered SC in Preclinical Group (HC < PC)				Altered SC in Alzheimer's Group (HC < AD)			
ROI-1	ROI-2	T-statistic	p-value	ROI-1	ROI-2	T-statistic	p-value
r-PCG	l-PreCG	-3.22	<0.001	r-PoCG	l-IFGtriang	-4.95	<0.001
r-CUN	l-STG	-3.07	<0.001	r-PCG	r-MFG	-4.72	<0.001
r-PCG	l-IFGtriang	-3.06	<0.001	l-STG	l-IFGtriang	-4.60	<0.001
r-TPOsup	r-SMG	-2.99	<0.001	r-IFGoperc	l-STG	-4.54	<0.001
r-ORBmid	l-FFG	-2.73	0.01	r-PCG	l-SFGdor	-4.23	<0.001
l-PCG	l-ROL	-2.71	0.01	r-PreCG	l-PoCG	-4.16	<0.001
r-HES	r-SFGfor	-2.66	0.01	r-IFGoperc	l-IPL	-4.06	<0.001
r-IFGoperc	l-SOG	-2.54	0.01	r-SFGfor	l-FFG	-4.03	<0.001
r-TPOsup	l-SOG	-2.49	0.02	r-PCG	r-SFGfor	-4.02	<0.001
r-PCG	l-ORBsup	-2.47	0.02	r-PreCG	l-STG	-3.95	<0.001

VI.III.ii . Whole-Brain Structural and Functional Connectivity

We compared the structural and functional connectivity between HCs and PCs and between HCs and ADs for whole brain connectivity using network based statistics (NBS) approach. We found decreased SC between right posterior cingulate and bilateral frontal regions (i.e. bilateral dorsal superior frontal, right interior frontal operculum, left inferior frontal triangular, and left orbital frontal) (Figure VI.3)(see also Table VI.1). Moreover, consistent with the decreased FC, both groups showed decreased SC between right inferior frontal and left occipital lobe. The disconnection was more pronounced in AD group (Figure VI.3 A). Both groups also showed increased SC with respect to HCs

(Figure VI.3 C-D). The SC within occipital and parietal regions was increased in both groups. Furthermore, increased connectivity in right hippocampus and posterior cingulate was observed both in PCs and ADs. In PC group, right hippocampus connectivity was increased between temporal (right medial temporal, fusiform gyrus), parietal (left posterior cingulate, right angular gyrus) and frontal (left inferior frontal triangular). In contrast, hippocampus SC was increased between occipital (bilateral medial occipital, calcarine) and bilateral posterior cingulate bilaterally in AD group.

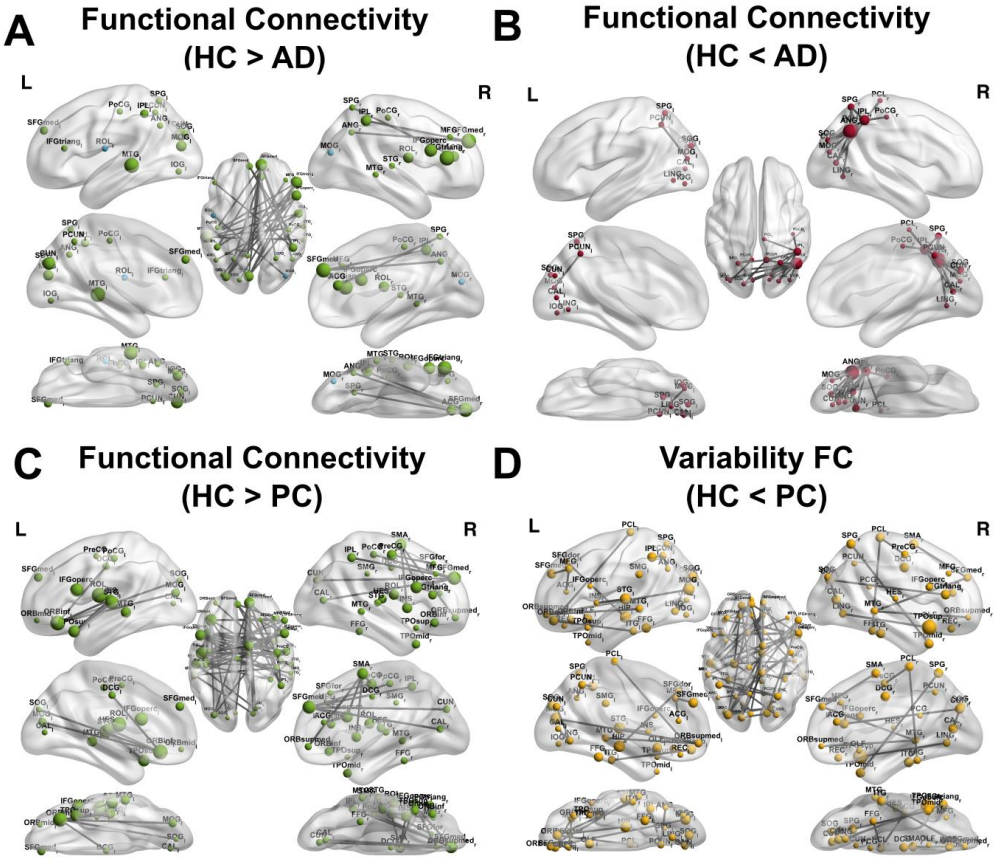

Figure VI.4. Significantly altered FC and vFC networks in preclinical (PC) and Alzheimer's disease (AD) groups. A. Decreased FC in AD. B. Increased FC in AD. C. Decreased FC in PC. D. Increased variability of FC in PC. The comparisons were done in NBS (permutation t-test, 5000 permutation, p-value < 0.05), adjusted connected components threshold to report top 1-2% of the connections. Green nodes indicate HCs have higher values, red nodes indicate ADs have higher values, yellow nodes indicate PCs have higher values.

We found that for both AD and PC groups the FC between left medial and inferior frontal regions and right occipital and bilateral parietal regions were significantly de-

creased relative to HCs (Figure VI.4)(Table VI.2). In particular, the core of the alterations was left superior frontal gyrus for both PC and AD groups (Figure VI.4 A-C). Regarding the right hemisphere, PC group showed decreased connectivity between right orbital frontal cortex and occipital lobe, while AD group showed decreases in the interhemispheric connections of the parietal regions (Figure VI.4A). We found no significant increase in FC of PC group. However, the results showed increased FC in a cluster of bilateral occipital regions centered at right angular gyrus in AD group (Figure VI.4B).

Table VI.2. Highest 10 Alterations in FC and v-FC

Altered FC in Preclinical Group (HC > PC)				Altered FC in Alzheimer's Group (HC > AD)			
ROI-1	ROI-2	T-statistic	p-value	ROI-1	ROI-2	T-statistic	p-value
r-ROL	l-ROL	3.72	<0.001	r-IPL	r-SPG	4.53	<0.001
r-IPL	l-SFGmed	3.55	<0.001	r-ANG	l-CAL	4.28	<0.001
r-HES	l-ORBinf	3.50	<0.001	r-PCUN	r-IPL	4.00	<0.001
r-MTG	l-DCG	3.48	<0.001	r-ANG	l-LING	4.00	<0.001
l-HES	l-ORBinf	3.44	<0.001	r-ANG	r-CAL	3.97	<0.001
r-SFGfor	r-PreCG	3.40	<0.001	r-REC	l-ORBsup	3.83	<0.001
r-SMA	r-PreCG	3.36	<0.001	r-ANG	r-SOG	3.77	<0.001
r-IFGtriang	l-ROL	3.32	<0.001	l-PCUN	l-SPG	3.72	<0.001
r-IFGoperc	l-ROL	3.32	<0.001	r-ANG	r-SPG	3.66	<0.001
r-HES	l-IFGoperc	3.26	<0.001	r-PCUN	r-SPG	3.53	<0.001
Altered vFC in Preclinical Group (HC < PC)				Altered FC in Alzheimer's Group (HC < AD)			
ROI-1	ROI-2	T-statistic	p-value	ROI-1	ROI-2	T-statistic	p-value
r-TPOsup	l-FFG	4.78	<0.001	r-IPL	r-SFGmed	-5.46	<0.001
r-ITG	l-ORBsup	3.95	<0.001	r-IFGtriang	l-CUN	-5.32	<0.001
l-PCUN	l-IPL	3.62	<0.001	r-IFGtriang	l-MOG	-5.28	<0.001
r-TPOsup	l-ITG	3.59	<0.001	r-IPL	l-SFGmed	-5.27	<0.001
r-TPOsup	l-OLF	3.52	<0.001	r-STG	l-MTG	-5.17	<0.001
r-SMA	l-REC	3.43	<0.001	r-MOG	l-ROL	-5.11	<0.001
l-MOG	l-ORBsupmed	3.35	<0.001	r-IFGoperc	l-MOG	-5.07	<0.001
r-HES	l-HIP	3.34	<0.001	r-IFGtriang	l-SOG	-5.03	<0.001
l-LING	l-CAL	3.32	<0.001	r-SFGmed	l-PoCG	-5.00	<0.001
r-ACG	l-STG	3.30	<0.001	r-MTG	l-MTG	-4.99	<0.001

VI.III.iii . Dynamic Functional Connectivity

We extended the analysis by considering temporal changes in functional connectivity (i.e. dynamic FC). We used sliding window analysis with 2 minutes windows (60 TR) with a sliding step size of 20 seconds (10 TR) to compute dFC. Then we defined the variability of each connection as the standard deviation of FC. Following a similar approach with the FC and SC comparisons, we checked whether some networks were significantly altered in PC and AD groups using NBS approach. We found no significant differences between HC and AD groups. However, we found widespread increases in variability of FC in PC group (Figure VI.4D). Not surprisingly, there was an overlap between decreased FC and increased variability of FC observed in PC group due to the inverse relationship between the mean and standard deviation of dFC. Nevertheless, we also observed some differences between the altered networks of FC and vFC in PC group. The alterations in FC were more dominant in frontal regions of right hemisphere and in occipital regions of left hemisphere. Contrastingly, in variability of FC, these alterations were evenly distributed over the cortex.

Finally, to understand how the variability of FC is related to connectivity dynamics, we checked its association with global connectivity measures. We computed the partial correlations between the variability strength of each region with coherence and metastability controlling for the rest of the regions (Figure VI.5 A-B). We found that variability of left-hippocampus (negatively) and right-inferior orbital frontal cortex (positively) was significantly correlated with both coherence and metastability, suggesting that increased variability in left-hippocampus impairs global dynamics, while increased variability in right-orbital frontal cortex reinforces them. We also demonstrated how the variability in these regions evolved across groups. Right orbital frontal cortex variability was stable for PC and GDS-3 groups, but sharply decreased in GDS-4 group (Figure VI.5C). The variability of left-hippocampus was increased in PC group, but then it monotonously decreased with the severity in the AD groups (Figure VI.5D).

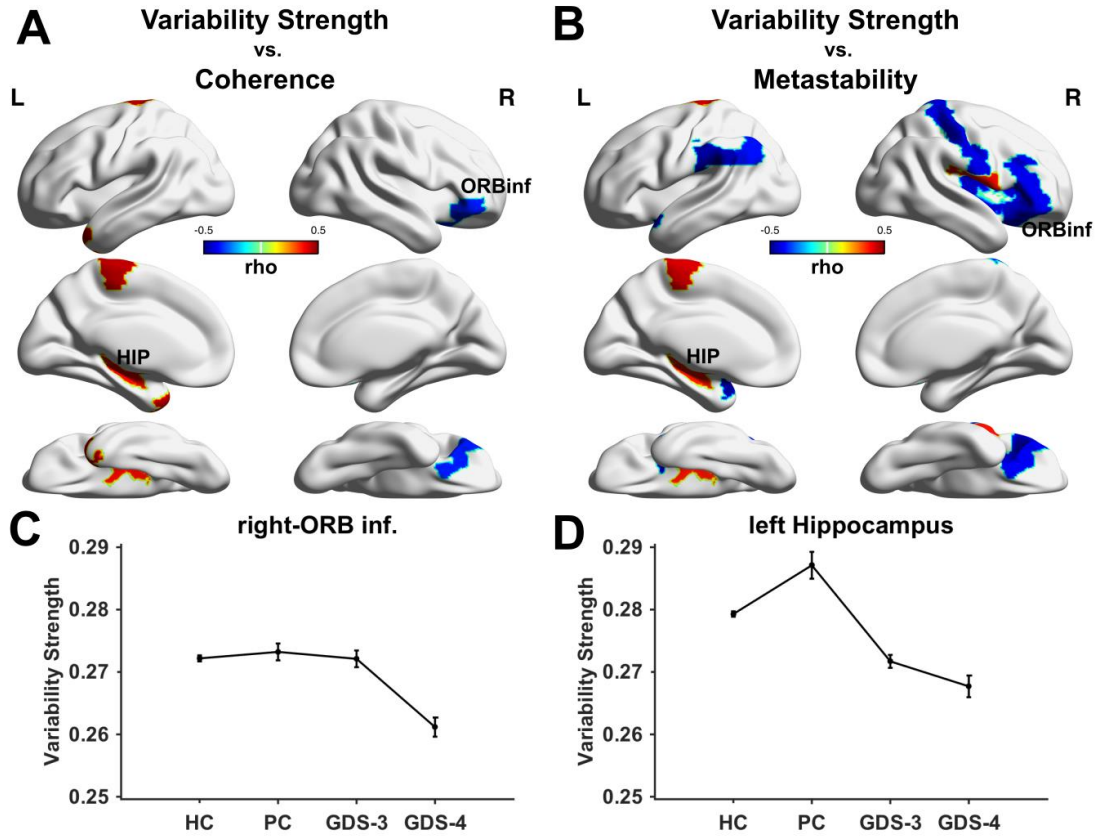

Figure VI.5. Relationship between variability strength of each node and global connectivity measures (coherence and metastability). A. Significant partial correlations between variability strength and coherence. B. Significant partial correlations between variability strength and metastability. C. Mean variability strengths of right inferior orbital frontal cortex in each group. C. Mean variability strengths of left hippocampus in each group. Errorbars represent SEM.

VI.III.iv . Relationship between connectivity and biomarkers

We investigated the relationship between clinical indicators and the strengths of the nodes in SC, FC, and vFC (Figure VI.6). Similar to the previous sections we used partial correlation between each measure controlling for confounding factors (age, gender and education). We found the higher association between Aβ-42 and FC strength, particularly in temporal lobe (Figure VI.6E). This association was shifted to frontal and parietal regions for t-tau and p-tau (Figure VI.6 F-G). Regarding SC, we found that both Aβ-42 and tau-tangles were correlated with SC strength in temporal lobe (Figure VI.6 B-D). However, we found very high correlation between posterior cingulate and Aβ-42

(Figure VI.6B). Moreover, the only modality that was correlated with APOE was SC (Figure VI.6A). Finally, we found that variability of FC was associated to cingulate cortex and frontal regions (Figure VI.6 H-J).

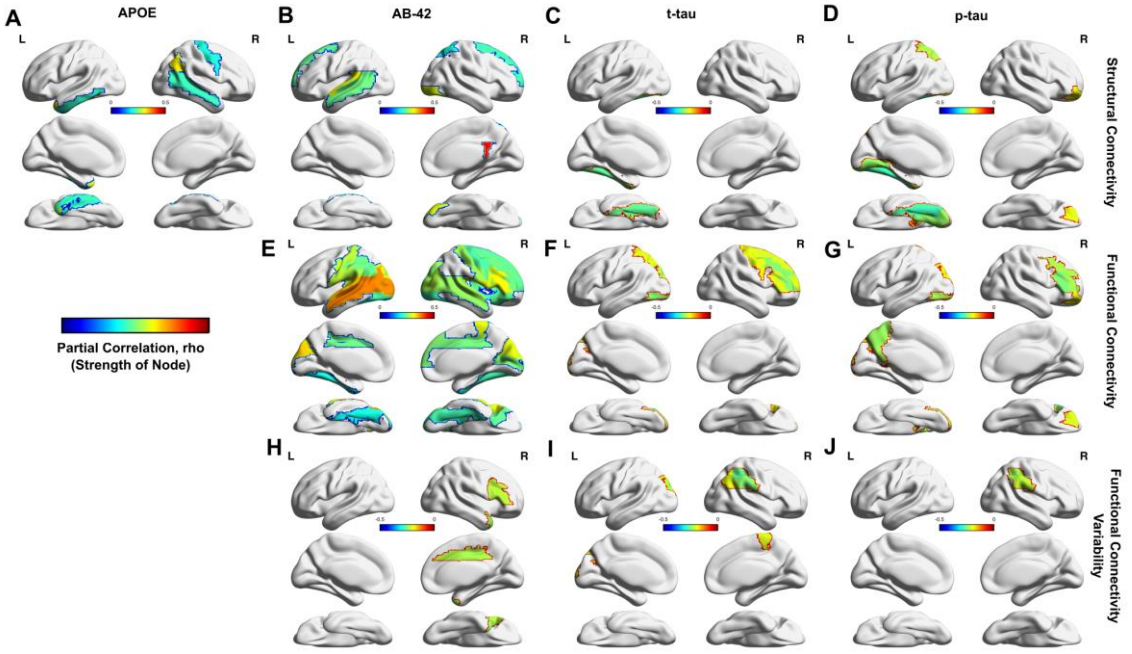

Figure VI.6. Relationship between FC, SC, and vFC strength with clinical indicators. A-D. Significant partial correlations between clinical indicators and SC strength. E-G. Significant partial correlations between clinical indicators and FC strength. H-J. Significant partial correlations between clinical indicators and vFC strength. The partial correlations were controlled for age, gender, and education level.

VI.III.v . Estimation of Whole-Brain Effective Connectivity

First, we found the optimal effective connectivity that minimizes the distance between empirical and simulated FC. We repeated the optimization procedure for different global coupling parameter values ranging between -0.1 to 0.1. We found the best fit at a = -0.05 for most of the subject, no significant difference observed between groups (Figure VI.7A). Then we compared the empirical and simulated connectivity measures (Figure VI.7 B-C). We found a very high correlation between empirical and simulated coherence ($r = 0.93$, $p < 0.0001$) and metastability ($r = 0.72$, $p < 0.0001$).

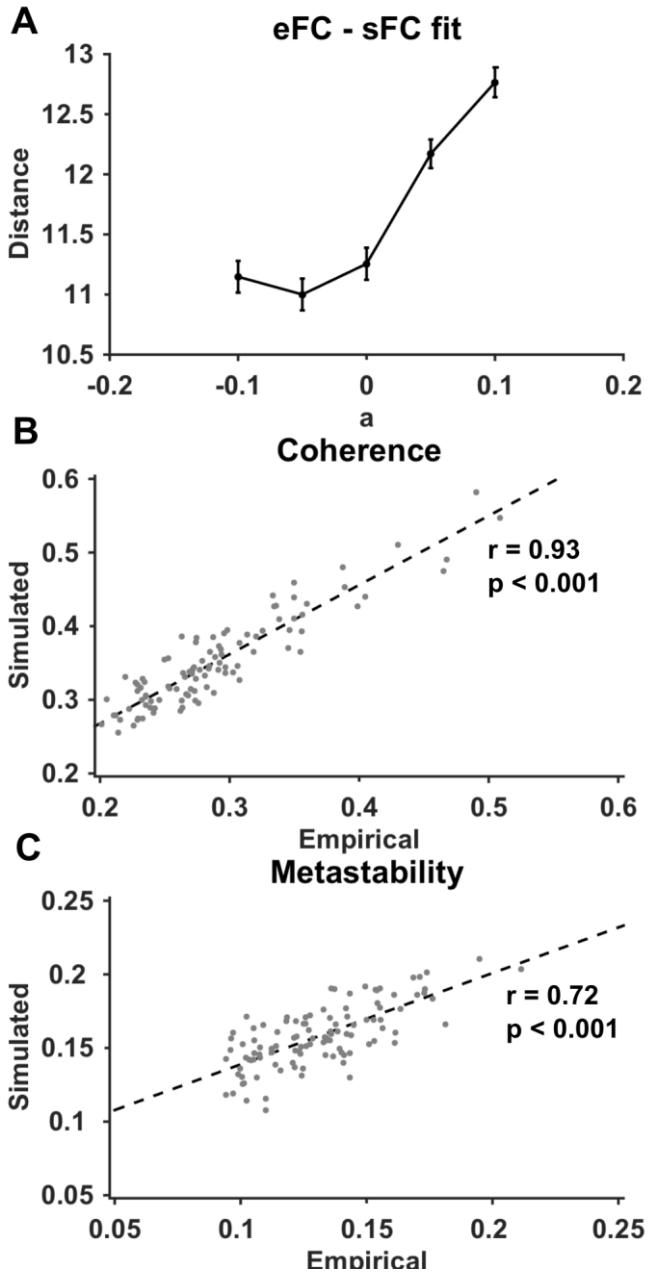

Figure VI.7. Simulation results. A. The average Euclidean distance between empirical and simulated FCs across bifurcation parameters. Errrorbars indicate SEM. B. Pearson's correlation coefficient between simulated and empirical coherence. C. Pearson's correlation coefficient between simulated and empirical metastability.

In a similar way for SC, FC, and v-FC, we compared significantly altered networks in EC using NBS. We found no significantly different networks between HC and PC groups. This result is interesting because it suggests that the differences observed in FC might be associated to the alterations in variability. In contrast, we found increased and

decreased connected networks in AD groups compared to HC group (Figure VI.8). In contrast to the impaired network observed in FC of AD group, we found that the core of the alteration was shifted to the interhemispheric connections of the temporal lobe (superior, medial, and inferior temporal gyri, temporal pole, Heschl gyrus, and fusiform gyrus). Furthermore, in right hemisphere the altered network was extending towards orbital frontal regions similar to the FC alterations in PC group (Figure VI.8A). The increased EC networks showed very similar patterns with the increased FC networks in AD. However, EC revealed the asymmetries in the network (Figure VI.8B). We showed that the increases in right angular gyrus EC was mostly in the incoming connections towards this region. In contrast, right inferior parietal lobe EC increase was in the outgoing connections. Moreover, the increased network extended towards frontal regions in EC case.

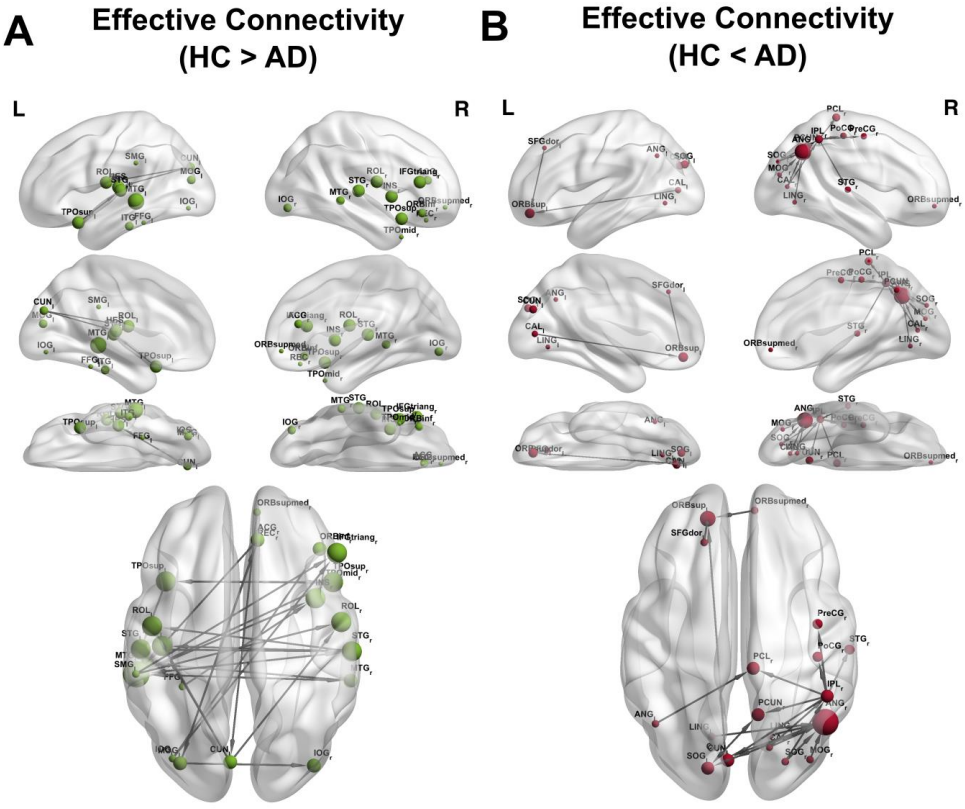

Figure VI.8. Significantly altered EC networks in Alzheimer's disease (AD) group compared to HCs. A. Decreased EC in AD. B. Increased EC in AD. The comparisons were done in NBS (permutation t-test, 5000 permutation, p-value < 0.05), adjusted connected components threshold to report top 1-2% of the connections. Green nodes indicate HCs have higher values, red nodes indicate ADs have higher values.

Finally, we compared the joint strength and asymmetry index between HC groups and PC and AD groups (Figure VI.9). We found decreased joint strength in temporal lobe and angular gyrus of AD group (Figure VI.9A), and abnormal asymmetry patterns in frontal and parietal regions (Figure VI.9B). In contrast, we found that the joint strength of left hippocampus was significantly lower in PC group (Figure VI.9C) and the asymmetry index of right posterior cingulate was shifted towards low output/high input (Figure VI.9D).

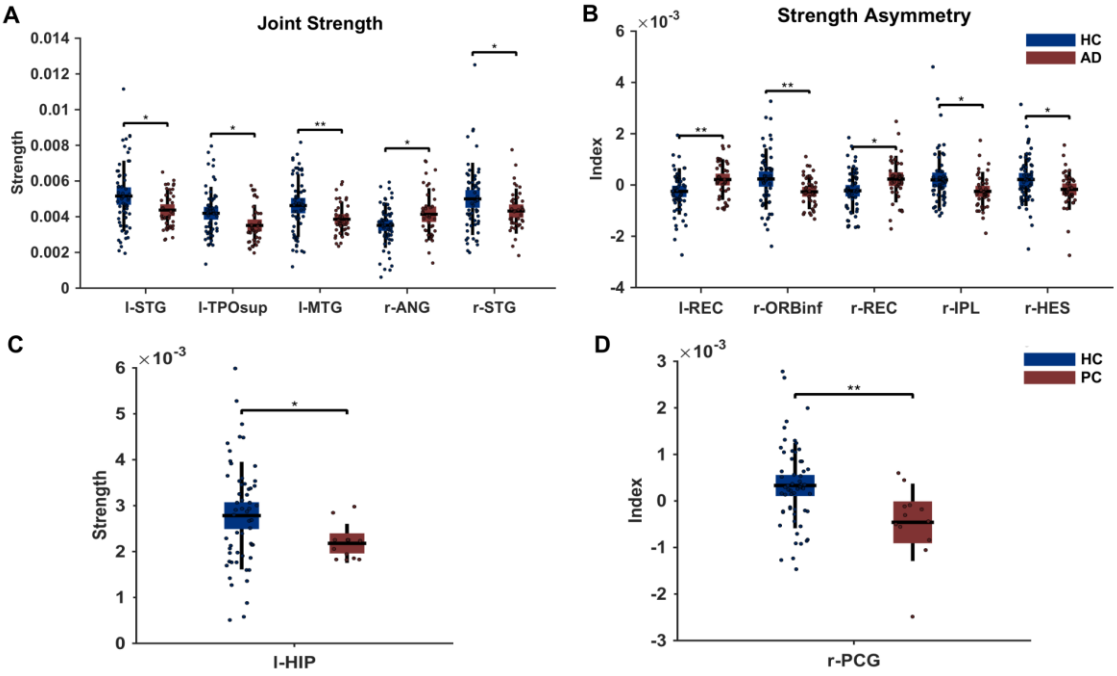

Figure VI.9. Joint strength and asymmetry index group comparisons between HC and PC and AD groups. A. Significantly different joint strengths in AD. B. Significantly different strength asymmetry indices in AD. C. Significantly different joint strengths in PC. B. Significantly different strength asymmetry indices in PC. Blue indicates healthy controls, red indicates clinical populations. The comparisons were done using permutation t-test (1000 permutations), corrected for multiple comparisons using FDR.

In order to refine the analysis, we compared the nodal metrics of inferred effective connectivity. First, we check the relationship between the biomarkers and the asymmetry index of the nodes defined by the difference between out- and in-strenght of each region (Figure VI.10). The effect was particularly higher in parietal and frontal regions. Furthermore, the asymmetry index of temporal regions and cingulate was correlated with APOE, anterior cingulate with Aβ-42. We found significant correlation between t-tau

and p-tau and rectus gyrus.

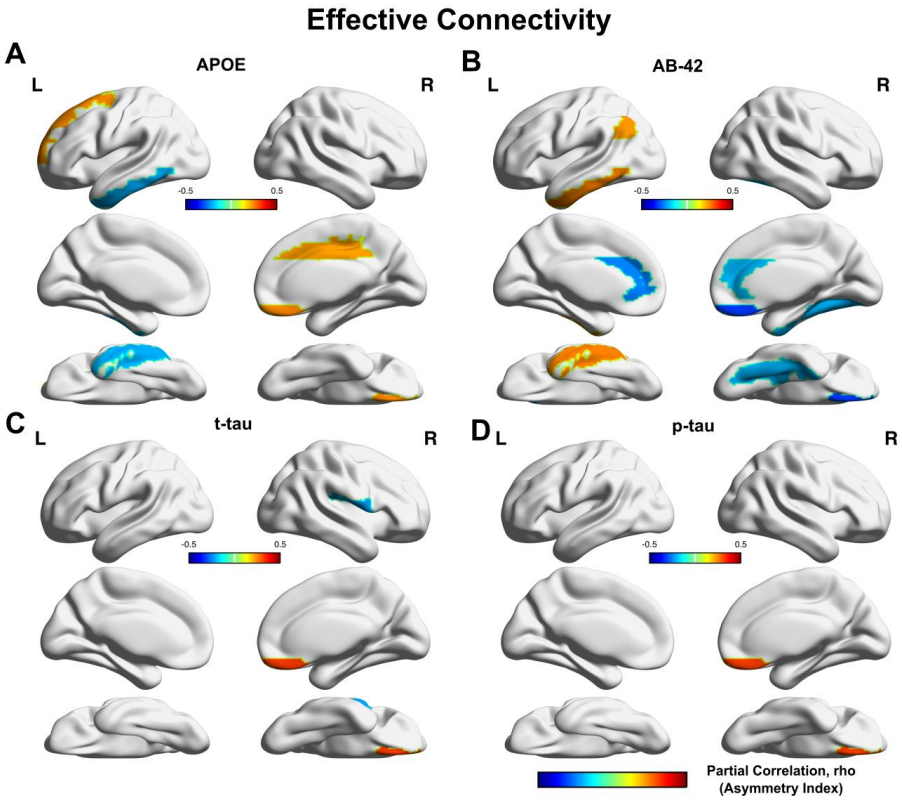

Figure VI.10. Relationship between strength asymmetry index of EC and biomarkers. Strength asymmetry index refers to the difference between out-strength and in-strength of a given node. A. APOE. B. AB-42. C. t-tau. D. p-tau. The partial correlations were controlled for age, gender, and education level.

VI.III.vi . Computational Modeling of the Altered FC Dynamics

In order to provide a complete mechanistic model, we used the proposed computational model to artificially disrupt the whole-brain dynamics in healthy controls. Given the estimated EC of the healthy controls, we simulated the entire dynamics with decreasing bifurcation parameter (a). As a reference, we computed the simulated FC and vFC at the optimal bifurcation point (i.e. $a = -0.05$) for each subject. Then, iteratively we decreased the bifurcation parameter by 0.001, spanning the values between -0.05 and -0.15. The purpose of this experiment was to identify the effect of noise in whole-brain dynamics. Bifurcation parameter values that are close to zero indicate that the whole-brain is operating near a critical point, in which the metastability of the system is max-

imized. As the negativity in bifurcation parameter increases, the system shifts to a regime where the dynamics are shaped by noise. Being specific, we hypothesized that the atrophy in brain regions in AD would eventually cause inefficient whole-brain coordination in the brain, and that his might be quantified as the level of divergence from the critical point.

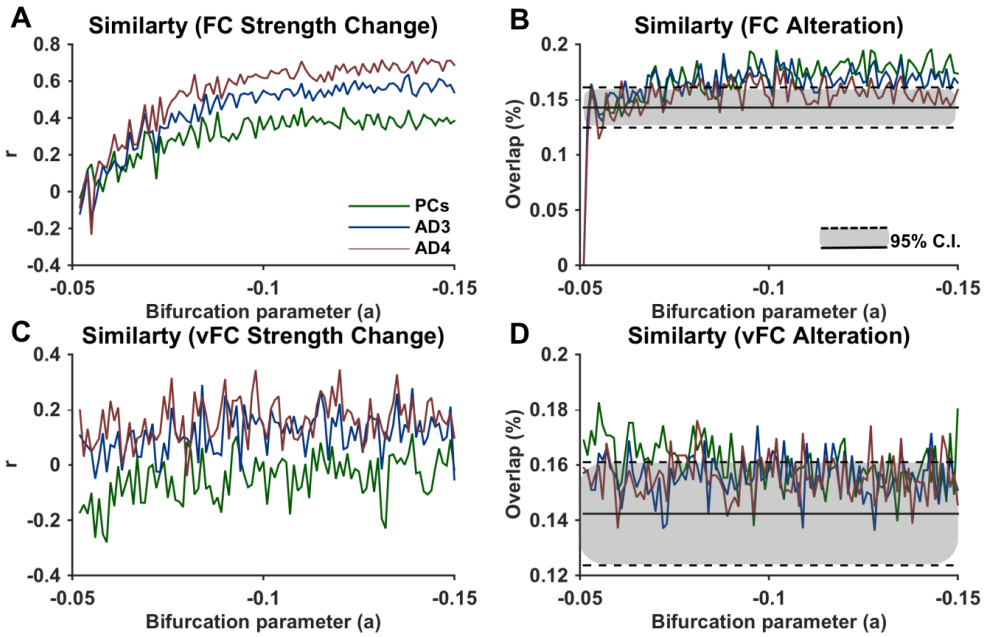

Figure VI.11. Model alterations in FC and vFC in healthy controls. A. Similarity between predicted and empirical changes in FC strength (Pearson's correlation coefficient). B. Similarity (overlap) between top 25% predicted and empirical changes in FC (Jaccard similarity). B. Similarity between predicted and empirical changes in variability of FC strength (Pearson's correlation coefficient). B. Similarity (overlap) between top 25% predicted and empirical changes in variability of FC (Jaccard similarity). Green lines indicate PC, blue lines indicate GDS-3, red lines indicate GDS-4. Gray shaded region and dashed lines indicate 95% confidence interval for the Jaccard similarities of surrogate networks with the same sparseness.

First, we computed the predicted alterations in FC and vFC (both in link and nodal scale) using the model. To compute the predicted alterations, we computed the changes in connectivity with respect to the reference point ($a = -0.05$). Then, we compared these changes to the ones that were observed in the empirical data (i.e. the differences between the connectivity in PC, GDS-3, GDS-4 groups and healthy controls). The similarity (Pearson's correlation coefficient) between predicted and empirical changes in strength of FC was increasing as the bifurcation parameter moved away from the criti-

cal point for all groups (Figure VI.11A). The maximum similarity reached r = 0.46, r = 0.64, and r = 0.72 for PC, GDS-3, and GDS-4 groups respectively. Regarding the strength of variability in FC of each node, the similarity was stable across the range (r = 0.11 for PC; r = 0.29 for GDS-3; r = 0.35 for GDS-4). Moreover, change of vFC strength in PC group also showed negative correlations with the empirical data (max r = -0.28).

We compared the overlap between predicted and empirical FC and vFC alterations in link level; we computed the Jaccard similarity (1 – overlap percentage) between the binarized alteration matrices. We defined the threshold to provide top 25% of the decreased connections in each domain. For statistical interpretation, we computed the Jaccard similarity of 1000 random surrogates (2000 matrices in total) with the same sparseness. Average Jaccard similarity for the surrogates was 0.14%, and 95% confidence interval was between 0.12 and 0.16. Similarly, we found that the overlap between highest 25% decrease in predicted and empirical FCs was increasing with decreasing bifurcation parameter, far above the 95% confidence interval (Figure VI.11B). The maximum overlaps were estimated as J = 0.20, J = 19, and J = 0.18 for PC, GDS-3, and GDS-4 groups, respectively. The similarities in vFC alterations were also higher than chance level, but stable over the parameter range (J = 0.18 for PCs; J = 0.17 for GDS-3; J = 0.8 for GDS-4) (Figure VI.11D).

Finally, we compared the alterations in the FC networks statistically between simulated FCs of the healthy subjects within the bifurcation parameter range (Table VI.3). First, we check the probability of increase in FC and vFC strength for the bifurcation parameter range (Figure VI.12A). We found that the probability of increased FC and vFC initially rises with decreasing bifurcation parameter, but then decays as the system shifts towards increased noise. The decay was much faster for FC, than vFC. We also compared the differences in FC networks at a = -0.06 and a = -0.1, with respect to the reference point a = -0.05 using NBS approach. A slight drop in bifurcation parameter caused widespread decreases in the cortex, however, the decreases were more pronounced between fronto-temporal and parietal-occipital regions, suggesting an anterior-posterior disconnection (Figure VI.12-top). On the other hand, the increases in FC were also sig-

nificant (Figure VI.12-bottom). In right hemisphere, we found significantly increased FC between hippocampus-inferior temporal gyrus and rectus-supplementary motor area. Rectus, superior frontal gyrus and supramarginal gyrus connectivity was also increased. Within right hemisphere, we found increased connectivity in posterior cingulate with central regions, dorsal cingulate, temporal pole and medial frontal gyrus. When the system moved further away from the critical point (a = -0.1), the significant increases disappeared. Furthermore, although the anterior-posterior disconnection pattern was evident, the core of the alterations was shifted towards orbital frontal cortex (Figure VI.12C). In addition, the alterations within Default Mode Network (DMN) related regions became more pronounces (posterior cingulate, precuneus, hippocampus…etc.). Third, the interhemispheric connections of posterior regions were also decreased.

Table VI.3. Highest 10 Alterations in Model FC

FC alteration (a = - 0.06)				FC alteration (a = - 0.1)			
Increased FC				Increased FC			
ROI-1	ROI-2	T-statistic	p-value	ROI-1	ROI-2	T-statistic	p-value
r-OLF	l-MFG	7.55	<0.001	r-MOG	l-PCG	15.18	<0.001
r-HIP	r-ORBsupmed	7.46	<0.001	l-LING	l-ORBmid	15.14	<0.001
r-HIP	l-MFG	7.36	<0.001	r-HIP	l-OLF	14.97	<0.001
r-SPG	r-REC	7.32	<0.001	r-PCUN	l-OLF	14.69	<0.001
r-SMG	l-TPOmid	7.10	<0.001	l-IFGtriang	l-ORBmid	14.45	<0.001
r-FFG	l-ANG	7.04	<0.001	l-TPOmid	l-SOG	14.19	<0.001
l-TPOmid	l-SMG	6.95	<0.001	r-PCG	l-OLF	14.15	<0.001
r-SPG	l-ORBsupmed	6.90	<0.001	r-SPG	l-IFGtriang	14.09	<0.001
l-IFGtriang	l-ORBmid	6.83	<0.001	l-ROL	l-ORBsup	14.04	<0.001
r-IPL	r-REC	6.79	<0.001	r-ORBsup	l-SMA	13.83	<0.001
Decreased FC							
ROI-1	ROI-2	T-statistic	p-value				
l-ITG	l-SMA	-6.41	<0.001				
r-TPOsup	r-PCG	-4.50	<0.001				
l-HIP	l-REC	-4.49	<0.001				
r-PCG	r-MFG	-4.29	<0.001				
r-PoCG	l-TPOmid	-4.11	<0.001				
l-IPL	l-IFGoperc	-4.00	<0.001				
r-PCG	r-DCG	-3.96	<0.001				
r-PreCG	l-ITG	-3.77	<0.001				
r-ITG	l-TPOmid	-3.72	<0.001				
l-SPG	l-SFGdor	-3.67	<0.001				

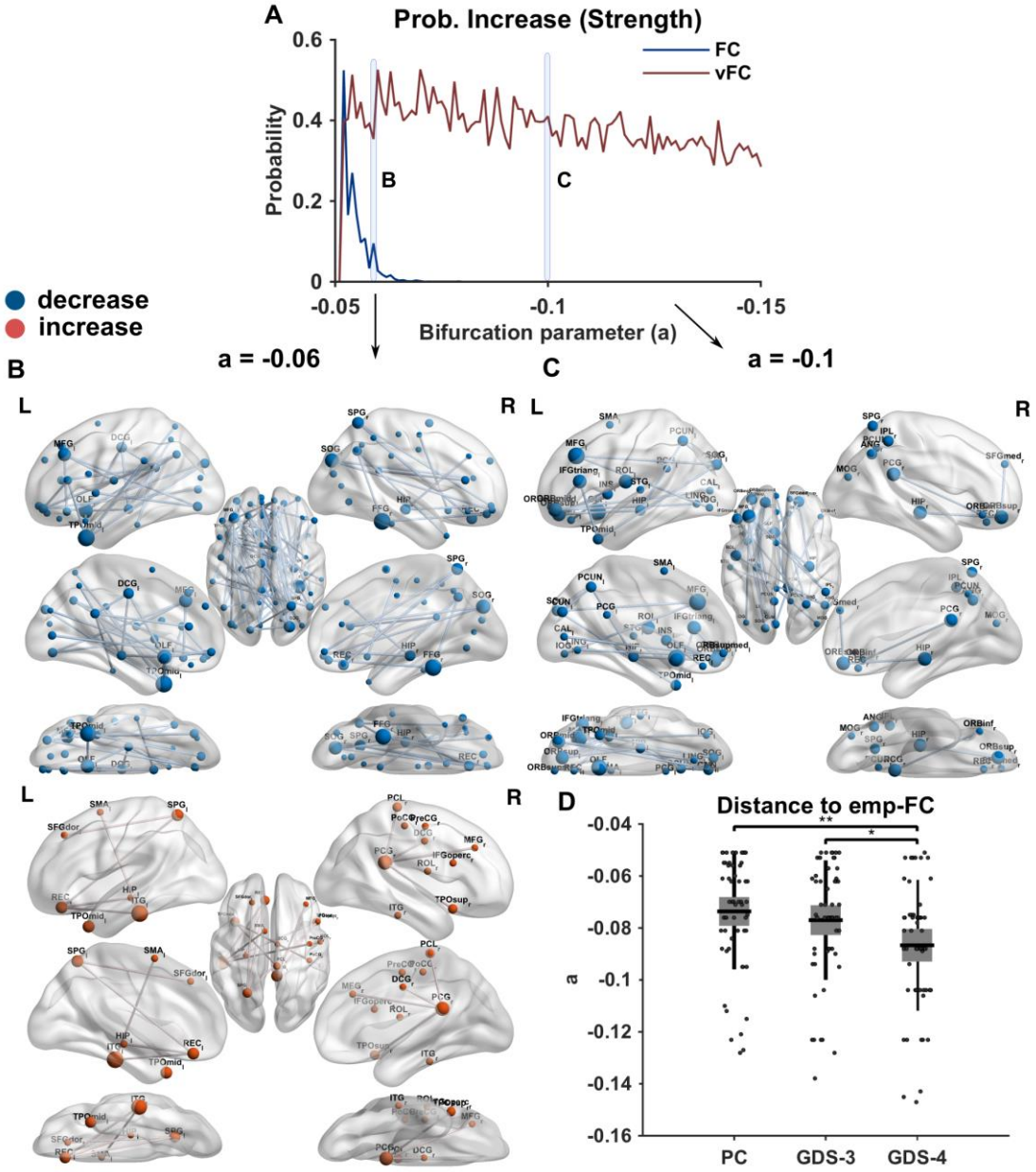

Figure VI.12. A. Probability of increase in FC strength (blue) and variability of FC strength (red). B. Significantly decreased (top) and increased (bottom) FC networks at a = -0.06. C. Significantly decreased FC networks at a = -0.1. Network comparisons were done in NBS (permutation t-test, 5000 permutation, p-value < 0.05). D. Comparisons between the bifurcation parameters in which the distance between average empirical FCs of each clinical group and disrupted FCs are minimal. Comparisons were done using permutation t-test (10000 permutations).

We also measured how the disrupted FC of healthy controls match to the empirical FCs of clinical populations. We computed the Euclidean distance between the simulated FC of each control and average FC of the PC, GDS-3, and GDS-4 groups within the bifurcation parameter range. Then, we compared the distributions of the bifurcation parame-

ter in which the minimum distance to each clinical population was observed. We found no significant differences between PC and GDS-3 groups, but GDS-4 group showed significantly more negative bifurcation parameter than PC and GDS-3 groups (Figure VI.12D).

VI.IV. Discussion

In this paper, we studied the connectivity of AD patients (along with the preclinical subjects) in multiple spatial and temporal modalities. In global level, we used the synchronization measures based on instantaneous phases of BOLD signals. We found differences across groups in coherence (synchronization index) and metastability (variability in global synchronization). Moreover, the power of these differences was increasing with the severity of the disease (but not for preclinical group).

The partial correlations between biomarkers and these measures suggested different role of each biomarkers in the global connectivity dynamics. We found that amyloid-beta (Aβ-42) was significant associated with the coherence. On the other hand, tau tangles were associated with the metastability. When we limited the analysis for only clinical and preclinical subjects, we found no significant correlations between coherence and biomarkers, but we still observed the significant correlations between metastability and tau tangles (t-tau: rho = -0.3, p = 0.04; p-tau: rho = -0.35, p = 0.02). These results show that accumulation of amyloid plaques is associated to the global decrease in connectivity, but it might not have a role in the progression of the disease. On the other hand, tau pathology is linked to the alterations in the richness of dynamic repertoire of the brain. This is consistent with the recent findings that although amyloid-β has a major impact on the neurodegeneration, it is functionally less relevant than tau tangles (Yoshiyama et al., 2013). Furthermore, based on these results we claim that metastability might a more robust measure that reflects the cognitive function of the brain (Deco and Kringelbach, 2014).

We also compared the association between connectivity strengths of the regions and the relevant biomarkers. We found that all biomarkers (Aβ-42, t-tau and p-tau) and the

number of APOE E4 alleles were significantly associated with the structural connectivity strength in temporal lobes, with some extensions towards fronto-parietal regions. One important distinction was that APOE and Aβ-42 was associated with the lateral parts of temporal lobes, while t-tau and p-tau was associated with the mid-inferior parts of the temporal lobes. Furthermore, Aβ-42 showed particularly high correlation with the SC strength in posterior cingulate cortex. This is consistent with the studies that investigate the spatial deposition of these biomarkers (Yoshiyama et al., 2013)(Figure VI.13). Functional connectivity measures did not show any correlations with APOE, and the biomarker-related changes in both FC and vFC strengths were spread towards frontal and posterior parts of the brain. Similarly, Aβ-42 showed widespread associations with the strength of static FC. The asymmetries in inferred EC showed correlations between cingulate cortex and APOE and Aβ-42. The asymmetry in rectus gyrus was consistently correlated with all biomarkers.

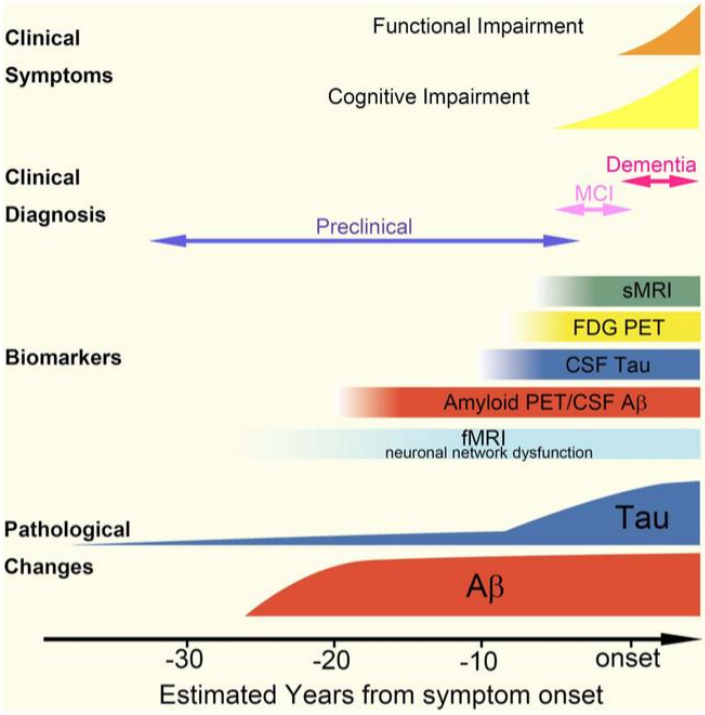

Figure VI.13. Relationship between biomarkers (amyloid beta and tau) and functional impairment. (adapted from Yoshiyama et al., 2012).

We also analyzed the group differences in the networks (structural, functional and model-based) between healthy control group, and PC and AD groups. Consistent with the

previous studies, we found disconnection between anterior and posterior parts of the brain in both PC and AD groups. Moreover, we found an increased FC in a cluster of parietal regions in AD patients. Although the differences observed in PC and AD groups were consistent compared to each other, variability of FC alterations suggested entirely different mechanism underlying these changes. We found no significantly different vFC networks between HC and AD groups. However, the variability in FC in PC group was significantly increased among the regions that contributed to the decreases in static FC. The difference between the alterations in FC and vFC of PC group was that the unstable networks had more power in temporal and parietal regions. We also check how the variability in FC is related to the global connectivity measures. We found that the variability strength in three regions was associated to coherence and metastability of the FC dynamics: Inferior orbital frontal (negative), hippocampus, and precentral gyrus (positive). Compared to the healthy controls, the variability strength in left hippocampus was increased (with no significance) in PC group, and then dropped sharply with the deterioration scale of the AD patients. We believe that this finding might have important implications in understanding the progression of Alzheimer's disease. Aβ-42 related neurodegeneration might cause instabilities in the FC dynamics, although the structural consequences of the neuron loss do not necessarily lead to cognitive impairment. The early role of Aβ in neurodegeneration without AD was recently discussed (Musiek and Holtzman, 2015). Our study showed that the neuronal basis of the transition between neurodegeneration and cognitive impairment might be understood by investigating the abnormalities in FC dynamics.

We supported our hypothesis using a computational model based on supercritical Hopf bifurcation. We inferred the whole-brain EC that gave rise to the observed rs-BOLD signals by minimizing the distance between empirical and simulated FCs. The heuristics also considered the time-lagged FC to ensure the uniqueness of the solution and to infer directed connectivity structure. The simulations successfully replicated the global connectivity patterns observed in the empirical data. When we compared the EC networks between groups, we found no differences between HC and PC groups. In contrast, AD group showed significant alterations in EC. In nodal level, however, PC group showed significant decrease in left hippocampus EC strength, and abnormal asymmetry in right

posterior cingulate cortex. These results also suggested that the origins of the differences observed in preclinical FC were temporal, nor spatial.

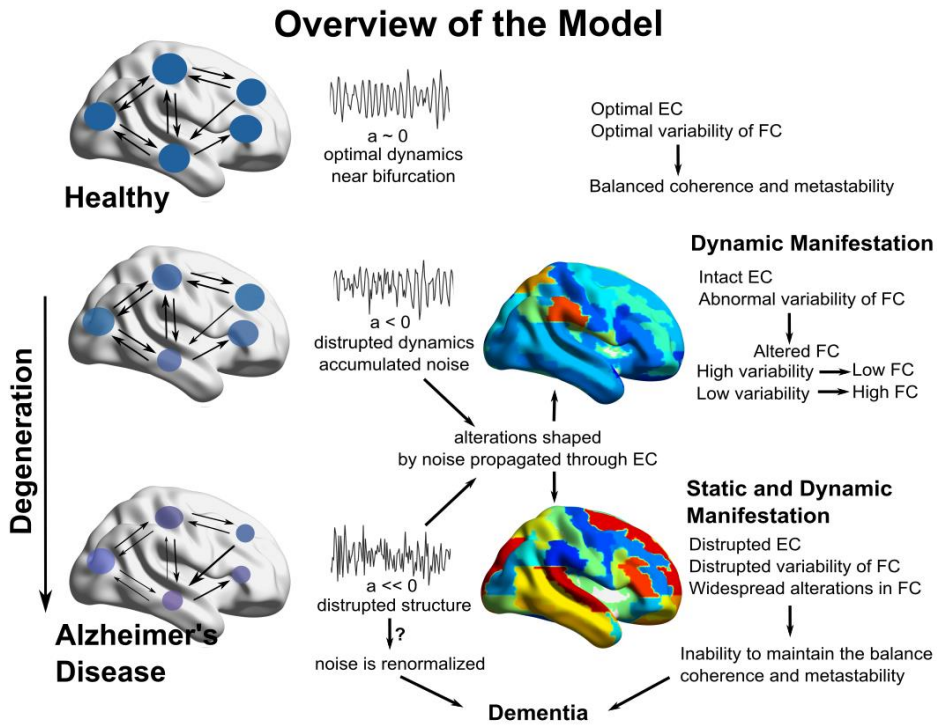

Figure VI.14. Overview of the model. Top panel: Healthy function of the brain. Middle panel: The initial consequences of atrophy (mild Alzheimer's disease). Bottom panel: The advancement of the disease.

Finally, we designed a computational experiment based on the inferred ECs of healthy control subjects. We gradually altered the bifurcation parameter in the Hopf Normal Model to obtain a noise driven regime due to the divergence from the critical point. Intriguingly, we found that the alterations in FC and vFC in the model was highly consistent with the empirical observations. Furthermore, the bifurcation parameter where the minimum proximity between disrupted HCs and severe AD group observed was significantly different that that for PC and milder AD groups.

The disrupted simulated FC of healthy controls also showed significantly increased connected between various regions, particularly the increased FC between fronto-parietal regions and inferior temporal lobe as well as posterior cingulate is similar to the observed differences in the literature. Interestingly, the noise induced increased-FC effect was disappeared as the bifurcation parameter diverged from the critical point. We

speculate that the local disconnections might be less relevant in the neuropathology of Alzheimer's disease. Instead, the disease might be related to the accumulation of simultaneous impairments through the propagation of noise in whole-brain level (Figure VI.14).

The model results also raised some questions. First, the model suggested that although the empirical FC dynamics of PC and AD groups were different, they might be considered as a part of the spectrum with respect to noise induced whole-brain dysfunction. Second, the similarity between model and empirical alterations was higher in AD group (especially for more severe group). Third, the model performed very poor at capturing the alterations in vFC of the PC group. Overall this might indicate a non-trivial compensation mechanism for neurodegeneration in preclinical individuals. In other words, we speculate that at this stage the outcome of the neuronal atrophy might be determined by peripheral mechanisms (e.g. involvement of neurotransmitters, non-neuronal cells…etc.) that modulate the temporal aspects of the connectivity. This is consistent with the previous studies that suggest amyloid associated abnormal DMN connectivity in elders without dementia (Yvette I. Sheline et al., 2010; Sperling et al., 2009). Another explanation might be found in other biological factors that define the vulnerability of some individuals to neurodegeneration-induced dementia. Being specific, the current hypotheses of Alzheimer's disease could be seen as an indicator of a chronic condition, which might or might not manifest itself as cognitive dysfunction. We suggest that future attempts to tackle AD should focus on the neuronal mechanisms behind dementia seperately. These proposed mechanisms, however, might be complex, and they might be beyond the scope of the current computational models.

VII. Discussion

"Essentially, all models are wrong, but some are useful"

Box and Draper, 1987

The current status of the research on resting-state fMRI and its clinical applications was briefly introduced in Chapter I. Following the discovery of temporal correlations in spontaneous neuronal fluctuations and associated resting-state networks, resting-state fMRI became one a central theme in the neuroscience community. Immediately, the clinical applications of rs-fMRI dominated the field. However, most of these studies were criticized as being exploratory and providing misleading *post-hoc* conclusions about the underlying neural mechanisms. Moreover, relatively recent findings on the non-stationary nature of spontaneous fluctuations have offered more questions than answers. Crucially, they are problematic because they are incomplete theoretical models that postulate how the spatiotemporal connectivity patterns arise.

We, in our study, endeavored to fill the gap between connectivity structure and functional relationship in the context of clinical disorders. First, we investigated the altered patterns in dynamic functional connectivity (dFC) in various clinical populations. We characterized the dynamic FC at the levels of global and local connectivity. As a global measure for FC dynamics, we used the first- and second-order statistics of the Kuramoto order parameter (i.e., coherence and metastability). Additionally, in Chapter III (Major Depressive Disorder) we introduced alternative measures such as inter-temporal closeness to quantify the richness of dynamic repertoire. On the local scale, we introduced the use of variability of FC (vFC) that quantified how an individual connection varied over time. We showed that dynamic FC provides a different perspective from which to understand the disease-related alterations in connectivity. Secondly, we went beyond exploratory analyses to propose various models for the inference of whole-brain EC from observed rs-fMRI BOLD signals. We showed that studying whole-brain EC is crucial for proposing mechanistic models that underlie clinical populations.

Chapter III introduced an exploratory study that used global and local measures of dFC investigating the richness of the dynamic repertoire in depressive patients. We showed that the stability of global functional states acquired by dynamic FC might quantify the restricted dynamic repertoire of brain states in major depressive disorder (MDD). Furthermore, we found that the variability of FC over time manifested distinct patterns of altered connectivity (in MDD patients) than the grand-average FC. For example, we observed that the restricted dynamic repertoire in MDD was accompanied by whole-brain hyper-synchronization, which affects mostly the regions associated with the default mode network (DMN). This result can be considered trivial because alterations in DMN connectivity are ubiquitous and observed in many other clinical conditions (see Chapter I). However, extensive spatiotemporal analysis of the data revealed that the hyper-synchronized activity in DMN was coupled with diminished variability in fronto-parietal control networks. This finding is important, given the implication that there might be non-trivial complex mechanisms underlying temporal correlations between regions, which shows similar manifestations despite having distinct origins.

We explored the effective connectivity (EC) between regions through computational modeling in order to reveal the origins of the alterations of FC in mental disorders. In Chapter IV we proposed a basic model relying on a simple autoregressive model with a multiplicative correlated noise component. Having this, we reliably inferred the whole-brain EC using an efficient heuristic (i.e., evolutionary) algorithm. The algorithm allowed us to infer optimal weights and directionality of the existing anatomical links. We implemented this method using a small sample of patients with Bipolar Disorder and healthy controls. The exploratory analysis showed patterns that were reminiscent of Chapter III, although in this case we found widespread decreases in FC with associated increases in the variability of FC. As expected, the affected regions were related to DMN. However, the inferred EC revealed possible origins of these alterations, namely decreased feedback connectivity from prefrontal brain regions to DMN and increased feed-forward involvement of limbic brain regions. Furthermore, counter-intuitively, the simulations using the linear autoregressive model based on inferred EC manifested many higher-order properties of the observed BOLD signals (such as coherence and metastability, principal components and variability of FC). The most important conse-

quences of these findings are as follows: First, whole-brain EC can provide a mechanistic explanation for abnormal connectivity in clinical conditions. Secondly, consistent with Chapter III, the origins of the alterations that are observed in FC are non-trivial (decreased FC might be associated with increased EC in distinct brain regions). Thirdly, in the absence of nonlinear influences, the causal interactions between brain regions might account for observed complex spatiotemporal patterns.

We also proposed nonlinear models to infer EC from FC. First, we used the Kuramoto model to characterize connectivity patterns in newborns and infants with intrauterine growth restriction (IUGR). This model comprised direct simulations of BOLD signals via coupled oscillators. The crucial difference of the model was that we characterized the FC between regions entirely on temporal evolution of the phase couplings between brain regions. We combined the dynamic FC approach based on Hilbert transform (as presented in Chapter III) and the whole-brain EC inference by computational modeling presented in Chapter IV. This way, we directly related the spatiotemporal characteristics of instantaneous phases in empirical data and the computational model. We showed hyper-synchronized networks in newborns with IUGR. As also discussed in Chapter III and Chapter IV, the hyper-synchronized networks were associated with distinct but overlapped networks having decreased variability in synchronization. These networks were generally related to orbital parts of the prefrontal cortex and subcortical regions. We found no significant connectivity alterations in infants with IUGR. The ECs, on the other hand, revealed completely different patterns. First, we found that the hyper-synchronized activity in newborns with IUGR was related to the decrease of EC between the previously found regions and the regions associated with DMN. These findings also illustrate that EC can provide mechanistic explanations by revealing distinct networks that might modulate the altered network in the observed data (i.e., underdeveloped DMN causing hyper-synchronized coupling between the prefrontal cortex and subcortical regions). Moreover, in this case the result was even more interesting because the hyper-synchronized (increased connectivity) was associated with decreases in underlying EC. Second important finding of this project was that unlike the empirical connectivity, EC revealed alterations in infants with IUGR. Given that the alteration found in infants with IUGR was partially overlapping with those in newborns and the fact that

the effects were reversed (i.e., increased EC), the results were particularly exciting. The results not only showed that EC might reveal obscured altered connectivity in empirical data, but also provide clinically useful information (e.g., possible developmental consequences of decreased EC in neonatal DMN).

Finally, in Chapter VI we studied the dynamic FC and EC of the patients with Alzheimer's Disease. Following the comparisons between whole-brain static and dynamics FC, we used normal form of supercritical Hopf bifurcation to infer EC from BOLD signals of the subjects. The study comprised Alzheimer's patients with different severity, and healthy and preclinical control subjects. We found partially overlapping networks with decreased FC in both preclinical and AD groups compared to healthy controls. AD patients also showed increased FC in highly clustered local networks. In brief, these differences suggested anterior-posterior disconnection associated with AD consistent with the previous literature. However, when we compared the variability of FC we only found increased FC variability in preclinical individuals with respect to HC subjects. Furthermore, we found that static and dynamic measures were related to distinct biomarkers, while the variability strength in key regions for AD (such as hippocampus) was associated with global connectivity measures (such as metastability). This raised the possibility that the progression of Alzheimer's Disease might follow a course that comprises the decoupling of brain regions due to increased noise, ultimately leading to dramatic loss in global functional integration. Fortunately, the model allowed us to test this hypothesis. Instead of proposing a lesion-based predictive model, we altered the bifurcation parameters of healthy control subjects in such a way that the local dynamics diverged from the critical point, giving rise to a noise-dominated regime. We argued that such a modification might mimic the impaired local activity due to neurodegeneration in the whole brain. We showed that as the simulated brain activity of healthy controls shifted toward noise, it manifested similar functional connectivity changes as observed in preclinical individuals and AD patients. Furthermore, the similarity of the artificially disrupted FCs of healthy controls showed patterns consistent with the severity of the disease (i.e., the optimal similarity was observed for more negative bifurcation parameters for severe AD than for milder ones and preclinicals). Finally, we demonstrated that the proposed mechanism might also account for the increased FC observed in AD.

In summary, we showed that exploration of dynamic FC (e.g., variability) and model-based estimation of whole-brain EC might respond to the current problems in resting-state fMRI research. Particularly, the two approaches can potentially provide information beyond conventional analysis techniques, and they might offer mechanistic explanations for mental disorders. However, it should be noted that the techniques presented in this thesis have limitations. The first limitation stems from the methodological concerns on fMRI. BOLD signals are not perfect representations of the neuronal activity because they are indirect measures that have limited temporal resolution and are confounded by various sources of physiological and mechanical noise. The second limitation, particularly regarding computational modeling, is that the current computing technology does not offer sufficient computational power to estimate whole-brain EC reliably. Despite the fact that they are reasonably successful, we believe the optimization procedures presented in this thesis are still suboptimal. Moreover, the validity of the approaches in this thesis requires further study involving verification of the methods through specific experimental studies (such as multimodal electrophysiological recordings). We believe that with the advancements in technology (regarding computing and neuroimaging), the approaches presented in this study can contribute to the emergence of novel and efficient techniques and ultimately help reveal the mysteries of the brain.

VII.I. What resting state tells about mental disorders?

In this thesis, we investigated the mechanistic principles behind mental disorders that can be revealed by resting-state fMRI. In this section, we discuss what resting-state fMRI tells about mental disorders. There is an extensive literature on alterations in structural and functional connectivity as well as other resting-state related measures such as amplitude of low-frequency fluctuations (ALFF) in clinical disorders. The most common interpretation of these alterations is increased/decreased communication between regions of the brain, being related to mental processes associated with the diseased condition. For example, in regard to mood disorders, researchers expect to find abnormal connections in the limbic regions related to emotion processing; or, in dementias (such as Alzheimer's Disease), the first suspect is hippocampus that is responsible for memories. This tendency stems from the established belief that neural correlates of mental disorders should reflect some sort of disconnection as it is observed in extraordinary clinical conditions (such as the historical cases introduced in Chapter I). As we already mentioned before, we believe that rare mental disorders have devastating consequences, but usually have relatively trivial causes. However, most of the prevalent diseases (such as major depression, Alzheimer's Disease, etc.) have complex, non-trivial mechanisms. This simple distinction has long been done in the field of genetics. The implication of this distinction is important because it changes the focus of the research. We argue that complex disorders should be treated as system malfunction syndromes, instead of disconnection syndromes. As we showed in four different clinical populations, the observed alterations in connectivity are often widespread. Presence of disconnection between several regions (as in lesion cases) is not enough to generate such widespread connectivity changes. In Chapter VI we illustrated how a simple alteration in whole-brain dynamics (such as noise) could give rise to complex patterns of increased/decreased in functional connectivity between various brain networks. Similarly, in all studies we found that the higher-order spatiotemporal measures (variability of FC, global coherence and metastability) were as informative conventional measures. Overall, these results suggest that underlying mechanisms of the complex disorders can only revealed by the effects of small deviations in dynamics on the entire system.

Related to the previous point, we claim that whole-brain connectivity patterns may play important role in discriminating different mental disorders. In Chapter II, we discussed how global connectivity patterns could classify brain activity at rest versus during task. We also demonstrated, in MDD patients, that whole brain FC of the patients could be separated from healthy controls without even concerning the details of the statistical comparisons. The recent research also supports this view.

Finally, resting-state fMRI signal not only comprises information regarding the functional links between two regions, but also reflects the dynamics of these links. We consistently found that in clinical conditions the grand average FC and variability of FC are altered in overlapped but distinct networks. This suggests that some mental disorders might have dynamic components as well as static components. For example, altered grand average FC in a network might be associated with abnormal variability of FC in another network. Revealing the disease specific mechanisms behind the interactions between static and dynamic FC features is beyond the scope of this thesis. However, we believe that our work might inspire novel applications in clinical neuroscience.

VII.II. What mental disorders tell about resting state?

We discussed what could we infer about mental disorders using resting-state experimental paradigm. Indeed, one of the ultimate goals of neuroscience is to understand the mechanisms behind mental disorders leading to medical practices that can treat these disorders effectively. Nevertheless, in neuroscience an observed phenomenon (such as resting-state fluctuations) can embrace as much unknowns as the question desired to be answered (such as mental disorders, consciousness…etc.). For this reason, we think that there is another side of our research question: What mental disorders can tell about resting-state fluctuations?

The abnormal connectivity reported by resting-state studies recurs in various clinical populations. Particularly, DMN and the regions associated with DMN are usually found altered. This suggests crucial role of DMN in mental processing. The well-studied research on structural and functional connectivity of the DMN showed that it contains highly central, hub regions. Anticevic et al., (2012) discussed the role of DMN suppression and its relationship with fronto-parietal control network in psychiatric disorders. In this thesis, we illustrated that multiple mechanisms may cause these abnormal connectivity in DMN. For example, we showed that, in MDD patients, restricted variability in fronto-parietal networks might cause insufficient perturbation in DMN leading to hypersynchronization. As another example, we showed that, in the context of Alzheimer's Disease, decreased whole-brain communication might lead to decreased FC in DMN.

We proposed several computational models to infer whole-brain EC from FC. However, evaluating the validity of whole-brain EC is not straightforward; it requires very well designed experiments to justify and interpret the results. Mental disorders allowed us to evaluate partially the validity of our approaches through the clinical relevance of the results. First, we found that EC is distinct from anatomical connectivity. Second, we showed that the directionality of EC is crucial to understand the dynamic fluctuations in FC. Finally, the results suggested that large-scale causal connectivity structure consists of projections to some medial brain regions (particularly DMN) from lateral parts of the

brain. This explains the findings that suggest propagation of BOLD signals from lateral to medial parts in the cortex observed in rats (Majeed et al., 2011).

Another important feature of resting state derives from the observations in dynamic FC. We found that the negative correlation between grand average FC and variability of FC in all dataset, although we also showed that this relationship weakened in bipolar disease patients. We believe that it is crucial to take into account the relationship between static and dynamic FC. As we mentioned before common interpretation of the increased/decreased FC is that the communication between regions increased or decreases. Our results showed that this interpretation is misleading. There are several scenarios that might be happening:

1. The link between two regions is intact, but the grand average FC is reduced due to increased variability of FC.
2. The link between two regions is intact, but the grand average FC is enhanced due to decreased variability of FC.
3. The link between two regions is impaired, but the grand average FC is compensated by the variability of FC.

Specifically, the intensity of grand average FC is not enough to explain the communication between two regions. It is important to note that this fact will eventually affect our judgments on healthy brain function. Presence of networks with increased FC does not necessarily mean that regions of this network are effectively exchanging information. In fact, a network of increased FC may indicate that the regions involved in this network might not be perturbed enough to manifest rich dynamic repertoire. Therefore, one must take into account the reasons behind the altered FC in order to draw conclusions on the functional relevance of this alteration.

VII.III. The future of resting-state studies

Our work proposed novel methods and findings to explore resting-state fMRI in clinical populations. We showed how dynamic FC and whole-brain EC estimation might contribute to the understanding of spontaneous fluctuations in clinical context. In this section, we discuss the implications of our works on future research.

VII.III.i . Predictive models for mental disorders

We discussed that several networks in the brain (particularly DMN) are more vulnerable to disease related alterations in resting-state FC. For this reason, the specificity and clinical utility of resting-state FC has been questioned. We proposed exploratory (dynamic FC) and mechanistic (EC estimation) approaches to overcome this problem. We showed that although widespread changes involving similar network has been observed in various disorders, dFC and EC might unveil distinct mechanisms causing these changes. However, possible mechanistic explanations need further verification.

Regarding dynamic FC, we believe that carefully designed electrophysiological experiments are needed to understand the interplay between static FC and variability of FC. To our knowledge there are no studies that directly address this issue. Simultaneous recordings of fMRI with high-temporal resolution techniques such as MEG, EEG, and LFP might be useful for the verification of our approaches. Furthermore, non-invasive stimulation techniques such as deep brain stimulation (DBS) and transmagnetic stimulation (TMS) are promising tools to study dynamic interactions between brain regions. We believe that our research might offer a framework to study how the spontaneous fluctuations in entire brain respond to external stimulation.

Model-based whole-brain EC estimation is a particularly interesting and promising approach. Being able to characterize the underlying causal interactions in the brain allows us to build a theoretical framework for the brain function. An example might be estimating the evolution of EC over time. Specifically, one can estimate the dynamic FC

with high temporal resolution (i.e., using Hilbert transform), the EC might be estimated for each functional state in time. The changes in causal structure of the links might provide interesting phenomena. For example, the some features of EC might be changing in spontaneous, gradual or periodic manners.

The models proposed in this paper suffered from the fact that the fMRI BOLD signals are indirect measures of brain activity. Omitting hemodynamic responses restricted the realism of the models, but this was compensated given the enhanced implications of the models (i.e., whole-brain EC). We note that brain research is not limited to fMRI, and there are whole sets of alternative techniques that can measure neuronal responses directly (such as MEG). Future applications might focus these techniques to provide deeper insights.

We already proposed two examples of predictive models in clinical context. In bipolar Disorder, we modified the global coupling strength and measured how fast/slow the functional connectivity responds to this modification. We showed that brain regions related to limbic processing and salience are more sensitive to global conductivity changes. This effect might provide novel perspectives to study addiction, pleasure, stress response and mood disorders. In contrast, the same analysis showed that sensory regions are resilient to the global changes in connectivity. Again, this might be useful as a means to understand how the brain organizes sensory inputs. The reactivity of certain networks might be relevant to clinical conditions such as schizophrenia. Recent studies already provide evidence for the relationship between ketamine induced connectivity alterations and mental disorders (Anticevic et al., 2015).

VII.III.ii . Biophysical models

In this thesis, we used three different computational models to simulate spontaneous fluctuations. All of these models were phenomenological in nature. We believe that simplified models are more useful given the enormous complexity of the research question. As the complexity of the model increased, the chance of capturing subtle features in the observed data decreases. Therefore, we argue that simple models can be consid-

ered as the first option before diving into deeper analyses. Furthermore, complex models are usually computationally expensive limiting the parameter space that can be explored. However, at some point the use of biophysically realistic models is essential to understand the brain dynamics.

We also considered using biophysically realistic whole-brain models in this thesis. Particularly, we focused on balanced dynamic mean-field (bDMF) model to simulate whole-brain activity. In Chapter I, we already introduced bDMF model. This model provided an efficient method to estimate the covariance matrices of the simulated time series. Nevertheless, dDMF model needs an additional heuristic approach in order to keep the system in spontaneous state (i.e., at 3 Hz firing rate attractor state). It is possible to modify the model to overcome this problem.

Given original implementation of (Wong and Wang, 2006) with the external noise current that drives the system, we approximated the steady-state solution using Monte-Carlo simulations. This method reduced the computation time dramatically. Then, we estimated the optimal inhibitory efficiency for a single node given some external input (representing the inputs from other populations). As a result, the optimal parameters that kept the system in balance (3 Hz firing rate) might be computed without computationally expensive heuristics. The purpose of improving the model was to include additional parameters into the model such as recurrent synaptic strengths and feed-forward inhibitory effective connectivity. We believe that exploring inhibitory EC and recurrent synaptic strength might be useful in clinical populations. For example, feedback and feed-forward inhibitory connections might be instrumental in disorders such as Parkinson's Disease, essential tremor and anxiety disorders.

Nevertheless, the model suffered from "curse of dimensionality" such that as the number of regions increased the correlation coefficient between regions reduced dramatically. Furthermore, the available optimization algorithms were computationally expensive given the complexity of the model. We believe that these problems can be easily solved in future studies. Improved and more specialized biophysical models might offer better and realistic understanding of mental disorders.

Appendix 1. Materials and Methods: MDD

Participants

Twenty-seven MDD patients were recruited from the Mood Disorders Unit of the University Hospital of Bellvitge. Eligible participants were adult outpatients with a primary diagnosis of MDD as assessed by the Structured Clinical Interview for DSM-IV Axis I Disorders - Clinician Version (SCID), as made by two senior psychiatrists who reached a consensus for each item. Upon inclusion, each patient had a Hamilton Depression Scale (HAM-D 17) score equal to or greater than 18 (see supplementary material). The exclusion criteria included the presence or history of other Axis I diagnoses, relevant medical or neurological disorders and an abnormal clinical MRI upon radiological inspection. Concurrently, a group of 27 healthy volunteers comparable in gender, age, handedness and years of education participated in the study. A complete medical interview was conducted with each prospective control subject in order to exclude anyone with relevant medical or neurological disorders, history of substance abuse and psychiatric illness. Each of the patients and control subjects submitted a written informed consent for participation in the study, such consent form having been approved by the Research and Ethics Committee of the University Hospital of Bellvitge.

fMRI Acquisition and Preprocessing

Image acquisition was accomplished with a 1.5 tesla Signa system (GE Healthcare, Milwaukee, WI, USA) equipped with an eight-channel phased-array head coil and single-shot echoplanar imaging (EPI) software. Functional sequences consisted of gradient-recalled acquisitions in the steady state (time of repetition [TR], 2,000 ms; time of echo [TE], 50 ms; pulse angle, 90º) within a 24-cm field of view, a 64 x 64-pixel matrix and a slice thickness of 4 mm (inter-slice gap, 1.5 mm). Twenty-two slices parallel to the anterior-posterior commissure line covered the entire brain. The sequence included four additional dummy volumes to facilitate the equilibrium of magnetization,

thus totaling 120 volumes per session. A high-resolution T1-weighted anatomical image was obtained for each subject using a three-dimensional fast spoiled gradient inversion-recovery prepared sequence with 130 contiguous slices in the axial plane (repetition time = 11.8ms, echo time = 4.2 ms and flip angle = 90º, within a 30-cm field of view, a 256x256 pixel matrix and a slice thickness of 1.2 mm).

Subsequent to inspection for the presence of artifacts, high-resolution T1-weighted anatomical images were pre-processed in accordance with a standard protocol involving tissue segmentation, normalization and smoothing. Image segmentation was performed by means of the "new segment" algorithm, as implemented in SPM8 (Wellcome Trust Centre for Neuroimaging, University College London, UK; http://www.fil.ion.ucl.ac.uk/spm/). Specifically, we obtained gray- and white-matter image segments from native-space MRIs, although we discarded the final output images from this pre-processing step and reserved the rigidly transformed versions for use in DARTEL normalization (Ashburner, 2007). Thus, with the "Create Templates" function, images were iteratively matched to a template generated from their own mean so that we could then generate a series of templates with increasing resolution. Subsequently, native-space gray- and white-matter images were registered to the highest resolution template within a highly dimensional, diffeomorphic framework. Spatially normalized tissue maps were then modulated by the Jacobian determinants derived from the corresponding flow-fields to restore volumetric information. Finally, images were smoothed with an 8mm full-width at half-maximum isotropic Gaussian kernel.

For each subject, all functional images were realigned to the first image in the series and re-sliced, and a mean functional image was created. Structural images were co-registered to the mean functional image and normalized to the original T1 space by means of the segmentation tool. Next, the atlas of Automated Anatomical Labeling (AAL) (Tzourio-Mazoyer et al., 2002) was denormalized to that T1 space using an inverse function of spatial transformation and masked through binarized, subjective tissue probability mapping in order to isolate the mean value of the regions from the gray matter. The following mask was used: [Atlas*(GM>WM)*(GM>CSF)*(GM>0.1)] where

GM is the gray matter, WM is the white matter and CSF is the cerebrospinal fluid. Next, the movements were regressed from the processed time series at the voxel level using the 24 Volterra-series-expanded parameters of movement.

Appendix 2. Supplementary Materials: MDD

Participants

The demographical data of the participants is presented in supplementary table 1. In addition, partial correlations between clinical indicators showed no interaction among the variables (supplementary table 2).

	Healthy Controls		Major Depression Disorder	
Sample Size	27		27	
Age (years)	45.52	± 9.5	44.96	± 11.48
Gender	18 F / 9 M		22 F / 5 M	
HDRS			21.74	± 2.19
Age of Onset (years)			35.33	± 10.48
Episode Duration (days)			422.30	± 307.24
Drug Washout			20/27	

Supplementary Table 1. Demographic Data of Clinical Sample

	Gender	Duration of Disease	HDRS	Episode Duration	Drug Washout
Gender		-0.02	0.2	-0.34	-0.26
Duration of Disease			-0.2	-0.22	-0.06
HDRS				-0.1	0.28
Episode Duration					-0.39
Drug Washout					

Supplementary Table 2. Analysis of Variability of Clinical indicators. The partial correlation (rho) between variables are given. No significant interaction between variables were found.

Dynamic Functional Connectivity

The Hilbert transform, $S(t) = A\cos(\varphi(t))$S(t) = Acos(φ(t)) of the preprocessed BOLD time series broke the signal down to an analytical signal *S(t)* with an instantaneous phase *φ(t)* and amplitude *A*. For each time instance *t*, the difference between the phases of the respective ROIs was calculated as $\Delta\varphi_{ij}(t) = \varphi_i(t) - \varphi_j(t)$, where *i* and *j* are the

indices of each ROI. Then, instantaneous coupling matrices (ICMs), *C(t)*C(t) were constructed using the phase differences normalized between 0 and 1, thereby representing perfect synchronization and perfect synchronization respectively, such that:

$$C_{ij}(t) = 2\pi / \Delta j_{ij}(t).$$

Global synchronization *G(t)* G(t)was calculated using binarized ICMs (i.e., binary connectivity matrix $C^b(t)$ comprising phase differences less than $\pi/8$. Where N is the number of ROIs:

$$C^b(t) = \begin{bmatrix} C^b_{ij}(t) = 1, & if\ \Delta j_{ij} < \pi/8 \\ C^b_{ij}(t) = 0, & otherwise \end{bmatrix}$$

Finally, the percentage of existing connections at each binary ICM was defined as global synchronization.

$$G(t) = 100\left(\frac{\sum_{i,j \in N} C^b_{ij}(t)}{\frac{N!}{(N-2)!2!}}\right)$$

The similarities between the ICMs ($r^t_{t,t+\delta}$), where time point $t \in T$ tϵT and adjacent time point $(t+\delta) \in \{[1, \max(1, t-t)]\} \cup \{[\min(T, t+t), T]\}$ with the given time lag $t \in [0, 20\,\text{sec.}]$were quantified for each subject as the correlation coefficient between two matrices at each instance. Moreover, because global synchronization also affects the similarity between ICMs, the similarity of each ICM to the overall average dFC was taken as a reference. Similarity to the reference was calculated as the correlation coefficient between each ICM and the average dFC ($\hat{r}_t$). Thus, the intertemporal closeness (ITC^t) was defined as the proportion of similarities between ICMs that were smaller than the average similarity to the reference (i.e., the probability of observing greater similarity between instances than their similarity to the global phase-coupling matrix).

$$r_{t,t+\delta}^{t} = \frac{\sum_{i=1,j=1}^{N} (C_{ij}(t) - \hat{C}(t))(C_{ij}(t+\delta) - \hat{C}(t+\delta))}{\sqrt{\sum_{i=1,j=1}^{N} (C_{ij}(t) - \hat{C}(t))^2 \sum_{i=1,j=1}^{N} (C_{ij}(t+\delta) - \hat{C}(t+\delta))^2}}$$

$$\hat{r}_t = \frac{\sum_{i=1,j=1}^{N} (C_{ij}(t) - \hat{C}(t))(C_{ij}(t) - \bar{\hat{C}})}{\sqrt{\sum_{i=1,j=1}^{N} (C_{ij}(t) - \hat{C}(t))^2 \sum_{i=1,j=1}^{N} (C_{ij}(t) - \bar{\hat{C}})^2}}$$

$$\hat{C}_{ij} = \frac{\sum_{t=1}^{T} C_{ij}}{T}$$

The variability in each pair in ICMs, $C_{ij}(t)$ was considered at the nodal level. The variability of functional connectivity (vFC) was computed as the index of dispersion (IoD_{ij}) $= \sigma^2_{C_{ij}} / \mu_{C_{ij}}$) of the coupling between each pair, and this was calculated for each subject.

To characterize temporal stability, we considered each instantaneous coupling matrix in d-FC as an independent state. For each subject 101 instantaneous coupling matrices (ICM) were extracted using Hilbert Transform. ICMs were averaged over time to obtain average connectivity matrix (av-FC). Then, for each subject we calculated the correlation coefficient between each ICM pair and the correlation coefficient between each ICM and av-FC. The distribution of correlation coefficients (Pearson's r) among ICM pairs were monotonously decreasing with a very-low median ($r < 0.1$). Furthermore, there was a very high correlation ($r > 0.5$) between each ICM and its neighbors. On the other hand, trivially, correlation coefficients between each ICM and av-FC were normally distributed with an average value around 0.35. In other words, d-FC built on both stationary and non-stationary components. However, in this analysis rather than investigating the stationarity of the FC, we assumed that each ICM based upon the av-FC and highly overlapping transient deviances from av-FC. Therefore, the analysis of stability using inter-temporal closeness with time lags aimed to quantify the intensity and duration of the transient deviances.

To validate this approach we implemented the same analysis on surrogate time-series. BOLD-time series of each ROI were transformed into frequency domain using FFT. Then, the phases were shuffled in frequency domain and inverse-transformed into time-domain. This approach destroyed fluctuations in global synchronization (but also correlation structures) in d-FC. No differences were observed in the probability distributions of the correlation coefficients among ICMs and the correlation coefficients of each ICM and av-FC. Moreover, high correlation between neighboring ICMs remained intact. However, despite the qualitative similarities of ITC of surrogate time-series, the significant difference between MDD patients and healthy controls disappeared (permutation test, $p = 0.3$). We used another surrogate set by shuffling instantaneous coupling between each pair over time to preserve av-FC structure. This time the patterns in correlation coefficient between ICMs and av-FC completely destroyed and ITC became 0 for all subjects.

Spectral Analysis of BOLD time-series

Spectral analysis of raw BOLD time-series revealed an increased power in low-frequencies as observed in many resting-state fMRI studies. We used band-pass filter in a narrow range (0.04-0.07 Hz), which was shown to be resilient to physiological noise and optimized for Hilbert Transform (Glerean et al., 2012). In order to understand the relationship between these low-frequency fluctuations and global-local alterations, we checked the correlation between band power of 0.04-0.07 Hz and global synchronization, and we compared 0.04-0.07 Hz band power of each ROI in MDD and HC groups. There was a significant correlation between global synchronization (i.e. % of synchronization based on d-FC) and 0.04-0.07 Hz power. Furthermore, MDD patients had increased (0.04-0.07 Hz) band-power in right MFG, SPG, PCUN, PCL and decreased band-power in left TPOmid. These alterations in band-power appeared to be related to the differences in functional connectivity. However, the decreased band-power in l-TPOmid was only evident when we used group-ICA (i.e. increased variability in auditory network in MDD). In addition, we observed that in contrary to 0.04-0.07 Hz range, MDD patients had slightly decreased power in frequency bands below and above the narrow-band.

The Spatio-Temporal Properties of Global Average Signal (GAS)

The results from global and local connectivity were observed to be linked to global average signal. We believe that this relationship might be crucial in understanding discrepancies in the literature. To check this relationship we calculated the GAS of the BOLD time-series of each subject and transformed it into z-scores. We defined global up- and down-states as GAS z-score greater than 1 and less than -1, respectively. Then, we calculated the mean BOLD signal at these global up- and down-states. The topology of the global up-state and down-state was negatively correlated ($r = -0.93$, $p < 0.001$). The consequence of this negative correlation was that some ROIs were very sensitive to GAS fluctuations (i.e. ROIs that peak at up-state, dip at down-state). We observed that dorsal cingulate gyrus, medial frontal gyrus, superior and medial temporal regions, and inferior parietal lobule were fluctuating with GAS, while subcortical regions and orbital frontal regions were insensitive GAS.

Furthermore, we repeated the same analysis with d-FC: Global Synchronizations (or Kuramo order parameter) of each subject were converted into z-scores, and global-up and -down states were defined as Global Synchrony greater than 1 and less then -1, respectively. Then, average coupling matrices for up and down states were calculated. The results showed that during global-up states (wide-spread synchronization of the brain) occipital and parietal regions (including DMN related regions such as precuneus, cuneus, medial frontal and medial temporal...etc) were highly connected. Interestingly, during wide-spread desynchronization, the connectivity in frontal regions (particularly orbital frontal) were increased. Therefore, GAS might be manifested as a connectivity wave propagating from lateral (down-state) to medial (up-state), orbito-frontal (down-state) to occipital regions (up-state), consistent with the previous findings in dynamic FC.

Appendix 3. Materials and Methods: Bipolar

Subjects

Patients were recruited from a pool of over 600 patients enrolled in the systematic prospective naturalistic follow-up study of the Bipolar Disorders Program of the Hospital Clinic and University of Barcelona, whose characteristics have been described elsewhere (Popovic et al., 2014). Psychiatric diagnoses were formulated by trained psychiatrists according to DSM-IV-TR criteria and confirmed by Structured Clinical Interview for DSM-III-R-axis I (SCID-I) and axis II -SCID-II (First, 2002, 2001). The severity of the patient's clinical status was evaluated with the 17-item Hamilton Depression Rating Scale (HDRS-17) (Bobes et al., 2003), the Young Mania Rating Scale (YMRS) (Colom et al., 2002) and the Modified Clinical Global Impression Scale for Bipolar Disorder (CGI-BP-M) (Vieta Pascual et al., 2002). Patient's functioning was rated by the means of Functioning Assessment Short Test (FAST) and medical comorbidities by Charlson Comorbidity Index CGI-BP-M.

We analyzed 13 healthy adults (average age and standard deviation 28.7 ± 3.8 years of age, 10 males) and 8 patients with BP disorder (54 ± 13.2 years of age, 5 males) with a minimum score of 20 on the 17-item Hamilton Rating Scale for Depression (HDRS-17). Patients were included and imaged at the time of suffering an acute depressive relapse (within the first week from onset). Patients were maintained in their previous medication until performing MRI studies. Exclusion criteria included co-morbid Axis I psychiatric conditions, an Axis II diagnosis as determined by the Structured Clinical Interview for DSM-IV Axis II Personality Disorders (SCID-II), a concurrent neurological disorder or an acute medical condition that could interfere with the assessments. The Ethical and Research Committee of the Hospital Clinic approved the study and patients were included after their physicians obtained signed informed consent.

fMRI acquisition and pre-processing

The subjects were instructed to rest while keeping their eyes closed in a 14-min resting-state scan. Brain images were acquired on a 3 Tesla TrioTim scanner (Siemens, Erlangen, Germany) using the 8-channel phased-array head coil supplied by the vendor. A custom-built head holder was used to prevent head movement, and earplugs were used to attenuate scanner noise. High-resolution three-dimensional T1-weighted magnetization prepared rapid acquisition gradient echo (MPRAGE) images were acquired for anatomic reference (TR=2200ms, TE=3ms, FA=7^{o}, 1.0mm isotropic voxels). T2-weighted scan was used in order to identify pathological findings (TR=3780ms, TE=96ms, FA=120^{o}, voxel size 0.8x0.6x3.0mm, 3.0mm thick, 0.3mm gap between slices, 40 axial slices). Functional data were acquired using a gradient-echo echo-planar pulse sequence sensitive to blood oxygenation level-dependent (BOLD) contrast (TR=2000ms, TE=30ms, FA=85^{o}, 3.0mm isotropic voxels, 3.0mm thick, no gap between slices).

fMRI data were preprocessed using SPM8 (http://www.fil.ion.ucl.ac.uk/spm) including compensation of systematic, slice-dependent time shifts, motion correction, and normalization to the atlas space of the Montreal Neurological Institute (MNI) (SPM8). We used the SPM connectivity toolbox *Conn* (http://web.mit.edu/swg/software.htm) with a temporal filtering that remove constant offsets and linear trends over each run but retained frequencies below 0.1 Hz. Data was spatially smoothed using a standard 8 mm full-width half-maximum Gaussian blur. The brains were parceled into 82 regions based on scale 33 Lausanne Atlas.

The group comparisons for FC for each individual connection were performed using Network Based Statistics (NBS) toolbox (Zalesky et al., 2010). We used permutation t-test with 5000 permutations with p-value threshold $p < 0.05$. We iterated over the threshold for connected component size between the values 1 and 5 using a step size of 0.05. For the ease of interpretation, we chose the threshold that gives the networks comprising 2% of the connections with the highest t-statistic. The networks were visualized using BrainNet Viewer toolbox in Matlab (Xia et al., 2013).

Acquisition of Structural Connectivity Matrices

DSI data was acquired in the same scanning session with 515 gradient directions at a max b-value of 8000 s/mm2 (TR/TE=8200/164 ms) and voxel size of 2x2x3mm^3 maximum diffusion gradient intensity: 80 mT/m with a total acquisition time of 35.42 min. Vector table of total directions: 127 directions if only one bval=0 and 130 directions if one bval=0 per vector table.

Appendix 4. Materials and Methods: IUGR

Subjects

The subjects considered in our study were recruited from a larger prospective research program on IUGR involving fetal assessment and short- and long-term postnatal follow-up at Hospital Clinic (Barcelona-Spain). We studied two different cohorts, one of them evaluated in the neonatal period (one month corrected age), and the other evaluated at one year of age. Both cohorts were split into two groups: IUGR, defined as fetuses with estimated fetal weight below the 10^{th} centile at birth according to local standards (Figueras et al., 2008); and control subjects which were chosen from fetuses with fetal estimated weight between the 10^{th} and 90^{th} centile according to local standards (Figueras et al., 2008).

The neonatal cohort consists on 40 subjects: 24 IUGR and 16 controls. The one-year-old cohort comprised 19 infants with IUGR and 22 healthy controls, in total 41 subjects. Pregnancies were dated according to the first-trimester crown-rump length measurements (Robinson and Fleming, 1975). Infants with chromosomal, genetic, or structural defects and signs of intrauterine infection or neonatal early onset sepsis as defined by positive blood culture within the first 72 h of life were excluded from this study. Gestational age (GA), birth weight, gender, maternal education, maternal smoking status, Apgar at 5 min, umbilical artery pH and neonatal complications including late-onset sepsis, necrotizing enterocolitis and chronic lung disease were recorded for each subject. The study protocol was approved by the local Ethics Committee, and written informed consent was obtained from the parents or legal guardians of all participants.

Neurobehavioral assessment

Neurobehavioral performance in the neonate cohort was assessed at neonatal age using Neonatal Behavioral Assessment Scale (NBAS) (Nugent and Brazelton, 2000). Cortical and subcortical functions were evaluated in 35 items grouped into 6 clusters: habitua-

tion, motor, social-interactive, organization of state, regulation of state, autonomous nervous system and attention.

Neurodevelopmental outcome of the one-year-old cohort was assessed at 21 months of corrected age (CA) (± 3 months) with the Bayley Scale for Infant and Toddler Development, Third edition (BSID-III), in five distinct scales: cognitive; language; motor; socio-emotional behavior; and adaptive behavior. Abnormal BSID-III was defined as a score below 85 in any of the five different scales (Anderson et al., 2010). A single trained psychologist examiner with previous experience with the BSID-III performed all developmental examinations. The examiner was not informed about the infant medical history.

MRI acquisition

MRI was performed around one month corrected age for neonates, and 12 ± 2 months corrected age for infants during natural sleep after feeding the baby. All acquired images were visually inspected for apparent artifacts and anomalies and subjects excluded accordingly. Structural, diffusion and functional MRI were performed using a TIM TRIO 3.0 T whole body MR scanner (Siemens, Germany). Due to the inversion in the brain tissue contrast at neonatal and one-year-old periods, different structural acquisition was performed at each cohort. For neonates, anatomical T2-weighted images were acquired with 45 axial slices with 2-mm slice thickness, 256x256 in-plane acquisition matrix, FOV = 160x160 mm², voxel size of 0.625x0.625x2 mm², TR=5460ms and TE=91ms. At one year of age, T1-weighted images were acquired by MPRAGE sequence, comprising 192 sagittal slices, 256x256 in-plane acquisition matrix, FOV =200x200mm², voxel size of 0.86x0.86x0.9mm², TR=2050ms and TE=2.41 ms.

Diffusion acquisition paremeters were also adapted to the specific features of each range of age. In both cohorts, images were acquired by using a single-shot Echo-Planar Imaging (SE-EPI) sequence comprising a baseline image without diffusion weight (b=0 s/mm²) and 30 diffusion directions. The b-value was set to 750 s/mm² in the neonatal cohort, while b=1000 s/mm^2 was applied at one year of age. Other acquisition parame-

ters for the neonatal cohort were TR=6000ms, TE=100ms, 40 axial slices, slice thickness 1.4 mm with no inter-slice gap, FOV=134x134 ms, 188x188 in-plane acquisition matrix, resulting in a voxel dimension of 1.4x1.4x1.4 mm^3 . For the one-year-old cohort, parameters were TR=9300ms, TE=94 ms, 40 axial slices, slice thickness 3 mm with no interslice gap, FOV=200x200 mm^2, 122x122 in-plane acquisition matrix, resulting in a voxel dimension of 1.64x1.64x3 mm^2.

Functional MRI data were acquired in both cohorts using EPI sequence with TR=2000ms, TE=20ms, 42 axial slices with 2-mm slice thickness, 80x80 in-plane acquistion matrix, FOV = 160x160 mm^2, obtaining a spatial resolution of 2x2x2 mm^3. Resting-state functional activity was assessed during 8 minutes of natural sleep (240 EPI volumes). The first volumes were discarded to allow for accommodating T1-equilibrium processes.

Image preprocessing

Image preprocessing was similar for both cohorts. From the structural images each subject's brain was parcelated into 90 regions by means of elastic registration to a reference atlas. AAL atlas adapted to neonatal population in a T2-weighted template was used for neonates and AAL adapted to one-year-old population in a T1-weighted template was used for the older cohort (Shi et al., 2011). White matter (WM), gray matter (GM) and cerebrospinal fluid (CSF) segmentation was performed using the unified segmentation model (Ashburner and Friston, 2005) with tissue probability maps adapted to each group of age (Shi et al., 2011).

Diffusion weighted images were corrected for eddy currents effects and simple head motions using FMRIB's Diffusion Toolbox (FSL 4.1; www.fmrib.ox.ac.uk/fsl). Fiber tracts were estimated by diffusion tensor imaging (DTI)-based deterministic tractography using MedINRIA 1.9 (www-sop.inria.fr/asclepios/software/MedINRIA/), considering a Fractional Anisotropy (FA) threshold of 0.1.

fMRI preprocessing was mainly performed with SPM8 package, including correction of

intra-volume time differences, inter-volume geometric displacements using a six-parameter rigid transformation and spatial smoothing using a Gaussian kernel with 2mm full width at half maximum. Correction of head motion effects in the signal was performed by regressing out the 6 parameters previously estimated.

Assessment of the Structural Connectome

From the AAL-brain parcellation and the streamlines resulting from the tractography algorithm, a structural connectivity matrix was computed for each subject. Regions in the AAL atlas were considered as the network nodes, and two nodes were considered to be connected if there was at least one streamline whose end points belong to the corresponding pair of regions. The weight of the connection was defined as the average FA in all the streamlines connecting each pair of regions.

Graph Metrics

In order to characterize the functional and effective networks, we used graph metrics. For the functional network, at a global scale, we measure perturbational integration (Deco and Kringelbach, 2014). For the average phase-lock values (PLS) of each subject, we measured the size of the largest component of the connected sub-graph (M) after binarizing the matrix using an absolute threshold, θ, between 0 and 1 (with a step size of 0.01). Then, we integrated M with respect to the threshold, θ. Finally; we normalized the measure by the maximal number of connected brain areas.

To evaluate EC, we used joint strength and strength asymmetry. Joint strength was computed as the sum of all incoming and outgoing connections of a particular node. Strength asymmetry, on the other hand, was defined as the difference between outgoing connections and incoming connections. Specifically, negative strength asymmetry indicated that a node is input dominated (*in-strength* > *out-strength*), while positive strength asymmetry indicated output dominance (*out-strength* > *in-strength*).

Statistical Analyses

Group comparisons of whole-brain connectivity for functional and structural connectivity were performed in NBS toolbox in Matlab. Permutation t-test with 5000 permutations was implemented on each connection, and connected component threshold was tested between 1 and 5. For EC comparisons, directed version of NBS toolbox was used. Remaining comparisons were done using permutation t-test with 10000 permutations, and in case of multiple comparisons, False Discovery Rate (FDR) with Benjamini-Hochberg algorithm was implemented.

The relationship between the measures described in this study and the behavioral assessments was quantified as partial correlation coefficients controlled for GA, sex, maternal smoking status and weight percentile.

Appendix 5. Supplementary Tables: IUGR

Supplementary Table 1.

Average Phase-Lock Synchronization in Neonates

Pair	Social-Interactive	Organization of State	Regulation of State	Autonomic Nervous System	Attention	Percentile
PreCG_l-ACG_r	-0.0041	0.1211	0.0090	-0.4258*	0.1254	-0.6407**
PreCG_l-MOG_r	0.0028	0.0424	0.1612	-0.4425*	0.0532	-0.4973**
ORBsup_l -CAU_l	0.0827	-0.2140	0.1653	-0.2132	0.1703	-0.2996
ORBmid_l -CAU_l	0.0699	-0.0067	-0.1371	-0.1280	0.1064	-0.3086
ORBmid_l -LING_r	-0.0447	0.1590	-0.0572	-0.3588	0.0695	-0.5041**
ORBinf_l -IOG_l	-0.0469	-0.1355	0.0023	-0.4354*	0.0575	-0.4225*
ORBinf_l -CAU_l	-0.0454	-0.0350	-0.1194	-0.2797	0.0125	-0.3431
ORBinf_l -ORBmid_r	-0.2724	-0.0875	-0.0865	-0.2623	-0.1856	-0.3900*
ORBinf_l -LING_r	-0.0035	0.2040	0.1354	-0.5220**	0.0162	-0.3447
OLF_l-IOG_l	-0.1119	-0.0552	0.0343	-0.2230	0.0407	-0.4600*
ORBsupmed_l -LING_l	-0.0326	-0.1348	0.0607	-0.2634	0.0506	-0.4240*
ORBsupmed_l -IOG_l	-0.1410	-0.0610	0.0127	-0.4483*	-0.0394	-0.3522
REC_l-HES_r	-0.1784	-0.0485	-0.0050	-0.3461	-0.1035	-0.4710**
REC_l-STG_r	-0.1489	0.2248	-0.1673	-0.3384	-0.0885	-0.3820*
ACG_l-CAU_l	0.1273	-0.1683	0.1229	-0.2126	0.1692	-0.3738*
AMYG_l -PAL_l	-0.2373	0.0878	0.0771	-0.2625	-0.1765	-0.4023*
AMYG_l -AMYG_r	-0.1634	-0.3507	-0.0784	-0.0834	-0.1065	-0.2235
AMYG_l -LING_r	-0.2608	0.2292	-0.0360	-0.4795**	-0.0638	-0.4807**
LING_l -PUT_l	-0.3797*	-0.0160	-0.0629	-0.3605	-0.2666	-0.2337
IOG_l-CAU_l	-0.1528	-0.1812	-0.1497	-0.3076	-0.1206	-0.3408
IOG_l-PUT_l	-0.2080	-0.0075	-0.1450	-0.2923	-0.0952	-0.2793
IOG_l-INS_r	0.0338	-0.0221	-0.0733	-0.1858	0.0331	-0.2500
FFG_l-CAU_l	-0.2027	-0.0048	0.1295	-0.5425**	-0.2066	-0.4155*
FFG_l-CAL_r	0.0187	0.2387	0.0345	-0.1965	0.1232	-0.5442**
FFG_l-STG_r	0.0044	0.4227*	-0.1317	-0.3420	-0.0390	-0.4946**
CAU_l-PUT_l	-0.2111	-0.0378	-0.0926	-0.2988	-0.0809	-0.2231
CAU_l-ORBmid_r	-0.2315	0.1404	-0.2775	-0.3405	-0.0472	-0.3768*
CAU_l-ACG_r	0.0561	-0.0317	0.0001	-0.2320	0.1694	-0.3560
PUT_l-THA_l	-0.2524	0.1625	0.1377	-0.1946	-0.0907	-0.2810
PUT_l-ACG_r	-0.2356	-0.0826	-0.1870	-0.3749*	-0.1584	-0.4192*
PUT_l-LING_r	-0.4186*	0.2337	-0.0269	-0.4235*	-0.4187*	-0.2933
TPOmid_l -STG_r	-0.2507	0.2727	-0.2998	-0.1233	-0.0711	-0.3144
ITG_l-STG_r	-0.0741	0.3984*	0.0442	-0.4201*	-0.0679	-0.4351*
OLF_r-CAL_r	-0.1614	-0.1835	-0.0292	-0.3192	0.0344	-0.3334

OLF_r-PUT_r	-0.2330	-0.0115	-0.0684	-0.2700	-0.0410	-0.4199*
INS_r-ACG_r	-0.2686	0.1211	-0.1529	-0.4592*	-0.1499	-0.5031**
INS_r-PUT_r	-0.3875*	0.1768	-0.0337	-0.4616*	-0.2653	-0.3525
HIP_r-HES_r	-0.3351	0.1839	-0.2104	-0.6162**	-0.3881*	-0.4010*

Index of Dispersion of Phase-Lock Synchronization in Neonates

Pair	Social-Interactive	Organization of State	Regulation of State	Autonomic Nervous System	Attention	Percentile
PreCG_l-ACG_r	0.0156	0.0133	-0.0663	0.3011	-0.1354	0.6116**
PreCG_l-MOG_r	0.0341	-0.0081	-0.1386	0.1927	-0.0063	0.4526*
SFGdor_l -SOG_r	0.2010	0.0815	0.0918	0.3750*	0.0318	0.2618
ORBsup_l -ORBinf_l	0.1263	0.2457	-0.1984	0.3195	0.0777	0.1612
ORBsup_l -CAU_l	-0.0963	0.0869	-0.1206	0.3285	-0.1559	0.3490
ORBmid_l -LING_r	0.0611	-0.0032	-0.0204	0.2185	-0.1051	0.4289*
IFGtriang_l -STG_r	0.0389	-0.3470	0.0352	0.4178*	-0.0415	0.4568*
ORBinf_l -PUT_r	0.2051	-0.1114	0.1988	0.3159	0.2269	0.4166*
ROL_l-TPOmid_l	0.4481*	0.0171	0.2705	0.2938	0.2380	0.4752**
REC_l-INS_l	0.3663	-0.0545	0.0786	0.4159*	0.3486	0.3300
REC_l-PoCG_l	0.0503	-0.0603	-0.1801	0.2941	0.0108	0.2675
REC_l-ROL_r	0.1059	0.1025	0.0264	0.1055	0.0249	0.2833
REC_l-STG_r	0.0029	-0.1875	0.0905	0.3660	0.0172	0.3255
INS_l-PHG_l	0.1606	-0.0688	0.1079	0.2378	0.1278	0.2623
DCG_l-LING_r	-0.0558	-0.1479	0.0612	0.4183*	-0.0962	0.5499**
PCG_l-AMYG_l	-0.1404	-0.1457	-0.3034	0.1949	-0.2577	0.4160*
AMYG_l -LING_r	0.2198	-0.1208	-0.1743	0.4800**	-0.0010	0.4207*
SOG_l-CAU_l	0.0618	-0.0548	0.0471	0.5444**	0.0921	0.2087
SOG_l-SFGfor_r	0.0010	-0.0165	0.1788	0.1524	-0.2385	0.4974**
FFG_l-SMG_l	-0.1496	0.0470	-0.2354	0.1197	-0.2912	0.4220*
FFG_l-LING_r	-0.1565	-0.3405	-0.2955	0.3438	-0.1651	0.5789**
FFG_l-SOG_r	0.1487	0.0209	0.2586	0.3125	0.1623	0.1206
FFG_l-STG_r	-0.0464	-0.4399*	-0.0665	0.4305*	-0.0027	0.7026**
PoCG_l -TPOmid_l	0.3468	-0.0312	0.2009	0.4278*	0.2738	0.2998
IPL_l-PUT_r	-0.0537	-0.1488	0.0023	0.0656	-0.1222	0.5096**
CAU_l-MTG_l	-0.0178	0.0567	-0.2785	0.3931*	0.0249	0.3857*
CAU_l-CUN_r	-0.0295	-0.2551	0.0582	0.5931**	-0.0042	0.5037**
PUT_l-LING_r	0.2473	-0.3783*	0.0333	0.3107	0.2507	0.2985
STG_l-PUT_r	0.4065*	-0.1633	0.2060	0.3556	0.3206	0.4018*
TPOsup_l -LING_r	0.2558	-0.2219	-0.0424	0.4597*	0.1399	0.4096*
MTG_l-STG_r	0.1625	-0.3966*	0.3321	0.3803*	0.1938	0.3100
TPOmid_l -INS_r	0.4374*	-0.0920	0.3822*	0.1636	0.2945	0.3155
ITG_l-INS_r	0.0866	-0.4195*	-0.0315	0.3459	-0.0045	0.5464**
ITG_l-STG_r	0.0147	-0.5077**	-0.1160	0.4688*	0.1377	0.4380*
INS_r-ACG_r	0.3486	-0.1689	0.2865	0.4949**	0.2357	0.4033*
INS_r-PUT_r	0.2821	-0.1999	0.0810	0.3871*	0.1325	0.3532
PoCG_r -PUT_r	0.0969	-0.1779	0.1028	0.3473	0.1509	0.4159*

PUT_r-STG_r	0.2562	-0.2551	0.1001	0.3775*	0.1944	0.3996*
THA_r-STG_r	0.2506	-0.2276	0.2236	0.3514	0.2656	0.2741

* p < 0.05, ** p < 0.01

Supplementary Table 2.

Effective Connectivity of Neonates

Pair	Social-Interactive	Organization of State	Regulation of State	Autonomic Nervous System	Attention	Percentile
SMA_l-PCUN_l	-0.0568	-0.4586*	-0.0601	0.4909**	-0.1405	0.4789**
SFGmed_l-PUT_l	-0.1396	-0.2779	-0.0724	0.0359	-0.1292	0.3909*
SFGmed_l-MTG_l	0.1091	-0.2237	0.1543	0.0314	0.1638	0.4295*
INS_l-SFGmed_l	-0.4386*	-0.1460	-0.5548**	0.0033	-0.4734**	0.1718
CAL_l-STG_r	0.1690	-0.0798	-0.0076	0.2511	0.1475	0.2501
SPG_l-MTG_l	0.0483	-0.1589	-0.0244	0.3624	0.1388	0.1797
IPL_l-MTG_l	0.0718	-0.1207	-0.0640	0.4458*	0.2087	0.2271
PCUN_l-ORBinf_l	0.0768	0.1159	0.1241	0.0190	0.1592	0.3062
PCUN_l-SMA_l	-0.0557	-0.4279*	-0.0520	0.4722**	-0.1295	0.4573*
PCUN_l-MTG_l	-0.3413	-0.1767	-0.1474	0.1536	-0.1129	0.4001*
PCUN_l-MTG_r	-0.1664	0.0436	-0.0564	0.1673	-0.1380	0.2287
PUT_l-SFGmed_l	-0.1667	-0.2430	-0.0595	-0.0075	-0.1355	0.3661
THA_l-IFGoperc_l	-0.2582	0.1256	-0.0623	-0.2367	-0.2487	0.2911
MTG_l-SFGmed_l	0.1073	-0.1656	0.1313	0.0477	0.1583	0.4580*
MTG_l-SPG_l	0.0637	-0.1254	-0.0555	0.3442	0.1399	0.0949
MTG_l-IPL_l	0.0631	-0.1081	-0.0583	0.4828**	0.1974	0.2334
MTG_l-PCUN_l	-0.3517	-0.2027	-0.1576	0.1318	-0.1189	0.4027*
MTG_l-PCUN_r	0.0637	-0.0227	0.0975	0.1443	0.1080	0.4566*
SFGmed_r-TPOsup_r	0.2107	-0.0309	-0.0248	0.2994	0.1129	0.2013
AMYG_r-ANG_r	0.2403	-0.1217	0.3733*	0.1022	0.2420	0.4145*
ANG_r-ORBinf_r	0.2190	-0.0106	-0.0682	0.4017*	0.2020	0.2671
ANG_r-AMYG_r	0.2256	-0.1263	0.3639	0.1081	0.2299	0.4421*
ANG_r-CAU_r	-0.0853	0.0081	0.0977	0.2904	-0.0662	0.3361
ANG_r-TPOmid_r	0.1336	0.1055	-0.0337	0.2132	0.0892	0.3916*
PCUN_r-MTG_l	0.0575	-0.0756	0.1013	0.1681	0.0982	0.5132**
PCUN_r-TPOsup_r	-0.0743	-0.2231	-0.0888	0.3953*	-0.1714	0.6675**
PCUN_r-MTG_r	0.2509	-0.1091	0.1447	0.3822*	0.1848	0.5918**
PCUN_r-TPOmid_r	0.2025	-0.1168	0.2436	0.2918	0.2412	0.3931*
CAU_r-REC_l	0.3327	0.0372	0.1173	0.1517	0.1864	0.4028*
CAU_r-ANG_r	-0.1406	0.0391	0.0460	0.3066	-0.1286	0.3306
STG_r-CAL_l	0.1852	-0.0680	0.0200	0.2260	0.1545	0.1974
TPOsup_r-CAL_l	-0.1005	-0.0387	0.0204	0.2869	-0.0033	0.2770
TPOsup_r-SFGmed_r	0.2130	-0.0755	-0.0048	0.2985	0.1021	0.2069
TPOsup_r-PCUN_r	-0.0040	-0.2310	-0.0776	0.4314*	-0.1208	0.6821**

MTG_r-PCUN_l	-0.0878	-0.0391	-0.0286	0.2563	-0.0679	0.2788
MTG_r-THA_l	-0.0845	-0.2672	0.2824	0.1525	-0.1758	0.6533**
MTG_r-PCUN_r	0.2509	-0.0827	0.1506	0.3519	0.1613	0.6165**
TPOmid_r-ANG_r	0.1103	0.1064	-0.0165	0.2172	0.0412	0.4249*
TPOmid_r-PCUN_r	0.1924	-0.1213	0.2486	0.2715	0.2702	0.3516

* p < 0.05, ** p < 0.01

Supplementary Table 3.

Effective Connectivity of Infants

Pair	Adaptation	Cognitive	Language	Motor	Social	Percentile
ROL_l-DCG_l	0.2789	-0.3333	-0.0634	-0.1411	0.3340	-0.2566
DCG_l-SOG_l	0.0855	-0.2136	-0.1596	-0.1130	-0.1333	-0.5255*
DCG_l-MOG_l	0.1237	0.1925	0.1061	0.0040	0.1639	-0.2561
DCG_l-IPL_l	0.2007	-0.1652	-0.1170	-0.3581	0.3994	-0.4252
DCG_l-ANG_l	0.1613	-0.0631	0.0862	-0.1922	0.4825*	-0.1395
PHG_l-ANG_l	0.0107	-0.1946	-0.1426	0.0020	-0.1326	-0.3253
LING_l-MTG_l	0.0260	-0.0984	0.0390	-0.0490	0.0846	-0.4826*
SOG_l-PCUN_l	0.5319*	-0.2894	-0.1617	-0.3625	0.4652*	-0.3244
MOG_l-IOG_l	-0.1579	-0.5370*	-0.2314	-0.1443	-0.2840	-0.5317*
IOG_l-MOG_l	-0.1954	-0.5462*	-0.2285	-0.1415	-0.2906	-0.5006*
IOG_l-PCUN_l	0.1916	-0.3971	-0.3835	-0.4359	0.1726	-0.1772
FFG_l-MTG_l	-0.0785	-0.5318*	-0.3066	-0.2459	-0.1952	-0.2633
FFG_l-FFG_r	-0.4681*	-0.2352	-0.2212	-0.0247	-0.3289	-0.2157
SPG_l-CUN_l	0.1297	-0.2322	-0.3297	-0.0600	-0.0902	-0.1535
SPG_l-PUT_l	0.2666	-0.4671*	-0.1723	-0.4832*	0.1586	-0.4908*
IPL_l-DCG_l	0.1994	-0.1560	-0.1355	-0.3789	0.4030	-0.4195
IPL_l-STG_l	0.1961	-0.2562	0.2647	0.0490	0.3120	-0.4877*
ANG_l-PHG_l	-0.0333	-0.2349	-0.1693	-0.0151	-0.1521	-0.2883
PCUN_l-CUN_l	0.0046	-0.1982	-0.1422	-0.0017	0.1334	-0.0326
PCUN_l-SOG_l	0.4898*	-0.2728	-0.1372	-0.3232	0.4823*	-0.2913
PCUN_l-IOG_l	0.1624	-0.3844	-0.3503	-0.3711	0.1440	-0.1713
PCUN_l-CUN_r	0.2256	0.0674	-0.1003	-0.0500	0.0305	-0.4672*
PCUN_l-LING_r	-0.0935	0.0803	-0.2014	0.1677	-0.3003	-0.3282
PUT_l-PUT_r	-0.4371	-0.2009	-0.0274	0.0258	-0.0922	-0.2088
PAL_l-PCUN_r	0.2966	-0.1803	0.1949	-0.1298	0.5290*	-0.3405
STG_l-IPL_l	0.2403	-0.2657	0.2689	0.0376	0.3483	-0.4923*
STG_l-SMG_r	0.4158	-0.3291	-0.0951	-0.1760	0.2008	-0.5062*
MTG_l-PHG_l	0.0434	-0.1670	-0.0593	0.0263	-0.0217	-0.5121*
MTG_l-LING_l	-0.0477	-0.1105	0.0742	0.0128	0.0650	-0.4351
IFGoperc_r-ORBinf_r	0.1764	0.0484	0.2352	0.3235	0.0070	-0.4845*
IFGtriang_r -ORBinf_r	0.2242	-0.2055	0.0058	0.0552	0.1272	-0.1912
ORBinf_r-IFGtriang_r	0.1487	-0.2653	0.0005	0.0952	0.0666	-0.1757

ORBinf_r-DCG_r	0.2036	-0.3790	-0.2633	-0.3709	-0.0948	-0.3105
INS_r-PCL_r	-0.2165	-0.0264	-0.0455	0.2399	-0.2474	-0.2660
DCG_r-HES_r	0.6152**	-0.1731	-0.2427	-0.4107	0.1486	-0.4362
DCG_r-STG_r	0.1665	0.0695	0.1150	-0.0279	0.0876	-0.3433
PCG_r-PHG_l	0.4392	-0.2963	-0.0995	-0.2732	0.4262	-0.4926*
CUN_r-PCUN_l	0.2819	0.0600	-0.1036	-0.0440	0.0501	-0.4888*
CUN_r-PoCG_r	0.2269	-0.1214	-0.0984	-0.1321	-0.1222	-0.5462*
LING_r-PCUN_l	-0.1238	0.1005	-0.2156	0.1400	-0.2824	-0.3363
LING_r-PCUN_r	-0.3187	-0.1810	-0.0573	0.2357	-0.0032	0.0186
FFG_r-FFG_l	-0.4489	-0.2284	-0.1821	-0.0020	-0.2898	-0.2128
PoCG_r-CUN_r	0.2378	-0.1046	-0.1144	-0.1305	-0.1118	-0.5403*
SMG_r-STG_l	0.4504	-0.3014	-0.0972	-0.1450	0.1481	-0.5224*
SMG_r-STG_r	0.0759	-0.0158	0.3357	0.3051	0.3053	-0.1595
PCUN_r-LING_r	-0.3136	-0.1931	-0.0579	0.2428	0.0092	-0.0175
PCUN_r-PCL_r	-0.1123	-0.0778	-0.0110	-0.0748	0.0021	-0.1147
PCL_r-INS_r	-0.2168	0.0207	-0.0009	0.2746	-0.2115	-0.2630
PCL_r-PCUN_r	-0.0962	-0.0766	-0.0233	-0.0854	0.0722	-0.0684
CAU_r-PUT_r	-0.1412	0.0353	0.0637	-0.1901	0.2221	-0.2804
PUT_r-PUT_l	-0.4401	-0.1904	-0.0006	0.0429	-0.1016	-0.2269
PUT_r-CAU_r	-0.1116	0.0051	0.0265	-0.2222	0.2367	-0.2806
PUT_r-THA_r	0.2321	-0.1149	-0.0916	-0.1817	0.3454	-0.3681
THA_r-PUT_r	0.1662	-0.1342	-0.1373	-0.1960	0.2926	-0.3507
HES_r-DCG_r	0.5591*	-0.1590	-0.2542	-0.4394	0.1740	-0.4311
STG_r-SMG_r	0.1023	-0.0462	0.3016	0.2738	0.3115	-0.1943
TPOsup_r-IFGtriang_r	-0.2010	0.0004	0.1948	0.3804	-0.2280	-0.2361

* p < 0.05, ** p < 0.01

Appendix 6. Materials and Methods: AD

Subjects

A total of 109 participants (58HC, 12 PC, 23 MCI and 16AD) were recruited at the Alzheimer's disease and other cognitive disorders unit, from the Hospital Clinic of Barcelona. The study was approved by the local ethics committee and all participants gave written informed consent to participate in the study. All subjects underwent clinical and neuropsychological assessment, MRI scanning and were submitted to a lumbar puncture to quantify the content of $A\beta_{42}$, p-tau and p-tau in CSF. CSF biomarker quantitation was done at the local laboratory by means of ELISA (Enzyme-Linked ImmunoSorbent Assay kits, Innogenetics, Ghent, Belgium). An interdisciplinary clinical committee formed by two neurologists and one neuropsychologist established the diagnoses. HC and PC presented no evidence of cognitive impairment on any of the administered neuropsychological tests, but PC presented an abnormal level of CSF-$A\beta_{42}$ (below 500pg/ml). MCI and AD presented signs of dementia. MCI patients had an objective memory deficit, defined as an abnormal score on the total recall measure of the Free and Cued Selective Reminding Test (FCRST), impairment on one or more of the other cognitive tests or preserved activities of daily living, as measured by the Functional Activities Questionnaire (FAQ score <6). The NINCDS-ADRDA criteria were applied for probable AD diagnosis, taking into account clinical information and objective measures derived from the FAQ and neuropsychological results. All included AD patients were in the mild stages of the disease (Global Deterioration Scale = 4). Diagnostic classification was made independent of CSF results.

Genomic DNA was extracted from peripheral blood of probands using the QIAamp DNA blood minikit (Qiagen AG, Basel, Switzerland). Apolipoprotein E genotyping was performed by polymerase chain reaction amplification and HhaI restriction enzyme digestion.

Image acquisition

Subjects were examined on a 3T MRI scanner (Magnetom Trio Tim, Siemens, Erlangen, Germany) at the image core facilities of IDIBAPS (Barcelona, Spain). MRI session included a high-resolution three-dimensional structural T1-weighted image (sagittal MPRAGE; TR = 2300ms, TE = 2.98ms; matrix size = 256 × 256 x 240; isometric voxel 1 x 1 x 1 mm3), a ten minute resting state fMRI (rs-fMRI; 300 volumes, TR = 2000ms, TE = 16ms, 128 x 128 x 40 matrix, voxel size=1.72 x 1.72 x 3 mm3) and two DTI (30 directions with b value=1000 s/mm2 and one b0; TR = 7700ms, TE = 89ms; matrix size = 122 x 122 x 60; voxel size 2.05 x 2.05 x 2 mm3).

Image preprocessing

The pre-processing pipeline of rs-fMRI consisted in the slice-timing correction, the realignment and reslice, smoothing with a Gaussian kernel (FWHM = 5mm), second order detrending and regressing out Volterra expanded parameters of movement (24 parameters), mean white matter (WM) signal, cerebro-spinal fluid (CSF) mean signal and nulling regressors (Lemieux et al., 2007). The quality criteria to consider a volume wrong and to override it by a nulling regressor, was that its correlation coefficient (cc) with the mean image of its serie were beyond three standard deviations (cc < 0.991) from the mean cc of all the images from all subjects to their corresponding mean image (mean cc = 0.995). No subjects presented more than 15% of bad volumes, being the average percentage of bad volumes of 1.6% and the standard deviation of 3.7%. To obtain the time series of each AAL region, AAL atlas was adapted to every subject native space by coregistering it to the T1 structural image by mean of ANTS (UPENN, UVA and UIowa, USA; http://stnava.github.io/ANTs/). AAL maps in native space were resliced to fMRI resolution using nearest neighbor interpolation and masked with the gray mater (GM) mask. GM mask was constructed for every subject from the tissue probability maps resulted from segmentation of T1 images. The mask was formed by those voxels whose probability of belonging to GM was bigger than the probability of belonging to any other tissue. GM masks were dilated one voxel to include edges and to fill noise-related small gaps and, finally, resliced to fMRI resolution. Time series were obtained by averaging the fMRI signal in the each area of the GM-masked AAL atlas in native

space. The software used for the whole fMRI pre-processing, a part of the above mentioned ANTS, was a homemade MATLAB (Mathworks, Sherborn, MA, USA) script mostly formed by functions from SPM package (Wellcome Trust Center for Neuroimaging; UCL, UK; http://www.fil.ion.ucl.ac.uk/spm/).

Structural connectivity matrices.

Diffusion weighted images (DWI) were first corrected for eddy current distortions using FMRIB Software Library (FSL) package (Jenkinson et al., 2012). We denoised resulting data using the overcomplete local PCA method described in (Manjón et al., 2013). Similarly, T1-weighted image were denoised using a non-local mean filter (Coupe et al., 2008) and then corrected for the usual acquisition bias with the N4 method from the Advanced Normalization Tools (ANT) package (Tustison et al., 2010). Anatomical images were then segmented with the Statistical Parametric Mapping (SPM) VBM8 toolbox (Ashburner and Friston, 2000) to create grey matter (GM), white matter (WM) and cerebro-spinal fluid (CSF) probabilistic maps. Bias-corrected T1 images were then coregistered to the non-gradient diffusion image and to the MNI template using respectively ANT's elastic and symmetric method (Avants et al., 2011). Brain regions of the Anatomical Automatic Labeling (AAL) template (Tzourio-Mazoyer et al., 2002) were then resampled to the anatomical and diffusion space of each subject. Finally, FSL's Bedpostx and Probtrackx tractography was performed with default parameters on AAL regions, resulting in a 90x90 connectivity matrix.

Appendix 7. Materials and Methods: Movie vs. Rest

Study design

Twenty-four right-handed young, healthy volunteers (15 females, 20–31 years old) participated in the study. They were informed about the experimental procedures, which were approved by the Ethics Committee of the Chieti University, and signed a written informed consent. The study included a resting state and a natural vision condition. In the resting state, participants fixated a red target with a diameter of 0.3 visual degrees on a black screen. In the natural-vision condition, subjects watched (and listened) to 30 minutes of the movie "The Good, the Bad and the Ugly" in a window of 24x10.2 visual degrees. Visual stimuli were projected on a translucent screen using an LCD projector, and viewed by the participants through a mirror tilted by 45 degrees. Auditory stimuli were delivered using MR-compatible headphones.

Data acquisition

Functional imaging was performed with a 3T MR scanner (Achieva; Philips Medical Systems, Best, The Netherlands) at the Institute for Advanced Biomedical Technologies in Chieti, Italy. The functional images were obtained using T2*-weighted echo-planar images (EPI) with BOLD contrast using SENSE imaging. EPIs comprised of 32 axial slices acquired in ascending order and covering the entire brain (32 slices, 230 x 230 in-plane matrix, TR/TE=2000/35, flip angle = 90°, voxel size=2.875×2.875×3.5 mm3). For each subject, 2 and 3 scanning runs of 10 minutes duration were acquired for resting state and natural vision, respectively. Each run included 5 dummy volumes – allowing the MRI signal to reach steady state, and an additional 300 functional volumes that were used for analysis. Eye position was monitored during scanning using a pupil-corneal reflection system at 120 Hz (Iscan, Burlington, MA, USA). A three-dimensional high-resolution T1-weighted image, for anatomical reference, was acquired using an MP-RAGE sequence (TR/TE=8.1/3.7, voxel size=0.938x0.938x1 mm3) at the end of the scanning session.

Data processing

Data preprocessing was performed using SPM5 (Wellcome Department of Cognitive Neurology, London, UK) running under MATLAB (The Mathworks, Natick, MA). The preprocessing steps involved the following: (1) correction for slice-timing differences (2) correction of head-motion across functional images, (3) coregistration of the anatomical image and the mean functional image, and (4) spatial normalization of all images to a standard stereotaxic space (Montreal Neurological Institute, MNI) with a voxel size of 3×3×3 mm3. Furthermore, the BOLD time series in MNI space were subjected to spatial independent component analysis (ICA) for the identification and removal of artifacts related to blood pulsation, head movement and instrumental spikes (Sui et al., 2009). This BOLD artifact removal procedure was performed by means of the GIFT toolbox (Medical Image Analysis Lab, University of New Mexico). No global signal regression or spatial smoothing was applied.

For each recording session (subject and run), we extracted the mean BOLD time series from the 66 regions of interest (ROIs) of the brain atlas used in Hagmann et al. (2008): see Supplementary Table 1 for details. For each ROI, we calculated an overall percent signal change value in the natural vision condition using the resting state condition as baseline. For resting state and natural vision sessions separately, we concatenated the BOLD time series for each region, and calculated the 66x66 correlation matrix representing the FC between each pair of cortical areas.

Structural Connectivity Matrix

Anatomical connectivity was estimated from Diffusion Spectrum Imaging (DSI) data collected in five healthy right-handed male participants (Hagmann et al., 2008; Honey et al., 2009). The grey matter was first parcellated into 66 ROIs, using the same low-resolution atlas used for the FC analysis (Hagmann et al., 2008). For each subject, we performed white matter tractography between pairs of cortical areas to estimate a neuroanatomical connectivity matrix. The coupling weights between two brain areas were quantified using the fibre tract density, and were proportional to a normalised number of detected tracts. The structural matrix (SC) was then obtained by averaging the matrices over subjects.

BIBLIOGRAPHY

Achard, S., Salvador, R., Whitcher, B., Suckling, J., Bullmore, E., 2006. A Resilient, Low-Frequency, Small-World Human Brain Functional Network with Highly Connected Association Cortical Hubs. J. Neurosci. 26, 63–72. doi:10.1523/JNEUROSCI.3874-05.2006

Agosta, F., Pievani, M., Geroldi, C., Copetti, M., Frisoni, G.B., Filippi, M., 2012. Resting state fMRI in Alzheimer's disease: beyond the default mode network. Neurobiol. Aging 33, 1564–1578. doi:10.1016/j.neurobiolaging.2011.06.007

Ajilore, O., Zhan, L., Gadelkarim, J., Zhang, A., Feusner, J.D., Yang, S., Thompson, P.M., Kumar, A., Leow, A., 2013. Constructing the resting state structural connectome. Front. Neuroinformatics 7, 30. doi:10.3389/fninf.2013.00030

Alaerts, K., Geerlings, F., Herremans, L., Swinnen, S.P., Verhoeven, J., Sunaert, S., Wenderoth, N., 2015. Functional Organization of the Action Observation Network in Autism: A Graph Theory Approach. PloS One 10, e0137020. doi:10.1371/journal.pone.0137020

Albert, N.B., Robertson, E.M., Miall, R.C., 2009. The Resting Human Brain and Motor Learning. Curr. Biol. 19, 1023–1027. doi:10.1016/j.cub.2009.04.028

Alexopoulos, G.S., Hoptman, M.J., Kanellopoulos, D., Murphy, C.F., Lim, K.O., Gunning, F.M., 2012. Functional connectivity in the cognitive control network and the default mode network in late-life depression. J. Affect. Disord. 139, 56–65. doi:10.1016/j.jad.2011.12.002

Allen, E.A., Damaraju, E., Plis, S.M., Erhardt, E.B., Eichele, T., Calhoun, V.D., 2014. Tracking Whole-Brain Connectivity Dynamics in the Resting State. Cereb. Cortex 24, 663–676. doi:10.1093/cercor/bhs352

Allen, G., Barnard, H., McColl, R., Hester, A.L., Fields, J.A., Weiner, M.F., Ringe, W.K., Lipton, A.M., Brooker, M., McDonald, E., Rubin, C.D., Cullum, C.M., 2007. Reduced hippocampal functional connectivity in Alzheimer disease. Arch. Neurol. 64, 1482–1487. doi:10.1001/archneur.64.10.1482

Alstott, J., Breakspear, M., Hagmann, P., Cammoun, L., Sporns, O., 2009. Modeling the Impact of Lesions in the Human Brain. PLoS Comput Biol 5, e1000408. doi:10.1371/journal.pcbi.1000408

Anand, A., Li, Y., Wang, Y., Wu, J., Gao, S., Bukhari, L., Mathews, V.P., Kalnin, A., Lowe, M.J., 2005. Activity and Connectivity of Brain Mood Regulating Circuit in Depression: A Functional Magnetic Resonance Study. Biol. Psychiatry 57, 1079–1088. doi:10.1016/j.biopsych.2005.02.021

Anderson, P.J., De Luca, C.R., Hutchinson, E., Roberts, G., Doyle, L.W., Victorian Infant Collaborative Group, 2010. Underestimation of developmental delay by the new Bayley-III Scale. Arch. Pediatr. Adolesc. Med. 164, 352–356. doi:10.1001/archpediatrics.2010.20

Andrews-Hanna, J.R., Snyder, A.Z., Vincent, J.L., Lustig, C., Head, D., Raichle, M.E., Buckner, R.L., 2007. Disruption of large-scale brain systems in advanced aging. Neuron 56, 924–935. doi:10.1016/j.neuron.2007.10.038

Anticevic, A., Cole, M.W., Murray, J.D., Corlett, P.R., Wang, X.-J., Krystal, J.H., 2012. The role of default network deactivation in cognition and disease. Trends Cogn. Sci. 16, 584–592. doi:10.1016/j.tics.2012.10.008

Anticevic, A., Corlett, P.R., Cole, M.W., Savic, A., Gancsos, M., Tang, Y., Repovs, G., Murray, J.D., Driesen, N.R., Morgan, P.T., Xu, K., Wang, F., Krystal, J.H., 2015. N-Methyl-D-Aspartate Receptor Antagonist Effects on Prefrontal Cortical Connectivity Better Model Early Than Chronic Schizophrenia. Biol. Psychiatry, N-Methyl-D-Aspartate Receptor Deficits and Schizophrenia 77, 569–580. doi:10.1016/j.biopsych.2014.07.022

Arieli, A., Sterkin, A., Grinvald, A., Aertsen, A., 1996. Dynamics of ongoing activity: explanation of the large variability in evoked cortical responses. Science 273, 1868–1871.

Ashburner, J., 2007. A fast diffeomorphic image registration algorithm. NeuroImage 38, 95–113. doi:10.1016/j.neuroimage.2007.07.007

Ashburner, J., Friston, K.J., 2005. Unified segmentation. NeuroImage 26, 839–851. doi:10.1016/j.neuroimage.2005.02.018

Ashburner, J., Friston, K.J., 2000. Voxel-based morphometry--the methods. NeuroImage 11, 805–821. doi:10.1006/nimg.2000.0582

Avants, B.B., Tustison, N.J., Song, G., Cook, P.A., Klein, A., Gee, J.C., 2011. A reproducible evaluation of ANTs similarity metric performance in brain image registration. NeuroImage 54, 2033–2044. doi:10.1016/j.neuroimage.2010.09.025

Avery, J.A., Drevets, W.C., Moseman, S.E., Bodurka, J., Barcalow, J.C., Simmons, W.K., 2014. Major Depressive Disorder Is Associated With Abnormal Interoceptive Activity and Functional Connectivity in the Insula. Biol. Psychiatry, Neurostimulation Treatments for Depression 76, 258–266. doi:10.1016/j.biopsych.2013.11.027

Aymé, S., Schmidtke, J., 2007. Networking for rare diseases: a necessity for Europe. Bundesgesundheitsblatt - Gesundheitsforschung - Gesundheitsschutz 50, 1477–1483. doi:10.1007/s00103-007-0381-9

Bai, J.P.F., Bell, R., Buckman, S., Burckart, G.J., Eichler, H.-G., Fang, K.C., Goodsaid, F.M., Jusko, W.J., Lesko, L.L., Meibohm, B., Patterson, S.D., Puig, O., Smerage, J.B., Snider, B.J., Wagner, J.A., Wang, J., Walton, M.K., Weiner, R., 2011. Translational biomarkers: from preclinical to clinical a report of 2009 AAPS/ACCP Biomarker Workshop. AAPS J. 13, 274–283. doi:10.1208/s12248-011-9265-x

Bailey, D.L., Townsend, D.W., Valk, P.E., Maisey, M.N. (Eds.), 2005. Positron Emission Tomography. Springer-Verlag, London.

Bandettini, P.A., Jesmanowicz, A., Wong, E.C., Hyde, J.S., 1993. Processing strategies for time-course data sets in functional MRI of the human brain. Magn. Reson. Med. 30, 161–173.

Barttfeld, P., Uhrig, L., Sitt, J.D., Sigman, M., Jarraya, B., Dehaene, S., 2015. Signature of consciousness in the dynamics of resting-state brain activity. Proc. Natl. Acad. Sci. 112, 887–892. doi:10.1073/pnas.1418031112

Baschat, A.A., 2004. Pathophysiology of fetal growth restriction: implications for diagnosis and surveillance. Obstet. Gynecol. Surv. 59, 617–627.

Bassan, H., Stolar, O., Geva, R., Eshel, R., Fattal-Valevski, A., Leitner, Y., Waron, M., Jaffa, A., Harel, S., 2011. Intrauterine growth-restricted neonates born at term or

preterm: how different? Pediatr. Neurol. 44, 122–130. doi:10.1016/j.pediatrneurol.2010.09.012
Basser, P.J., Mattiello, J., LeBihan, D., 1994. MR diffusion tensor spectroscopy and imaging. Biophys. J. 66, 259–267. doi:10.1016/S0006-3495(94)80775-1
Bassett, D.S., Nelson, B.G., Mueller, B.A., Camchong, J., Lim, K.O., 2012. Altered resting state complexity in schizophrenia. NeuroImage 59, 2196–2207. doi:10.1016/j.neuroimage.2011.10.002
Batalle, D., Eixarch, E., Figueras, F., Muñoz-Moreno, E., Bargallo, N., Illa, M., Acosta-Rojas, R., Amat-Roldan, I., Gratacos, E., 2012. Altered small-world topology of structural brain networks in infants with intrauterine growth restriction and its association with later neurodevelopmental outcome. NeuroImage 60, 1352–1366. doi:10.1016/j.neuroimage.2012.01.059
Batalle, D., Muñoz-Moreno, E., Figueras, F., Bargallo, N., Eixarch, E., Gratacos, E., 2013. Normalization of similarity-based individual brain networks from gray matter MRI and its association with neurodevelopment in infants with intrauterine growth restriction. NeuroImage 83, 901–911. doi:10.1016/j.neuroimage.2013.07.045
Bear, M.F., Connors, B.W., Paradiso, M.A., 2007. Neuroscience. Lippincott Williams & Wilkins.
Beckmann, C.F., DeLuca, M., Devlin, J.T., Smith, S.M., 2005. Investigations into resting-state connectivity using independent component analysis. Philos. Trans. R. Soc. B Biol. Sci. 360, 1001–1013. doi:10.1098/rstb.2005.1634
Beckmann, C.F., Smith, S.M., 2004. Probabilistic independent component analysis for functional magnetic resonance imaging. IEEE Trans. Med. Imaging 23, 137–152. doi:10.1109/TMI.2003.822821
Benjamini, Y., Yekutieli, D., 2001. The control of the false discovery rate in multiple testing under dependency. Ann. Stat. 29, 1165–1188. doi:10.1214/aos/1013699998
Berman, M.G., Misic, B., Buschkuehl, M., Kross, E., Deldin, P.J., Peltier, S., Churchill, N.W., Jaeggi, S.M., Vakorin, V., McIntosh, A.R., Jonides, J., 2014. Does resting-state connectivity reflect depressive rumination? A tale of two analyses. NeuroImage 103, 267–279. doi:10.1016/j.neuroimage.2014.09.027
Berman, M.G., Peltier, S., Nee, D.E., Kross, E., Deldin, P.J., Jonides, J., 2011. Depression, rumination and the default network. Soc. Cogn. Affect. Neurosci. 6, 548–555. doi:10.1093/scan/nsq080
Betti, V., Penna, S. Della, de Pasquale, F., Mantini, D., Marzetti, L., Romani, G.L., Corbetta, M., 2013. Natural scenes viewing alters the dynamics of functional connectivity in the human brain. Neuron 79, 782–797. doi:10.1016/j.neuron.2013.06.022
Birn, R.M., 2012. The role of physiological noise in resting-state functional connectivity. NeuroImage 62, 864–870. doi:10.1016/j.neuroimage.2012.01.016
Biswal, B., Yetkin, F.Z., Haughton, V.M., Hyde, J.S., 1995. Functional connectivity in the motor cortex of resting human brain using echo-planar MRI. Magn. Reson. Med. Off. J. Soc. Magn. Reson. Med. Soc. Magn. Reson. Med. 34, 537–541.
Blennow, K., de Leon, M.J., Zetterberg, H., 2006. Alzheimer's disease. Lancet Lond. Engl. 368, 387–403. doi:10.1016/S0140-6736(06)69113-7
Bluhm, R., Williamson, P., Lanius, R., Théberge, J., Densmore, M., Bartha, R., Neufeld, R., Osuch, E., 2009. Resting state default-mode network connectivity

in early depression using a seed region-of-interest analysis: Decreased connectivity with caudate nucleus. Psychiatry Clin. Neurosci. 63, 754–761. doi:10.1111/j.1440-1819.2009.02030.x

Bobes, J., Bulbena, A., Luque, A., Dal-Ré, R., Ballesteros, J., Ibarra, N., Grupo de Validacion en Espanol de Escalas Psicometricas, 2003. [A comparative psychometric study of the Spanish versions with 6, 17, and 21 items of the Hamilton Depression Rating Scale]. Med. Clínica 120, 693–700.

Bohr, I.J., Kenny, E., Blamire, A., O'Brien, J.T., Thomas, A., Richardson, J., Kaiser, M., 2013. Resting-state functional connectivity in late-life depression: higher global connectivity and more long distance connections. Neuropsychiatr. Imaging Stimul. 3, 116. doi:10.3389/fpsyt.2012.00116

Boly, M., Garrido, M.I., Gosseries, O., Bruno, M.-A., Boveroux, P., Schnakers, C., Massimini, M., Litvak, V., Laureys, S., Friston, K., 2011. Preserved Feedforward But Impaired Top-Down Processes in the Vegetative State. Science 332, 858–862. doi:10.1126/science.1202043

Boutros, N., Torello, M.W., Burns, E.M., Wu, S.S., Nasrallah, H.A., 1995. Evoked potentials in subjects at risk for Alzheimer's disease. Psychiatry Res. 57, 57–63.

Breakspear, M., Terry, J.R., Friston, K.J., 2003. Modulation of excitatory synaptic coupling facilitates synchronization and complex dynamics in a biophysical model of neuronal dynamics. Netw. Bristol Engl. 14, 703–732.

Brier, M.R., Thomas, J.B., Ances, B.M., 2014. Network dysfunction in Alzheimer's disease: refining the disconnection hypothesis. Brain Connect. 4, 299–311. doi:10.1089/brain.2014.0236

Broca, P.P., 1861. Perte de la parole, ramollissement chronique et destruction partielle du lobe antérieur gauche du cerveau. Bull Soc Anthropol 2, 301–321.

Brodersen, K.H., Schofield, T.M., Leff, A.P., Ong, C.S., Lomakina, E.I., Buhmann, J.M., Stephan, K.E., 2011. Generative Embedding for Model-Based Classification of fMRI Data. PLoS Comput Biol 7, e1002079. doi:10.1371/journal.pcbi.1002079

Brookes, M.J., Woolrich, M., Luckhoo, H., Price, D., Hale, J.R., Stephenson, M.C., Barnes, G.R., Smith, S.M., Morris, P.G., 2011. Investigating the electrophysiological basis of resting state networks using magnetoencephalography. Proc. Natl. Acad. Sci. 108, 16783–16788. doi:10.1073/pnas.1112685108

Broyd, S.J., Demanuele, C., Debener, S., Helps, S.K., James, C.J., Sonuga-Barke, E.J.S., 2009. Default-mode brain dysfunction in mental disorders: A systematic review. Neurosci. Biobehav. Rev. 33, 279–296. doi:10.1016/j.neubiorev.2008.09.002

Brunel, N., Wang, X.J., 2001. Effects of neuromodulation in a cortical network model of object working memory dominated by recurrent inhibition. J. Comput. Neurosci. 11, 63–85.

Büchel, C., Friston, K.J., 1997. Modulation of connectivity in visual pathways by attention: cortical interactions evaluated with structural equation modelling and fMRI. Cereb. Cortex 7, 768–778. doi:10.1093/cercor/7.8.768

Buckner, R.L., Andrews-Hanna, J.R., Schacter, D.L., 2008. The brain's default network: anatomy, function, and relevance to disease. Ann. N. Y. Acad. Sci. 1124, 1–38. doi:10.1196/annals.1440.011

Bullmore, E.T., Bassett, D.S., 2011. Brain graphs: graphical models of the human brain connectome. Annu. Rev. Clin. Psychol. 7, 113–140. doi:10.1146/annurev-clinpsy-040510-143934

Bush, K., Zhou, S., Cisler, J., Bian, J., Hazaroglu, O., Gillispie, K., Yoshigoe, K., Kilts, C., 2015. A deconvolution-based approach to identifying large-scale effective connectivity. Magn. Reson. Imaging. doi:10.1016/j.mri.2015.07.015

Buxton, R.B., Wong, E.C., Frank, L.R., 1998. Dynamics of blood flow and oxygenation changes during brain activation: The balloon model. Magn. Reson. Med. 39, 855–864. doi:10.1002/mrm.1910390602

Cabral, J., Hugues, E., Kringelbach, M.L., Deco, G., 2012a. Modeling the outcome of structural disconnection on resting-state functional connectivity. NeuroImage 62, 1342 – 1353. doi:10.1016/j.neuroimage.2012.06.007

Cabral, J., Hugues, E., Sporns, O., Deco, G., 2011. Role of local network oscillations in resting-state functional connectivity. NeuroImage 57, 130–139. doi:10.1016/j.neuroimage.2011.04.010

Cabral, J., Kringelbach, M.L., Deco, G., 2014. Exploring the network dynamics underlying brain activity during rest. Prog. Neurobiol. 114, 102–131. doi:10.1016/j.pneurobio.2013.12.005

Cabral, J., Kringelbach, M.L., Deco, G., 2012b. Functional graph alterations in schizophrenia: a result from a global anatomic decoupling? Pharmacopsychiatry 45 Suppl 1, 57–64.

Cabral, J., Luckhoo, H., Woolrich, M., Joensson, M., Mohseni, H., Baker, A., Kringelbach, M.L., Deco, G., 2014. Exploring mechanisms of spontaneous MEG functional connectivity: How delayed network interactions lead to structured amplitude envelopes of band-pass filtered oscillations. Neuroimage 90, 423–435.

Calhoun, V.D., Kiehl, K.A., Pearlson, G.D., 2008. Modulation of temporally coherent brain networks estimated using ICA at rest and during cognitive tasks. Hum. Brain Mapp. 29, 828–838. doi:10.1002/hbm.20581

Carbonell, F., Bellec, P., Shmuel, A., 2011. Global and System-Specific Resting-State fMRI Fluctuations Are Uncorrelated: Principal Component Analysis Reveals Anti-Correlated Networks. Brain Connect. 1, 496–510. doi:10.1089/brain.2011.0065

Carhart-Harris, R.L., Leech, R., Hellyer, P.J., Shanahan, M., Feilding, A., Tagliazucchi, E., Chialvo, D.R., Nutt, D., 2014. The entropic brain: a theory of conscious states informed by neuroimaging research with psychedelic drugs. Front. Hum. Neurosci. 8, 20. doi:10.3389/fnhum.2014.00020

Cavanna, A.E., Trimble, M.R., 2006. The precuneus: a review of its functional anatomy and behavioural correlates. Brain 129, 564–583. doi:10.1093/brain/awl004

Celone, K.A., Calhoun, V.D., Dickerson, B.C., Atri, A., Chua, E.F., Miller, S.L., DePeau, K., Rentz, D.M., Selkoe, D.J., Blacker, D., Albert, M.S., Sperling, R.A., 2006. Alterations in memory networks in mild cognitive impairment and Alzheimer's disease: an independent component analysis. J. Neurosci. Off. J. Soc. Neurosci. 26, 10222–10231. doi:10.1523/JNEUROSCI.2250-06.2006

Cerliani, L., Mennes, M., Thomas, R.M., Di Martino, A., Thioux, M., Keysers, C., 2015. Increased Functional Connectivity Between Subcortical and Cortical Resting-State Networks in Autism Spectrum Disorder. JAMA Psychiatry 72, 767–777. doi:10.1001/jamapsychiatry.2015.0101

Chang, C., Glover, G.H., 2010. Time–frequency dynamics of resting-state brain connectivity measured with fMRI. NeuroImage 50, 81–98. doi:10.1016/j.neuroimage.2009.12.011

Chen, H., Duan, X., Liu, F., Lu, F., Ma, X., Zhang, Y., Uddin, L.Q., Chen, H., 2015. Multivariate classification of autism spectrum disorder using frequency-specific resting-state functional connectivity-A multi-center study. Prog. Neuropsychopharmacol. Biol. Psychiatry 64, 1–9. doi:10.1016/j.pnpbp.2015.06.014

Cherkassky, V.L., Kana, R.K., Keller, T.A., Just, M.A., 2006. Functional connectivity in a baseline resting-state network in autism. Neuroreport 17, 1687–1690. doi:10.1097/01.wnr.0000239956.45448.4c

Chung, K., Deisseroth, K., 2013. CLARITY for mapping the nervous system. Nat. Methods 10, 508–513. doi:10.1038/nmeth.2481

Cohen, D., 1968. Magnetoencephalography: evidence of magnetic fields produced by alpha-rhythm currents. Science 161, 784–786.

Colom, F., Vieta, E., Martínez-Arán, A., Garcia-Garcia, M., Reinares, M., Torrent, C., Goikolea, J.M., Banús, S., Salamero, M., 2002. [Spanish version of a scale for the assessment of mania: validity and reliability of the Young Mania Rating Scale]. Med. Clínica 119, 366–371.

Connolly, C.G., Wu, J., Ho, T.C., Hoeft, F., Wolkowitz, O., Eisendrath, S., Frank, G., Hendren, R., Max, J.E., Paulus, M.P., Tapert, S.F., Banerjee, D., Simmons, A.N., Yang, T.T., 2013. Resting-State Functional Connectivity of Subgenual Anterior Cingulate Cortex in Depressed Adolescents. Biol. Psychiatry 74, 898–907. doi:10.1016/j.biopsych.2013.05.036

Conturo, T.E., Lori, N.F., Cull, T.S., Akbudak, E., Snyder, A.Z., Shimony, J.S., McKinstry, R.C., Burton, H., Raichle, M.E., 1999. Tracking neuronal fiber pathways in the living human brain. Proc. Natl. Acad. Sci. U. S. A. 96, 10422–10427.

Cordes, D., Haughton, V., Carew, J.D., Arfanakis, K., Maravilla, K., 2002. Hierarchical clustering to measure connectivity in fMRI resting-state data. Magn. Reson. Imaging 20, 305–317. doi:10.1016/S0730-725X(02)00503-9

Cordes, D., Haughton, V.M., Arfanakis, K., Carew, J.D., Turski, P.A., Moritz, C.H., Quigley, M.A., Meyerand, M.E., 2001. Frequencies Contributing to Functional Connectivity in the Cerebral Cortex in "Resting-state" Data. Am. J. Neuroradiol. 22, 1326–1333.

Coupe, P., Yger, P., Prima, S., Hellier, P., Kervrann, C., Barillot, C., 2008. An optimized blockwise nonlocal means denoising filter for 3-D magnetic resonance images. IEEE Trans. Med. Imaging 27, 425–441. doi:10.1109/TMI.2007.906087

Craddock, N., Owen, M.J., 2010. Data and clinical utility should be the drivers of changes to psychiatric classification. Br. J. Psychiatry J. Ment. Sci. 197, 158; author reply 158–159. doi:10.1192/bjp.197.2.158

Craddock, R.C., Holtzheimer, P.E., Hu, X.P., Mayberg, H.S., 2009. Disease state prediction from resting state functional connectivity. Magn. Reson. Med. 62, 1619–1628. doi:10.1002/mrm.22159

Cullen, K.R., Gee, D.G., Klimes-Dougan, B., Gabbay, V., Hulvershorn, L., Mueller, B.A., Camchong, J., Bell, C.J., Houri, A., Kumra, S., Lim, K.O., Castellanos, F.X., Milham, M.P., 2009. A preliminary study of functional connectivity in comorbid adolescent depression. Neurosci. Lett. 460, 227–231. doi:10.1016/j.neulet.2009.05.022

Cuthbert, B.N., Insel, T.R., 2013. Toward the future of psychiatric diagnosis: the seven pillars of RDoC. BMC Med. 11, 126. doi:10.1186/1741-7015-11-126

Damaraju, E., Allen, E.A., Belger, A., Ford, J.M., McEwen, S., Mathalon, D.H., Mueller, B.A., Pearlson, G.D., Potkin, S.G., Preda, A., Turner, J.A., Vaidya, J.G., van Erp, T.G., Calhoun, V.D., 2014. Dynamic functional connectivity analysis reveals transient states of dysconnectivity in schizophrenia. NeuroImage Clin. 5, 298–308. doi:10.1016/j.nicl.2014.07.003

Damoiseaux, J.S., Beckmann, C.F., Arigita, E.J.S., Barkhof, F., Scheltens, P., Stam, C.J., Smith, S.M., Rombouts, S. a. R.B., 2008. Reduced resting-state brain activity in the "default network" in normal aging. Cereb. Cortex 18, 1856–1864. doi:10.1093/cercor/bhm207

Damoiseaux, J.S., Greicius, M.D., 2009. Greater than the sum of its parts: a review of studies combining structural connectivity and resting-state functional connectivity. Brain Struct. Funct. 213, 525–533. doi:10.1007/s00429-009-0208-6

Damoiseaux, J.S., Rombouts, S. a. R.B., Barkhof, F., Scheltens, P., Stam, C.J., Smith, S.M., Beckmann, C.F., 2006. Consistent resting-state networks across healthy subjects. Proc. Natl. Acad. Sci. 103, 13848–13853. doi:10.1073/pnas.0601417103

Dandash, O., Harrison, B.J., Adapa, R., Gaillard, R., Giorlando, F., Wood, S.J., Fletcher, P.C., Fornito, A., 2015. Selective augmentation of striatal functional connectivity following NMDA receptor antagonism: implications for psychosis. Neuropsychopharmacol. Off. Publ. Am. Coll. Neuropsychopharmacol. 40, 622–631. doi:10.1038/npp.2014.210

Daunizeau, J., Friston, K.J., Kiebel, S.J., 2009. Variational Bayesian identification and prediction of stochastic nonlinear dynamic causal models. Phys. Nonlinear Phenom. 238, 2089–2118. doi:10.1016/j.physd.2009.08.002

Dauwels, J., Vialatte, F., Musha, T., Cichocki, A., 2010. A comparative study of synchrony measures for the early diagnosis of Alzheimer's disease based on EEG. NeuroImage 49, 668–693. doi:10.1016/j.neuroimage.2009.06.056

David, O., Guillemain, I., Saillet, S., Reyt, S., Deransart, C., Segebarth, C., Depaulis, A., 2008. Identifying Neural Drivers with Functional MRI: An Electrophysiological Validation. PLoS Biol 6, e315. doi:10.1371/journal.pbio.0060315

De Bie, H.M.A., Oostrom, K.J., Boersma, M., Veltman, D.J., Barkhof, F., Delemarre-van de Waal, H.A., van den Heuvel, M.P., 2011. Global and Regional Differences in Brain Anatomy of Young Children Born Small for Gestational Age. PLoS ONE 6, e24116. doi:10.1371/journal.pone.0024116

Deco, G., Corbetta, M., 2011. The Dynamical Balance of the Brain at Rest. The Neuroscientist 17, 107–123. doi:10.1177/1073858409354384

Deco, G., Jirsa, V.K., 2012. Ongoing Cortical Activity at Rest: Criticality, Multistability, and Ghost Attractors. J. Neurosci. 32, 3366–3375. doi:10.1523/JNEUROSCI.2523-11.2012

Deco, G., Jirsa, V., McIntosh, A.R., Sporns, O., Kötter, R., 2009a. Key role of coupling, delay, and noise in resting brain fluctuations. Proc. Natl. Acad. Sci. 106, 10302–10307. doi:10.1073/pnas.0901831106

Deco, G., Kringelbach, M.L., 2014. Great expectations: using whole-brain computational connectomics for understanding neuropsychiatric disorders. Neuron 84, 892–905. doi:10.1016/j.neuron.2014.08.034

Deco, G., McIntosh, A.R., Shen, K., Hutchison, R.M., Menon, R.S., Everling, S., Hagmann, P., Jirsa, V.K., 2014a. Identification of Optimal Structural Connectivity Using Functional Connectivity and Neural Modeling. J. Neurosci. 34, 7910–7916. doi:10.1523/JNEUROSCI.4423-13.2014

Deco, G., Ponce-Alvarez, A., Hagmann, P., Romani, G.L., Mantini, D., Corbetta, M., 2014b. How Local Excitation-Inhibition Ratio Impacts the Whole Brain Dynamics. J. Neurosci. 34, 7886–7898. doi:10.1523/JNEUROSCI.5068-13.2014

Deco, G., Ponce-Alvarez, A., Mantini, D., Romani, G.L., Hagmann, P., Corbetta, M., 2013. Resting-State Functional Connectivity Emerges from Structurally and Dynamically Shaped Slow Linear Fluctuations. J. Neurosci. 33.

Deco, G., Rolls, E.T., Romo, R., 2009b. Stochastic dynamics as a principle of brain function. Prog. Neurobiol. 88, 1 – 16. doi:10.1016/j.pneurobio.2009.01.006

Deco, G., Thiele, A., 2009. Attention – oscillations and neuropharmacology. Eur. J. Neurosci. 30, 347–354. doi:10.1111/j.1460-9568.2009.06833.x

De Luca, M., Beckmann, C.F., De Stefano, N., Matthews, P.M., Smith, S.M., 2006. fMRI resting state networks define distinct modes of long-distance interactions in the human brain. NeuroImage 29, 1359–1367. doi:10.1016/j.neuroimage.2005.08.035

Denis Jordan, R.I., 2013. Simultaneous Electroencephalographic and Functional Magnetic Resonance Imaging Indicate Impaired Cortical Top-Down Processing in Association with Anesthetic-induced Unconsciousness. Anesthesiology 119. doi:10.1097/ALN.0b013e3182a7ca92

Dennis, E.L., Thompson, P.M., 2014. Functional brain connectivity using fMRI in aging and Alzheimer's disease. Neuropsychol. Rev. 24, 49–62. doi:10.1007/s11065-014-9249-6

Dickerson, B.C., Salat, D.H., Bates, J.F., Atiya, M., Killiany, R.J., Greve, D.N., Dale, A.M., Stern, C.E., Blacker, D., Albert, M.S., Sperling, R.A., 2004. Medial temporal lobe function and structure in mild cognitive impairment. Ann. Neurol. 56, 27–35. doi:10.1002/ana.20163

Di, X., Biswal, B.B., 2014. Identifying the default mode network structure using dynamic causal modeling on resting-state functional magnetic resonance imaging. NeuroImage 86, 53–59. doi:10.1016/j.neuroimage.2013.07.071

Dubois, J., Benders, M., Borradori-Tolsa, C., Cachia, A., Lazeyras, F., Leuchter, R.H.-V., Sizonenko, S.V., Warfield, S.K., Mangin, J.F., Hüppi, P.S., 2008. Primary cortical folding in the human newborn: an early marker of later functional development. Brain 131, 2028–2041. doi:10.1093/brain/awn137

Dunn, O.J., 1959. Estimation of the Medians for Dependent Variables. Ann. Math. Stat. 30, 192–197. doi:10.1214/aoms/1177706374

Eixarch, E., Meler, E., Iraola, A., Illa, M., Crispi, F., Hernandez-Andrade, E., Gratacos, E., Figueras, F., 2008. Neurodevelopmental outcome in 2-year-old infants who were small-for-gestational age term fetuses with cerebral blood flow redistribution. Ultrasound Obstet. Gynecol. Off. J. Int. Soc. Ultrasound Obstet. Gynecol. 32, 894–899. doi:10.1002/uog.6249

Fair, D.A., Cohen, A.L., Dosenbach, N.U.F., Church, J.A., Miezin, F.M., Barch, D.M., Raichle, M.E., Petersen, S.E., Schlaggar, B.L., 2008. The maturing architecture of the brain's default network. Proc. Natl. Acad. Sci. 105, 4028–4032. doi:10.1073/pnas.0800376105

Fair, D.A., Cohen, A.L., Power, J.D., Dosenbach, N.U.F., Church, J.A., Miezin, F.M., Schlaggar, B.L., Petersen, S.E., 2009. Functional Brain Networks Develop from a "Local to Distributed" Organization. PLoS Comput Biol 5, e1000381. doi:10.1371/journal.pcbi.1000381

Fan, J., Xu, P., Van Dam, N.T., Eilam-Stock, T., Gu, X., Luo, Y., Hof, P.R., 2012. Spontaneous brain activity relates to autonomic arousal. J. Neurosci. Off. J. Soc. Neurosci. 32, 11176–11186. doi:10.1523/JNEUROSCI.1172-12.2012

Felleman, D.J., Van Essen, D.C., 1991. Distributed hierarchical processing in the primate cerebral cortex. Cereb. Cortex N. Y. N 1991 1, 1–47.

Ferguson, M.A., Anderson, J.S., 2012. Dynamical stability of intrinsic connectivity networks. NeuroImage 59, 4022–4031. doi:10.1016/j.neuroimage.2011.10.062

Ferrari, A.J., Charlson, F.J., Norman, R.E., Patten, S.B., Freedman, G., Murray, C.J.L., Vos, T., Whiteford, H.A., 2013. Burden of Depressive Disorders by Country, Sex, Age, and Year: Findings from the Global Burden of Disease Study 2010. PLoS Med 10, e1001547. doi:10.1371/journal.pmed.1001547

Figueras, F., Meler, E., Iraola, A., Eixarch, E., Coll, O., Figueras, J., Francis, A., Gratacos, E., Gardosi, J., 2008. Customized birthweight standards for a Spanish population. Eur. J. Obstet. Gynecol. Reprod. Biol. 136, 20–24. doi:10.1016/j.ejogrb.2006.12.015

Filippi, M., Agosta, F., 2011. Structural and functional network connectivity breakdown in Alzheimer's disease studied with magnetic resonance imaging techniques. J. Alzheimers Dis. JAD 24, 455–474. doi:10.3233/JAD-2011-101854

Fillard, P., Descoteaux, M., Goh, A., Gouttard, S., Jeurissen, B., Malcolm, J., Ramirez-Manzanares, A., Reisert, M., Sakaie, K., Tensaouti, F., Yo, T., Mangin, J.-F., Poupon, C., 2011. Quantitative evaluation of 10 tractography algorithms on a realistic diffusion MR phantom. NeuroImage 56, 220–234. doi:10.1016/j.neuroimage.2011.01.032

First, M., 2002. Structured Clinical Interview for DSM-IV-TR Axis I Disorders, Research Version, Non-Patient Edition (SCID-I/P).

First, M., 2001. Structured Clinical Interview for DSM-IV-TR Axis I Disorders, Research Version, Patient Edition (SCID-I/P).

Fitzhugh, R., 1961. Impulses and Physiological States in Theoretical Models of Nerve Membrane. Biophys. J. 1, 445–466.

Fox, M.D., Greicius, M., 2010. Clinical applications of resting state functional connectivity. Front. Syst. Neurosci. 4, 19. doi:10.3389/fnsys.2010.00019

Fox, M.D., Raichle, M.E., 2007. Spontaneous fluctuations in brain activity observed with functional magnetic resonance imaging. Nat. Rev. Neurosci. 8, 700–711. doi:10.1038/nrn2201

Fox, M.D., Snyder, A.Z., Vincent, J.L., Corbetta, M., Essen, D.C.V., Raichle, M.E., 2005. The human brain is intrinsically organized into dynamic, anticorrelated functional networks. Proc. Natl. Acad. Sci. U. S. A. 102, 9673–9678. doi:10.1073/pnas.0504136102

Fox, M.D., Zhang, D., Snyder, A.Z., Raichle, M.E., 2009. The Global Signal and Observed Anticorrelated Resting State Brain Networks. J. Neurophysiol. 101, 3270–3283. doi:10.1152/jn.90777.2008

Fransson, P., 2005. Spontaneous low-frequency BOLD signal fluctuations: An fMRI investigation of the resting-state default mode of brain function hypothesis. Hum. Brain Mapp. 26, 15–29. doi:10.1002/hbm.20113

Fransson, P., Skiöld, B., Engström, M., Hallberg, B., Mosskin, M., Åden, U., Lagercrantz, H., Blennow, M., 2009. Spontaneous Brain Activity in the Newborn Brain During Natural Sleep—An fMRI Study in Infants Born at Full Term. Pediatr. Res. 66, 301–305. doi:10.1203/PDR.0b013e3181b1bd84

Fransson, P., Skiöld, B., Horsch, S., Nordell, A., Blennow, M., Lagercrantz, H., Åden, U., 2007. Resting-state networks in the infant brain. Proc. Natl. Acad. Sci. 104, 15531–15536. doi:10.1073/pnas.0704380104

Friston, K.J., 2011. Functional and Effective Connectivity: A Review. Brain Connect. 1, 13–36. doi:10.1089/brain.2011.0008

Friston, K.J., Buechel, C., Fink, G.R., Morris, J., Rolls, E., Dolan, R.J., 1997. Psychophysiological and modulatory interactions in neuroimaging. NeuroImage 6, 218–229. doi:10.1006/nimg.1997.0291

Friston, K.J., Harrison, L., Penny, W., 2003. Dynamic causal modelling. NeuroImage 19, 1273–1302.

Friston, K.J., Kahan, J., Biswal, B., Razi, A., 2014a. A DCM for resting state fMRI. NeuroImage 94, 396–407. doi:10.1016/j.neuroimage.2013.12.009

Friston, K.J., Kahan, J., Razi, A., Stephan, K.E., Sporns, O., 2014b. On nodes and modes in resting state fMRI. NeuroImage 99, 533–547. doi:10.1016/j.neuroimage.2014.05.056

Friston, K.J., Ungerleider, L.G., Jezzard, P., Turner, R., 1995. Characterising modulatory interactions between V1 and V2 in human cortex with fMRI. Hum Brain Map 2, 211–224.

Friston, K., Mattout, J., Trujillo-Barreto, N., Ashburner, J., Penny, W., 2007. Variational free energy and the Laplace approximation. NeuroImage 34, 220–234. doi:10.1016/j.neuroimage.2006.08.035

Fukunaga, M., Horovitz, S.G., van Gelderen, P., de Zwart, J.A., Jansma, J.M., Ikonomidou, V.N., Chu, R., Deckers, R.H.R., Leopold, D.A., Duyn, J.H., 2006. Large-amplitude, spatially correlated fluctuations in BOLD fMRI signals during extended rest and early sleep stages. Magn. Reson. Imaging 24, 979–992. doi:10.1016/j.mri.2006.04.018

Gao, W., Zhu, H., Giovanello, K.S., Smith, J.K., Shen, D., Gilmore, J.H., Lin, W., 2009. Evidence on the emergence of the brain's default network from 2-week-old to 2-year-old healthy pediatric subjects. Proc. Natl. Acad. Sci. 106, 6790–6795. doi:10.1073/pnas.0811221106

Gazzaniga, M.S., Bogen, J.E., Sperry, R.W., 1963. Laterality effects in somesthesis following cerebral commissurotomy in man. Neuropsychologia 1, 209–215.

Geschwind, N., 1965a. Disconnexion syndromes in animals and man I. Brain 88.

Geschwind, N., 1965b. Disconnexion syndromes in animals and man II. Brain 88.

Ghosh, A., Rho, Y., McIntosh, A.R., Kötter, R., Jirsa, V.K., 2008. Noise during Rest Enables the Exploration of the Brain's Dynamic Repertoire. PLoS Comput Biol 4, e1000196. doi:10.1371/journal.pcbi.1000196

Gigandet, X., Hagmann, P., Kurant, M., Cammoun, L., Meuli, R., Thiran, J.-P., 2008. Estimating the confidence level of white matter connections obtained with MRI tractography. PloS One 3, e4006. doi:10.1371/journal.pone.0004006

Gilson, M., Moreno-Bote, R., Ponce-Alvarez, A., Ritter, P., Deco, G., submitted. Inference of Directed Effective Connectivity from fMRI Functional Connectivity Reveals Asymmetries of Cortical Connectome. PLoS Comput. Biol.

Glerean, E., Salmi, J., Lahnakoski, J.M., Jaaskelainen, I.P., Sams, M., 2012. Functional Magnetic Resonance Imaging Phase Synchronization as a Measure of Dynamic Functional Connectivity. Brain Connect. 2, 91–101. doi:10.1089/brain.2011.0068

Goebel, R., Roebroeck, A., Kim, D.-S., Formisano, E., 2003. Investigating directed cortical interactions in time-resolved fMRI data using vector autoregressive modeling and Granger causality mapping. Magn. Reson. Imaging 21, 1251–1261. doi:10.1016/j.mri.2003.08.026

Goldenberg, D., Galván, A., 2015. The use of functional and effective connectivity techniques to understand the developing brain. Dev. Cogn. Neurosci. 12, 155–164. doi:10.1016/j.dcn.2015.01.011

Gong, Q., He, Y., 2015. Depression, neuroimaging and connectomics: a selective overview. Biol. Psychiatry 77, 223–235. doi:10.1016/j.biopsych.2014.08.009

Greicius, M., 2008. Resting-state functional connectivity in neuropsychiatric disorders. Curr. Opin. Neurol. 21, 424–430. doi:10.1097/WCO.0b013e328306f2c5

Greicius, M.D., Flores, B.H., Menon, V., Glover, G.H., Solvason, H.B., Kenna, H., Reiss, A.L., Schatzberg, A.F., 2007. Resting-state functional connectivity in major depression: abnormally increased contributions from subgenual cingulate cortex and thalamus. Biol. Psychiatry 62, 429–437. doi:10.1016/j.biopsych.2006.09.020

Greicius, M.D., Kiviniemi, V., Tervonen, O., Vainionpää, V., Alahuhta, S., Reiss, A.L., Menon, V., 2008. Persistent default-mode network connectivity during light sedation. Hum. Brain Mapp. 29, 839–847. doi:10.1002/hbm.20537

Greicius, M.D., Krasnow, B., Reiss, A.L., Menon, V., 2003. Functional connectivity in the resting brain: A network analysis of the default mode hypothesis. Proc. Natl. Acad. Sci. 100, 253–258. doi:10.1073/pnas.0135058100

Greicius, M.D., Srivastava, G., Reiss, A.L., Menon, V., 2004. Default-mode network activity distinguishes Alzheimer's disease from healthy aging: Evidence from functional MRI. Proc. Natl. Acad. Sci. U. S. A. 101, 4637–4642. doi:10.1073/pnas.0308627101

Greicius, M.D., Supekar, K., Menon, V., Dougherty, R.F., 2009. Resting-State Functional Connectivity Reflects Structural Connectivity in the Default Mode Network. Cereb. Cortex 19, 72–78. doi:10.1093/cercor/bhn059

Grimm, S., Ernst, J., Boesiger, P., Schuepbach, D., Boeker, H., Northoff, G., 2011. Reduced negative BOLD responses in the default-mode network and increased self-focus in depression. World J. Biol. Psychiatry 12, 627–637. doi:10.3109/15622975.2010.545145

Guo, W., Sun, X., Liu, L., Xu, Q., Wu, R., Liu, Z., Tan, C., Chen, H., Zhao, J.-P., 2011. Disrupted regional homogeneity in treatment-resistant depression: A resting-state fMRI study. Prog. Neuropsychopharmacol. Biol. Psychiatry 35, 1297–1302. doi:10.1016/j.pnpbp.2011.02.006

Gusnard, D.A., 2005. Being a self: Considerations from functional imaging. Conscious. Cogn., The Brain and Its Self 14, 679–697. doi:10.1016/j.concog.2005.04.004

Gusnard, D.A., Akbudak, E., Shulman, G.L., Raichle, M.E., 2001. Medial prefrontal cortex and self-referential mental activity: Relation to a default mode of brain function. Proc. Natl. Acad. Sci. 98, 4259–4264. doi:10.1073/pnas.071043098

Gusnard, D.A., Raichle, M.E., 2001. Searching for a baseline: Functional imaging and the resting human brain. Nat. Rev. Neurosci. 2, 685–694. doi:10.1038/35094500

Habas, C., Kamdar, N., Nguyen, D., Prater, K., Beckmann, C.F., Menon, V., Greicius, M.D., 2009. Distinct Cerebellar Contributions to Intrinsic Connectivity Networks. J. Neurosci. 29, 8586–8594. doi:10.1523/JNEUROSCI.1868-09.2009

Hagmann, P., Cammoun, L., Gigandet, X., Meuli, R., Honey, C.J., Wedeen, V.J., Sporns, O., 2008a. Mapping the Structural Core of Human Cerebral Cortex. PLoS Biol 6, e159. doi:10.1371/journal.pbio.0060159

Hagmann, P., Cammoun, L., Gigandet, X., Meuli, R., Honey, C.J., Wedeen, V.J., Sporns, O., 2008b. Mapping the structural core of human cerebral cortex. PLoS Biol. 6, e159. doi:10.1371/journal.pbio.0060159

Hagmann, P., Kurant, M., Gigandet, X., Thiran, P., Wedeen, V.J., Meuli, R., Thiran, J.-P., 2007. Mapping human whole-brain structural networks with diffusion MRI. PloS One 2, e597. doi:10.1371/journal.pone.0000597

Hamilton, J.P., Furman, D.J., Chang, C., Thomason, M.E., Dennis, E., Gotlib, I.H., 2011. Default-Mode and Task-Positive Network Activity in Major Depressive Disorder: Implications for Adaptive and Maladaptive Rumination. Biol. Psychiatry, Neural Connectivity, Ruminations, and Suicide 70, 327–333. doi:10.1016/j.biopsych.2011.02.003

Handwerker, D.A., Roopchansingh, V., Gonzalez-Castillo, J., Bandettini, P.A., 2012. Periodic changes in fMRI connectivity. NeuroImage 63, 1712–1719. doi:10.1016/j.neuroimage.2012.06.078

Harlow, J., 1868. Recovery from the passage of an iron bar through the head. Publ Mass Med Soc 2.

Harrison, L., Penny, W.D., Friston, K., 2003. Multivariate autoregressive modeling of fMRI time series. NeuroImage 19, 1477–1491. doi:10.1016/S1053-8119(03)00160-5

Harrison, S.J., Woolrich, M.W., Robinson, E.C., Glasser, M.F., Beckmann, C.F., Jenkinson, M., Smith, S.M., 2015. Large-scale probabilistic functional modes from resting state fMRI. NeuroImage 109, 217–231. doi:10.1016/j.neuroimage.2015.01.013

Havlicek, M., Roebroeck, A., Friston, K., Gardumi, A., Ivanov, D., Uludag, K., 2015. Physiologically informed dynamic causal modeling of fMRI data. NeuroImage 122, 355–372. doi:10.1016/j.neuroimage.2015.07.078

Hedden, T., Van Dijk, K.R.A., Becker, J.A., Mehta, A., Sperling, R.A., Johnson, K.A., Buckner, R.L., 2009. Disruption of functional connectivity in clinically normal older adults harboring amyloid burden. J. Neurosci. Off. J. Soc. Neurosci. 29, 12686–12694. doi:10.1523/JNEUROSCI.3189-09.2009

Hellyer, P.J., Shanahan, M., Scott, G., Wise, R.J.S., Sharp, D.J., Leech, R., 2014. The Control of Global Brain Dynamics: Opposing Actions of Frontoparietal Control and Default Mode Networks on Attention. J. Neurosci. 34, 451–461. doi:10.1523/JNEUROSCI.1853-13.2014

Herman, G.T., 2009. Fundamentals of Computerized Tomography, Advances in Pattern Recognition. Springer London, London.

Hindriks, R., van Putten, M.J.A.M., Deco, G., 2014. Intra-cortical propagation of EEG alpha oscillations. NeuroImage 103, 444–453. doi:10.1016/j.neuroimage.2014.08.027

Hochberg, Y., Benjamini, Y., 1990. More powerful procedures for multiple significance testing. Stat. Med. 9, 811–818. doi:10.1002/sim.4780090710

Hodgkin, A.L., Huxley, A.F., 1952. A quantitative description of membrane current and its application to conduction and excitation in nerve. J. Physiol. 117, 500–544.

Honey, C.J., Kötter, R., Breakspear, M., Sporns, O., 2007. Network structure of cerebral cortex shapes functional connectivity on multiple time scales. Proc. Natl. Acad. Sci. 104, 10240–10245. doi:10.1073/pnas.0701519104

Honey, C.J., Sporns, O., Cammoun, L., Gigandet, X., Thiran, J.P., Meuli, R., Hagmann, P., 2009. Predicting human resting-state functional connectivity from structural connectivity. Proc. Natl. Acad. Sci. 106, 2035–2040. doi:10.1073/pnas.0811168106

Horovitz, S.G., Braun, A.R., Carr, W.S., Picchioni, D., Balkin, T.J., Fukunaga, M., Duyn, J.H., 2009. Decoupling of the brain's default mode network during deep sleep. Proc. Natl. Acad. Sci. 106, 11376–11381. doi:10.1073/pnas.0901435106

Horovitz, S.G., Fukunaga, M., de Zwart, J.A., van Gelderen, P., Fulton, S.C., Balkin, T.J., Duyn, J.H., 2008. Low frequency BOLD fluctuations during resting wakefulness and light sleep: A simultaneous EEG-fMRI study. Hum. Brain Mapp. 29, 671–682. doi:10.1002/hbm.20428

Horwitz, B., 2003. The elusive concept of brain connectivity. NeuroImage 19, 466–470.

Horwitz, B., Hwang, C., Alstott, J., 2013. Interpreting the effects of altered brain anatomical connectivity on fMRI functional connectivity: a role for computational neural modeling. Front. Hum. Neurosci. 7, 649. doi:10.3389/fnhum.2013.00649

Huettel, S.A., McCarthy, G., 2001. Regional differences in the refractory period of the hemodynamic response: An event-related fMRI study. NeuroImage 14, 967–976. doi:10.1006/nimg.2001.0900

Huisman, T.A.G.M., 2003. Diffusion-weighted imaging: basic concepts and application in cerebral stroke and head trauma. Eur. Radiol. 13, 2283–2297. doi:10.1007/s00330-003-1843-6

Hutchison, R.M., Morton, J.B., 2015. Tracking the Brain's Functional Coupling Dynamics over Development. J. Neurosci. 35, 6849–6859. doi:10.1523/JNEUROSCI.4638-14.2015

Hutchison, R.M., Womelsdorf, T., Allen, E.A., Bandettini, P.A., Calhoun, V.D., Corbetta, M., Penna, S. Della, Duyn, J.H., Glover, G.H., Gonzalez-Castillo, J., Handwerker, D.A., Keilholz, S., Kiviniemi, V., Leopold, D.A., de Pasquale, F., Sporns, O., Walter, M., Chang, C., 2013. Dynamic functional connectivity: Promise, issues, and interpretations. NeuroImage, Mapping the Connectome 80, 360–378. doi:10.1016/j.neuroimage.2013.05.079

Iturria-Medina, Y., Canales-Rodríguez, E.J., Melie-García, L., Valdés-Hernández, P.A., Martínez-Montes, E., Alemán-Gómez, Y., Sánchez-Bornot, J.M., 2007. Characterizing brain anatomical connections using diffusion weighted MRI and graph theory. NeuroImage 36, 645–660. doi:10.1016/j.neuroimage.2007.02.012

Izhikevich, E.M., Edelman, G.M., 2008. Large-scale model of mammalian thalamocortical systems. Proc. Natl. Acad. Sci. U. S. A. 105, 3593–3598. doi:10.1073/pnas.0712231105

Jarvis, S., Glinianaia, S.V., Torrioli, M.-G., Platt, M.-J., Miceli, M., Jouk, P.-S., Johnson, A., Hutton, J., Hemming, K., Hagberg, G., Dolk, H., Chalmers, J., 2003. Cerebral palsy and intrauterine growth in single births: European collaborative study. The Lancet 362, 1106–1111. doi:10.1016/S0140-6736(03)14466-2

Jenkinson, M., Beckmann, C.F., Behrens, T.E.J., Woolrich, M.W., Smith, S.M., 2012. FSL. NeuroImage 62, 782–790. doi:10.1016/j.neuroimage.2011.09.015

J. Kiviniemi, V., Haanpää, H., Kantola, J.-H., Jauhiainen, J., Vainionpää, V., Alahuhta, S., Tervonen, O., 2005. Midazolam sedation increases fluctuation and synchrony of the resting brain BOLD signal. Magn. Reson. Imaging 23, 531–537. doi:10.1016/j.mri.2005.02.009

Jones, D.T., Vemuri, P., Murphy, M.C., Gunter, J.L., Senjem, M.L., Machulda, M.M., Przybelski, S.A., Gregg, B.E., Kantarci, K., Knopman, D.S., Boeve, B.F., Petersen, R.C., Jack, C.R., Jr, 2012. Non-Stationarity in the "Resting Brain's" Modular Architecture. PLoS ONE 7, e39731. doi:10.1371/journal.pone.0039731

Kang, J., Wang, L., Yan, C., Wang, J., Liang, X., He, Y., 2011. Characterizing dynamic functional connectivity in the resting brain using variable parameter regression and Kalman filtering approaches. NeuroImage 56, 1222–1234. doi:10.1016/j.neuroimage.2011.03.033

Kapur, S., Phillips, A.G., Insel, T.R., 2012. Why has it taken so long for biological psychiatry to develop clinical tests and what to do about it? Mol. Psychiatry 17, 1174–1179. doi:10.1038/mp.2012.105

Kasthuri, N., Hayworth, K.J., Berger, D.R., Schalek, R.L., Conchello, J.A., Knowles-Barley, S., Lee, D., Vázquez-Reina, A., Kaynig, V., Jones, T.R., Roberts, M., Morgan, J.L., Tapia, J.C., Seung, H.S., Roncal, W.G., Vogelstein, J.T., Burns, R., Sussman, D.L., Priebe, C.E., Pfister, H., Lichtman, J.W., 2015. Saturated Reconstruction of a Volume of Neocortex. Cell 162, 648–661. doi:10.1016/j.cell.2015.06.054

Kelly, A.M.C., Uddin, L.Q., Biswal, B.B., Castellanos, F.X., Milham, M.P., 2008. Competition between functional brain networks mediates behavioral variability. NeuroImage 39, 527–537. doi:10.1016/j.neuroimage.2007.08.008

Kennis, M., Rademaker, A.R., van Rooij, S.J.H., Kahn, R.S., Geuze, E., 2015. Resting state functional connectivity of the anterior cingulate cortex in veterans with and without post-traumatic stress disorder. Hum. Brain Mapp. 36, 99–109. doi:10.1002/hbm.22615

Kim, D.-J., Bolbecker, A.R., Howell, J., Rass, O., Sporns, O., Hetrick, W.P., Breier, A., O'Donnell, B.F., 2013. Disturbed resting state EEG synchronization in bipolar disorder: A graph-theoretic analysis. NeuroImage Clin. 2, 414–423. doi:10.1016/j.nicl.2013.03.007

Koch, W., Teipel, S., Mueller, S., Buerger, K., Bokde, A.L.W., Hampel, H., Coates, U., Reiser, M., Meindl, T., 2010. Effects of aging on default mode network activity in resting state fMRI: does the method of analysis matter? NeuroImage 51, 280–287. doi:10.1016/j.neuroimage.2009.12.008

Kötter, R., 2004. Online retrieval, processing, and visualization of primate connectivity data from the CoCoMac database. Neuroinformatics 2, 127–144. doi:10.1385/NI:2:2:127

Kucyi, A., Davis, K.D., 2014. Dynamic functional connectivity of the default mode network tracks daydreaming. NeuroImage 100, 471–480. doi:10.1016/j.neuroimage.2014.06.044

Kuramoto, Y., 1986. Chemical Oscillations, Waves, and Turbulence. Springer-Verl. Berl.-Heidelb.-N. Y.-Tokyo 66, 296–296. doi:10.1002/zamm.19860660706

Lai, M.-C., Lombardo, M.V., Chakrabarti, B., Sadek, S.A., Pasco, G., Wheelwright, S.J., Bullmore, E.T., Baron-Cohen, S., MRC AIMS Consortium, Suckling, J., 2010. A shift to randomness of brain oscillations in people with autism. Biol. Psychiatry 68, 1092–1099. doi:10.1016/j.biopsych.2010.06.027

Laufs, H., Krakow, K., Sterzer, P., Eger, E., Beyerle, A., Salek-Haddadi, A., Kleinschmidt, A., 2003. Electroencephalographic signatures of attentional and cognitive default modes in spontaneous brain activity fluctuations at rest. Proc. Natl. Acad. Sci. 100, 11053–11058. doi:10.1073/pnas.1831638100

Le Bihan, D., Breton, E., Lallemand, D., Grenier, P., Cabanis, E., Laval-Jeantet, M., 1986. MR imaging of intravoxel incoherent motions: application to diffusion and perfusion in neurologic disorders. Radiology 161, 401–407. doi:10.1148/radiology.161.2.3763909

Le Bihan, D., Iima, M., 2015. Diffusion Magnetic Resonance Imaging: What Water Tells Us about Biological Tissues. PLoS Biol. 13, e1002203. doi:10.1371/journal.pbio.1002203

Leech, R., Sharp, D.J., 2014. The role of the posterior cingulate cortex in cognition and disease. Brain J. Neurol. 137, 12–32. doi:10.1093/brain/awt162

Lemieux, L., Salek-Haddadi, A., Lund, T.E., Laufs, H., Carmichael, D., 2007. Modelling large motion events in fMRI studies of patients with epilepsy. Magn. Reson. Imaging 25, 894–901. doi:10.1016/j.mri.2007.03.009

Leonardi, N., Richiardi, J., Van De Ville, D., 2013. Functional connectivity eigennetworks reveal different brain dynamics in multiple sclerosis patients, in: 2013 IEEE 10th International Symposium on Biomedical Imaging (ISBI). Presented at the 2013 IEEE 10th International Symposium on Biomedical Imaging (ISBI), pp. 528–531. doi:10.1109/ISBI.2013.6556528

Leonardi, N., Shirer, W.R., Greicius, M.D., Van De Ville, D., 2014. Disentangling dynamic networks: Separated and joint expressions of functional connectivity patterns in time. Hum. Brain Mapp. 35, 5984–5995. doi:10.1002/hbm.22599

Leonardi, N., Van De Ville, D., 2015. On spurious and real fluctuations of dynamic functional connectivity during rest. NeuroImage 104, 430–436. doi:10.1016/j.neuroimage.2014.09.007

Lewis, C.M., Baldassarre, A., Committeri, G., Romani, G.L., Corbetta, M., 2009. Learning sculpts the spontaneous activity of the resting human brain. Proc. Natl. Acad. Sci. 106, 17558–17563. doi:10.1073/pnas.0902455106

Liang, M., Zhou, Y., Jiang, T., Liu, Z., Tian, L., Liu, H., Hao, Y., 2006. Widespread functional disconnectivity in schizophrenia with resting-state functional magnetic resonance imaging. Neuroreport 17, 209–213.

Li, B., Liu, L., Friston, K.J., Shen, H., Wang, L., Zeng, L.-L., Hu, D., 2013. A Treatment-Resistant Default Mode Subnetwork in Major Depression. Biol. Psychiatry, Sources of Treatment Resistance in Depression: Inflammation and Functional Connectivity 74, 48–54. doi:10.1016/j.biopsych.2012.11.007

Liston, C., Chen, A.C., Zebley, B.D., Drysdale, A.T., Gordon, R., Leuchter, B., Voss, H.U., Casey, B.J., Etkin, A., Dubin, M.J., 2014. Default Mode Network Mechanisms of Transcranial Magnetic Stimulation in Depression. Biol. Psychiatry, Molecular and Neural Systems In Depression 76, 517–526. doi:10.1016/j.biopsych.2014.01.023

Liu, Y., Liang, M., Zhou, Y., He, Y., Hao, Y., Song, M., Yu, C., Liu, H., Liu, Z., Jiang, T., 2008. Disrupted small-world networks in schizophrenia. Brain J. Neurol. 131, 945–961. doi:10.1093/brain/awn018

Li, W., Antuono, P.G., Xie, C., Chen, G., Jones, J.L., Ward, B.D., Franczak, M.B., Goveas, J.S., Li, S.-J., 2012. Changes in regional cerebral blood flow and functional connectivity in the cholinergic pathway associated with cognitive perfor-

mance in subjects with mild Alzheimer's disease after 12-week donepezil treatment. NeuroImage 60, 1083–1091. doi:10.1016/j.neuroimage.2011.12.077
Lizier, J.T., Heinzle, J., Horstmann, A., Haynes, J.-D., Prokopenko, M., 2010. Multivariate information-theoretic measures reveal directed information structure and task relevant changes in fMRI connectivity. J. Comput. Neurosci. 30, 85–107. doi:10.1007/s10827-010-0271-2
Logothetis, N.K., Pauls, J., Augath, M., Trinath, T., Oeltermann, A., 2001. Neurophysiological investigation of the basis of the fMRI signal. Nature 412, 150–157. doi:10.1038/35084005
Loo, C., Katalinic, N., Mitchell, P.B., Greenberg, B., 2011. Physical treatments for bipolar disorder: a review of electroconvulsive therapy, stereotactic surgery and other brain stimulation techniques. J. Affect. Disord. 132, 1–13. doi:10.1016/j.jad.2010.08.017
Lou, H.C., Luber, B., Crupain, M., Keenan, J.P., Nowak, M., Kjaer, T.W., Sackeim, H.A., Lisanby, S.H., 2004. Parietal cortex and representation of the mental Self. Proc. Natl. Acad. Sci. U. S. A. 101, 6827–6832. doi:10.1073/pnas.0400049101
Lui, S., Wu, Q., Qiu, L., Yang, X., Kuang, W., Chan, R.C.K., Huang, X., Kemp, G.J., Mechelli, A., Gong, Q., 2011. Resting-state functional connectivity in treatment-resistant depression. Am. J. Psychiatry 168, 642–648. doi:10.1176/appi.ajp.2010.10101419
Lustig, C., Snyder, A.Z., Bhakta, M., O'Brien, K.C., McAvoy, M., Raichle, M.E., Morris, J.C., Buckner, R.L., 2003. Functional deactivations: change with age and dementia of the Alzheimer type. Proc. Natl. Acad. Sci. U. S. A. 100, 14504–14509. doi:10.1073/pnas.2235925100
Lv, P., Guo, L., Hu, X., Li, X., Jin, C., Han, J., Li, L., Liu, T., 2013. Modeling dynamic functional information flows on large-scale brain networks. Med. Image Comput. Comput.-Assist. Interv. MICCAI Int. Conf. Med. Image Comput. Comput.-Assist. Interv. 16, 698–705.
Lynall, M.-E., Bassett, D.S., Kerwin, R., McKenna, P.J., Kitzbichler, M., Muller, U., Bullmore, E., 2010. Functional connectivity and brain networks in schizophrenia. J. Neurosci. Off. J. Soc. Neurosci. 30, 9477–9487. doi:10.1523/JNEUROSCI.0333-10.2010
Majeed, W., Magnuson, M., Hasenkamp, W., Schwarb, H., Schumacher, E.H., Barsalou, L., Keilholz, S.D., 2011. Spatiotemporal dynamics of low frequency BOLD fluctuations in rats and humans. NeuroImage 54, 1140–1150. doi:10.1016/j.neuroimage.2010.08.030
Majeed, W., Magnuson, M., Keilholz, S.D., 2009. Spatiotemporal dynamics of low frequency fluctuations in BOLD fMRI of the rat. J. Magn. Reson. Imaging 30, 384–393. doi:10.1002/jmri.21848
Manjón, J.V., Coupé, P., Concha, L., Buades, A., Collins, D.L., Robles, M., 2013. Diffusion weighted image denoising using overcomplete local PCA. PloS One 8, e73021. doi:10.1371/journal.pone.0073021
Mantini, D., Perrucci, M.G., Gratta, C.D., Romani, G.L., Corbetta, M., 2007. Electrophysiological signatures of resting state networks in the human brain. Proc. Natl. Acad. Sci. 104, 13170–13175. doi:10.1073/pnas.0700668104
Margulies, D.S., Kelly, A.M.C., Uddin, L.Q., Biswal, B.B., Castellanos, F.X., Milham, M.P., 2007. Mapping the functional connectivity of anterior cingulate cortex. NeuroImage 37, 579–588. doi:10.1016/j.neuroimage.2007.05.019

Martinussen, M., Flanders, D.W., Fischl, B., Busa, E., Løhaugen, G.C., Skranes, J., Vangberg, T.R., Brubakk, A.-M., Haraldseth, O., Dale, A.M., 2009. Segmental brain volumes and cognitive and perceptual correlates in 15-year-old adolescents with low birth weight. J. Pediatr. 155, 848–853.e1. doi:10.1016/j.jpeds.2009.06.015

Ma, S., Calhoun, V.D., Phlypo, R., Adalı, T., 2014. Dynamic changes of spatial functional network connectivity in healthy individuals and schizophrenia patients using independent vector analysis. NeuroImage 90, 196–206. doi:10.1016/j.neuroimage.2013.12.063

Maximo, J.O., Keown, C.L., Nair, A., Müller, R.-A., 2013. Approaches to local connectivity in autism using resting state functional connectivity MRI. Front. Hum. Neurosci. 7, 605. doi:10.3389/fnhum.2013.00605

Maxim, V., Şendur, L., Fadili, J., Suckling, J., Gould, R., Howard, R., Bullmore, E., 2005. Fractional Gaussian noise, functional MRI and Alzheimer's disease. NeuroImage 25, 141–158. doi:10.1016/j.neuroimage.2004.10.044

Mazoyer, B., Zago, L., Mellet, E., Bricogne, S., Etard, O., Houdé, O., Crivello, F., Joliot, M., Petit, L., Tzourio-Mazoyer, N., 2001. Cortical networks for working memory and executive functions sustain the conscious resting state in man. Brain Res. Bull. 54, 287–298.

McCarton, C.M., Wallace, I.F., Divon, M., Vaughan, H.G., 1996. Cognitive and neurologic development of the premature, small for gestational age infant through age 6: comparison by birth weight and gestational age. Pediatrics 98, 1167–1178.

Messé, A., Benali, H., Marrelec, G., 2015. Relating structural and functional connectivity in MRI: a simple model for a complex brain. IEEE Trans. Med. Imaging 34, 27–37. doi:10.1109/TMI.2014.2341732

Messé, A., Rudrauf, D., Benali, H., Marrelec, G., 2014. Relating Structure and Function in the Human Brain: Relative Contributions of Anatomy, Stationary Dynamics, and Non-stationarities. PLoS Comput Biol 10, e1003530. doi:10.1371/journal.pcbi.1003530

Milgram, S., 1967. The Small-World Problem. Psychology Today 1, 61–67.

M. Kady, S., Gardosi, J., 2004. Perinatal mortality and fetal growth restriction. Best Pract. Res. Clin. Obstet. Gynaecol., Fetal Surveillance 18, 397–410. doi:10.1016/j.bpobgyn.2004.02.009

Moran, R.J., Jung, F., Kumagai, T., Endepols, H., Graf, R., Dolan, R.J., Friston, K.J., Stephan, K.E., Tittgemeyer, M., 2011. Dynamic Causal Models and Physiological Inference: A Validation Study Using Isoflurane Anaesthesia in Rodents. PLoS ONE 6, e22790. doi:10.1371/journal.pone.0022790

Morris, C., Lecar, H., 1981. Voltage oscillations in the barnacle giant muscle fiber. Biophys. J. 35, 193–213. doi:10.1016/S0006-3495(81)84782-0

Motulsky, A.G., 2006. Genetics of complex diseases. J. Zhejiang Univ. Sci. B 7, 167–168. doi:10.1631/jzus.2006.B0167

Murphy, K., Birn, R.M., Handwerker, D.A., Jones, T.B., Bandettini, P.A., 2009. The impact of global signal regression on resting state correlations: Are anti-correlated networks introduced? NeuroImage 44, 893–905. doi:10.1016/j.neuroimage.2008.09.036

Murray, E., Fernandes, M., Fazel, M., Kennedy, S.H., Villar, J., Stein, A., 2015. Differential effect of intrauterine growth restriction on childhood neurodevelopment: a

systematic review. BJOG Int. J. Obstet. Gynaecol. doi:10.1111/1471-0528.13435
Musiek, E.S., Holtzman, D.M., 2015. Three dimensions of the amyloid hypothesis: time, space and "wingmen." Nat. Neurosci. 800–806. doi:10.1038/nn.4018
Myers, R.E., Sperry, R.W., 1953. Interocular transfer of a visual form discrimination habit in cats after section of the optic chiasm and corpus callosum. Anat. Rec. 115.
Näätänen, R., Alho, K., 1995. Mismatch negativity--a unique measure of sensory processing in audition. Int. J. Neurosci. 80, 317–337.
Nagumo, J., Arimoto, S., Yoshizawa, S., 1962. An active pulse transmission line simulating nerve axon. Proc IRE 50, 2061–2070.
Nakagawa, T., Woolrich, M., Luckhoo, H., Joensson, M., Mohseni, H., Kringelbach, M.L., Jirsa, V., Deco, G., 2014. How delays matter in an oscillatory whole-brain spiking-neuron network model for MEG alpha-rhythms at rest. Neuroimage 87, 383–394.
Nijhuis, E.H.J., van Cappellen van Walsum, A.-M., Norris, D.G., 2013. Topographic hub maps of the human structural neocortical network. PloS One 8, e65511. doi:10.1371/journal.pone.0065511
Nomi, J.S., Uddin, L.Q., 2015. Developmental changes in large-scale network connectivity in autism. NeuroImage Clin. 7, 732–741. doi:10.1016/j.nicl.2015.02.024
Nugent, J., Brazelton, T., 2000. Preventive mental health: Uses of the Brazelton Scale. Wiley, New York, NY.
Ogawa, S., Lee, T.M., Kay, A.R., Tank, D.W., 1990. Brain magnetic resonance imaging with contrast dependent on blood oxygenation. Proc. Natl. Acad. Sci. U. S. A. 87, 9868–9872.
Olson, I.R., Plotzker, A., Ezzyat, Y., 2007. The Enigmatic temporal pole: a review of findings on social and emotional processing. Brain 130, 1718–1731. doi:10.1093/brain/awm052
Padilla, N., Falcón, C., Sanz-Cortés, M., Figueras, F., Bargallo, N., Crispi, F., Eixarch, E., Arranz, A., Botet, F., Gratacós, E., 2011. Differential effects of intrauterine growth restriction on brain structure and development in preterm infants: A magnetic resonance imaging study. Brain Res. 1382, 98–108. doi:10.1016/j.brainres.2011.01.032
Patel, R.S., Bowman, F.D., Rilling, J.K., 2006. A Bayesian approach to determining connectivity of the human brain. Hum. Brain Mapp. 27, 267–276. doi:10.1002/hbm.20182
Penny, W.D., Roberts, S.J., 2002. Bayesian multivariate autoregressive models with structured priors. IEE Proc. Vis. Image Signal Process. 149, 33–41. doi:10.1049/ip-vis:20020149
Penny, W.D., Stephan, K.E., Mechelli, A., Friston, K.J., 2004. Comparing dynamic causal models. NeuroImage 22, 1157–1172. doi:10.1016/j.neuroimage.2004.03.026
Petrella, J.R., Wang, L., Krishnan, S., Slavin, M.J., Prince, S.E., Tran, T.-T.T., Doraiswamy, P.M., 2007. Cortical deactivation in mild cognitive impairment: high-field-strength functional MR imaging. Radiology 245, 224–235. doi:10.1148/radiol.2451061847
Plassman, B.L., Langa, K.M., Fisher, G.G., Heeringa, S.G., Weir, D.R., Ofstedal, M.B., Burke, J.R., Hurd, M.D., Potter, G.G., Rodgers, W.L., Steffens, D.C., Willis,

R.J., Wallace, R.B., 2007. Prevalence of dementia in the United States: the aging, demographics, and memory study. Neuroepidemiology 29, 125–132. doi:10.1159/000109998

Ponce-Alvarez, A., Deco, G., Hagmann, P., Romani, G.L., Mantini, D., Corbetta, M., 2015. Resting-State Temporal Synchronization Networks Emerge from Connectivity Topology and Heterogeneity. PLoS Comput Biol 11, e1004100. doi:10.1371/journal.pcbi.1004100

Popovic, D., Torrent, C., Goikolea, J.M., Cruz, N., Sánchez-Moreno, J., González-Pinto, A., Vieta, E., 2014. Clinical implications of predominant polarity and the polarity index in bipolar disorder: a naturalistic study. Acta Psychiatr. Scand. 129, 366–374. doi:10.1111/acps.12179

Qi, Z., Wu, X., Wang, Z., Zhang, N., Dong, H., Yao, L., Li, K., 2010. Impairment and compensation coexist in amnestic MCI default mode network. NeuroImage 50, 48–55. doi:10.1016/j.neuroimage.2009.12.025

Quian Quiroga, R., Kraskov, A., Kreuz, T., Grassberger, P., 2002. Performance of different synchronization measures in real data: A case study on electroencephalographic signals. Phys. Rev. E 65, 041903. doi:10.1103/PhysRevE.65.041903

Raichle, M.E., MacLeod, A.M., Snyder, A.Z., Powers, W.J., Gusnard, D.A., Shulman, G.L., 2001. A default mode of brain function. Proc. Natl. Acad. Sci. 98, 676–682. doi:10.1073/pnas.98.2.676

Ramasubbu, R., Konduru, N., Cortese, F., Bray, S., Gaxiola, I., Goodyear, B., 2014. Reduced intrinsic connectivity of amygdala in adults with major depressive disorder. Neuropsychiatr. Imaging Stimul. 5, 17. doi:10.3389/fpsyt.2014.00017

Ramirez, M.J., Lai, M.K.P., Tordera, R.M., Francis, P.T., 2014. Serotonergic therapies for cognitive symptoms in Alzheimer's disease: rationale and current status. Drugs 74, 729–736. doi:10.1007/s40265-014-0217-5

Ramsey, J.D., Hanson, S.J., Hanson, C., Halchenko, Y.O., Poldrack, R.A., Glymour, C., 2010. Six problems for causal inference from fMRI. NeuroImage 49, 1545–1558. doi:10.1016/j.neuroimage.2009.08.065

Rashid, B., Damaraju, E., Pearlson, G.D., Calhoun, V.D., 2014. Dynamic connectivity states estimated from resting fMRI Identify differences among Schizophrenia, bipolar disorder, and healthy control subjects. Front. Hum. Neurosci. 8. doi:10.3389/fnhum.2014.00897

Razi, A., Kahan, J., Rees, G., Friston, K.J., 2015. Construct validation of a DCM for resting state fMRI. NeuroImage 106, 1–14. doi:10.1016/j.neuroimage.2014.11.027

Robinson, H.P., Fleming, J.E., 1975. A critical evaluation of sonar "crown-rump length" measurements. Br. J. Obstet. Gynaecol. 82, 702–710.

Rodrigues, P., Prats-Galino, A., Gallardo-Pujol, D., Villoslada, P., Falcon, C., Prčkovska, V., 2013. Evaluating Structural Connectomics in Relation to Different Q-space Sampling Techniques, in: Mori, K., Sakuma, I., Sato, Y., Barillot, C., Navab, N. (Eds.), Medical Image Computing and Computer-Assisted Intervention – MICCAI 2013, Lecture Notes in Computer Science. Springer Berlin Heidelberg, pp. 671–678.

Rogers, B.P., Katwal, S.B., Morgan, V.L., Asplund, C.L., Gore, J.C., 2010. Functional MRI and multivariate autoregressive models. Magn. Reson. Imaging 28, 1058–1065. doi:10.1016/j.mri.2010.03.002

Rogers, B.P., Morgan, V.L., Newton, A.T., Gore, J.C., 2007. Assessing functional connectivity in the human brain by fMRI. Magn. Reson. Imaging 25, 1347–1357. doi:10.1016/j.mri.2007.03.007

Rolls, E.T., Deco, G., 2011. Prediction of decisions from noise in the brain before the evidence is provided. Front. Neurosci. 5. doi:10.3389/fnins.2011.00033

Rombouts, S.A.R.B., Barkhof, F., Goekoop, R., Stam, C.J., Scheltens, P., 2005. Altered resting state networks in mild cognitive impairment and mild Alzheimer's disease: An fMRI study. Hum. Brain Mapp. 26, 231–239. doi:10.1002/hbm.20160

Rombouts, S.A.R.B., Damoiseaux, J.S., Goekoop, R., Barkhof, F., Scheltens, P., Smith, S.M., Beckmann, C.F., 2009. Model-free group analysis shows altered BOLD FMRI networks in dementia. Hum. Brain Mapp. 30, 256–266. doi:10.1002/hbm.20505

Rubinov, M., Sporns, O., 2010. Complex network measures of brain connectivity: uses and interpretations. NeuroImage 52, 1059–1069. doi:10.1016/j.neuroimage.2009.10.003

Sadeh, N., Spielberg, J.M., Miller, M.W., Milberg, W.P., Salat, D.H., Amick, M.M., Fortier, C.B., McGlinchey, R.E., 2015. Neurobiological indicators of disinhibition in posttraumatic stress disorder. Hum. Brain Mapp. 36, 3076–3086. doi:10.1002/hbm.22829

Sakoğlu, Ü., Pearlson, G.D., Kiehl, K.A., Wang, Y.M., Michael, A.M., Calhoun, V.D., 2010. A method for evaluating dynamic functional network connectivity and task-modulation: application to schizophrenia. Magn. Reson. Mater. Phys. Biol. Med. 23, 351–366. doi:10.1007/s10334-010-0197-8

Salomon, R., Bleich-Cohen, M., Hahamy-Dubossarsky, A., Dinstien, I., Weizman, R., Poyurovsky, M., Kupchik, M., Kotler, M., Hendler, T., Malach, R., 2011. Global functional connectivity deficits in schizophrenia depend on behavioral state. J. Neurosci. Off. J. Soc. Neurosci. 31, 12972–12981. doi:10.1523/JNEUROSCI.2987-11.2011

Salvador, R., Martínez, A., Pomarol-Clotet, E., Sarró, S., Suckling, J., Bullmore, E., 2007. Frequency based mutual information measures between clusters of brain regions in functional magnetic resonance imaging. NeuroImage 35, 83–88. doi:10.1016/j.neuroimage.2006.12.001

Sanz-Arigita, E.J., Schoonheim, M.M., Damoiseaux, J.S., Rombouts, S.A.R.B., Maris, E., Barkhof, F., Scheltens, P., Stam, C.J., 2010. Loss of "small-world" networks in Alzheimer's disease: graph analysis of FMRI resting-state functional connectivity. PloS One 5, e13788. doi:10.1371/journal.pone.0013788

Schmahmann, J.D., Pandya, D.N., Wang, R., Dai, G., D'Arceuil, H.E., Crespigny, A.J. de, Wedeen, V.J., 2007. Association fibre pathways of the brain: parallel observations from diffusion spectrum imaging and autoradiography. Brain 130, 630–653. doi:10.1093/brain/awl359

Schmidt, H., Petkov, G., Richardson, M.P., Terry, J.R., 2014. Dynamics on networks: the role of local dynamics and global networks on the emergence of hypersynchronous neural activity. PLoS Comput. Biol. 10, e1003947. doi:10.1371/journal.pcbi.1003947

Schotten, M.T. de, Dell'Acqua, F., Ratiu, P., Leslie, A., Howells, H., Cabanis, E., Iba-Zizen, M.T., Plaisant, O., Simmons, A., Dronkers, N.F., Corkin, S., Catani, M., 2015. From Phineas Gage and Monsieur Leborgne to H.M.: Revisiting Disconnection Syndromes. Cereb. Cortex bhv173. doi:10.1093/cercor/bhv173

Scoville, W.B., Milner, B., 1957. Loss of Recent Memory After Bilateral Hippocampal Lesions. J. Neurol. Neurosurg. Psychiatry 20, 11–21. doi:10.1136/jnnp.20.1.11
Shanahan, M., 2010. Metastable chimera states in community-structured oscillator networks. Chaos Woodbury N 20, 013108. doi:10.1063/1.3305451
Sheline, Y.I., Price, J.L., Yan, Z., Mintun, M.A., 2010. Resting-state functional MRI in depression unmasks increased connectivity between networks via the dorsal nexus. Proc. Natl. Acad. Sci. U. S. A. 107, 11020–11025. doi:10.1073/pnas.1000446107
Sheline, Y.I., Raichle, M.E., Snyder, A.Z., Morris, J.C., Head, D., Wang, S., Mintun, M.A., 2010. Amyloid plaques disrupt resting state default mode network connectivity in cognitively normal elderly. Biol. Psychiatry 67, 584–587. doi:10.1016/j.biopsych.2009.08.024
Shi, F., Yap, P.-T., Wu, G., Jia, H., Gilmore, J.H., Lin, W., Shen, D., 2011. Infant brain atlases from neonates to 1- and 2-year-olds. PloS One 6, e18746. doi:10.1371/journal.pone.0018746
Shimizu, S., Hoyer, P.O., Hyvärinen, A., Kerminen, A., 2006. A linear non-gaussian acyclic model for causal discovery. J. Mach. Learn. Res. 7, 2003–2030.
Shulman, G.L., Fiez, J.A., Corbetta, M., Buckner, R.L., Miezin, F.M., Raichle, M.E., Petersen, S.E., 1997. Common Blood Flow Changes across Visual Tasks: II. Decreases in Cerebral Cortex. J. Cogn. Neurosci. 9, 648–663. doi:10.1162/jocn.1997.9.5.648
Skranes, J., Lohaugen, G.C., Martinussen, M., Indredavik, M.S., Dale, A.M., Haraldseth, O., Vangberg, T.R., Brubakk, A.-M., 2009. White matter abnormalities and executive function in children with very low birth weight. Neuroreport 20, 263–266.
Skranes, J.S., Martinussen, M., Smevik, O., Myhr, G., Indredavik, M., Vik, T., Brubakk, A.-M., 2005. Cerebral MRI findings in very-low-birth-weight and small-for-gestational-age children at 15 years of age. Pediatr. Radiol. 35, 758–765. doi:10.1007/s00247-005-1446-2
Smith, J.F., Pillai, A., Chen, K., Horwitz, B., 2010. Identification and validation of effective connectivity networks in functional magnetic resonance imaging using switching linear dynamic systems. NeuroImage 52, 1027–1040. doi:10.1016/j.neuroimage.2009.11.081
Smith, S.M., Miller, K.L., Moeller, S., Xu, J., Auerbach, E.J., Woolrich, M.W., Beckmann, C.F., Jenkinson, M., Andersson, J., Glasser, M.F., Essen, D.C.V., Feinberg, D.A., Yacoub, E.S., Ugurbil, K., 2012. Temporally-independent functional modes of spontaneous brain activity. Proc. Natl. Acad. Sci. 109, 3131–3136. doi:10.1073/pnas.1121329109
Smith, S.M., Miller, K.L., Salimi-Khorshidi, G., Webster, M., Beckmann, C.F., Nichols, T.E., Ramsey, J.D., Woolrich, M.W., 2011. Network modelling methods for FMRI. NeuroImage 54, 875–891. doi:10.1016/j.neuroimage.2010.08.063
Sorg, C., Riedl, V., Mühlau, M., Calhoun, V.D., Eichele, T., Läer, L., Drzezga, A., Förstl, H., Kurz, A., Zimmer, C., Wohlschläger, A.M., 2007. Selective changes of resting-state networks in individuals at risk for Alzheimer's disease. Proc. Natl. Acad. Sci. U. S. A. 104, 18760–18765. doi:10.1073/pnas.0708803104
Sperling, R.A., Aisen, P.S., Beckett, L.A., Bennett, D.A., Craft, S., Fagan, A.M., Iwatsubo, T., Jack, C.R., Kaye, J., Montine, T.J., Park, D.C., Reiman, E.M., Rowe, C.C., Siemers, E., Stern, Y., Yaffe, K., Carrillo, M.C., Thies, B., Morri-

son-Bogorad, M., Wagster, M.V., Phelps, C.H., 2011. Toward defining the preclinical stages of Alzheimer's disease: recommendations from the National Institute on Aging-Alzheimer's Association workgroups on diagnostic guidelines for Alzheimer's disease. Alzheimers Dement. J. Alzheimers Assoc. 7, 280–292. doi:10.1016/j.jalz.2011.03.003

Sperling, R.A., Laviolette, P.S., O'Keefe, K., O'Brien, J., Rentz, D.M., Pihlajamaki, M., Marshall, G., Hyman, B.T., Selkoe, D.J., Hedden, T., Buckner, R.L., Becker, J.A., Johnson, K.A., 2009. Amyloid deposition is associated with impaired default network function in older persons without dementia. Neuron 63, 178–188. doi:10.1016/j.neuron.2009.07.003

Spisák, T., Jakab, A., Kis, S.A., Opposits, G., Aranyi, C., Berényi, E., Emri, M., 2014. Voxel-wise motion artifacts in population-level whole-brain connectivity analysis of resting-state FMRI. PloS One 9, e104947. doi:10.1371/journal.pone.0104947

Sporns, O., 2014. Contributions and challenges for network models in cognitive neuroscience. Nat. Neurosci. 17, 652–660. doi:10.1038/nn.3690

Sporns, O., Tononi, G., Kötter, R., 2005. The human connectome: A structural description of the human brain. PLoS Comput. Biol. 1, e42. doi:10.1371/journal.pcbi.0010042

Sripada, R.K., King, A.P., Garfinkel, S.N., Wang, X., Sripada, C.S., Welsh, R.C., Liberzon, I., 2012. Altered resting-state amygdala functional connectivity in men with posttraumatic stress disorder. J. Psychiatry Neurosci. JPN 37, 241–249. doi:10.1503/jpn.110069

Stephan, K.E., Kamper, L., Bozkurt, A., Burns, G.A., Young, M.P., Kötter, R., 2001. Advanced database methodology for the Collation of Connectivity data on the Macaque brain (CoCoMac). Philos. Trans. R. Soc. Lond. B. Biol. Sci. 356, 1159–1186. doi:10.1098/rstb.2001.0908

Stephan, K.E., Roebroeck, A., 2012. A short history of causal modeling of fMRI data. NeuroImage 62, 856–863. doi:10.1016/j.neuroimage.2012.01.034

Stephan, K.E., Weiskopf, N., Drysdale, P.M., Robinson, P.A., Friston, K.J., 2007. Comparing hemodynamic models with DCM. NeuroImage 38, 387–401. doi:10.1016/j.neuroimage.2007.07.040

Strakowski, S.M., Adler, C.M., Almeida, J., Altshuler, L.L., Blumberg, H.P., Chang, K.D., DelBello, M.P., Frangou, S., McIntosh, A., Phillips, M.L., Sussman, J.E., Townsend, J.D., 2012. The functional neuroanatomy of bipolar disorder: a consensus model. Bipolar Disord. 14, 313–325. doi:10.1111/j.1399-5618.2012.01022.x

Swartz, B.E., 1998. The advantages of digital over analog recording techniques. Electroencephalogr. Clin. Neurophysiol. 106, 113–117. doi:10.1016/S0013-4694(97)00113-2

Tagliazucchi, E., Balenzuela, P., Fraiman, D., Chialvo, D.R., 2012a. Criticality in Large-Scale Brain fMRI Dynamics Unveiled by a Novel Point Process Analysis. Front. Physiol. 3. doi:10.3389/fphys.2012.00015

Tagliazucchi, E., Carhart-Harris, R., Leech, R., Nutt, D., Chialvo, D.R., 2014. Enhanced repertoire of brain dynamical states during the psychedelic experience. Hum. Brain Mapp. 35, 5442–5456. doi:10.1002/hbm.22562

Tagliazucchi, E., Von Wegner, F., Morzelewski, A., Brodbeck, V., Laufs, H., 2012b. Dynamic BOLD functional connectivity in humans and its electrophysiological correlates. Front. Hum. Neurosci. 6, 339. doi:10.3389/fnhum.2012.00339

Thompson, G.J., Merritt, M.D., Pan, W.-J., Magnuson, M.E., Grooms, J.K., Jaeger, D., Keilholz, S.D., 2013. Neural correlates of time-varying functional connectivity in the rat. NeuroImage 83, 826–836. doi:10.1016/j.neuroimage.2013.07.036

Tolsa, C.B., Zimine, S., Warfield, S.K., Freschi, M., Rossignol, A.S., Lazeyras, F., Hanquinet, S., Pfizenmaier, M., Hüppi, P.S., 2004. Early Alteration of Structural and Functional Brain Development in Premature Infants Born with Intrauterine Growth Restriction. Pediatr. Res. 56, 132–138. doi:10.1203/01.PDR.0000128983.54614.7E

Toulmin, H., Beckmann, C.F., O'Muircheartaigh, J., Ball, G., Nongena, P., Makropoulos, A., Ederies, A., Counsell, S.J., Kennea, N., Arichi, T., Tusor, N., Rutherford, M.A., Azzopardi, D., Gonzalez-Cinca, N., Hajnal, J.V., Edwards, A.D., 2015. Specialization and integration of functional thalamocortical connectivity in the human infant. Proc. Natl. Acad. Sci. 112, 6485–6490. doi:10.1073/pnas.1422638112

Travers, J., Milgram, S., 1969. An Experimental Study of the Small World Problem. Sociometry 32, 425–443.

Tustison, N.J., Avants, B.B., Cook, P.A., Zheng, Y., Egan, A., Yushkevich, P.A., Gee, J.C., 2010. N4ITK: improved N3 bias correction. IEEE Trans. Med. Imaging 29, 1310–1320. doi:10.1109/TMI.2010.2046908

Tzourio-Mazoyer, N., Landeau, B., Papathanassiou, D., Crivello, F., Etard, O., Delcroix, N., Mazoyer, B., Joliot, M., 2002. Automated anatomical labeling of activations in SPM using a macroscopic anatomical parcellation of the MNI MRI single-subject brain. NeuroImage 15, 273–289. doi:10.1006/nimg.2001.0978

Uddin, L.Q., Clare Kelly, A. m., Biswal, B.B., Xavier Castellanos, F., Milham, M.P., 2009. Functional connectivity of default mode network components: Correlation, anticorrelation, and causality. Hum. Brain Mapp. 30, 625–637. doi:10.1002/hbm.20531

Umbricht, D., Koller, R., Schmid, L., Skrabo, A., Grübel, C., Huber, T., Stassen, H., 2003. How specific are deficits in mismatch negativity generation to schizophrenia? Biol. Psychiatry 53, 1120–1131.

Umbricht, D., Krljes, S., 2005. Mismatch negativity in schizophrenia: a meta-analysis. Schizophr. Res. 76, 1–23. doi:10.1016/j.schres.2004.12.002

Utevsky, A.V., Smith, D.V., Huettel, S.A., 2014. Precuneus Is a Functional Core of the Default-Mode Network. J. Neurosci. 34, 932–940. doi:10.1523/JNEUROSCI.4227-13.2014

van den Heuvel, M.P., Mandl, R.C.W., Kahn, R.S., Hulshoff Pol, H.E., 2009a. Functionally linked resting-state networks reflect the underlying structural connectivity architecture of the human brain. Hum. Brain Mapp. 30, 3127–3141. doi:10.1002/hbm.20737

van den Heuvel, M.P., Sporns, O., 2013. Network hubs in the human brain. Trends Cogn. Sci. 17, 683–696. doi:10.1016/j.tics.2013.09.012

van den Heuvel, M.P., Stam, C.J., Kahn, R.S., Hulshoff Pol, H.E., 2009b. Efficiency of functional brain networks and intellectual performance. J. Neurosci. Off. J. Soc. Neurosci. 29, 7619–7624. doi:10.1523/JNEUROSCI.1443-09.2009

van der Want, J.J., Klooster, J., Cardozo, B.N., de Weerd, H., Liem, R.S., 1997. Tract-tracing in the nervous system of vertebrates using horseradish peroxidase and its conjugates: tracers, chromogens and stabilization for light and electron microscopy. Brain Res. Brain Res. Protoc. 1, 269–279.

Vargas, C., López-Jaramillo, C., Vieta, E., 2013. A systematic literature review of resting state network—functional MRI in bipolar disorder. J. Affect. Disord. 150, 727–735. doi:10.1016/j.jad.2013.05.083

Vedel Jensen, E.B., Thorarinsdottir, T.L., 2007. A Spatio-Temporal Model for Functional Magnetic Resonance Imaging Data – with a View to Resting State Networks. Scand. J. Stat. 34, 587–614. doi:10.1111/j.1467-9469.2006.00554.x

Veer, I.M., Beckmann, C., Van Tol, M.-J., Ferrarini, L., Milles, J., Veltman, D., Aleman, A., Van Buchem, M.A., Van Der Wee, N.J.A., Rombouts, S.A.R., 2010. Whole brain resting-state analysis reveals decreased functional connectivity in major depression. Front. Syst. Neurosci. 4, 41. doi:10.3389/fnsys.2010.00041

Vieta Pascual, E., Torrent Font, C., Martínez-Arán, A., Colom Victoriano, F., Reinares Gabnepen, M., Benabarre Hernández, A., Comes Forastero, M., Goikolea Alberdi, J.M., 2002. [A user-friendly scale for the short and long term outcome of bipolar disorder: the CGI-BP-M]. Actas Esp. Psiquiatr. 30, 301–304.

Vincent, J.L., Patel, G.H., Fox, M.D., Snyder, A.Z., Baker, J.T., Van Essen, D.C., Zempel, J.M., Snyder, L.H., Corbetta, M., Raichle, M.E., 2007. Intrinsic functional architecture in the anaesthetized monkey brain. Nature 447, 83–86. doi:10.1038/nature05758

Vuksanović, V., Hövel, P., 2015. Dynamic changes in network synchrony reveal resting-state functional networks. Chaos Woodbury N 25, 023116. doi:10.1063/1.4913526

Waites, A.B., Stanislavsky, A., Abbott, D.F., Jackson, G.D., 2005. Effect of prior cognitive state on resting state networks measured with functional connectivity. Hum. Brain Mapp. 24, 59–68. doi:10.1002/hbm.20069

Wang, L., Benzinger, T.L., Hassenstab, J., Blazey, T., Owen, C., Liu, J., Fagan, A.M., Morris, J.C., Ances, B.M., 2015. Spatially distinct atrophy is linked to β-amyloid and tau in preclinical Alzheimer disease. Neurology 84, 1254–1260. doi:10.1212/WNL.0000000000001401

Wang, L., Hermens, D.F., Hickie, I.B., Lagopoulos, J., 2012. A systematic review of resting-state functional-MRI studies in major depression. J. Affect. Disord. 142, 6–12. doi:10.1016/j.jad.2012.04.013

Wang, L., Li, K., Zhang, Q.-E., Zeng, Y.-W., Jin, Z., Dai, W.-J., Su, Y.-A., Wang, G., Tan, Y.-L., Yu, X., Si, T.-M., 2013. Interhemispheric Functional Connectivity and Its Relationships with Clinical Characteristics in Major Depressive Disorder: A Resting State fMRI Study. PLoS ONE 8, e60191. doi:10.1371/journal.pone.0060191

Wang, L., Zang, Y., He, Y., Liang, M., Zhang, X., Tian, L., Wu, T., Jiang, T., Li, K., 2006. Changes in hippocampal connectivity in the early stages of Alzheimer's disease: evidence from resting state fMRI. NeuroImage 31, 496–504. doi:10.1016/j.neuroimage.2005.12.033

Wang, Y., Zhong, S., Jia, Y., Zhou, Z., Zhou, Q., Huang, L., 2015. Reduced interhemispheric resting-state functional connectivity in unmedicated bipolar II disorder. Acta Psychiatr. Scand. doi:10.1111/acps.12429

Watts, D.J., Strogatz, S.H., 1998. Collective dynamics of "small-world" networks. Nature 393, 440–442. doi:10.1038/30918

Wedeen, V.J., Hagmann, P., Tseng, W.-Y.I., Reese, T.G., Weisskoff, R.M., 2005. Mapping complex tissue architecture with diffusion spectrum magnetic resonance imaging. Magn. Reson. Med. 54, 1377–1386. doi:10.1002/mrm.20642

Wei, M., Qin, J., Yan, R., Bi, K., Liu, C., Yao, Z., Lu, Q., 2015. Association of resting-state network dysfunction with their dynamics of inter-network interactions in depression. J. Affect. Disord. 174, 527–534. doi:10.1016/j.jad.2014.12.020

Wei, M., Qin, J., Yan, R., Li, H., Yao, Z., Lu, Q., 2013. Identifying major depressive disorder using Hurst exponent of resting-state brain networks. Psychiatry Res. Neuroimaging 214, 306–312. doi:10.1016/j.pscychresns.2013.09.008

Weng, S.-J., Wiggins, J.L., Peltier, S.J., Carrasco, M., Risi, S., Lord, C., Monk, C.S., 2010. Alterations of resting state functional connectivity in the default network in adolescents with autism spectrum disorders. Brain Res. 1313, 202–214. doi:10.1016/j.brainres.2009.11.057

Whitfield-Gabrieli, S., Ford, J.M., 2012. Default Mode Network Activity and Connectivity in Psychopathology. Annu. Rev. Clin. Psychol. 8, 49–76. doi:10.1146/annurev-clinpsy-032511-143049

Wilson, H.R., Cowan, J.D., 1972. Excitatory and inhibitory interactions in localized populations of model neurons. Biophys. J. 12, 1–24. doi:10.1016/S0006-3495(72)86068-5

Wittchen, H.U., Jacobi, F., Rehm, J., Gustavsson, A., Svensson, M., Jönsson, B., Olesen, J., Allgulander, C., Alonso, J., Faravelli, C., Fratiglioni, L., Jennum, P., Lieb, R., Maercker, A., van Os, J., Preisig, M., Salvador-Carulla, L., Simon, R., Steinhausen, H.-C., 2011. The size and burden of mental disorders and other disorders of the brain in Europe 2010. Eur. Neuropsychopharmacol. J. Eur. Coll. Neuropsychopharmacol. 21, 655–679. doi:10.1016/j.euroneuro.2011.07.018

Wong, K.-F., Wang, X.-J., 2006. A Recurrent Network Mechanism of Time Integration in Perceptual Decisions. J. Neurosci. 26, 1314–1328. doi:10.1523/JNEUROSCI.3733-05.2006

Xia, M., Wang, J., He, Y., 2013. BrainNet Viewer: A Network Visualization Tool for Human Brain Connectomics. PLoS ONE 8, e68910. doi:10.1371/journal.pone.0068910

Yang, G.J., Murray, J.D., Repovs, G., Cole, M.W., Savic, A., Glasser, M.F., Pittenger, C., Krystal, J.H., Wang, X.-J., Pearlson, G.D., Glahn, D.C., Anticevic, A., 2014. Altered global brain signal in schizophrenia. Proc. Natl. Acad. Sci. U. S. A. 111, 7438–7443. doi:10.1073/pnas.1405289111

Yan, X., Brown, A.D., Lazar, M., Cressman, V.L., Henn-Haase, C., Neylan, T.C., Shalev, A., Wolkowitz, O.M., Hamilton, S.P., Yehuda, R., Sodickson, D.K., Weiner, M.W., Marmar, C.R., 2013. Spontaneous brain activity in combat related PTSD. Neurosci. Lett. 547, 1–5. doi:10.1016/j.neulet.2013.04.032

Yoshiyama, Y., Lee, V.M.Y., Trojanowski, J.Q., 2013. Therapeutic strategies for tau mediated neurodegeneration. J. Neurol. Neurosurg. Psychiatry 84, 784–795. doi:10.1136/jnnp-2012-303144

Yu, Q., Erhardt, E.B., Sui, J., Du, Y., He, H., Hjelm, D., Cetin, M.S., Rachakonda, S., Miller, R.L., Pearlson, G., Calhoun, V.D., 2015. Assessing dynamic brain graphs of time-varying connectivity in fMRI data: application to healthy con-

trols and patients with schizophrenia. NeuroImage 107, 345–355. doi:10.1016/j.neuroimage.2014.12.020

Zalesky, A., Fornito, A., Bullmore, E.T., 2010. Network-based statistic: Identifying differences in brain networks. NeuroImage 53, 1197–1207. doi:10.1016/j.neuroimage.2010.06.041

Zalesky, A., Fornito, A., Cocchi, L., Gollo, L.L., Breakspear, M., 2014. Time-resolved resting-state brain networks. Proc. Natl. Acad. Sci. 111, 10341–10346. doi:10.1073/pnas.1400181111

Zeng, L.-L., Shen, H., Liu, L., Wang, L., Li, B., Fang, P., Zhou, Z., Li, Y., Hu, D., 2012. Identifying major depression using whole-brain functional connectivity: a multivariate pattern analysis. Brain 135, 1498–1507. doi:10.1093/brain/aws059

Zhang, H.-Y., Wang, S.-J., Xing, J., Liu, B., Ma, Z.-L., Yang, M., Zhang, Z.-J., Teng, G.-J., 2009. Detection of PCC functional connectivity characteristics in resting-state fMRI in mild Alzheimer's disease. Behav. Brain Res. 197, 103–108. doi:10.1016/j.bbr.2008.08.012

Zhou, Y., Yu, C., Zheng, H., Liu, Y., Song, M., Qin, W., Li, K., Jiang, T., 2010. Increased neural resources recruitment in the intrinsic organization in major depression. J. Affect. Disord. 121, 220–230. doi:10.1016/j.jad.2009.05.029

Notes